Enhancing the Performance of Si/Gr Anodes by Evaluating the Impact of Electrolyte Formulations on the Solid Electrolyte Interphase

Zur Erlangung des akademischen Grades eines

DOKTORS DER NATURWISSENSCHAFTEN

(Dr. rer. nat.)

von der KIT-Fakultät für Chemie und Biowissenschaften

des Karlsruher Instituts für Technologie (KIT)

genehmigte

DISSERTATION

von

M. Sc. Lydia Gehrlein

1. Referent: Prof. Dr. Helmut Ehrenberg
2. Referent: Prof. Dr. Clemens Heske

Tag der mündlichen Prüfung: 18.07.2022

Selbständigkeitserklärung

Hiermit versichere ich, dass ich die vorliegende Arbeit selbstständig verfasst habe, dass ich keine anderen als die angegebenen Quellen und Hilfsmittel benutzt habe, dass ich die wörtlich oder inhaltlich übernommenen Stellen als solche gekennzeichnet habe und dass ich die Satzung des KIT zur Sicherung guter wissenschaftlicher Praxis in der jeweils gültigen Fassung beachtet habe.

Karlsruhe, den 31.05.2022

Lydia Gehrlein

Abstract

Lithium-ion batteries (LIB) are the most used mobile energy storage system. Their application to electric transportation and grid storage requires increasingly higher energy and power densities. One way to achieve higher energy densities is to replace graphite with silicon, a material with high theoretical capacity. However, silicon is difficult to integrate as anode material for LIBs because of its volume changes during cycling. The resulting mechanical strains particularly affect the stability of silicon particles, the electrode coating, and the solid electrolyte interphase (SEI). Especially the SEI's ability to accommodate silicon volume changes is fundamental to enabling the long cycle life of silicon-containing anodes. It is formed by solid electrolyte decomposition products which precipitate on the anode surface. Improving the SEI properties can be achieved by a smart selection of the electrolyte components. Ethylene carbonate (EC) is often one of the main electrolyte solvents. However, its decomposition products have a poor ability to accommodate the silicon volume changes. Therefore, this thesis investigates alternative electrolyte solvents based on their ability to form decomposition products with an improved ability to accommodate the silicon volume changes. For this, a systematic analysis of the SEI thickness and composition is performed with x-ray photoelectron spectroscopy (XPS). Electrode and SEI morphologies are analyzed via scanning electron microscopy (SEM). SEI properties and electrochemical performance are correlated for each electrolyte formulation.

Formulations based on fluoroethylene carbonate (FEC) as cosolvent form the first EC-free electrolyte class. FEC is mostly used as an electrolyte additive to increase the lifetime of silicon-containing anodes. However, it is consumed during cycling, resulting in a decrease in electrochemical performance, after its concentration drops below a certain level. A further benefit of FEC is that it exhibits similar lithium-ion transport properties to EC, making it a suitable replacement for EC. Two electrolyte formulations with different FEC concentrations are compared to an FEC-additive electrolyte.[1] Based on the results from XPS measurements, it is found that FEC decomposes to -C-O, DO (1,3-dioxolan-2-one), -CO_2Li, Li_2CO_3, and LiF. The species -C-O, DO, and -CO_2Li are most probably incorporated in a cross-linked polymer network. Due to its chemical environment, detecting DO is an unambiguous indicator for the presence of FEC decomposition products in the SEI, as this species does not form with any other electrolyte component. Compared to the FEC-additive electrolyte, Si/Gr electrodes cycled in FEC cosolvent formulations showed (1) better electrochemical performance, (2) extended

---

[1] 1 M $LiPF_6$ in 20FEC:80DMC or 50FEC:50DMC; 1 M $LiPF_6$ in 1:1 EC:DMC + 2 vol.% FEC

presence of FEC decomposition products in the SEI (as indicated by the detection of DO), (3) thinner SEI, and (4) formation of SiO_xF_y species. The improved electrochemical performance of FEC cosolvent formulations can be attributed to the presence of FEC decomposition products in the SEI, even after prolonged cycling. The formed cross-linked polymeric network consisting of -C-O, DO, and -CO_2Li most likely increases the SEI flexibility upon silicon volume changes. As a result, less electrolyte is consumed, resulting in a thinner SEI, reduced isolation of active material, and the ability to maintain the electrode integrity.

Glyoxylic acetals constitute the second EC-free electrolyte class. They are selected due to their low environmental impact and excellent thermal stabilities when used with graphite anodes. Among them, two glyoxal-based electrolytes (TMG and TEG)[1] are examined for the first time in combination with Si/Gr anodes and compared to two carbonate-based reference electrolytes.[2] Overall, Si/Gr anodes cycled in TEG exhibit the best capacity retention with higher capacities. To increase the ionic conductivity of TEG, propylene carbonate (PC) is added. The electrolyte formulation is improved by adding the electrolyte additive fluoroethylene carbonate (FEC). Despite this, Si/Gr anodes cycled in pure TEG electrolyte still perform better than those cycled in 30TEG:70PC-FEC. The TEG solvent forms a smoother and more interconnected SEI, which appears to have better adaptability to changes in silicon volume.

Both approaches provide electrolyte formulations that exhibit improved electrochemical performance compared to the investigated EC-containing reference electrolytes. The results of this thesis indicate that this is accomplished by forming an SEI with an increased ability to accommodate the silicon volume changes. Here, organic decomposition products incorporating long-chained polymeric networks are crucial. These findings contribute to the understanding of the relationship between electrolyte formulation, SEI, and electrochemical performance, thus helping to realize future silicon-based electrodes in LIBs.

---

[1] TMG: 1 M lithium bis(trifluoromethanesulfonyl)imide LiTFSI in 1,1,2,2-tetramethoxyethane and TEG: 1 M LiTFSI in 1,1,2,2-tetraethoxyethane

[2] 1 M LiTFSI in 1:1 EC:DMC and 1 M $LiPF_6$ in 1:1 EC:DMC

Kurzfassung

Lithium-Ionen-Batterien (LIB) sind das am häufigsten verwendete mobile Energiespeichersystem. Ihre Anwendung für den elektrischen Verkehr und die Netzspeicherung erfordert immer höhere Energie- und Leistungsdichten. Höhere Energiedichten können erreicht werden, indem Graphit durch Silizium ersetzt wird. Silizium zeigt sehr viel größere Kapazitäten als Graphit. Allerdings weist es starke Volumenveränderungen während des Zyklierens auf, was seine Anwendung als Anodenmaterial für LIBs erschwert. Besonders betroffen von der mechanischen Belastung sind die Stabilität der Siliziumpartikel, der Elektrodenbeschichtung und der Festkörper-Elektrolyt-Grenzphase (*solid electrolyte interphase,* SEI). Für eine lange Lebensdauer ist es von grundlegender Bedeutung, dass die SEI die Volumenänderungen des Siliziums ausgleichen kann. Die SEI wird durch feste Elektrolytzersetzungsprodukte auf der Anodenoberfläche gebildet. Ihre Eigenschaften können durch die intelligente Auswahl der Elektrolytkomponenten verbessert werden. Ethylencarbonat (EC) ist ein häufig verwendetes Elektrolytlösungsmittel, dessen Zersetzungsprodukte nur bedingt in der Lage, sind die Volumenänderungen des Siliziums auszugleichen. Daher untersucht diese Arbeit alternative Elektrolytlösungsmittel auf ihre Fähigkeit Zersetzungsprodukte zu bilden, die sich der Volumenänderung des Siliziums anpassen können. Eine systematische Analyse der SEI-Dicke und -Zusammensetzung erfolgt mit Röntgenphotoelektronenspektroskopie (XPS). Die Charakterisierung der Elektrodenmorphologie geschieht mittels Rasterelektronenmikroskopie (REM). Für jede Elektrolytformulierung erfolgt eine Korrelation zwischen den beobachteten SEI-Eigenschaften und der elektrochemischen Leistungsfähigkeit.

Elektrolyt-Formulierungen basierend auf Fluorethylencarbonat (FEC) bilden die erste untersuchte EC-freie Elektrolytklasse. FEC wird meist als Elektrolytadditiv verwendet, um die Lebensdauer von siliziumhaltigen Anoden zu verlängern. Allerdings nimmt dessen Konzentration während des Zyklierens ab. Die Verwendung von FEC als Co-Lösungsmittel soll deshalb den lebensverlängernden Effekt verstärken. Ein weiterer Vorteil von FEC ist, dass es ähnliche Lithium-Ionen-Transporteigenschaften wie EC aufweist und somit ein geeigneter Ersatz für EC ist. Es werden zwei Elektrolytformulierungen unterschiedlicher FEC-Konzentrationen mit einem FEC-Additiv Elektrolyten verglichen.[1] XPS-Messungen zeigen, dass die Zersetzung von FEC zur Bildung von -C-O, DO (1,3-Dioxolan-2-on), -CO_2Li, Li_2CO_3 und LiF führt. Die Spezies -C-O, DO und CO_2Li sind höchstwahrscheinlich in ein vernetztes Polymer eingebunden. Aufgrund seiner chemischen Umgebung ist das Detektieren von DO ein eindeutiger Indikator

---

[1] 1 M $LiPF_6$ in 20FEC:80DMC or 50FEC:50DMC; 1 M $LiPF_6$ in 1:1 EC:DMC + 2 vol.% FEC

für das Vorhandensein von FEC-Zerfallsprodukten in der SEI, da sich DO aus keiner anderen Elektrolytkomponente bildet. Im Vergleich zum FEC-Additiv Elektrolyten zeigen Si/Gr-Elektroden, die in FEC Co-Lösungsmittel-Formulierungen zykliert werden folgende Eigenschaften: (1) bessere elektrochemische Leistungsfähigkeit, (2) längere Anwesenheit von FEC-Zersetzungsprodukten im SEI (wie durch das Vorhandensein von DO angezeigt), (3) dünnere SEI und (4) Bildung von SiO_xF_y-Verbindungen. Die bessere elektrochemische Leistungsfähigkeit der FEC-Co-Lösungsmittel-Formulierungen kann auf die Anwesenheit von FEC-Zersetzungsprodukten in der SEI zurückgeführt werden. Das entstehende vernetzte Polymer aus -C-O, DO und CO_2Li ist selbst nach längerem Zyklieren in der SEI auffindbar und erhöht höchstwahrscheinlich die Flexibilität der Schicht. Infolgedessen wird weniger Elektrolyt verbraucht, was zu einer dünneren SEI führt. Die verminderte SEI-Bildung führt zu einer geringeren elektronischen Isolierung des Aktivmaterials. Somit bleibt die Integrität der Elektrode länger erhalten.

Acetale auf Glyoxalbasis bilden die zweite Elektrolytklasse, die in dieser Arbeit untersucht werden. Ihre Auswahl begründet sich durch eine geringe Umweltbelastung und eine hervorragende thermische Stabilität bei der Verwendung mit Graphitanoden. Zwei glyoxalbasierte Elektrolyte (TMG und TEG)[1] werden zum ersten Mal mit Si/Gr-Anoden untersucht. Weiterhin erfolgt ein Vergleich mit zwei EC-haltigen Referenzelektrolyten.[2] Insgesamt zeigen in TEG zyklierte Si/Gr-Anoden die beste Kapazitätsretention mit den höchsten Kapazitäten. Um die Ionenleitfähigkeit von TEG zu erhöhen, wird Propylencarbonat (PC) beigemischt. Eine Verbesserung der Elektrolytformulierung erfolgt durch die Zugabe des Elektrolytadditivs FEC. Trotzdessen schneiden Si/Gr-Anoden, die in reinem TEG-Elektrolyt betrieben werden besser ab, als solche, die in 30TEG:70PC-FEC zykliert werden. Das kann daran liegen, dass TEG eine gleichmäßigere und stärker vernetzte SEI bildet, die sich besser an die Volumenänderungen des Siliziumvolumens anpasst.

Beide Ansätze liefern Elektrolytformulierungen mit verbesserter elektrochemischer Leistungsfähigkeit. Die Ergebnisse der vorliegenden Arbeit deuten darauf hin, dass dies durch die Bildung einer SEI erreicht wird, die sich besser an die Veränderungen des Siliziumvolumens anpassen kann. Hierfür spielen vor allem organische Zersetzungsprodukte wie langkettige polymere Netzwerke eine entscheidende Rolle. Die Erkenntnisse dieser Arbeit tragen zum Verständnis des Verhältnisses zwischen Elektrolytformulierung, SEI und elektrochemischer Leistung bei und helfen so, künftige siliziumbasierte Anoden in LIBs zu realisieren.

---

[1] TMG: 1 M lithium bis(trifluoromethansulfonyl)imid LiTFSI in 1,1,2,2-tetramethoxyethan and TEG: 1 M LiTFSI in 1,1,2,2-tetraethoxyethan

[2] 1 M LiTFSI in 1:1 EC:DMC and 1 M $LiPF_6$ in 1:1 EC:DMC

Table of content

Abbreviations

DEC	diethyl carbonate
DMC	dimethyl carbonate
EC	ethylene carbonate
EMC	ethyl methyl carbonate
FEC	fluoroethylene carbonate
HOMO	highest occupied molecular orbital
LEDC	lithium ethylene dicarbonate
LPDC	lithium propylene dicarbonate
LIB	lithium-ion battery
$LiPF_6$	lithium hexafluorophosphate
LiTFSI	lithium bis(trifluoromethanesulfonyl)imide
LUMO	lowest unoccupied molecular orbital
OCV	open-circuit voltage
DO	1,3-dioxolan-2-one
PAA	poly(acrylic acid)
PC	propylene carbonate
PEO	polyethylene oxide
Poly(VC)	poly(vinylene carbonate)
REM	Rasterelektronenmikroskopie
SEI	solid electrolyte interphase
SEM	scanning electron microscopy
Si/Gr	silicon/graphite
TMG	1 M LiTFSI in 1,1,2,2-tetramethoxyethane
TEG	1 M LiTFSI in 1,1,2,2-tetraethoxyethane
VC	vinylene carbonate
XPS	x-ray photoelectron spectroscopy

List of figures

List of tables

1 Introduction

The “2030 climate and energy framework” developed by the European Commission targets a cut in greenhouse gas emissions by at least 40 %.[1] Lithium-ion batteries (LIBs) are one of the main technologies driving this change. Compared to other energy storage systems, LIBs are a highly advanced electrochemical storage technology with a favorable performance-to-cost ratio. Currently, they are primarily used in consumer devices but find more and more applications in the electric transportation sector and as home and grid storage. Consequently, a high interest exists in research and development of improved LIB technologies.

A state-of-the-art LIB generally includes a transition-oxide positive electrode and graphite negative electrode. Current research and development aims to increase the energy and power density of LiBs. Optimizing cell design and chemistry is key to achieving this. With regards to anode materials, silicon has gained a lot of attention due to its high theoretical capacity, its abundant supply of raw materials, as well as its low costs.[3] However, its implementation is mostly hindered by large volume changes of the silicon particles during lithiation and delithiation.[4] The volume changes lead to significant mechanical stress on the silicon particle, the electrode coating, and the solid electrolyte interphase (SEI).[5]–[15] To mitigate some of these strains, silicon is blended with graphite, as it buffers the volume changes and increases the electrical contact between silicon particles.[16]–[22] Still, silicon/graphite (Si/Gr) electrodes suffer rapid capacity decay, especially with high silicon loadings. Another improvement can be achieved by stabilizing the SEI upon silicon volume changes. The SEI is a result of electrolyte decomposition. Electrolytes for LIBs are typically not stable over the entire applied potential window, and they are reduced at low potentials on the anode side. Part of the resulting decomposition products precipitate on the anode surface, forming the SEI. This layer serves as a protective, electrically insulating barrier and usually prevents further excessive electrolyte decomposition. However, most electrolytes do not form a layer upon decomposition that can sustain the silicon volume changes. Hence, the SEI oftentimes cracks which leads to continuous re-exposure of active material and ongoing electrolyte decomposition. Ultimately, the electrolyte is depleted of lithium-ions which are irreversibly bound in the SEI. Excessive SEI formation also leads to the electrical isolation of active material. All these phenomena hasten the end-of-life of the cell.[7],[10]–[15] It is therefore important to develop electrolyte formulations which form a flexible and stable SEI upon decomposition while still meeting safety, conductivity, and viscosity requirements.

This thesis aims to evaluate the impact of electrolyte formulations on their ability to form an SEI that can better accommodate the silicon volume changes during cycling. State-of-the-art electrolytes use carbonate-based electrolytes containing 1 M $LiPF_6$ in a mixture of ethylene carbonate (EC) and dimethyl carbonate (DMC). These electrolyte formulations perform very poorly with silicon-containing anodes. Especially EC forms a very unstable SEI layer in combination with silicon.[23] Therefore, two alternative cosolvents fall into closer consideration: fluoroethylene carbonate (FEC) and glyoxylic acetals. FEC is already widely used as an electrolyte additive with silicon-containing anodes and has been shown to increase their lifetime. Glyoxylic acetals are a very new electrolyte solvent class and have only been analyzed with graphite anodes so far. The electrochemical performance of both electrolyte classes is measured via galvanostatic cycling with potential limitation (GCPL) and differential capacity analysis (dQ/dE). SEI properties such as composition and thickness are determined via x-ray photoelectron spectroscopy (XPS). XPS has high surface and chemical sensitivity and is, therefore, an ideal technique to gain chemical information about the SEI layer. In addition, the electrode morphology is analyzed via scanning electron microscopy (SEM). Obtained SEI properties are correlated to electrochemical performances of the different electrolyte formulations. Using these analyses, it will be possible to determine which formulation displays the best performance with Si/Gr anodes.

2 Theoretical Background

This chapter covers the basics of electrochemistry as well as working principles and key parameters of LIBs. Different LIB components such as cathode, anode, and electrolyte are detailed. Furthermore, the theoretical background for x-ray photoelectron spectroscopy (XPS) is presented.

2.1 Lithium-Ion-Batteries

2.1.1 Working Principles

A LIB consists of a positive and negative electrode that can reversibly incorporate and release lithium-ions. **Figure 1** shows a LIB based on a graphite anode and a lithium metal oxide ($LiMO_2$) cathode. Both electrodes are separated by an electron-insulating but ion-permeable membrane (i.e., separator) which is not visible in **Figure 1** for reasons of clarity. The electrolyte enables lithium-ion transport between both electrodes. A LIB is charged by applying an anodic current that causes oxidation of the transition metal of the cathode material. The electrons released during this redox reaction are conducted via an external electrical conductor to the negative pole, here graphite. To balance the charge, lithium ions migrate from the cobalt oxide lattice of the cathode to the graphite anode where they are intercalated. Upon discharge the reverse processes occur spontaneously, providing the desired electrical power. Hereby, electrons flow from the anode to the cathode via the external conductor. At the same time, lithium ions leave the anode and intercalate back into the positive electrode. The direction of the discharging process is displayed by arrows in **Figure 1**. Redox processes at the positive and negative electrodes are summarized by Eq. (1) and (2).

Anode: $$6 \cdot \mathrm{C} + \mathrm{x} \cdot \mathrm{Li}^{+} \rightleftharpoons \mathrm{Li}_{\mathrm{x}}\mathrm{C}_{6} \tag{1}$$

Cathode: $$\mathrm{Li}_{\mathrm{x}-1}M\mathrm{O}_{2} + \mathrm{x} \cdot \mathrm{Li}^{+} + \mathrm{x} \cdot \mathrm{e}^{-} \rightleftharpoons \mathrm{Li}M\mathrm{O}_{2} \tag{2}$$

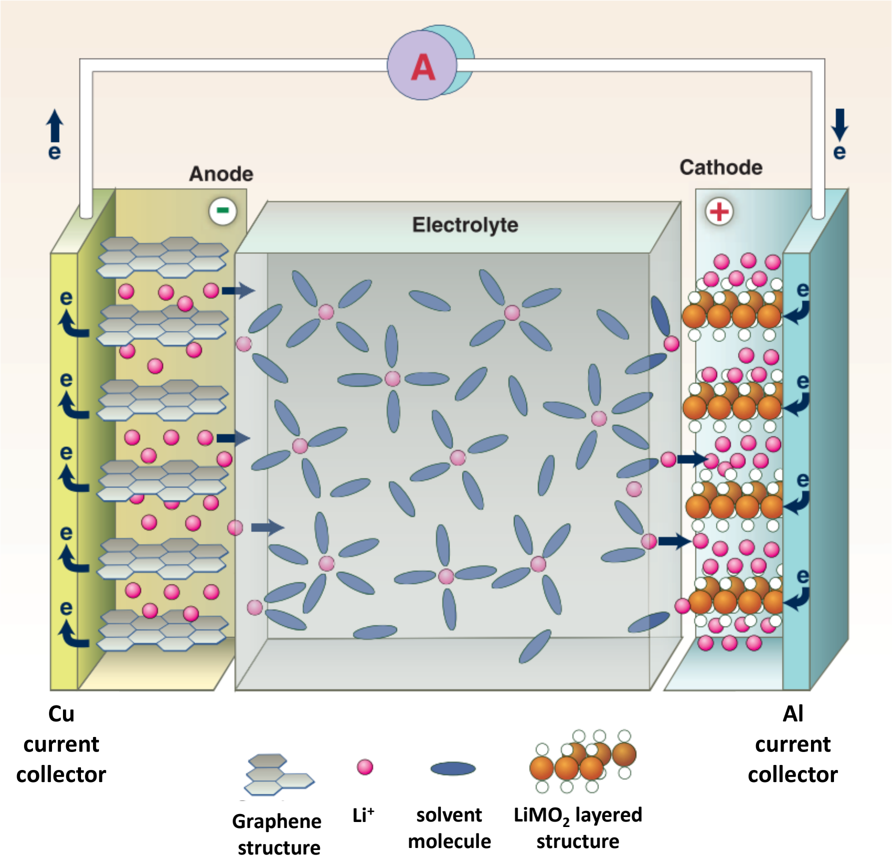

Figure 1: Schematic illustration of a lithium-ion battery. Adapted and modified from ref.[24].

2.1.2 Key Parameters

Battery Potential

In a battery, positive and negative electrodes have a corresponding inner potential $\Delta\phi_{e/s}$, which arises when two phases with different inner potentials are in contact, e.g., the electrode ϕ_e and electrolyte solution ϕ_s:

$$\Delta\phi_{e/s} = \phi_e - \phi_s \tag{3}$$

Let $\Delta\phi_{e/s}(cathode)$ be the cathode inner potential and $\Delta\phi_{e/s}(anode)$ the inner potential of the anode. If both electrodes are in electrical contact, an open-circuit voltage (OCV) $\Delta\Delta\phi$ can be measured, see Eq. (4):

$$\Delta\Delta\phi = \Delta\phi_{e/s}(cathode) - \Delta\phi_{e/s}(anode) \tag{4}$$

The larger $\Delta\Delta\phi$, the more energy is provided by the battery. Direct measurement of the inner potential $\Delta\phi_{e/s}$ is experimentally not feasible, since the measuring system will also possess a potential difference $\Delta\phi_{e/s}$. Any voltage measuring device connected to the system will therefore monitor a difference in the potential drops at the two electrode/solution interfaces. This problem is addressed by introducing reference electrodes (RE) which maintain a constant potential drop $\Delta\phi_{e/s}$ across its interface with the solution. Examples for RE are the standard hydrogen electrodes, and calomel or the silver/silver chloride electrode. In the case of LIBs, lithium-metal is used as a reference potential, which is then 0.00 V. In so-called half-cell setups, lithium metal serves as both reference and counter electrode. In a full-cell setup like LCO||graphite, the examination of processes occurring at exclusively one electrode can only be realized by a three-electrode cell setup. This thesis will only focus on a two-electrode setup.

Nernst Equation and Electrochemical Potential

The cell potential ΔE can be determined by the Nernst Equation, see Eq.(5):

$$\Delta E = \Delta E^0 - \frac{RT}{zF}\ln\prod_{i=1}^{k} a_i^{\nu_i} \tag{5}$$

where ΔE^0 is the cell potential at standard conditions, R the ideal gas constant, T the temperature, z the charge number of ion, F the Faradaic constant, and a_i the activity of ion i with stochiometric factor ν_i. The Nernst equation enables the determination of a cell potential ΔE by relating the measured cell potential to the reaction quotient $\left(\prod_{i=1}^{k} a_i^{\nu_i}\right)$. It also allows the accurate determination of equilibrium constants. From a thermodynamic perspective, the electrode potential ΔE can be correlated to Gibb’s free energy ΔG, see Eq. (6):

$$\Delta G = -z_i F \Delta E \tag{6}$$

Gibb’s free energy can predict the direction of a chemical reaction for constant temperature and pressure. For $\Delta G < 0$, the reaction is spontaneous and occurs without energy input. For $\Delta G > 0$, the reaction requires an input of external energy.

Battery Capacity and C-rate

The battery capacity represents the maximum amount of electrical charge Q that a battery can deliver or store. The charge Q is proportional to the time t when applying a constant current I:

$$Q = I \cdot t \tag{7}$$

In literature, the battery capacity is usually reported per mass in Ah g^{-1} or mAh g^{-1}, while electronic devices specify the capacity in Ah or mAh. The maximum capacity a material with molecular mass M can theoretically achieve is given by the theoretical capacity Q_{th}:

$$Q_{th} = \frac{z \cdot n \cdot F}{M} \tag{8}$$

where n is the maximum amount of insertable or extractable charge carriers with valence number z.

The C-rate indicates the time after which a cell is fully charged or discharged and is usually calculated with respect to the theoretical capacity of the material. Thus, C/5 means a complete charge or discharge of the battery after 5 hours. 2C stands for a complete discharge or charge in 30 minutes.

$$[C] = \frac{I}{Q} = \frac{1}{t} \tag{9}$$

Coulombic efficiency

The coulombic efficiency is the degree of reversibility of the charging and discharging process. It is calculated as the quotient of the charge and discharge capacities:

$$CE = \frac{Q_{charge}}{Q_{discharge}} \cdot 100 \tag{10}$$

Fully reversible processes would be indicated by CE = 100%, however, this can never be achieved by a battery, due to loss of lithium inventory and loss of active material.[25],[26] If 1000 stable cycles with more than 90 % capacity retention are desired, the averaged CE would have to be at least 99.99 %.[25]

Cycling stability, capacity retention, and cycle life

A battery is usually cycled under galvanostatic conditions (i.e., constant current) in a fixed voltage window. To determine how the capacity changes over cycling, it is plotted against the cycle number. Over time, the capacity decreases due to numerous degradation processes such as side reactions between electrode and electrolyte, loss of active electrode material, or the degradation of inactive components such as a binder, current collector, or separator.[27] Cycling conditions such as temperature or charge/discharge current also influence the cycling stability. To indicate how much capacity is retained after a number of cycles n, the capacity can be related to an earlier cycle, usually the first or the 2nd cycle:

$$Q_{ret} = \frac{Q_{n^{th}cycle}}{Q_{n-m^{th}cycle}} \tag{11}$$

The cycle life of rechargeable batteries is the number of charge/discharge cycles, which is feasible until the discharge capacity value falls below a certain limit of ≥ 80 %.[28] Accordingly, the longer a battery shows capacity retention above this limit the better its performance.

Gravimetric and volumetric energy density

The gravimetric or specific energy density w_m corresponds to the amount of energy stored in a given system per unit mass. A specific quantity always refers to the mass m_i of the components of the cell. The volumetric energy density w_v can be attributed to the electrical energy stored per unit volume V_i:

$$w_m = \frac{zF\Delta E}{\sum_i m_i}\left(\frac{Wh}{kg}\right) \quad or \quad w_v = \frac{zF\Delta E}{\sum_i V_i}\left(\frac{Wh}{L}\right) \tag{12}$$

Gravimetric/specific energies can also be calculated by multiplying capacity with the cell voltage, divided by the mass of anode and cathode:

$$w_m = \frac{Q(Ah) \cdot E_{we}(V)}{[m_{cathode} + m_{anode}](kg)} \tag{13}$$

The higher the gravimetric/specific energy density, the lighter the storage device can be. Also, the higher the volumetric energy density, the smaller the size of the battery. Because size and weight matter depending on the application, it is imperative to distinguish between both. In comparison to other rechargeable battery technologies such as nickel-cadmium or nickel-metal-hydride, LIBs offer one of the highest energy densities (100-265 Wh kg^{-1} or 250-670 Wh L^{-1}).[29],[30]

Gravimetric and volumetric power density

Gravimetric or specific power density and volumetric power density refer to the power (i.e., time rate of energy transfer) a battery can deliver per unit mass or volume, respectively:

$$p_m = \frac{\mathrm{I}\Delta E}{\sum_i m_i}\left(\frac{W}{kg}\right) \quad or \quad p = \frac{I\Delta E}{\sum_i V_i}\left(\frac{W}{L}\right) \tag{14}$$

High power densities enable high charge and discharge currents necessary for high power applications. Compared to the energy density, which states how much energy can be stored, power density asserts how fast the energy is delivered.

2.1.3 Components

Positive Electrode

Current cathode materials can be divided into three classes: layered oxides, spinels, and olivines. Layered oxides have the general formula $LiMO_2$, where M represents an electrochemically active transition metal such as manganese, nickel, cobalt, or mixtures of these. Due to 2d diffusion pathways, lithium intercalation and extraction are fast and reversible. However, only 50% of the lithium can be extracted from the material, otherwise, the structure collapses. Therefore, the theoretical capacity of ~274 mAh g^{-1} for $LiCoO_2$ which indicates the removal of all lithium-ions, cannot be achieved.[31] In addition, layered oxides suffer safety issues such as the release of gaseous oxygen and thermal runaway.[32] By introducing certain transition metals into the crystal structure, the material $LiNi_xMn_yCo_zO_2$ (NMC, with $0<x,y,z<1$) is obtained. NCM111 (i.e., $LiNi_{0.33}Mn_{0.33}Co_{0.33}O_2$) exhibits higher specific capacities than $LiCoO_2$ (170 mAh g^{-1} vs. 145 mAh g^{-1}) as well as greater structural stability. Spinels such as $LiMn_2O_4$ are another class of cathode materials.[33] They are cost-effective, environmentally friendly, and show very stable cycling behavior at room temperature.[34] However, they display lower capacities compared to NCM (~120 mAh g^{-1} of practical capacity). Among olivine-based materials, $LiFePO_4$ has been commercialized. It is characterized by high safety and good environmental compatibility. However, it shows lower specific capacity and gravimetric energy density than NCM. An overview of the crystal structures of the different materials is given in **Figure 2**.

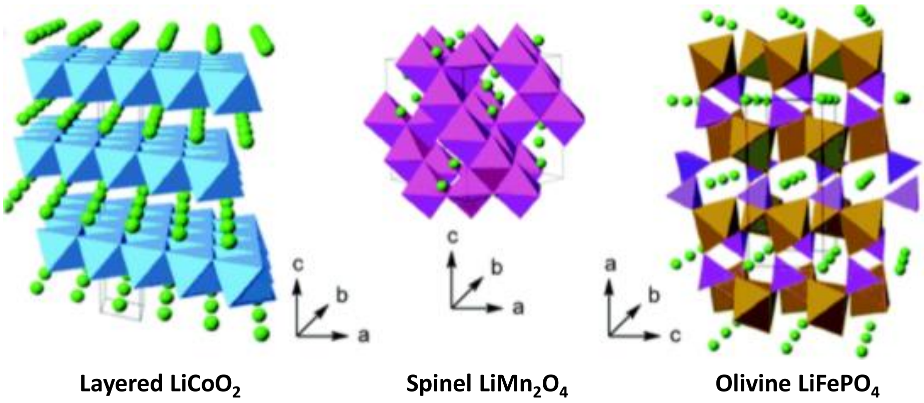

Figure 2: Crystal structures of insertion compounds LCO, LMO, and LFP according to dimensionality of Li^+ ions. Adapted and modified from ref.[35]

Negative Electrode

Negative electrode materials can be divided into three classes[36]:

1) Intercalation/ de-intercalation materials: carbon-based materials, graphene, TiO_2, $Li_4Ti_5O_{12}$, etc.

2) Alloy/de-alloying materials: Si, Ge, Sn, SnO_2, etc.

3) Conversion materials: transition metal oxides (Mn_xO_y, NiO, CuO, etc.)

Only carbon-based intercalation and silicon-based alloying materials will be discussed in this section.

Carbon-based materials can be divided into two categories, according to the degree of crystallinity and carbon atom stacking:[37],[38] SOFT carbon, where most of the crystallites are stacked in the same direction, and HARD carbon, where crystallites have disordered orientations. SOFT carbon or graphitic carbon have been state-of-the-art anode materials for more than 20 years. Alongside their low cost and high abundancy,[39],[40] they stand out from all other materials for several reasons: (1) The low redox potential of graphitic carbon vs. lithium maximizes the potential difference to the positive electrode; (2) A reversible capacity of around 350-370 mAh g^{-1} with coulombic efficiencies above 99 %, leading to long cycle life of the LIB; (3) High lithium diffusivity, high electric conductivity, and a moderate volume expansion upon lithium de-/intercalation.[41]

Graphite is made of sp^2 hybridized graphene layers that are linked by van der Waals forces and π-π interactions of the delocalized electron orbitals.[42],[43] In bulk graphite, these graphene layers can be stacked in two ways: the thermodynamically more stable ABAB sequence with hexagonal symmetry (~70 %) and in the less stable ABCABC sequence with rhombohedral symmetry (~30 %).[37],[44]–[46] This results in an anisotropic layered structure with basal and edge planes. Electrochemical intercalation of lithium-ion occurs on the graphite edge planes. Here, weak van der Waals forces allow for the expansion of the interlayer distance and the insertion of the ions. An idealized sketch of the lithium-intercalation process can be seen in **Figure 3**. When applying a constant current, plateaus and jumps in the voltage response are observed. A galvanostatic potential plateau corresponds to a specific stage of lithium intercalation, while jumps in potential are attributed to the transition from one intercalation stage to another. There are six stages of lithium intercalation: 1L, 4, 3, 2L, 2, and 1 (L indicates lithium-ions that are not perfectly ordered within the layers).[47]–[50] In the first Stage 1L, lithium-ions are randomly intercalated into the graphite particle, similar to solid-solution-type intercalation. A first-order phase transition occurs from Stage 1L to Stage 4, in which every fourth interlayer is filled with lithium-ions. This is followed by the transition to Stage 3 and Stage 2L, where every third and second interlayer is filled, respectively. However, the definite structure of the Stage 2L phase is still discussed. Subsequent transition to Stage 2 involves an increase in lithium content within the same interlayer (i.e., every 2nd layer), accompanied by an enhancement in-plane ordering. The last transition to Stage 1 leads to the filling of every interlayer by lithium-ions, resulting in an overall stochiometric of LiC_6. By summing up the specific capacities of each intercalation stage, a theoretical specific capacity of 372 mAh g^{-1} can be achieved.

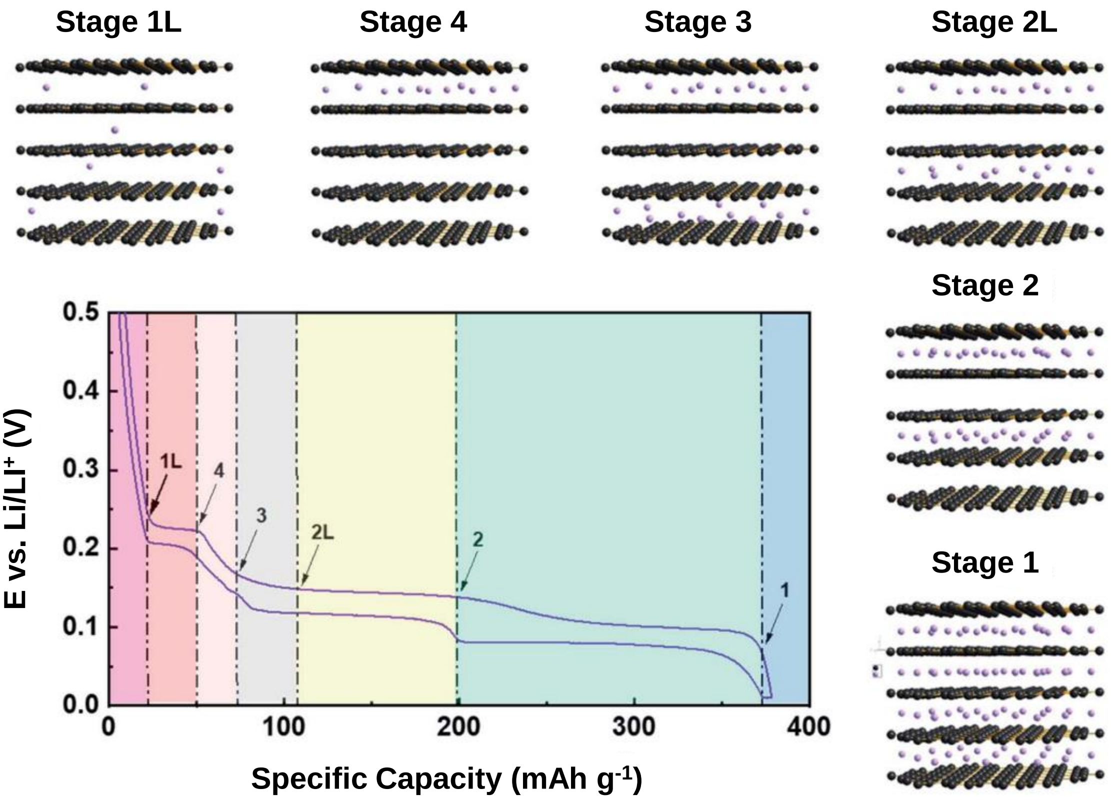

Figure 3: Stage formation during electrochemical intercalation of lithium into graphite. Adapted and modified from ref.[42]

The main drawback of graphite anodes is their low volumetric capacity when compared to other anode material candidates such as silicon, silicon oxide, tin, or tin oxide. Higher volumetric capacities are needed because the market demand for higher energy densities is growing.[51] Therefore, high-capacity anode materials have been extensively studied. One approach consists of investigating alloying materials based on silicon ($Li_{15}Si_4$, 3579 mAh g^{-1}), tin ($Li_{22}Sn_5$, 990 mAh g^{-1}), or germanium ($Li_{15}Ge_4$, 1600 mAh g^{-1}).[51] Another approach is based on conversion materials containing transition metal oxides such as Mn_xO_y, NiO, or CuO.

While conversion materials display low coulombic efficiencies and a large potential hysteresis, alloying materials suffer from large volume changes upon de-/lithiation, which leads to a poor cycle life. Nevertheless, silicon has gained high research interest due to its high specific capacity, low cost, and high abundance.[3]

Lithiation of crystalline silicon (c-Si) occurs via a two-phase mechanism in which the crystalline silicon is consumed to form lithiated amorphous silicon (Li_xSi), see **Figure 4**.[52]–[56] The partially lithiated silicon particles are separated from the still un-lithiated silicon core by a sharp reaction front. This has been explained by the large activation energy required to break up the crystalline silicon matrix.[55],[57] Upon further lithiation, the solid-state amorphization continues until the c-Si is fully lithiated and no crystallinity remains. While the formation of this amorphous a-Li_xSi phase is metastable at room temperature, it is still kinetically preferred over the intermetallic Li_xSi_y phases which form at 415°C (i.e., $Li_{12}Si_7$, Li_7Si_3, $Li_{13}Si_4$, $Li_{22}Si_5$).[52]–[54],[57] Below 50 mV vs Li/Li^+, the amorphous a-Li_xSi phase suddenly crystallizes to form $Li_{15}Si_4$, as is indicated by the red arrow in **Figure 4**.[58]–[60] $Li_{15}Si_4$ is not the most lithium-rich phase of the Li-Si diagram and is, like a-Li_xSi, metastable. In fact, silicon can theoretically form $Li_{22}Si_5$ phases which display a capacity of 4200 mAh g^{-1}. However, this phase has not been observed upon electrochemical lithiation, because its formation is kinetically hindered. Instead, $Li_{15}Si_4$ formation is favored as it displays similar local atomic environments to the a-Li_xSi phases.[58],[61],[62] Upon delithiation, the crystalline $Li_{15}Si_4$ transforms back to amorphous silicon in which state it remains during the whole delithiation process. At the beginning of the second lithiation process, a new plateau can be observed, corresponding to the lithiation of the amorphous silicon.

The main drawback of pure silicon anodes is the high volume increase of the silicon particle during lithiation (up to 300 %) and a subsequent decrease upon delithiation. Hereby, silicon particles are exposed to stresses which can cause fracture and mechanical degradation. Stresses can occur during single-phase and two-phase de-/lithiation. Upon single-phase de-/lithiation, the stress is more likely diffusion-induced and arises from inhomogeneous volume changes upon lithiation.[63]–[68] Although the outer shell grows in volume, the inner region contains less lithium and expands less. Stress during two-phase lithiation was found to be mainly caused by hoop tension.[69],[70] The two-phase reaction occurs during the first lithiation process, where unreacted crystalline silicon is converted to lithiated amorphous silicon. Hereby, the concentration of lithium ions changes over a sharp reaction front. Further lithiation at this reaction front causes volume expansion at the front, which pushes out already-lithiated material near the surface and eventually causes hoop tension. This tension at the surface can lead to crack initiation at the surface of silicon particles.[69],[71] Upon continuous cycling, the crack can propagate and ultimately lead to particle pulverization.[72],[73] Furthermore, the stress in silicon particles has been found to contribute to the voltage hysteresis present during charging/discharging.[74] Additionally, huge stresses developed at the Si/Li_xSi interphase reduce the thermodynamic driving force for the lithiation reaction.[75] This has a direct consequence on battery operation since the slowing of the reaction could limit charging rates.[56]

Another consequence of silicon particle expansion/contraction is the mechanical stress on the SEI, leading to continuous reactions at the electrode/electrolyte interphase. This part will be discussed in more detail in **Chapter 3**. To minimize the problems associated with high volume changes, several strategies are employed. They either involve changing the electrode composition (e.g., silicon morphology, binder) or altering the electrolyte formulation. Electrode composition may be modified by surface coating, special binder materials, or the blending of silicon with graphite. Electrolyte formulation highly influences the properties of the SEI. A smart selection of electrolyte components can improve the elasticity of this layer. For more details see **Chapter 3**.

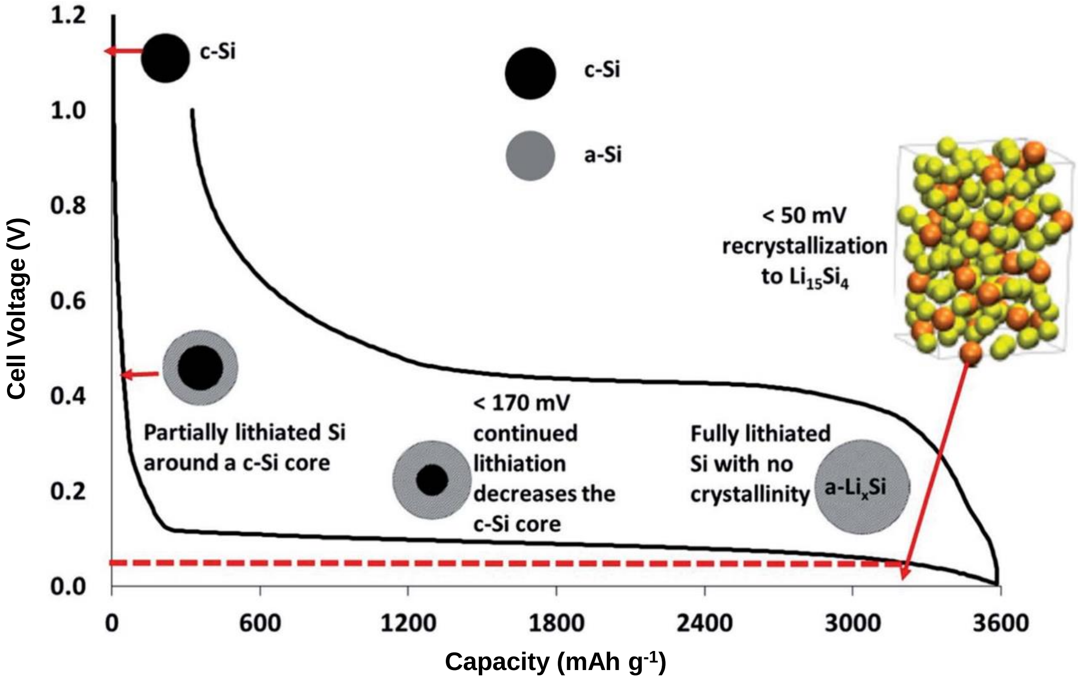

Figure 4: Galvanostatic charge/discharge of Si powder electrode at room temperature showing key lithiation steps. Adapted and modified from ref. [76]

Electrolyte

The function of an electrolyte in a LIB is to conduct lithium-ions. Materials with this property can be divided into three categories:[77]

- liquid electrolytes: aqueous electrolytes, non-aqueous electrolytes, ionic liquids
- polymer electrolytes: gel-like polymers, solid polymers
- solid electrolytes. inorganic ceramics

Only non-aqueous liquid electrolytes will be discussed in the following section. Performant electrolyte formulations are always a balance between physical properties, safety, price, availability, and stable SEI formation. Liquid, non-aqueous electrolytes usually consist of a lithium salt dissolved in a mixture of one or more organic solvent(s).

Electrolyte salts. Electrolyte salts must meet a broad range of properties such as high solubility in the electrolyte solvent(s), thermal stability, passivation of the aluminum current collector, stability against hydrolysis, and the formation of a stable SEI layer.[77]–[80] An overview of different lithium salts is given in **Table 1**, while molecular structures are displayed in **Figure 5**. Note that properties refer to their use when combined with non-aqueous organic solvents. Lithium hexafluorophosphate ($LiPF_6$) is used almost exclusively in commercial LIBs as it has demonstrated the best balance of the discussed properties required for application.

Table 1: Selection of lithium-salts and qualitative comparison of their physical properties.[81]

Salt	Thermal stability	Conductivity in aprotic solvents	Aluminum passivation	Undergoes hydrolysis	Safety
$LiPF_6$	low	high	yes, high	yes (forms HF)	toxic
LiTFSI	high	medium	no	no	toxic
$LiB(C_2O_4)_2$	high	medium	yes	no	safer
$LiClO_4$	high	high	yes, medium	no	explosive
$LiBF_4$	medium	low	yes, high	low	safer
$LiSO_3CF_3$	high	low	no	no	safer

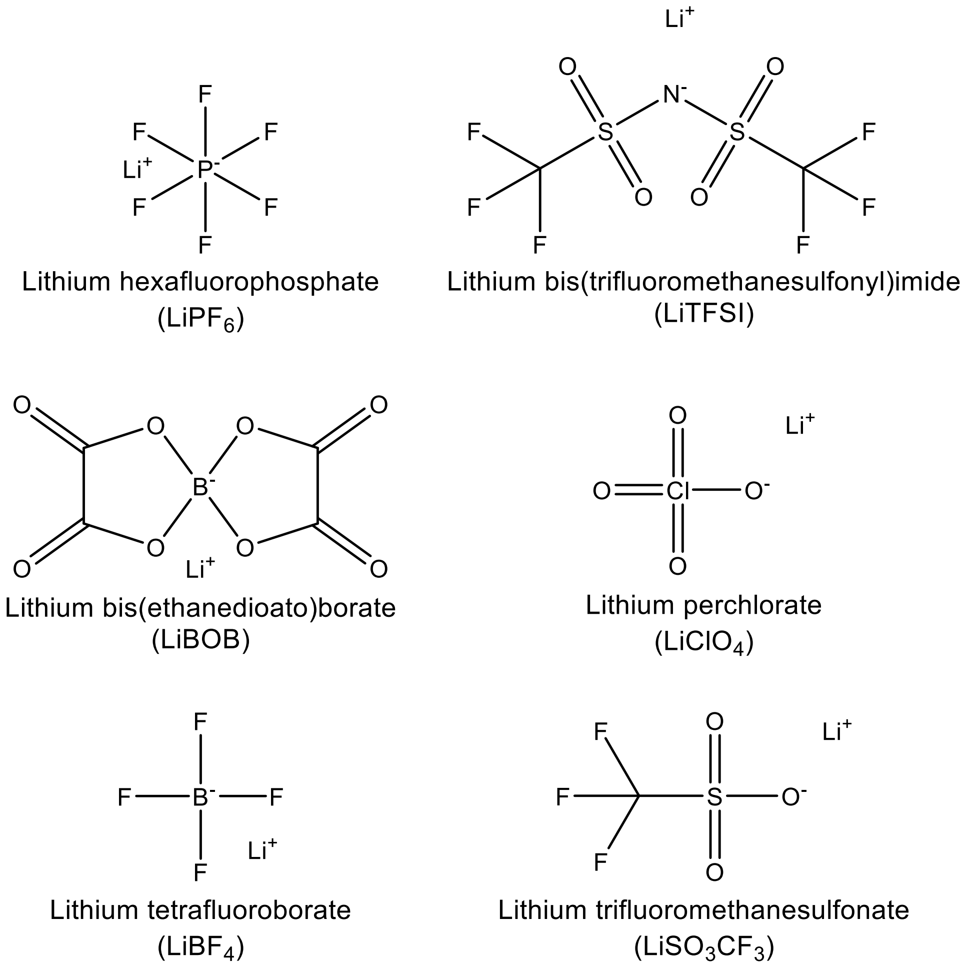

Lithium hexafluorophosphate ($LiPF_6$)

Lithium bis(trifluoromethanesulfonyl)imide (LiTFSI)

Lithium bis(ethanedioato)borate (LiBOB)

Lithium perchlorate ($LiClO_4$)

Lithium tetrafluoroborate ($LiBF_4$)

Lithium trifluoromethanesulfonate ($LiSO_3CF_3$)

Figure 5: Molecular structures of common lithium salts.

Organic solvents. Organic solvents should display high chemical and electrochemical stability, a wide operating temperature range, and high flame retardance.[78],[79],[82] Most used electrolyte solvents are carbonate-based. Physical properties such as relative permittivity or dielectric constant (ε_r), viscosity (η_0), melting point (mp), boiling point (bp), and flash point (fp) are displayed in **Table 2**. Molecular structures of corresponding solvent molecules are shown in **Figure 6**.

Table 2: Physical properties of carbonate solvents (ε_r and η_0 at 40 °C).[82]

Solvent	ε_r	η_0 (mPa s)	mp (°C)	bp (°C)	fp (°C)
EC	90	1.9	36	238	143
PC	65	2.5	-49	242	138
DMC	3.1	0.59	5	90	17
EMC	3.0	0.65	-53	108	23
DEC	2.8	0.75	-74	127	25

Electrolytic conductivity of a lithium salt in an organic solvent is, among other things, dependent on the dielectric constant and viscosity of the electrolyte solvent.[83] High dielectric constants are desired because they allow better shielding of the oppositely charged ions, thereby preventing ion association and irreversible salt precipitation. Low viscosities increase ion mobility and allow rapid ion transport between the electrodes. **Table 2** shows cyclic carbonates display higher dielectric constants but also higher viscosities. By contrast, linear carbonates show lower viscosities but also lower dielectric constants. Therefore, electrolyte solvents are usually made of a mixture of cyclic (e.g., ethylene carbonate (EC) or propylene carbonate (PC)) and linear carbonates (e.g., dimethyl carbonate (DMC), diethyl carbonate (DEC), or ethyl methyl carbonate (EMC)). LP30 is an example of a commercial electrolyte solution, which uses 1 mol l^{-1} of $LiPF_6$ in a 1:1 mixtures of EC:DMC.

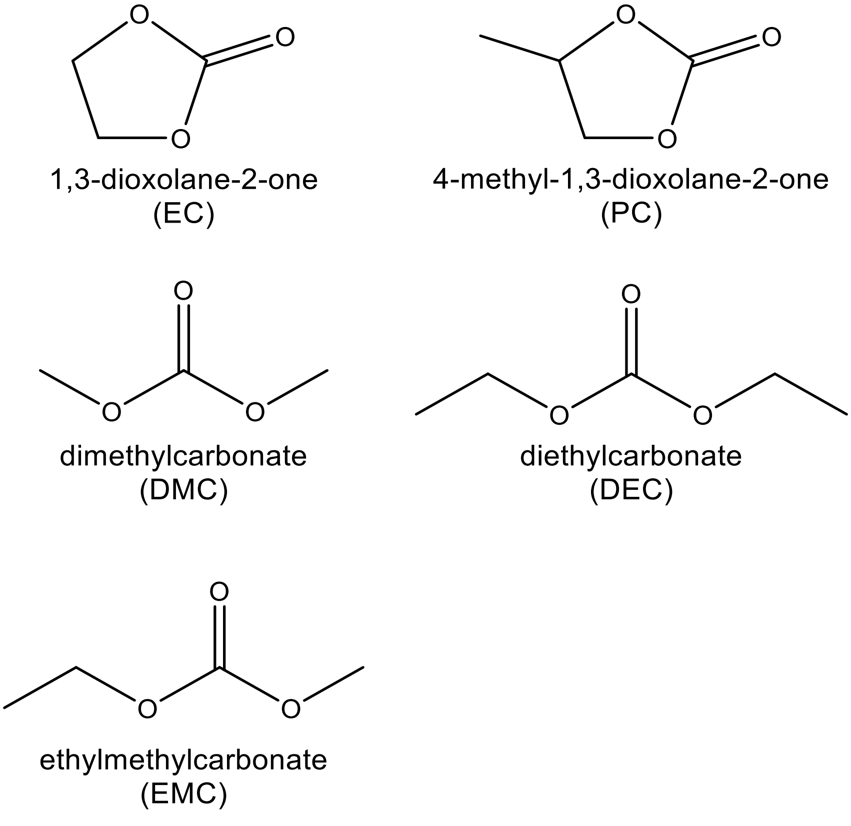

Figure 6: Molecular structures of common organic electrolyte solvents.

Electrolyte additives. Electrolyte formulations are usually optimized by adding a small amount (i.e., 2-10 vol.%) of a solid or liquid compound. Additives are mainly employed to improve certain performance parameters of a battery such as (1) safety, (2) SEI and/or CEI formation on anode and cathode, respectively, and (3) physical electrolyte properties such as ionic conductivity and viscosity. **Figure 7** displays a selection of different electrolyte additives. Battery safety can be enhanced by using flame retardant additives based on phosphates such as triphenylphosphate (TPP) or tris(2,2,2-trifluoroethyl)phosphate (TFP).[84]–[86] In order to achieve better SEI stabilities on the anode, a variety of additives has been investigated.[87] Most of them display higher reduction potentials than the electrolyte solvents, which diminishes the solvent reduction and leads to predominately additive-derived SEIs.[88] The most common additive to improve SEI properties on graphite is vinylene carbonate (VC).[89] While some studies have investigated VC for silicon-based anodes, fluoroethylene carbonate (FEC) is typically preferred.[90] Additives to improve the CEI on the cathode side usually display lower oxidation potentials than the electrolyte solvents. This diminishes both solvent oxidation at the positive electrode side and gas formation during cycling or open-circuit storage.[91] They typically contain C-F bonds ranging from 1,1,2,2-tetrafluoroethyl 2,2,3,3-tetrafluoropropyl ether (TTE)[92] to fluoroethylene carbonate (FEC).[93] However, the efficacity of FEC as high voltage additive is still disputed and it has been unable to suppress electrode cross-talk, i.e., transition metal dissolution from the cathode and deposition on the anode.[94] Lithium difluorophosphate (LiDFP) has shown to be very effective in suppressing cross-talk.[94] It also improves the coulombic efficiency, cycle lifetime, and decreases parasitic heat flow.[95],[96] Other additives to enhance CEI properties at high voltages and high temperatures are sulfur-based, such as 1,3,2-dioxathiolane-2,2-dioxide (DTD), 1,3-propane sultone (PS), or 1,2,6-oxadithiane 2,2,6,6-tetraoxide (ODTO).[88],[91] Lithium borate-based additives demonstrated to stabilize the high-temperature capacity of spinel $LiMn_2O_4$ (e.g., lithium bis(oxalato)borate (LiBOB), lithium difluoro(oxalato)borate (LiDFOB), or lithium difluoro bis(oxalate)phosphate (LiDFBOP)).[97],[98]

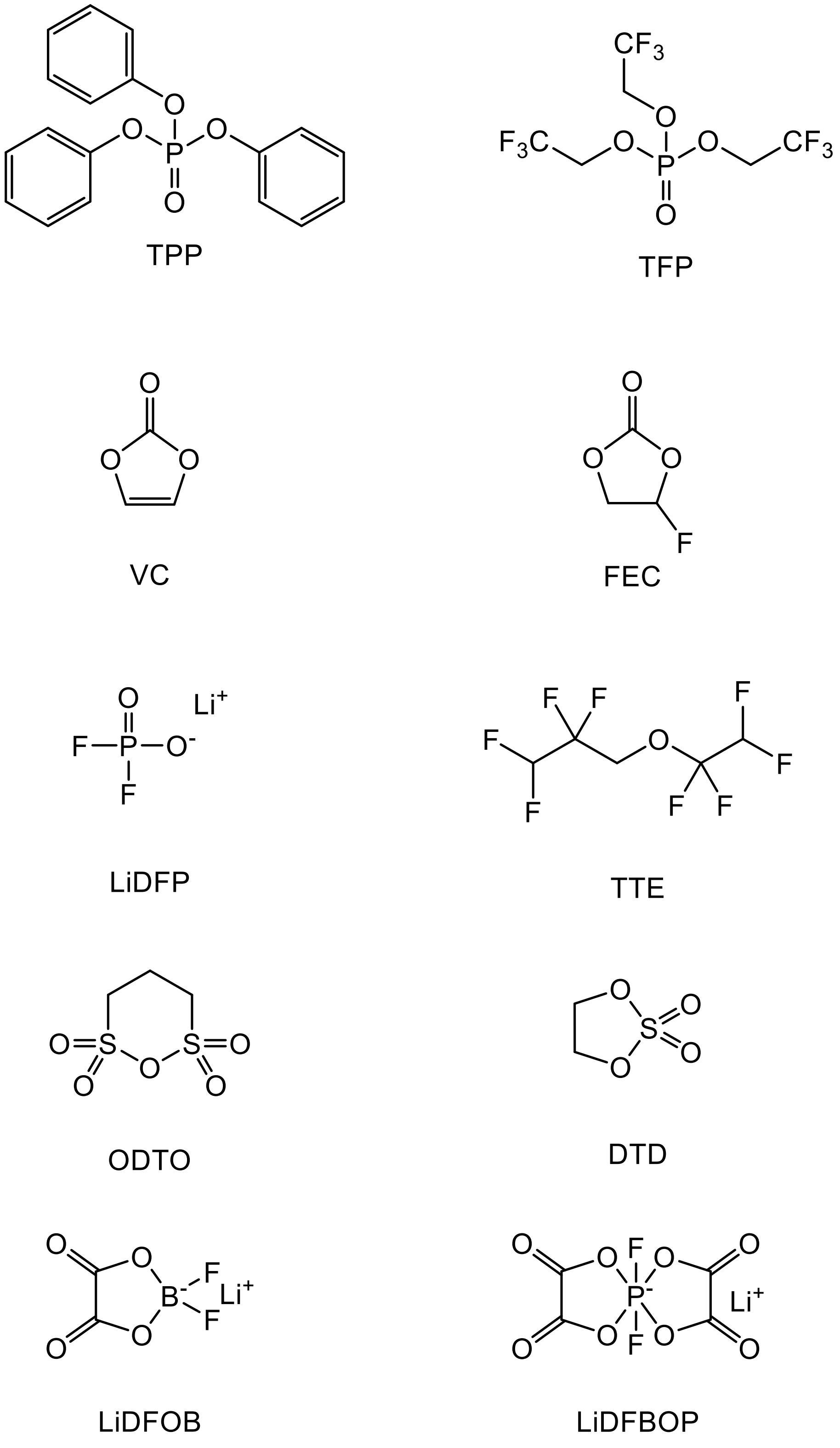

TPP TFP

VC FEC

LiDFP TTE

ODTO DTD

LiDFOB LiDFBOP

Figure 7: Molecular structures of selected electrolyte additives.

2.1.4 Solid Electrolyte Interphase (SEI)

When cycling a battery, electrochemical processes such as lithium intercalation into the graphite anode occur at potentials between 0.2-0.01 V vs Li/Li$^+$.[99] Most organic non-aqueous electrolytes are thermodynamically not stable in this voltage range and are being reduced to liquid, gaseous, and solid products. The solid decomposition products precipitate on the anode surface upon reduction and form the so-called solid electrolyte interphase (SEI). Peled proposed the SEI concept in 1979, claiming that alkali metals are covered by a surface layer that develops from reactions between the metal and the solution.[100] He further argued that the character of this interphase influences self-discharge rates and battery performance.[101]

The electrochemical stability of electrolytes is a complex issue, requiring consideration of solvent redox potentials, reactions between solvent molecules and electrolyte salts, surfaces of the electrode materials, and Fermi level of the electron in solution.[102] Oftentimes, the stability of electrolytes is defined by the energy level of the HOMO[1] and LUMO[2] of the electrolyte. This implies that the electrolyte is reduced at electron energies higher than LUMO level and reduced at electron energies lower than HOMO level. However, using HOMO and LUMO levels to describe electrochemical stability often leads to an erroneous representation. The concept is derived from electronic properties of isolated molecules and does not consider all species participating in redox reactions.[102] It is more correct to speak of the potential of electrolyte reduction or oxidation. The potential of oxidation or reduction of a solvent is related to the redox potential of said solvent as well as its reactions with other solvent molecules and electrolyte salts. Figure **8(a)** shows the negative and positive potential limits for the electrolyte stability and the energy levels of HOMO and LUMO. The levels are clearly at different energies.

The SEI is formed to a large extent during the first cycle because the anode surface is still uncovered, thus leading to strong electrolyte reduction. The exact electrolyte decomposition pathway is still under debate, and two concepts exist to explain the electrolyte reduction mechanism. One-electron transfer to the electrolyte is proposed at high potentials, while a two-electron transfer is suggested for lower lithiation potentials. The resulting decomposition products of different electrolyte solvents (EC, PC, DMC) and salts ($LiPF_6$ and LiTFSI) are displayed in **Figure 9**. Inorganic carbonates are thermodynamically more stable than organic carbonates. The actual chemical composition of the SEI is, however, diverse and

---

[1] HOMO: Highest Occupied Molecular Orbital

[2] LUMO: Lowest Unoccupied Molecular Orbital

disturbed by trace amounts of contaminants such as water.[103]–[105] Initial SEI products also degrade over time or react with each other.[106],[107] It is generally accepted for the SEI to form a dual-layer structure with a more compact and inorganic inner layer and a porous, more organic outer layer, see **Figure 8(b)**.[99],[108],[109] Many decomposition products are irreversibly formed and deplete the lithium reservoir, which causes large capacity losses and low coulombic efficiencies in the first cycle. Once formed, the SEI ideally acts as a protective insulating barrier, minimizing further electrolyte reduction, while still allowing Li^+ transport.[110] However, cycling results in the continuous growth of SEI thickness, which heavily affects battery performance. Different models for long-term growth mechanisms such as solvent diffusion, electron tunneling, electron conduction, or Li-interstitial diffusion have been proposed and are displayed in **Figure 8(c)**. A robust and stable SEI is necessary to guarantee high capacity retention and LIB lifetime. However, controlling SEI formation is difficult because SEI formation, growth, chemical composition, morphology**,** and stability depend on various factors. These include the type and morphology of the active material, electrolyte composition, electrochemical operating parameters, and cell temperature. In addition, for accurate control, SEI formation would have to be monitored in situ, which is still technically and spectroscopically challenging.

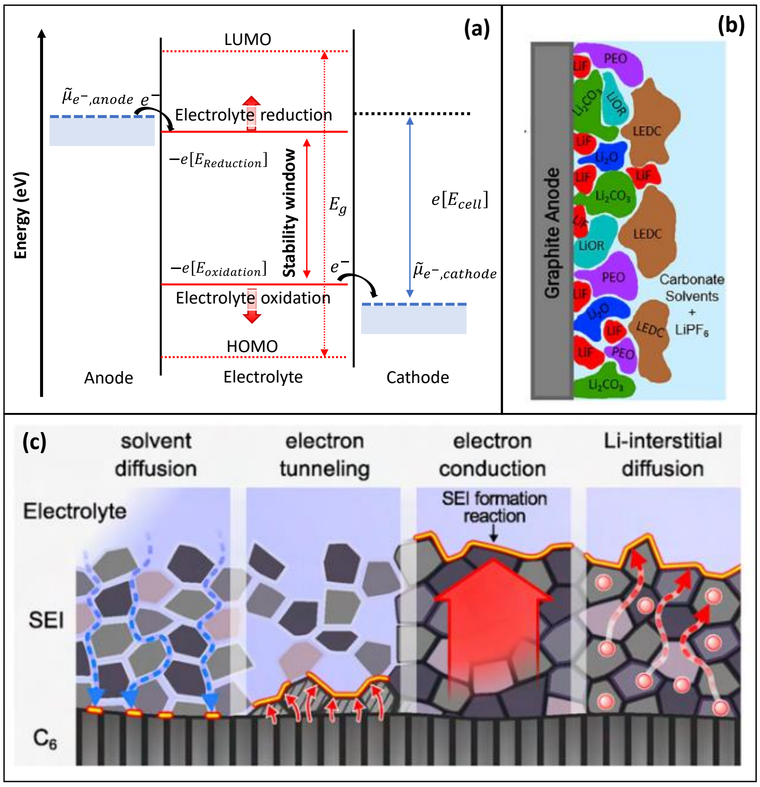

Figure 8: (a) Negative and positive potential limits for the electrolyte stability, and the energy levels of HOMO and LUMO, adapted from ref.[102] (b) dual-layer structure of the SEI, adapted from ref.[99] (c) Models for long-term SEI growth mechanisms, adapted from ref.[103]

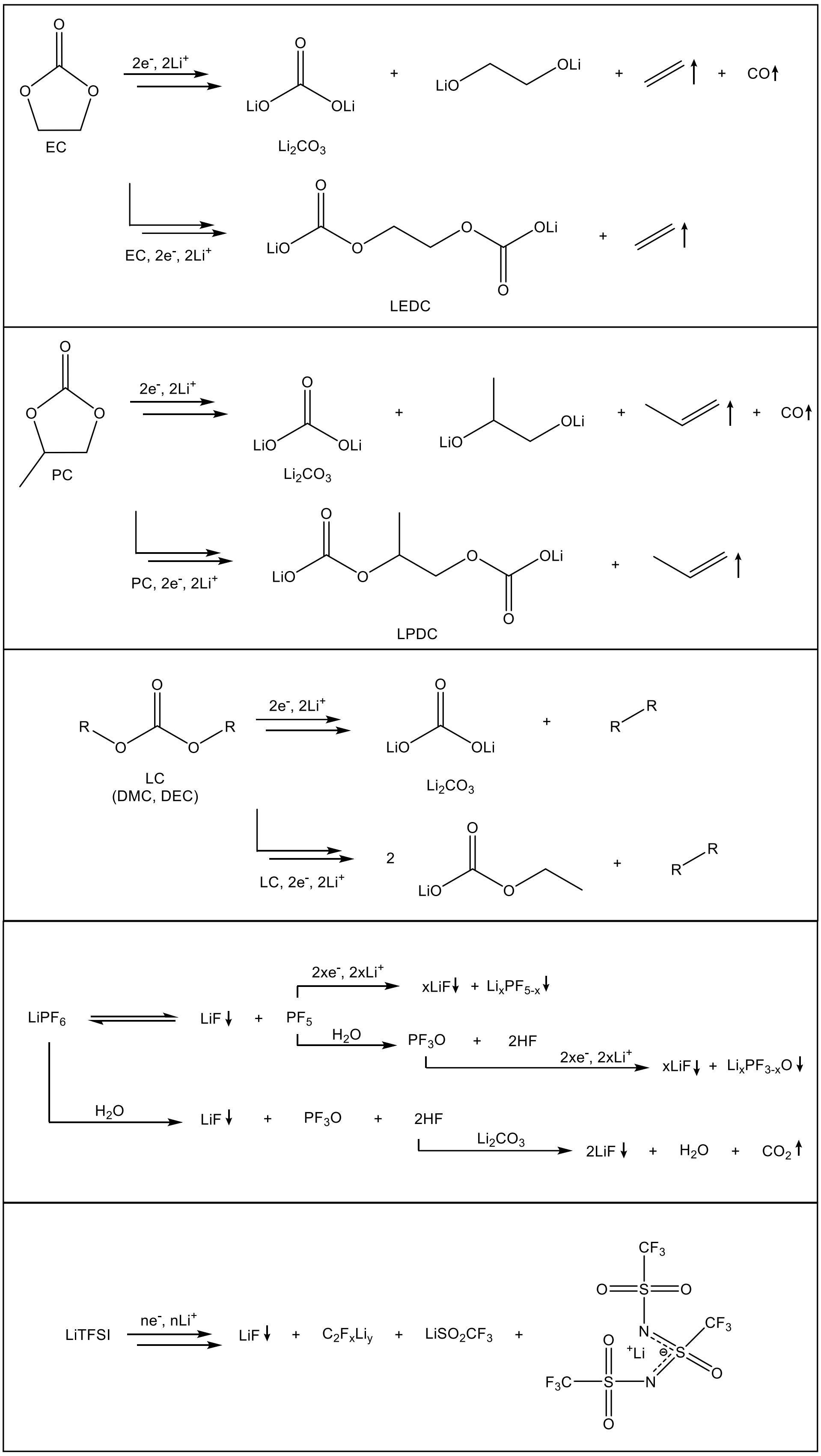

Figure 9: Decomposition products of ethylene carbonate (EC)[111]–[113], propylene carbonate (PC)[78],[111],[113],[114], dimethyl carbonate (DMC)[115],[116], lithium hexafluorophosphate ($LiPF_6$)[78],[116] and lithium bis(trifluoromethanesulfonyl) imide (LiTFSI)[115],[117]. Reaction pathways were adapted from ref.[118]

2.2 X-Ray Photoelectron Spectroscopy (XPS)

Surface analysis with XPS is conducted by irradiating a sample with monoenergetic soft x-rays (e.g., Al-K_α 1486.6 eV) and analyzing the energy of the emitted electrons.[119] Emission of these electrons is caused by the photoelectric effect, in which electrons of atoms in the surface region are liberated by absorbing a photon, see **Figure 10(a)**. Electrons from a higher energy level are used to fill vacancies caused by the removal of core electrons. This results in a release of energy and the emission of Auger electrons, see **Figure 10(b)**.

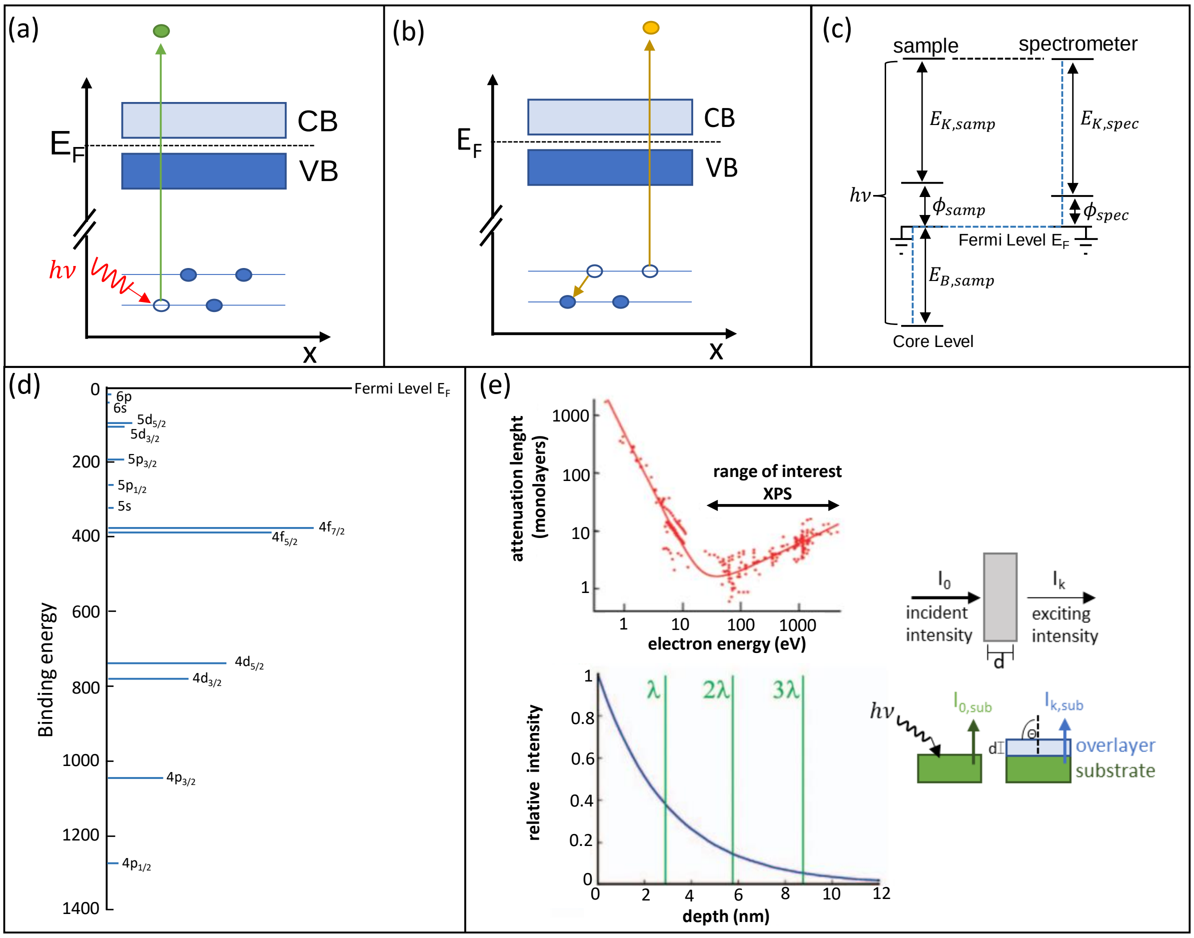

Figure 10: (a) Photoelectric effect generating photoelectron and (b) Emitted Auger electron due to relaxation of the excited ions remaining after photoemission. (c) Energy level diagram of sample and spectrometer in electrical contact with each other, grounded and with aligned Fermi level, adapted from ref.[120] (d) Relative binding energies for Uranium. The line lengths indicate the relative probabilities of the various ionization processes, adapted from ref.[119] (e) Top left: Attenuation length as a function of electron kinetic energy. Bottom left: Relative intensity as a function of depth for Si 2p electron emitted from silicon as a result of K_α-Al radiation, adapted from ref.[121] Right: in the presence of an overlayer, the intensity of the substrate signal is attenuated as a function of Beer's law, adapted from ref.[122]

The probability to generate a photoelectron is given by Fermi's Golden Rule. It describes the transition rate w_{fi} from one initial eigenstate $|i\rangle$ (i.e., electron wave function of the ground state) to the final state $|f\rangle$ (i.e., the electron wave function of the final state in the continuum) as a result of a perturbation (i.e., photon or dipole operator: $\vec{e}\vec{\nabla}$), see Eq.(15):

$$w_{fi} = \frac{4\pi^2}{h} \left|\langle f|\vec{e}\vec{\nabla}|i\rangle\right|^2 \delta(E_f - E_i - h\nu) \tag{15}$$

where h is the Planck constant, $h\nu$ the photon energy, and $\delta(E_f - E_i - h\nu)$ corresponds to the Dirac delta distribution and allows a transition only for $\delta(E_f - E_i - h\nu) = \delta(0) = 1$. E_f is the energy state of the final state and equals the kinetic energy E_k of the photoelectron and its interaction with the surrounding electrons $E_f(N-1)$, see Eq.(16). Energy states of the initial state E_i correspond to the interaction with the surrounding electrons $E_f(N-1)$, after photoelectron emission and the binding energy E_b, see Eq.(17). Substituting Eq.(16) and Eq.(17) in $\delta(E_f - E_i - h\nu)$ leads to the kinetic energy of the emitted photoelectron, see Eq.(18).

$$E_f = E_k + E_f(N-1) \tag{16}$$

$$E_i = E_f(N-1) - E_b \tag{17}$$

$$E_k = h\nu - E_b \tag{18}$$

When measuring XPS, the photoelectron is usually not generated from an isolated atom but from a solid. Therefore, the kinetic energy of the generated photoelectron must be complemented by a work function ϕ that describes the minimum energy required to remove the electron from the surface of a solid, see Eq.(19).

$$E_k = h\nu - E_b - \phi_{samp} \tag{19}$$

If the measured sample is in Ohmic contact with the spectrometer, their Fermi levels align, see **Figure 10(c)**. With this, one does not need to know the work function of the sample but can use the work function of the spectrometer, see Eq.(20). The latter can be determined by measuring the Fermi level of a metallic sample whose binding energy is set to zero.

$$E_k = h\nu - E_b - \phi_{samp} + (\phi_{samp} - \phi_{spec}) = h\nu - E_b - \phi_{spec} \tag{20}$$

The binding energy can be approximated to the binding energy of the atomic orbital from which the electron originates, also known as Koopman-Energy or "frozen orbital". In reality, the binding energy is also influenced by final state effects such as the orbital relaxation upon ionization E_{rel}, and the electron correlation ΔE_c which will be changed after ionization. In an atom, electrons from different orbitals (i.e., s, p, d, and f) are emitted with different probabilities, see the example of Uranium in **Figure 10(d)**. Here, the Fermi level corresponds to zero binding energy (by definition), and the depth beneath the Fermi level indicates the relative energy of the ion remaining after electron emission, i.e., the binding energy.[119] The line length indicates the relative probabilities of the various ionization processes. Due to the coupling of the orbital momentum of electrons with their spin (i.e., spin-orbit coupling), the p, d, and f levels become split, leading to $p_{1/2}$, $p_{3/2}$, $d_{3/2}$, $d_{5/2}$, $f_{5/2}$, and $f_{7/2}$. Because each element has a unique set of binding energies, XPS can be used to identify and determine the concentrations of the elements on the surface.[119] In addition, the binding energy is dependent on the chemical environment, making it possible to identify the chemical state of the element. For example, -C-C and -C-H bonds have the lowest binding energy for organic compounds (at 285 eV). Bond to oxygen (e.g., -C-O or -C(=O)O), the electron density of the carbon atom decreases due to the larger electronegativity of the oxygen. This leads to a shift to higher binding energies for the carbon in -C-O (286.5 eV) and -C(=O)O (288 eV) environment.

The surface sensitivity of XPS is given by the fact that electrons interact strongly with matter. Photoelectrons tend to scatter inelastically on their way to the surface, losing energy. In fact, only those electrons that originate within tens of angstroms below the surface can leave the surface without energy loss. Electrons that leave the surface without inelastic scattering produce the peaks in the spectra, while electrons that lose energy due to inelastic collisions form the background. The average distance that an electron can travel between inelastic collisions is called inelastic mean free path, or IMFP (λ). 95% of all generated photoelectrons emerge from a depth of 3λ, see **Figure 10(e)**. The IMFP is dependent on both the initial kinetic energy of the photoelectron and the nature of the sample. Denser elements and core electrons with greater binding energies will have smaller IMFPs. As can be seen in **Figure 10(e)**, the number of photoelectrons without energy losses decreases exponentially with the sample depth and can be described by Beer's law:

$$I = I_0 \cdot \exp\left(-\frac{d}{\lambda\, cos(\Theta)}\right) \tag{21}$$

where I_0 corresponds to the incident intensity, d the sample depth, and Θ the angle relative to the surface normal. As the right part of **Figure 10(e)** displays, the thickness d of an overlayer can then be approximated by the attenuated intensity of the substrate signal with overlayer $I_{k,s}$ divided by the intensity of the pure substrate $I_{0,s}$:

$$d = -\lambda \cdot \cos(\theta) \cdot \ln\left(\frac{I_{k,s}}{I_{0,s}}\right) \tag{22}$$

XPS can further give a quantitative description of the composition of the surface region of the sample under investigation. For this to be achieved, spectral intensities I must be related to the number of atoms n in a homogenous sample emitting electrons which contribute to the spectrum as well as several additional factors, see Eq.(23):

$$I = n \cdot f \cdot \sigma \cdot \theta \cdot \lambda \cdot A \cdot T \tag{23}$$

where f is the x-ray flux, σ the photoelectric cross-section, θ the angular efficiency factor, λ the IMFP, A the sample area, and T the detection efficiency. Not all terms are known with sufficient accuracy for the first-principle method to be of practical use.[123] Instead, the intensities of the unknown sample are compared to reference intensities either obtained by calculation or by measurement of standard spectra, see Eq.(24) with sensitivity factor $S = f \cdot \sigma \cdot \theta \cdot \lambda \cdot A \cdot T$:

$$\frac{n_1}{n_2} = \frac{I_1/S_1}{I_2/S_2} \tag{24}$$

A photoelectron spectrometer consists of an x-ray source (e.g., K_α-aluminum), electron optics, a hemisphere analyzer, and a detector. A detailed overview of the setup is shown in **Figure 11**. X-rays are generated by an x-ray source and monochromatized via a single crystal, which also focuses the x-rays on the probed sample. The emitted photoelectrons are adjusted to the pass energy by electron optics before entering the hemispherical energy analyzer. The pass energy of the analyzer is fixed to maintain a constant energy resolution. Electrons are detected via a multichannel detector in the number of electrons for a given detection time and energy.[119] Scanning for different energies is accomplished by applying variable electrostatic fields before the analyzer.[119]

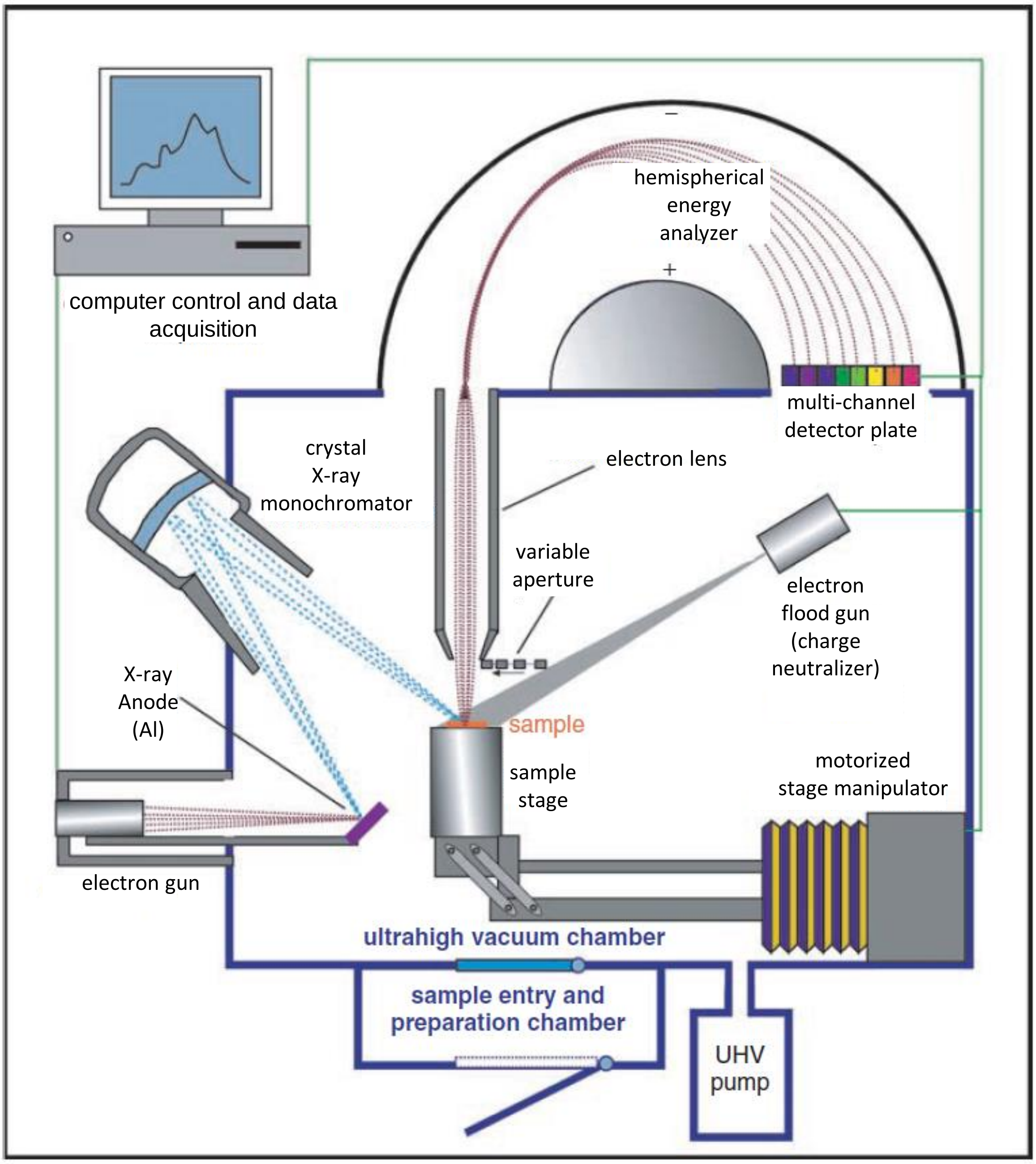

Figure 11: Schematic setup of a photoelectron spectrometer, adapted from ref.[122]

3 State-of-the-art

This chapter provides an overview of current research on Si/Gr anodes and covers the challenges of implementing silicon-containing anodes. The main focus lies in ways to improve the SEI stability. Different SEI characterization methods are briefly outlined, with a focus on XPS. Gaps in literature are addressed which will be filled by this thesis.

3.1 Si/Gr as anode material

Batteries for electric vehicles or other mobile energy storage applications require higher energy density. This can be achieved by either increasing the potential difference between the positive and the negative electrode or the specific capacity of each electrode.[6],[17] Among anode materials, silicon attracts a lot of attention for its high abundance, low cost, and high theoretical capacity of 3579 mAh g^{-1}.[3] However, its main disadvantage is the large volume expansion[124] (up to 300 %) during lithiation of the silicon particles, as well as large volume decrease upon particle delithiation, entailing the following phenomena:[4]

(1) Pulverization and degradation of the silicon particles leading to a loss of available active material during cycling[5],[6],[8],[9]

(2) Stress on the electrode coating[6],[9],[125]

(3) High mechanical strain on the SEI leading to cracks and re-exposure of formally covered electrode material. This results in continuous side reactions at the silicon/electrolyte interface, depleting the electrolyte of lithium, increasing the resistance of the SEI, and electrically isolating silicon particles[7],[10]–[15]

All phenomena are illustrated schematically in **Figure 12(a)**. As a result of these factors, the electrode integrity degrades and the electrochemical performance drops over time, ultimately resulting in the end-of-life of the cell.[10],[126] To date, different strategies exist to address these challenges.

The first one focuses on optimizing electrode material and composition. Pulverization can be partially reduced by using nano-sized silicon particles instead of micro-sized.[69] Blending silicon with carbon materials such as graphite,[16]–[22] graphene,[127] or carbon-nanotubes,[128] can reduce stress on the electrode coating, see **Figure 12(b)**. This provides empty spaces and buffers the silicon volume changes.[21] Additionally, graphite mitigates the electrical contact losses between silicon particles due to its conductive properties.[22] It also decreases electrolyte consumption, leading to longer cycle life.[9] However, the more silicon is present in these blends, the faster the decrease in electrochemical performance.[9],[17] Another way to minimize stress on the electrode coating and resulting contact losses between active materials and conductive agents is achieved through three-dimensional binder networks, which maintain the electrode structure during the volume changes, see **Figure 12(c)**.[90],[129]

The second strategy concentrates on increasing the volume accommodating properties of the SEI. Such an increase in flexibility reduces the mechanical strain. The SEI flexibility is largely determined by the nature of the electrolyte decomposition products, which are influenced by the electrolyte formulation. Most used carbonate-based electrolytes contain mixtures of cyclic EC with linear DMC, DEC, or EMC solvents. The SEI composition is largely dominated by EC decomposition products such as lithium carbonate (Li_2CO_3), lithium alkoxi compounds (LiOR), lithium ethylene dicarbonate (LEDC), and polyethylene oxide (PEO), see **Figure 12(d)**.[104],[99] In particular, LEDC and PEO are suspected of not being able to accommodate the volume changes of the silicon particles. NMR analyses of cycled electrolyte solutions detected a high concentration of short-chain lithium alkyl carbonates and PEO-type oligomers, suggesting high solubility of these decomposition products.[23] Electrolyte salt decomposition usually leads to inorganic species. For example, $LiPF_6$ forms LiF, Li_xPF_y, and Li_xPOF_yupon reduction.[130] It is unlikely that salt decomposition products will increase the SEI flexibility during silicon volume changes since these species are not mechanically flexible. However, the presence of salt decomposition products may lead to other advantages. A high LiF concentration can increase lithium-ion conductivity in the SEI.[131],[132]

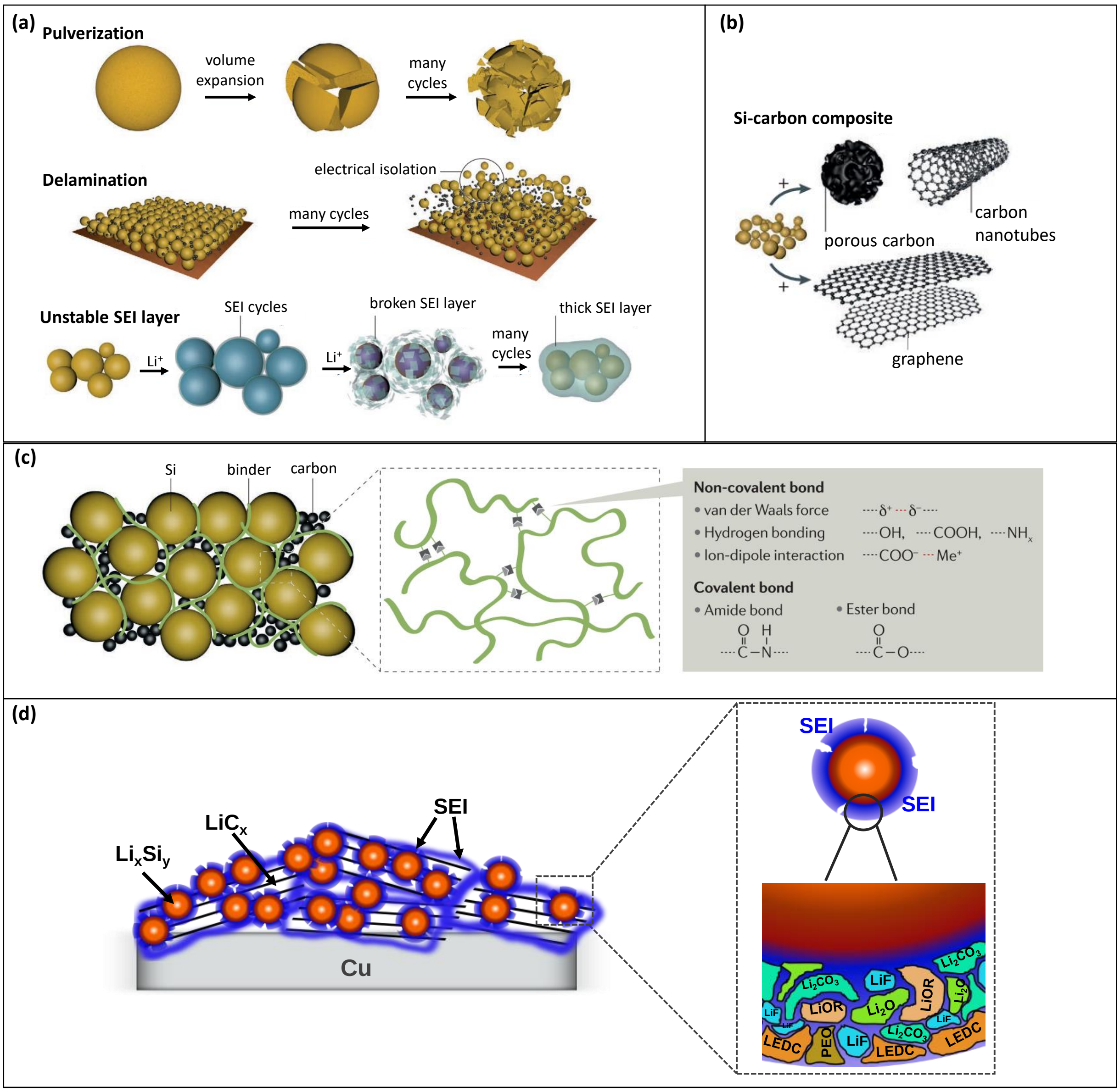

Figure 12: (a) Main degradation mechanisms of silicon anodes (adapted from ref.[133]), (b) Various Si-C composites (adapted from ref.[133]), (c) Various binder concepts for silicon anodes (adapted from ref.[133]), (d) Schematic SEI composition on silicon when cycled in carbonate-based electrolytes (i.e. $LiPF_6$ in 1:1 mixture of EC:DMC) in absence of additives.

Currently, the most common way to improve the electrochemical performance of Si/Gr anodes is to use electrolyte additives. Compared to the electrolyte solvents, the additives employed are being reduced at higher potentials. This leads to an initial SEI layer which is more abundant in additive decomposition products. For silicon, two additives have received a lot of attention: vinylene carbonate (VC) and fluoroethylene carbonate (FEC).[90] VC enhances the cycle life as well as the thermal stability of the lithiated silicon anode.[90] Upon reduction, it undergoes electrochemically induced polymerization, leading to the formation of poly(VC)[134], see **Figure 13(a)**. This polymer is considered to make the SEI denser and more stretchable.[135] However, the surface film shows high resistance for Li^+ migration, turning VC unfavorable for high power applications.[136] In contrast, the SEI displays additional LiF nanocrystals embedded within the surface film when using FEC. These nanocrystals are suspected to offer much better conductivity for Li^+, thus showing excellent requirements for high power applications.[136] Several FEC decomposition mechanisms have been proposed to date. An overview of possible SEI products is given in **Figure 13(b)**. Direct reduction of FEC with Li-Naphthalene resulted in the formation of cross-linked polymerized vinylene carbonate (poly(VC)) units as detected by ssNMR, XPS, and FTIR.[134] Electrochemically generated FEC decomposition products revealed polymers with poly(VC) as well as PEO units.[137] Other known FEC decomposition products include LiF, Li_2CO_3, carboxylic, and carbonyl environments as well as acetal-based compounds.[134] Regarding the formation of C-F environments, the literature is divided. C-F groups have been suggested by XPS measurements and might result from the ring-opening of the FEC molecule, leading to $-CF-OCO_2-$ species.[138] However, ss-NMR was not able to detect such C-F environments.[137],[139] Due to the high electronegativity of fluorine, it is more likely that the FEC molecule will decompose by breaking the -CF bond, resulting in LiF and an organic polymer. Furthermore, the presence of FEC seems to promote the formation of organosiloxane (i.e., -Si-C-) species and thereby influence the adhesion of the organic SEI to the silicon surfaces.[137]

The stabilizing effect of FEC is largely attributed to the formation of a polymer species that can adapt to changes in the electrode volume. As previously mentioned, EC decomposition leads to the formation of short-chain polyethers (PEO) and LEDC species. In presence of silicon, these compounds do not form a stable SEI and detach from the surface layer. However, when using FEC-containing, EC-based electrolytes no EC decomposition compounds are found in the electrolyte.[23] This strongly suggests that the cross-linked nature of these polymers stabilizes the SEI during the electrode volume changes.

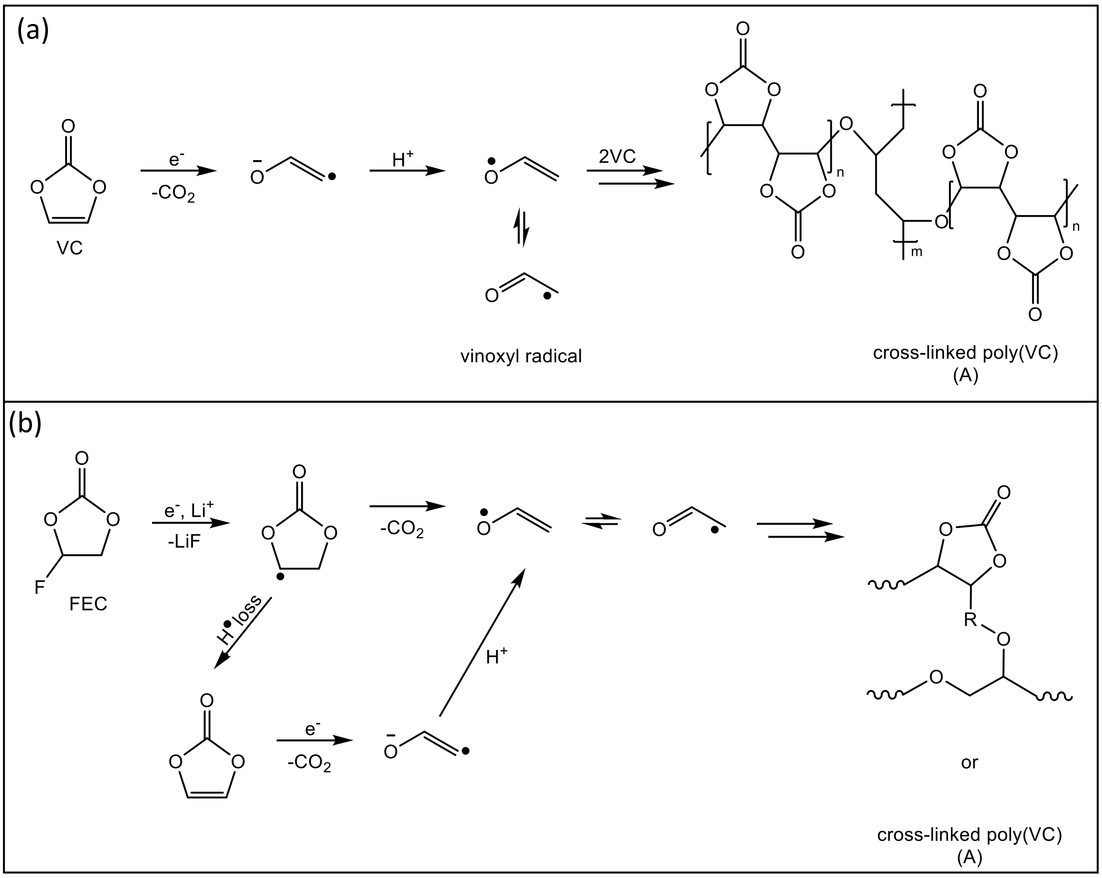

Figure 13: Possible reaction scheme for (a) VC and (b) FEC decomposition, adapted from ref.[134],[137]

One of the main drawbacks of FEC is its continuous consumption upon cycling as shown by OEMS.[140] Consumption of FEC is dependent on the relation between the FEC concentration and the amount of active material in the electrode (i.e., $\mu mol_{FEC}/mg_{electrode}$). Particularly the amount of silicon in the electrode affects the amount of FEC reduced.[17] The stabilizing effect of FEC is retained only as long as the additive is present in the electrolyte. Once depleted, EC reduction occurs, followed by an increase in cell polarization and a rapid capacity drop. By increasing the FEC concentration in the electrolyte, the stabilizing effect can be retained for a longer time. In other words, the more FEC present in the electrolyte, the longer the cycle-life of silicon anodes. Since FEC has similar permittivity to EC, the electrolyte salt $LiPF_6$ is sufficiently dissociated, allowing EC to be completely removed from the electrolyte formulation.[82] Additionally, an electrolyte devoid of EC will not form any EC decomposition products in the SEI, which has shown a very poor ability to accommodate the silicon volume changes. Only a few studies exist investigating FEC cosolvent.[141]–[144] Etacheri *et al.* analyzed the electrochemical performance of the electrolyte formulation 1 M $LiPF_6$ in 1:1 FEC:DMC when cycled with silicon-nanowire (SiNW) anodes in a half-cell setup with lithium metal as the counter electrode. When compared to the LP30 electrolyte, the FEC-based formulation leads to (1) the complete lithiation of the SiNW as evidenced by TEM, (2) a thinner SEI as seen with

SEM, and (3) less carbon-oxygen species as detected by XPS.[142] Schiele *et al.* investigated the gaseous decomposition products with OEMS of silicon electrodes cycled in the electrolyte 1 M $LiPF_6$ in 1:1 FEC:EMC.[143] They found the main gaseous decomposition products to be H_2 and CO_2, while the analysis of an EC:EMC reference electrolyte yielded H_2, C_2H_4, and CO. To date, there is still discord about the true nature of the species formed that stabilize the SEI upon silicon volume changes. Especially XPS investigations do not deliver conclusive results. Also, no correlation is made between different SEI properties and electrochemical performance. **Chapter 5** of this thesis presents a new fitting model for FEC decomposition products. It support the formation of a polymer network, which is hypothesized to stabilize the SEI upon the silicon volume changes. A systematic investigation is provided about the SEI composition and thickness formed by FEC containing electrolytes. As a result, the strong correlations between electrolyte formulation, SEI properties, and electrochemical performance is uncovered.

Another approach to improve the electrochemical performance of Si/Gr anodes is by investigating alternatives to carbonate-based electrolytes. Ethers[145],[146] and nitrile functionalized siloxanes have been examined with silicon-containing anodes but show low reversibility.[147]–[149] Glyoxylic acetals have not yet been explored as potential electrolyte solvents for silicon-containing anodes. To date, two glyoxylic solvents were investigated with graphite anodes, namely 1,1,2,2-tetramethoxyethane (TMG) and 1,1,2,2-tetraethoxyethane (TEG), see **Figure 14**. When used with lithium bis(trifluoromethansulfonyl)imide (LiTFSI) as electrolyte salt, these solvents showed good cyclability at 60°C and room temperature.[150]–[152]

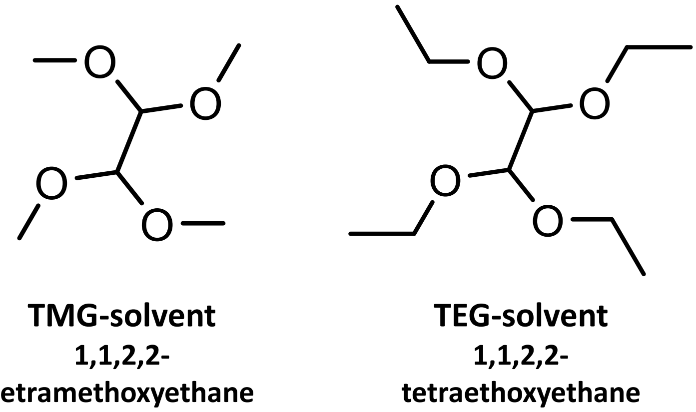

Figure 14: Molecular structures of 1,1,2,2-tetramethoxyethane (TMG) and 1,1,2,2-tetraethoxyethane (TEG).

However, some challenges remain with this solvent class as it exhibits lower ionic conductivities and higher viscosities compared to carbonates-based formulations, see **Table 3**. Mixing glyoxylic acetals with other solvents such as EC, DMC, and PC can overcome these disadvantages. The resulting viscosities and conductivities are similar to those found in state-of-the-art electrolytes.[153] Köps *et al.* have found that among all mixtures, 30TEG:70PC (3:7) performed best when used in graphite half-cells.[153] Atik *et al.* have investigated a 1:1 30TEG:70PC-LiBOB mixture in NMC622||graphite full-cells which displayed good cycling performance.[154] In general, PC electrolyte solvents are known to co-intercalate with the solvated lithium-ions in between graphene layers causing the exfoliation of graphite.[155] Co-intercalation reactions can be suppressed by using certain electrolyte additives, or cosolvents with higher reduction potentials than PC.[156] So far, it seems that TEG suppresses the PC co-intercalation, as no characteristic phenomena like very large lithiation plateaus were observed in literature.[153] Overall, glyoxylic acetals showed very promising combination with graphite, making them interesting candidates for Si/Gr anodes. Also, there is limited research investigating the nature of their decomposition products and SEI properties. **Chapter 6** of this work studies the interplay between SEI properties and electrochemical performances of pure TEG and TMG formulations. The use of the TEG electrolyte is demonstrated to be favorable to the electrochemical performance of silicon-containing anodes. In addition, 30TEG:70PC mixtures with a lower viscosity and higher ionic conductivities than the pure TEG formulation are analyzed and optimized for use with Si/Gr anodes.

Table 3: Physical properties of LP30, TEG, and TMG.[150],[157]

	T_m (°C)	F_p (°C)	Viscosity (20°C, mPas)	Conductivity (mS cm^{-1})	Toxicity
LP30 1mol $LiPF_6$ in EC:DMC (1:1)	-20.5	31	4.44	10.7	High
TEG 1mol LiTFSI in TEG	-35	71	11	1.5	Low
TMG 1mol LiTFSI in TMG	-73.2	53	9	1.5	Low

3.2 SEI Analysis Methods

The solid electrolyte interphase (SEI) is a protective layer formed at the negative electrode of LIBs from electrolyte degradation. Its quality strongly influences battery performance, irreversible charge loss, cyclability, graphite exfoliation, and safety.[158] Therefore, it is essential to understand the nature and composition of this layer. Characterization of the SEI is usually done ex-situ, i.e., the cell is opened after the electrochemical experiment and the anode is subsequently washed in an electrolyte-like solvent to remove salt residues. However, while electrolyte components are removed by the washing procedure, there is always an uncertainty to what degree SEI parts are also being removed. Also, contact with water and air can result in modifications of the SEI composition. For example, $ROCO_2Li$ or ROLi species can react in presence of CO_2 to form Li_2CO_3, while $ROCO_2Li$ can react with water yielding Li_2CO_3, CO_2, and ROH.[159]–[161] Therefore, all experiments have to be carried out under inert atmosphere.

Due to the thin nature of the SEI, surface analysis techniques are best suited to probe this layer. These include methods like x-ray photoelectron spectroscopy (XPS)[161]–[163], atomic force microscopy (AFM)[12],[108], and time of flight secondary-ion mass spectrometry (TOF-SIMS)[164]–[166]. Scanning electron microscopy (SEM)[167] and tunneling electron microscopy (TEM)[7],[168],[169] are used for imaging the SEI. Fourier transformed infrared spectroscopy (FTIR)[170] and Raman spectroscopy[171],[172] provide information about functional groups in the surface layer. Solid-sate nuclear magnetic resonance spectroscopy (ss-NMR) gives insights into bulk SEI composition.[23],[137] Studying SEI kinetics can be achieved by impedance spectroscopy (EIS).[173] This variety of complementary methods is required to understand the complex properties of the SEI.

XPS is a method of choice when studying the SEI composition as it has high surface and chemical sensitivity. Surface sensitivity of laboratory x-ray sources is in the range of around 5-10 nm, enabling the detection and quantification of all elements (except H and He) present in that layer. It further provides information about the chemical environments of the detected elements. This makes XPS an ideal technique for probing the SEI. The evolution of surface species during cycling can be tracked by comparing the spectra of different cycling stages. Additionally, XPS allows to estimate the SEI layer thickness. Analyzing changes in SEI composition and thickness can help explain how the layer affects the electrochemical performance. Decomposition products of numerous electrolyte formulations on different electrode materials can be found in literature.[115],[163],[174] **Table 4** displays binding energies of the most common SEI species when using electrolytes based on EC:DMC with either $LiPF_6$ or LiTFSI as electrolyte salt. Characteristic binding energies of different graphite and silicon species are also presented. All binding energies were shifted with respect to saturated hydrocarbon (i.e., 285 eV).

Table 4: Binding energies of common SEI species, functional groups of SEI species, and anode compounds (i.e., graphite and silicon).[115],[163],[174] Energies are given relative to saturated hydrocarbon (C1s = 285.0 eV).

Compound	**C1s (eV)**	**O1s (eV)**	**F1s (eV)**	**Li1s (eV)**	**P2p (eV)**	**Si2p (eV)**	**N1s (eV)**	**S2p (eV)**
LiF[163]			684.9-685.2	55.9-56				
Li_xPF_y $LiPF_6$[163]			687.2	57.2	137.2-137.5			
Li_xPOF_y[163]			688		134.5			
LiTFSI[115]	293.0	533.0	688.6	56.6			399.6	169.4
Li_3N[175]							397.6	
Li_2SO_3[117],[175]								167.3
Li_2O[161]		528.3		53.7				
Li_2CO_3[174]	290.1	531.8-532		55.5				
$ROCO_2Li$[174]	290.1	532.5		55.5				
$-(C=O_a)-O_b$[176]	288.9-290.1	O_a: 532.2 O_b: 533.5						
-C=O[176]	287.9-288	532.3						
-C-O[174]	286.4-286.7	533.3						
-C-H[176]	285							
Graphite[177]	284.4							
LiC_6[178]	283.2[1]							
Si^0 [179],[180]						99.4		
SiO_2[179],[180]						103.5-104		
Li_xSi[179],[180]						687.7-688.2		
Li_xSiO_y[179],[180]						101.3		

---

[1] Binding energy highly dependent on state of charge of the battery, see ref.[178]

For conductive samples, the binding energy is usually referenced to the Fermi level of the spectrometer. However, with nonconductive samples, such as the SEI, an internal point of binding reference is needed. This is why all binding energies are referenced to the binding energy of saturated hydrocarbon at 285 eV. In most cases, this leads to very reproducible binding energies of the species displayed above.[115],[163],[174] While SEI species usually shift to the expected binding energy values after referencing, bulk species oftentimes show a different relative shift. For example, Maibach *et al.* have shown that after hydrocarbon calibration, the graphite peak is separated by 2.6 eV from the -CH-peak in a fully lithiated electrode.[181] In a fully delithiated electrode, the difference between graphite and -CH amounted only to 1.8 eV. By contrast, in a pristine electrode, a difference of 0.8 eV is observed. The authors concluded that the binding energy position of hydrocarbons located at the sample surface is not representative of underlaying bulk material. Furthermore, they explain the relative shift in binding energy by an electric potential gradient at the buried interface between the electrode and the SEI. This gradient is influenced by the state of charge of the electrode as well as dipole moments of different SEI species.

Laboratory photoelectron spectrometers using an Aluminum K_α x-ray source produce fixed photon energy of around 1.48 keV, resulting in an information depth of around 3λ or approximatively 10 nm. Investigating deeper layers is important because the abundance of SEI species can vary throughout the layer and influence its stability upon cycling. The SEI is accepted as being a quasi bilayered structure with a more inorganic inner part and a more organic outer part. With a laboratory setup, deeper SEI layers are probed by sputtering the surface with argon ions or ion clusters to remove the outermost layers. This method is destructive and might induce changes in the SEI during the measurement. A nondestructive method is to increase the photon energy to around 5-10 keV as is done at a synchrotron. In this thesis, all XPS measurements were done with an incident photon energy of around 1.48 keV and sputtering has been conducted only occasionally.

Limitations of XPS are numerous: Radiation damage by x-rays or charge neutralizers can induce changes in the SEI composition, as is discussed in **Chapter 4.5**. Quantification is difficult when substrate and SEI have the same elements. Poor electrical conductivity makes phase identification difficult, especially for elements where different species exhibit similar binding energies such as various lithium compounds. It is hard to know the actual molecular structure of the different SEI species because the same functional group present in different molecules emerges as one peak. This makes. Unambiguous peak assignment often requires the analysis of reference samples. In some cases, these molecules have to be synthesized prior to their analysis. Here, other methods such as NMR can provide additional information. Controlling the sample preparation before XPS measurements is crucial. In summary, knowledge about all these parameters is essential for developing a suitable XPS fitting model.

All ex-situ analysis methods have in common that the cell is generally opened after the electrochemical measurement, leading to possible changes in the SEI layer during sample preparation. Furthermore, ex-situ methods make it very difficult to follow dynamic changes in SEI properties during cycling. Increasingly, in-situ analysis methods have been developed to monitor the SEI during electrochemical cycling. Methods such as online electrochemical mass spectrometry (OEMS) and electrochemical quartz crystal microbalance (EQCM) have gained much attention.[182] OEMS can not only determine the evolution rate of most commonly observed gases during SEI formation such as H_2, CO_2, and C_2H_4, but also establish their individual contribution to the total gassing of the cell.[183],[184] EQCM monitors the mass deposition on model electrodes during operation with unparalleled sensitivity.[182],[185] Both in-situ techniques have the advantage that they detect changes over the entire electrode and not just local changes as with XPS, FTIR, or Raman. Increasingly, in-situ FTIR and Raman techniques are also being developed to characterize changes in the SEI during cycling.[186]–[190] Because of special pumping techniques and analyzer design, it is also possible to measure XPS on liquids, enabling in-situ measurements of the SEI at the interface between the liquid electrolyte and solid electrode.[191]–[193] Within this thesis, laboratory-scale near ambient pressure XPS (NAP-XPS) was conducted on model electrolyte systems. The experiments were carried out in collaboration with SPECS in Berlin. As this thesis focuses on analyzing the SEI on Si/Gr anodes, the obtained results are not discussed here, but were published under the title "Probing Lithium-Ion Battery Electrolytes with Laboratory Near-Ambient Pressure XPS".[194]

4 Experimental

This chapter details the electrode preparation as well as the electrolyte formulations used in this work. It states the parameters for electrochemical experiments. Furthermore, the chosen settings for XPS sample preparation and XPS measurements are explained and justified.

4.1 Electrode Preparation

Si/Gr electrodes were prepared using a slurry of 81 wt.% graphite (SFG6L, Imerys Graphite & Carbon, Switzerland), 9 wt.% silicon nanopowder (Nanostructured & Amorphous Materials Inc., 50-100 nm, purity > 99%), 5 wt.% carbon nanofibers (Showa Denko), and 5 wt.% lithium-polyacrylic acid binder solution. The binder solution was obtained by diluting a ready-made 45 wt.% polyacrylic acid in a water solution (Sigma Aldrich) and subsequently adding lithium-hydroxide (LiOH, Sigma Aldrich) until a pH of 6.5 was reached. The slurries were prepared in a two-step process. The premixing was done in a planetary mixer (Thinky ARV-310P). Hereby, silicon nanopowder (9 wt.%) was mixed with carbon nanofibers (5 wt.%) and graphite (81 wt.%) in water: ethanol mixture of 1:1.2. Subsequently, the mixture was dried and gradually transferred into a glass vial containing the binder solution. To break particle agglomeration, mixing was performed via ultrasonic dispersion with an ultrasonic homogenizer (Kinematica, Polytron PT 2500). The obtained slurry was coated on a copper foil with a doctor blade (wet thickness was set to 150 µm) and later dried at room temperature overnight. Individual electrodes were cut into discs of 12 mm diameter and dried under vacuum at 120 °C for 12 h. The resulting electrodes had a silicon-graphite mass loading of around 2.8 -3.1 mg/cm^2.

4.2 Electrolyte Formulations

All electrolytes were prepared in an argon filled glove-box with H_2O and O_2 values below 1 ppm. The electrolyte salts lithium hexafluorophosphate ($LiPF_6$, Merck) and lithium bis(trifluoromethanesulfonyl)imide (LiTFSI, Merck) were dried under vacuum at 110 °C for 12 hours before use. The electrolyte solvents dimethyl carbonate (DMC), fluoroethylene carbonate (FEC), ethylene carbonate (EC), and propylene carbonate (PC) were purchased from Merck and dried over a molecular sieve before usage (water content <15 ppm as measured by Karl-Fischer titration). The solvents TMG and TEG were obtained from Weylchem and dried with an over-pressure Schlenk filtration through vacuum-pre-dried aluminum oxide (water content <15 ppm as measured by Karl-Fischer titration). Battery-grade LP30 electrolyte (i.e., 1 M $LiPF_6$ in 1:1 ethylene carbonate: dimethyl carbonate, Merck) was used as received (water content <10 ppm as measured by Karl-Fischer titration). **Table 5** gives an overview of the used electrolyte mixtures in this thesis.

Table 5: Electrolyte mixtures used.

	Labelling	Composition	Salt	Additive
Carbonate-based	LP30	50 vol.% EC 50 vol.% DMC	1 M $LiPF_6$	none
	2FEC:98LP30	49 vol.% EC 49 vol.% DMC	1 M $LiPF_6$	2 vol.% FEC
	10FEC:90LP30	45 vol.% EC 45 vol.% DMC	1 M $LiPF_6$	10 vol.% FEC
	20FEC:80DMC	20 vol.% FEC 80 vol.% DMC	1 M $LiPF_6$	none
	50FEC:50DMC	50 vol.% FEC 50 vol.% DMC	1 M $LiPF_6$	none
	L-E/D	50 vol.% EC 50 vol.% DMC	1 M LiTFSI	none
Glyoxal-based	TEG	100 vol.% TEG	1 M LiTFSI	none
	TMG	100 vol.% TMG	1 M LiTFSI	none
	30TEG:70PC	30 vol.% TEG 70 vol.% PC	1 M LiTFSI	none
	30TEG:70PC-10FEC	27 vol.%TEG 63 vol.% PC	1 M LiTFSI	10 vol.% FEC

4.3 Cell Assembly

Half-cells were assembled in an argon-filled glovebox with H_2O and O_2 values below 1 ppm. A CR2025-type coin cell setup was used from PI-KEM. The cells consisted of a Si/Gr working electrode, a microporous polypropylene separator (Celgard 2325), a glass fiber separator (VWR), and a lithium foil (thickness: 0.25mm, purity: 99.9 %, PI-KEM) as the counter electrode. The Celgard 2325 separator was applied directly on the electrode surface to protect the surface from glass fiber contaminations. 150 µL of the respective electrolyte solution was used. All cells were sealed with by hydraulic crimping machine (MSK-110, MTI Corporation) at 50 kg cm^{-2}.

4.4 Electrochemical Cycling Parameters

Galvanostatic cycling with potential limitation (GCPL) was performed with a multichannel potentiostat (VMP3 & BCS, Bio-Logic) at 25 °C in a climate chamber (Binder). All potentials are given in reference to Li/Li^+. An initial formation cycle at C/20 (1C = 623 mAh g^{-1}) was carried out for all cells. At the end of every lithiation step, a constant-current constant-voltage (CCCV) was applied at C/5 for 30 minutes. This ensured complete formation of $Li_{15}Si_4$ phase during silicon lithiation. Half-cells with 2FEC:98LP30, 20FEC:80DMC, and 50FEC:50FEC electrolytes were cycled for five cycles at C/10. Subsequent cycles were performed at a lithiation rate of C/10 and a delithiation-rate of C/3 between 1.5 V – 0.01 V. For all other electrolyte formulations, half-cells were cycled at a lithiation and delithiation rate of C/10 between 1.5 V – 0.01 V.

4.5 Post-Mortem Analysis

X-Ray photoelectron spectroscopy (XPS)

XPS measurements were carried out with a K-alpha spectrometer from Thermo-Fisher Scientific applying a micro-focused, monochromated Al-K_α x-ray beam with 400 µm spot size. A pass energy of 50 eV was used. Data acquisition and handling were done via the Thermo Avantage software by K.L. Parry *et. al.*[195] Spectra were fitted with one or more Voigt profiles (BE inaccuracy: ± 0.2 eV) via the Powell algorithm. The Voigt profile was obtained from the sum of the Gaussian and Lorentz components. A customized *smart* background function within the Avantage software was selected. It is based on the Shirley background with the additional constraint that the background should not be of a greater intensity than the actual data at any point in the region. Scofield sensitivity factors were applied for quantification. All spectra were referenced in binding energy to the hydrocarbon C 1s peak at 285 eV. For clarity of presentation, all spectra were normalized in intensity to [1,0]. The following part describes method-induced damages (i.e., x-ray beam and neutralizer) observed during XPS measurements and explains how the measurements were carried out. An analysis of the way in which washing alters the surface composition is provided as well, justifying the chosen preparation method.

X-ray beam damages: Exposure of the SEI to the x-ray beam during the time of analysis required for data acquisition may cause damage to the surface. Certain compounds of sulfur, fluorine, or nitrogen are very sensitive to the photon radiation. To minimize x-ray beam induced damages, these elements were always analyzed before carbon, oxygen, lithium, or silicon. Also, all spectra were recorded in iteration mode, i.e., one spectrum for one element at a time. Thus, it was possible to identify possible beam damage during the measurement period. **Figure 15** displays exemplary recorded iteration spectra for an Si/Gr electrode cycled in 1 M LiTFSI in TEG for 10 cycles. The spectra are displayed as recorded without any intensity normalization and binding energy correction. It can be seen, that for the C1s spectra only small changes occur between the six iterations. By contrast, the F1s, N1s and S2p spectra display larger changes during the measurement. Especially in the lower binding region, the signal increases in all spectra, as indicated by the red arrow. The further processing procedure only considered iterations that showed minimal changes. For most samples and spectra, the first two or three iterations were averaged and fitted.

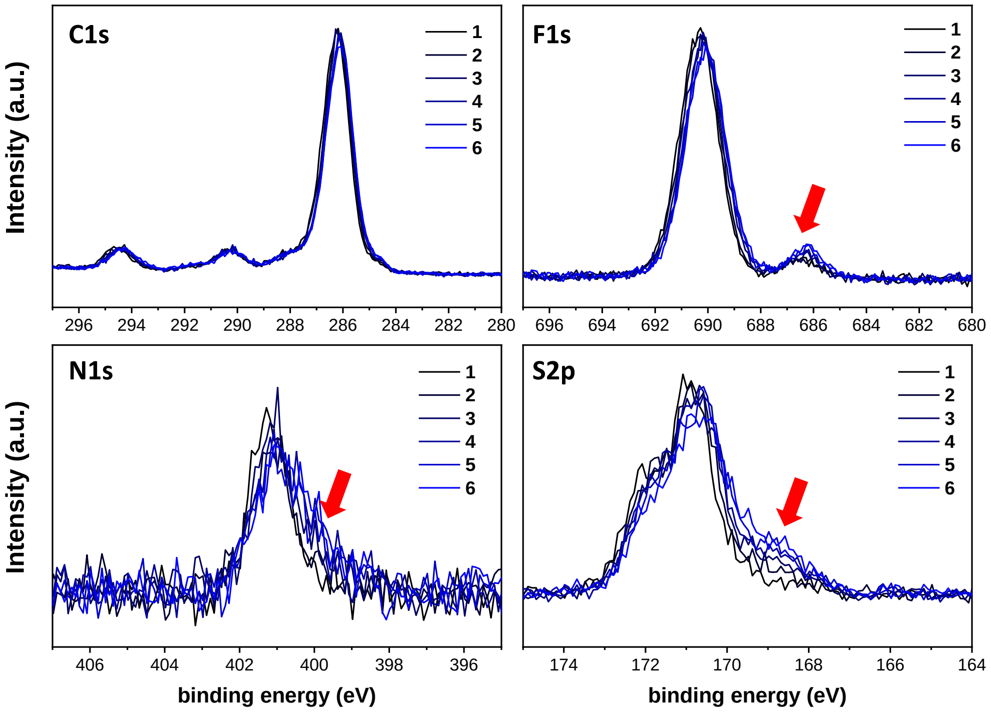

Figure 15: Iteration of C1s, F1s, N1s, and S2p spectra to illustrate the XPS beam damage on the SEI.

Charge neutralizer: The emission of photoelectrons leaves behind positive charges in the sample. In electrically conductive samples, these holes are easily filled up with electrons. However, in non-conductive samples, the positive charge can accumulate at the surface. This positive charge affects the XPS spectrum by causing peaks to shift to higher binding energies and to become distorted. Positive charge accumulation can be neutralized by replenishing with electrons from an external source. The Thermo Fischer K-Alpha spectrometer uses a combination of electron beam and ion beam for charge neutralization. Surfaces containing SEI products are usually non-conductive, which could motivate the use of a charge neutralizer. However, the neutralizer induces changes in SEI composition during the experiment, as can be seen in **Figure 16**. It displays the surface of a Si/Gr electrode cycled 100 times in 2FEC:98LP30. When measuring with the charge compensator (or flood gun – FG) a shift to smaller binding energies is observed for all spectra. Also, a decrease in peak width is overserved. Regarding the C1s spectra, no real changes occur during the measurement with the flood gun. For the O1s spectra, a new species emerges at around 529 eV, corresponding to Li_2O. This compound further increases during the measurement time, indicating continuous Li_2O formation. The F1s spectrum without flood-gun displays higher intensities for the $LiPF_6/Li_xPF_y$ peak at 688-689 eV and lower intensities for LiF at around 686 eV. With flood-gun, this ratio is reversed, i.e., higher intensities for LiF and lower intensities for $LiPF_6/Li_xPF_y$. Similarly, the intensity of $LiPF_6/Li_xPF_y$ at around 138 eV in the P2p spectra decreased when using the charge neutralizer. To prevent these induced changes in the SEI, no charge neutralizer is used during XPS measurements conducted in this thesis.

Washing procedure and system stability: At the end of every electrochemical experiment, the chosen cell potential was held for a certain duration until the current reached 0.5 µA. By doing so, the system was stabilized, and electrochemical reactions for the desired potential were completed. Cell potentials held after the experiment varied from 2.5 V, 1.3 V, 0.9 V, 0.8 V, 0.5 V, and 0.01 V during the first lithiation. Stabilization of all delithiated electrodes was done at 1.5 V. Approximatively two hours were required for the current to reach 0.5 µA. **Figure 17** displays the potential holding step after e.g., the last delithiation. Also shown is the subsequent potential relaxation to around 1.2-1.0 V. All delithiated electrodes for XPS measurements were opened at 1.2-1.0 V. Lithiated electrodes were opened at 0.01 V-0.02 V to ensure that fully lithiated electrodes were analyzed.

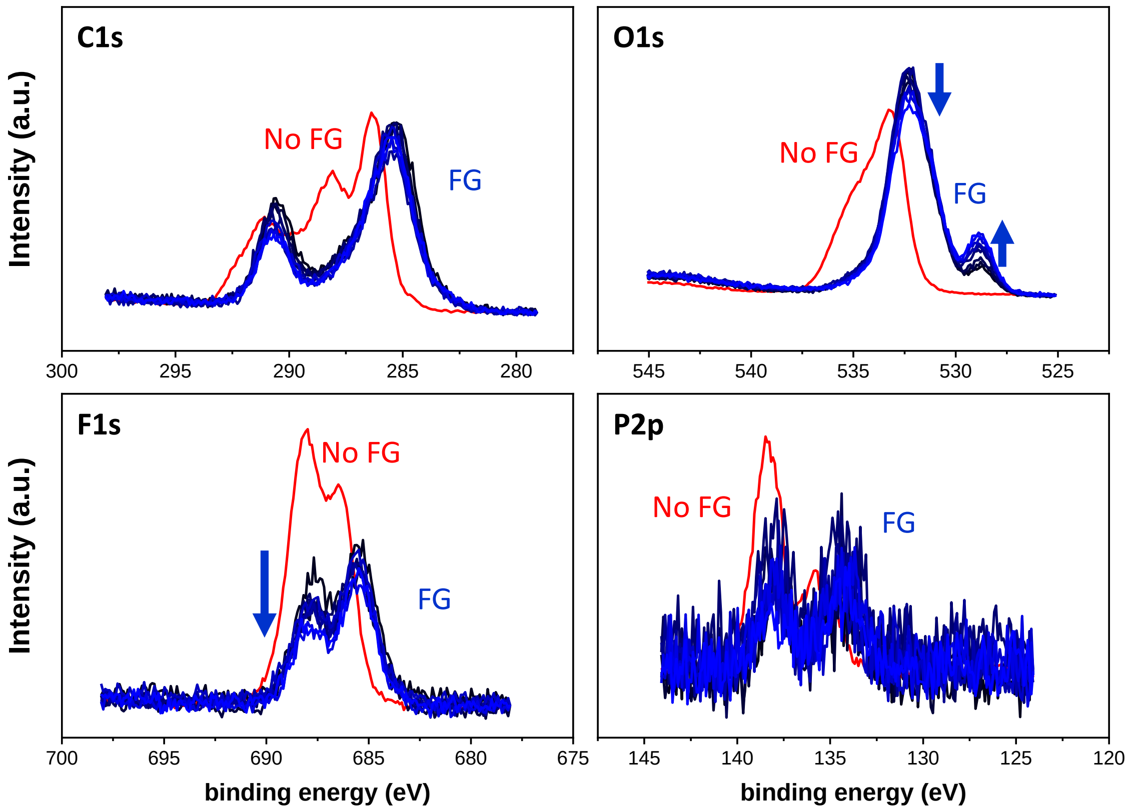

Figure 16: Influence of the charge neutralizer (Flood-Gun, FG). The area of all spectra is normalized to zero. No binding energy correction was applied.

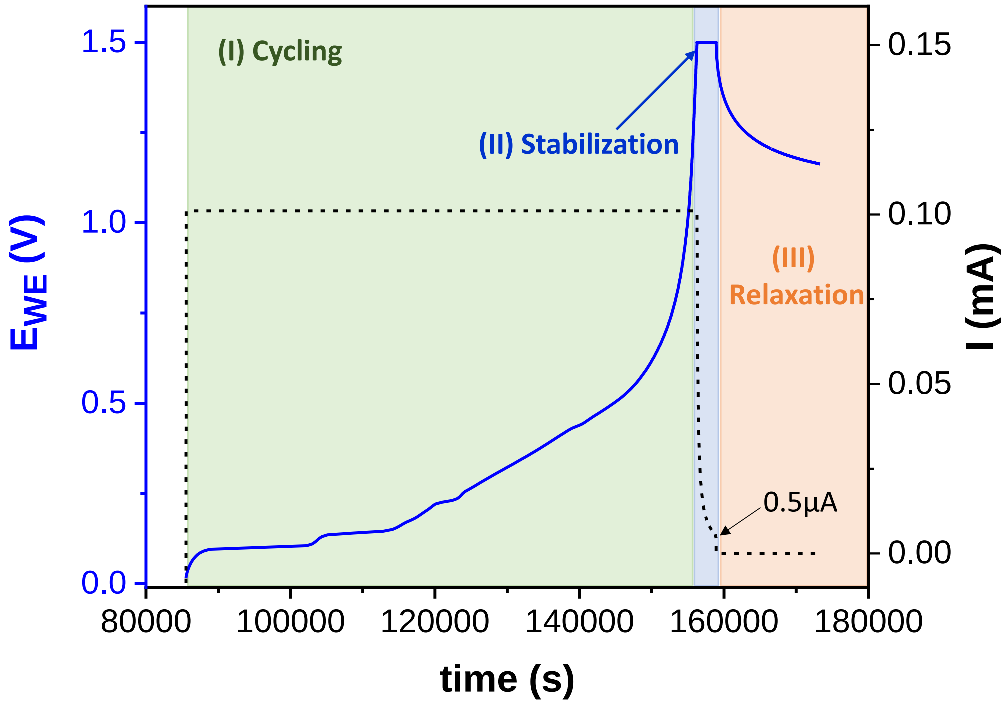

Figure 17: Potential held after electrochemical cycling (e.g., after the last delithiation at 1.5 V), until a current of 0.5 µA is reached. In this way, it is assured that the electrochemical reaction is complete.

XPS is an ex-situ method, i.e., the cell is opened in an argon-filled glovebox (H_2O & O_2 < 0.01 ppm) after the electrochemical measurements. The electrode is then washed with a solvent similar to the electrolyte to remove electrolyte solvent and salt residues. However, studies showed that this also changes the SEI composition.[196]–[198] Somerville *et al*. determined that washing removes fluorine containing compounds such as LiF.[199] To determine the effect of the washing procedure on the surface composition, the following three washing procedures were investigated and compared with an unwashed surface: a) three-times rinsed or hosed down, b) 1 min submersion, and c) 5 min submersion. **Figure 18** shows C1s, O1s, F1s, and P2p spectra of the same Si/Gr electrode cycled in LP30 electrolyte after the first delithiation. The electrode was then cut into four pieces and treated with DMC according to the three washing procedures mentioned above. The surface of the unwashed electrode part (black) displays very similar C1s, O1, and P2p spectra to the rinsed part (red). A long submersion (green) leads to the decrease of C-O species. A shorter submersion (blue) diminished in intensities of -C-H, -C-O, -CO_2, and -CO_3 environments. Corresponding observations can be made in the O1s. Overall, C1s and O1s spectra display relatively small differences between the different washing methods. By contrast, F1s and P2p spectra show a much stronger dependence on the washing procedure. Interestingly, the unwashed sample displays a high peak corresponding to LiF. This peak decreases by a large amount with all three washing methods. While LiF is highly insoluble in the DMC solvent,[200] its removal is probably due to mechanical removal. Literature reports confirm these observations.[161],[199] The peak corresponding to $LiPF_6$ salt residue and Li_xPF_y decomposition products only decreases in intensity after the longer submersion of the electrode. A similar trend can be observed for this species in the P2p spectra.

To avoid the drastic removal of LiF, which is an important component of the SEI, the long submersion was disregarded. A second comparison was conducted to decide between the rinsed and short submersion procedures. Therefore, three Si/Gr electrodes were cycled ten times in LP30. The electrode was then cut into two pieces and every piece was either rinsed or submerged, resulting in six data points (i.e., two for each electrode) for each washing method. The spectra were fitted and the standard deviation of the six data points for the different compounds was calculated, see **Figure 19**. Rinsing the electrode leads to higher standard deviations, and therefore to lower reproducibility, especially for salt residues and LiF. For this reason, all electrodes were washed exclusively via a one-minute immersion.

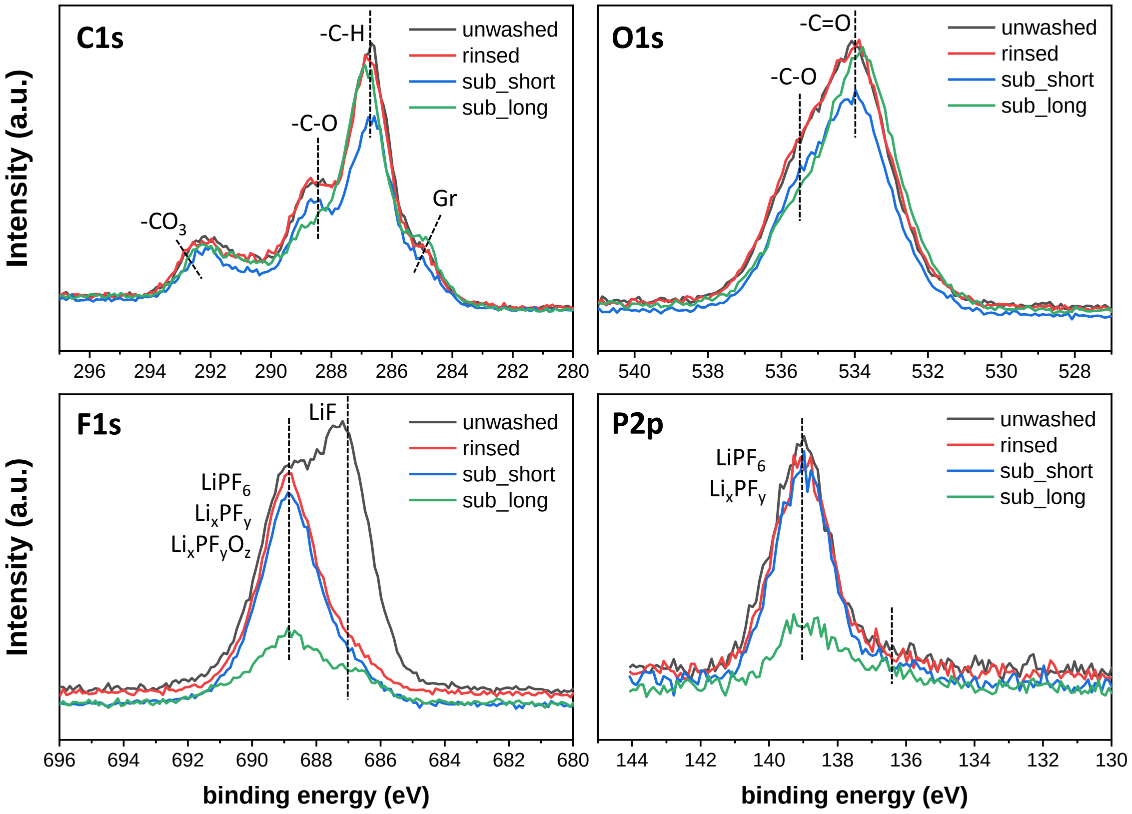

Figure 18: Influence of different washing procedures on the composition of the C1s, O1s, F1s, and P2p spectra of Si/Gr electrodes after the first delithiation at 1.5 V. All electrodes were cycled in LP30 electrolyte.

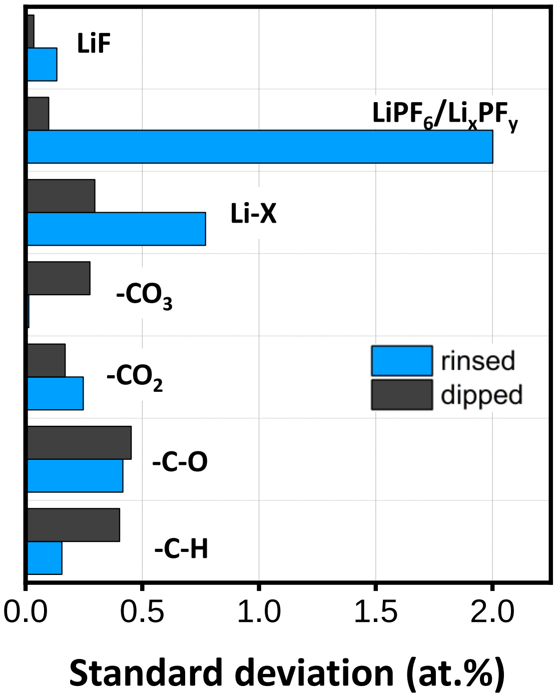

Figure 19: Standard deviation of atomic percentages of different SEI species after rinsing or dipping the Si/Gr electrode in 500 µL DMC washing solution.

DMC was used as a washing solvent for all electrodes that were cycled in carbonate-containing electrolytes, i.e., EC, DMC, FEC, or PC. The choice was motivated by the good solubility of the $LiPF_6$ or LiTFSI electrolyte salt in DMC, as well as its low evaporation temperature. Fast evaporation also reduces the amount of DMC washing solution residue left on the electrode surface. For the glyoxal-based electrolytes, TMG and TEG solvents are used as washing solutions. In each case, 500 µL of washing solution was used. After washing, all electrodes were dried and mounted on a sample holder using conductive copper tape. Transfer to the XP spectrometer was done via a transfer module under inert gas conditions.

Scanning electron microscopy (SEM). Cycled electrodes were washed in the respective solvent, mounted on a sample holder, and transferred under inert gas conditions to the SEM. SEM measurements were conducted using a thermal field emission scanning electron microscope (FESEM, Carl Zeiss SMT AG) equipped with energy-dispersive spectroscopy (EDS, Quantax 400 SDD, Bruker) at an acceleration voltage of 7 kV.

5 Fluoroethylene Carbonate as Electrolyte Solvent

In this chapter, FEC is considered as a cosolvent to replace EC. Two electrolyte formulations containing 1 M $LiPF_6$ in 20 vol.% FEC : 80 vol.% DMC and 50 vol.% FEC : 50 vol.% DMC are analyzed in terms of their electrochemical performance and SEI properties. A comparison is made with an electrolyte comprising EC as cosolvent and FEC as electrolyte additive.[1] This work provides an in-depth study on the interplay between (1) FEC electrolyte concentrations, (2) amounts of FEC decomposition products detected in the SEI, and (3) electrochemical performance of silicon-containing anodes. Several studies have analyzed gaseous or liquid FEC decomposition products, however, investigations on solid decomposition products with XPS remain contradictory. By developing a new XPS fitting model, this chapter examines how FEC improves the SEI during silicon volume changes.

5.1 Electrochemical Performance

Figure 20 shows galvanostatic cycling of 10%-Si/Gr half-cells cycled in the respective electrolytes 2FEC:98LP30 (blue), 20FEC:80DMC (black), and 50FEC:50DMC (green). All cells display similar initial lithiation capacities of around 765 mAh g^{-1}, independent of the electrolyte. This value is much higher than the expected theoretical capacity of 623 mAh g^{-1} because of extensive SEI formation during the first lithiation. Therefore, resulting coulombic efficiencies amount to only 80-83 %. After the first delithiation, a capacity of around 620 mAh g^{-1} is reached, which is close to the theoretical one. Upon cycling, the cell containing 2FEC:98LP30 exhibits the fastest capacity fade. After around 40 cycles, a linear decrease can be observed, which results in a capacity loss of 309 mAh g^{-1} after 100 cycles. Capacity retention amounts to only 51 % compared to the second cycle capacity. The loss in electrochemical activity can also be observed in the coulombic efficiency plot, where efficiencies are decreasing to 98 %. By contrast, when using the FEC cosolvent electrolytes, a more stable cycling behavior is achieved. Electrodes cycled in 20FEC:80DMC and 50FEC:50DMC exhibit higher lithiation capacity retentions after 100 cycles when compared to the second cycle, amounting to 78 % and 79 % respectively.

---

[1] 1 M $LiPF_6$ in 1:1 EC:DMC + 2 vol.% FEC

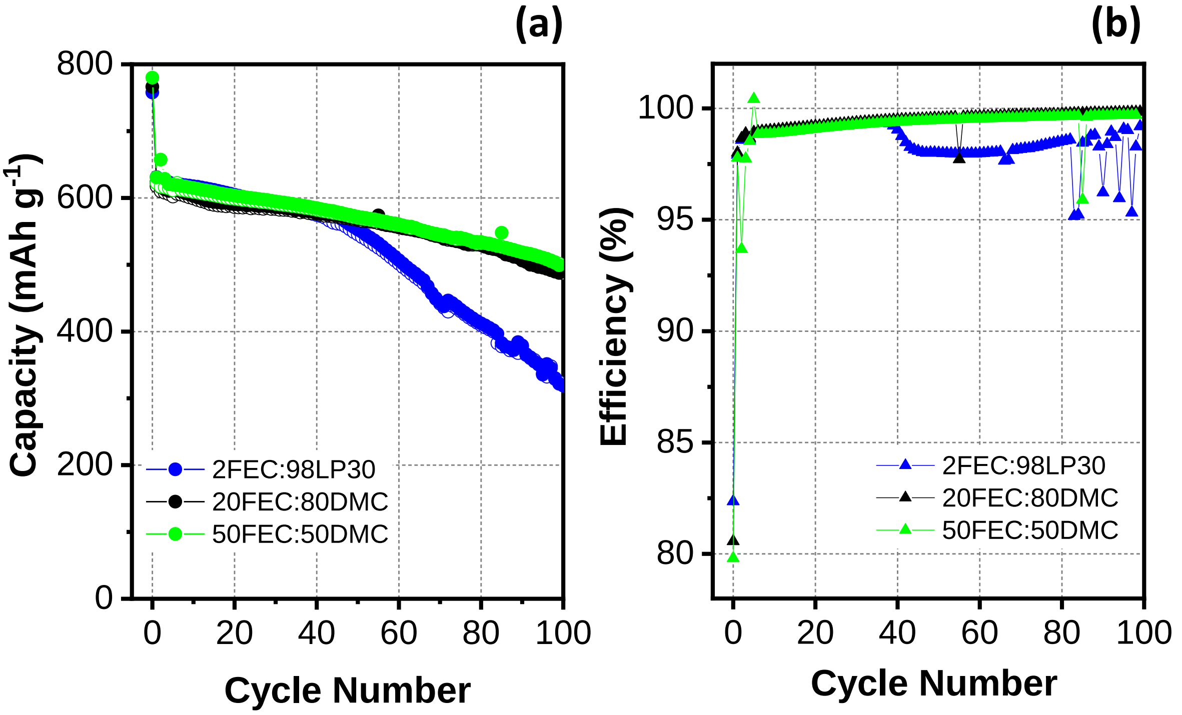

Figure 20: (a) Cycling stabilities and (b) coulombic efficiencies of Si/Gr electrodes cycled in 2FEC:98LP30 (blue), 20FEC:80DMC (black), 50FEC:50DMC (green) electrolytes.

Figure 21(a) displays the dQ/dE signals for selected cycles. During the first lithiation (black line), four minima can be observed which correspond to different intercalation reactions of lithium-ions into graphite: 0.2 V (stage IV), 0.13 V (stage III, LiC_{30}), 0.1 V (stage II, LiC_{12}), and 0.07 V (stage I, LiC_6).[201],[202] Lithiation of silicon is more difficult to discern in the dQ/dE profiles as the alloying reactions extend over the whole lithiation profile. Crystalline silicon is lithiated via a two-phase mechanism resulting in amorphous silicon-lithium alloys (Li_xSi).[52]–[55] At the end of the first lithiation, this amorphous phase reacts to crystalline $Li_{15}Si_4$, corresponding to the minima at 0.04 V in the dQ/dE plot.[58]–[60] During delithiation, $Li_{15}Si_4$ transforms back to amorphous silicon in which state it remains during further cycling. In subsequent cycles, a new signal is observed at around 0.3 V corresponding to the lithiation of this amorphous phase. Enlargement of this region is displayed for each electrolyte case as insets in **Figure 21(a)**. GCPL profiles are displayed in **Figure 21(b)**, in which every plateau corresponds to a peak in the dQ/dE plots at the respective potential. GCPLs profiles with steeper courses produce dQ/dE plots with broader peaks.

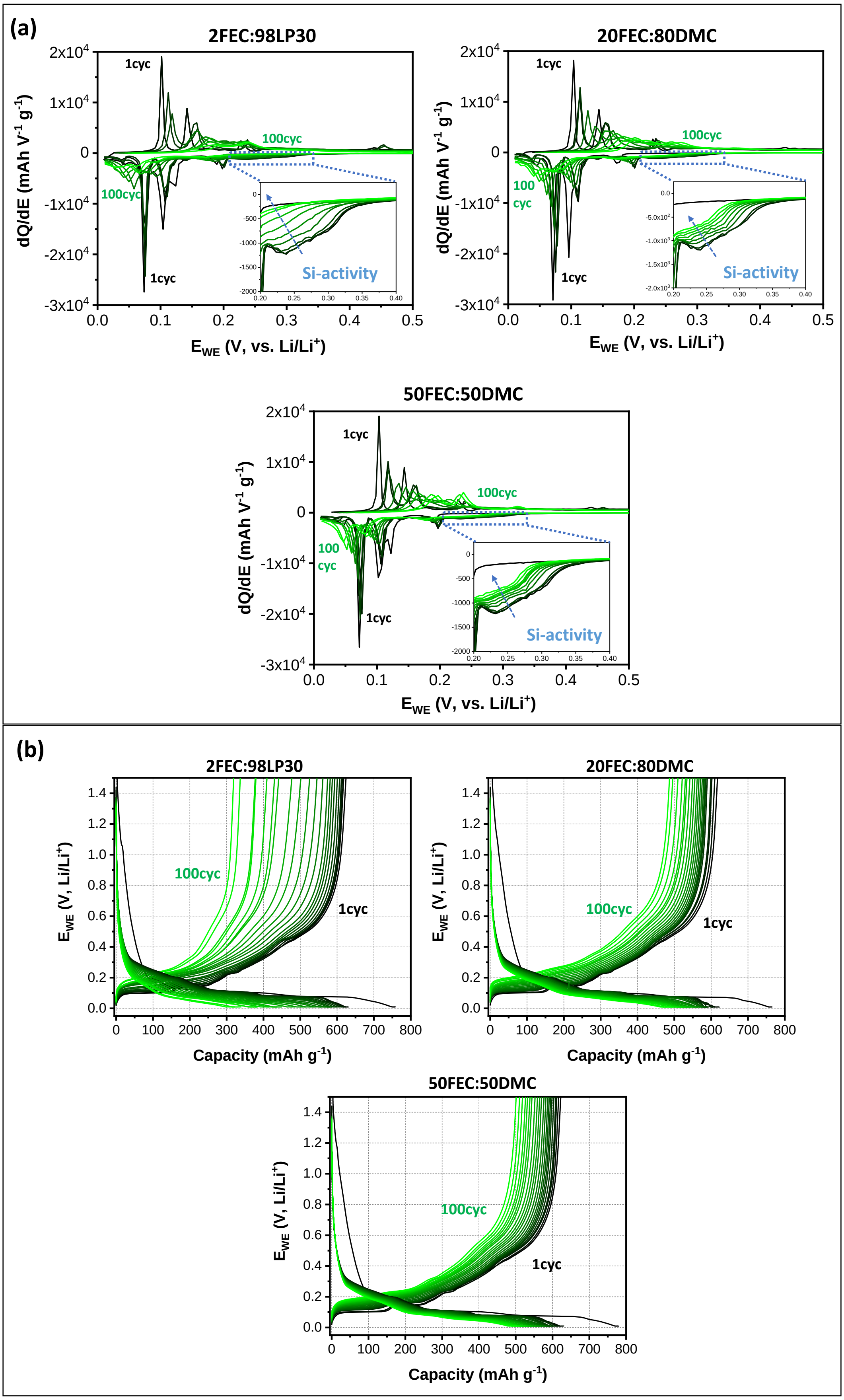

Figure 21: (a) dQ/dE plots and (b) GCPL of Si/Gr electrodes cycled in 2FEC:98LP30, 20FEC:80DMC, and 50FEC:50DMC electrolytes, respectively.

Upon cycling, a decrease in electrochemical activity is seen for all electrolyte formulations. dQ/dE plots show a decrease in intensity for all peaks, while the GCPL profiles display receding length of the corresponding plateaus. Furthermore, plateaus shift towards higher potentials (during delithiation) and lower potentials (during lithiation). A shift of the lithiation and delithiation potential can be explained by overpotentials emerging during cycling on the Si/Gr anode and the lithium metal counter electrode. Furthermore, the intensity of the graphite peaks decreases in all three dQ/dE plots upon cycling. This can be due to either damaged graphite particles or to a loss in electrode integrity. The former can be excluded by Raman measurements of Si/Gr anodes after 100 cycles in each electrolyte. As can be seen in **Figure A1**, the graphite bands D, G, and 2D are detected for all three electrolyte cases. This excludes damage to the graphite particle and indicates that graphite is still able to intercalate and deintercalate lithium-ions. Considering the theoretical capacity of 10%-Si/Gr anodes of 623 mAh g^{-1}, 322 mAh g^{-1} of this capacity result from silicon, while graphite contributes with 301 mAh g^{-1}. Electrodes cycled in the FEC cosolvent electrolytes display a capacity of around 500 mAh g^{-1} after 100 cycles. This capacity is only achieved if both graphite and silicon are electrochemically active. As shown in the dQ/dE inset of **Figure 21(a)**, silicon is still active after 100 cycles even though a decrease is observed upon cycling. Graphite also displays a decrease in activity over time. The decrease in capacity observed for the 20FEC:80DMC and 50FEC:50DMC formulations is due to a drop in the electrochemical activity of both silicon and graphite. However, it is difficult to determine to what degree silicon and graphite as receding in activity. Cycled in the FEC additive formulation, the electrode shows a capacity of only 320 mAh g^{-1} after 100 cycles. The dQ/dE displays a much stronger drop in graphite activity and silicon activity than compared to the dQ/dE of the FEC cosolvent formulations. Especially silicon seems to suffer a higher loss, see inset of **Figure 21(a)**. Most likely, the decrease in electrochemical activity is the result of a loss of electrode integrity. This can be caused by a thick SEI layer on top of graphite and silicon particles, resulting in the electrical isolation of the particles.

A positive effect of FEC on electrochemical performance and more specifically on the retention of silicon activity has been demonstrated in several studies.[9],[10],[136],[138],[140],[142],[203]–[206] Jung *et al.* showed that FEC is consumed in every cycle and when depleted, the cell performance drops dramatically.[140] Hereby, the consumption of FEC is dependent on the relation between FEC concentration and the amount of active material in the electrode (i.e., $\mu mol_{FEC}/mg_{electrode}$). In the present case, all electrodes exhibited the same amount of silicon and similar mass loading of 2.8-3.1 mg cm^{-2}. Even though FEC consumption on the lithium metal counter electrode has been observed in the literature[140], an analogous effect between the cells can be assumed. The drop in capacity for the electrode cycled in the FEC-additive electrolyte 2FEC:98LP30 shows the fastest capacity decrease because FEC seems to be depleted earlier. With FEC as a cosolvent, a sufficient amount of FEC is still present in the electrolyte after 100 cycles. Consequently, the stabilizing effect is retained for a longer period. The following part investigates how the different FEC electrolyte concentrations influence SEI composition, thickness, and morphology. A correlation is attempted between SEI properties and electrochemical performance.

5.2 SEI analysis

SEI thickness approximation

Eq.(22) in **Chapter 2.2** shows the thickness of an overlayer such as the SEI is dependent on the emission angle and the inelastic mean free path (IMFP). In this thesis, the emission angle is constant at 90° for all measurements. To determine the IMFP, the chemical composition of the SEI has to be considered. However, the SEI is composed of different inorganic and organic components which are distributed throughout the layer, rendering it highly inhomogeneous. To approximate the organic part of the SEI, polyethylene (PE) is generally used, while LiF and Li_2CO_3 are good representants of the inorganic part. **Table 6** displays IMFP values of these species. Methyl methacrylate (PMMA) is used as an example for polymeric species containing oxygen atoms. IMFP values for PE, PMMA, and LiF are taken from literature at an electron kinetic energy in the respective material of 1200 eV.[207],[208] The value results with respect to the kinetic energy of a C1s photoelectron when excited by Al-K_α radiation.[1] The IMFP value for Li_2CO_3[2] was calculated with the NIST database.[209] Also shown are the calculated overlayer thicknesses with Eq.(22) for each IMFP value with an exemplary intensity ratio of 0.1. The results show that even if the IMFP are close to each other, the obtained thicknesses can differ up to 1.5 nm. Therefore, this thesis only approximates the SEI thickness.

Table 6: IMFP values of PE, LiF, and Li_2CO_3 and overlayer thickness calculated with respect to Eq.(22). Electron kinetic energy of 1200 eV.

Species	IMFP (nm)	Exemplary intensity ratio	Calculated overlayer thickness d (nm)
PE	3.7	0.1	8.5
PMMA	3.9	0.1	9.0
LiF	3.2	0.1	7.4
Li_2CO_3	3.4	0.1	7.8

The SEI thickness approximation considers how much a certain bulk electrode peak is attenuated by the SEI layer. Therefore, the area under a C1s graphite peak after cycling is divided by the area of a pristine graphite peak, see **Figure 22** and Eq.(25):

---

[1] 1486 eV-285 eV ~ 1200 eV

[2] band gap of 7 eV[229] and density of 2.11 g cm^{-3}, kinetic energy ~ 1200 eV

$$attenuation = \frac{A(graphite)_{SEI}}{A(graphite)_{pristine}} \tag{25}$$

The obtained attenuation value does not give an actual layer thickness but a qualitative description that indicates how much the graphite signal is weakened by the SEI layer. High attenuation values indicate more graphite and thereby a thinner overlayer.

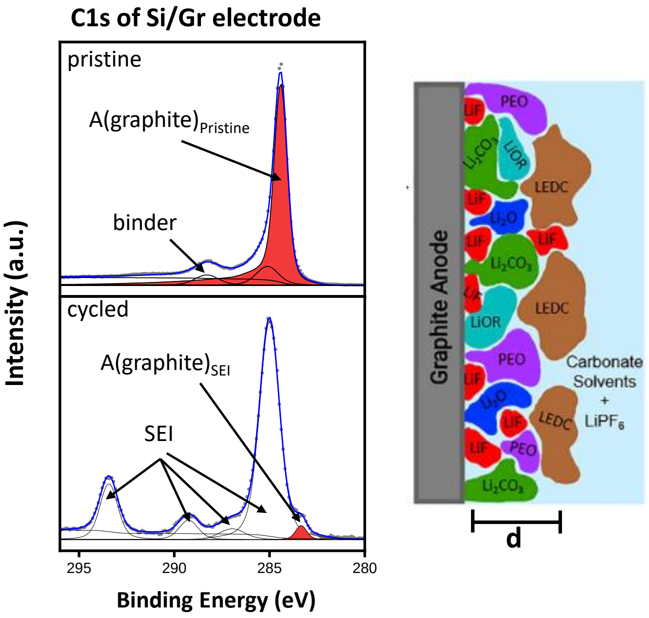

Figure 22: Attenuation of the graphite signal by an SEI overlay.

Figure 23 illustrates the attenuation of the graphite signal at different cycling stages with respect to the electrolyte formulation. The calculation was conducted for Si/Gr anodes cycled to 0.8 V and 0.01 V during the 1st lithiation, as well as to 1.5 V after the 1st, 10th, and 100th delithiation. At 0.8 V, a graphite signal is observed for all electrolyte formulations as is indicated by attenuation values of around 0.7 to 0.5. Because carbonate-based solvents are known to be reduced at around 1.2-0.9 V vs Li/Li$^+$, the SEI is still thin at this early stage.[210] In the fully lithiated state at 0.01 V, the value drops considerably for all FEC contents, indicating a thicker SEI layer on top of the graphite particles. After the first delithiation at 1.5 V, the attenuation value increases for all three electrolytes due to a decrease in SEI thickness from the lithiated to the delithiated state. This phenomenon of changes in SEI thickness is called SEI breathing and is a commonly observed process for silicon-containing electrodes.[211],[212] After 10 cycles, a small drop in attenuation is observed for each electrolyte case. This decrease is even stronger after 100 cycles, indicating the formation of a thick SEI layer. In the case of 2FEC:98LP30, no graphite is detected, while only a small intensity remains for 20FEC:80DMC and 50FEC:50DMC. Overall, a correlation between signal attenuation and FEC electrolyte concentration can be observed for the cycling stages 0.01 V, 1, 10, and 100 cycles. The less FEC present in the electrolyte, the thicker the approximated SEI thickness: 2FEC:98LP30 > 20FEC:80DMC > 50FEC:50DMC.

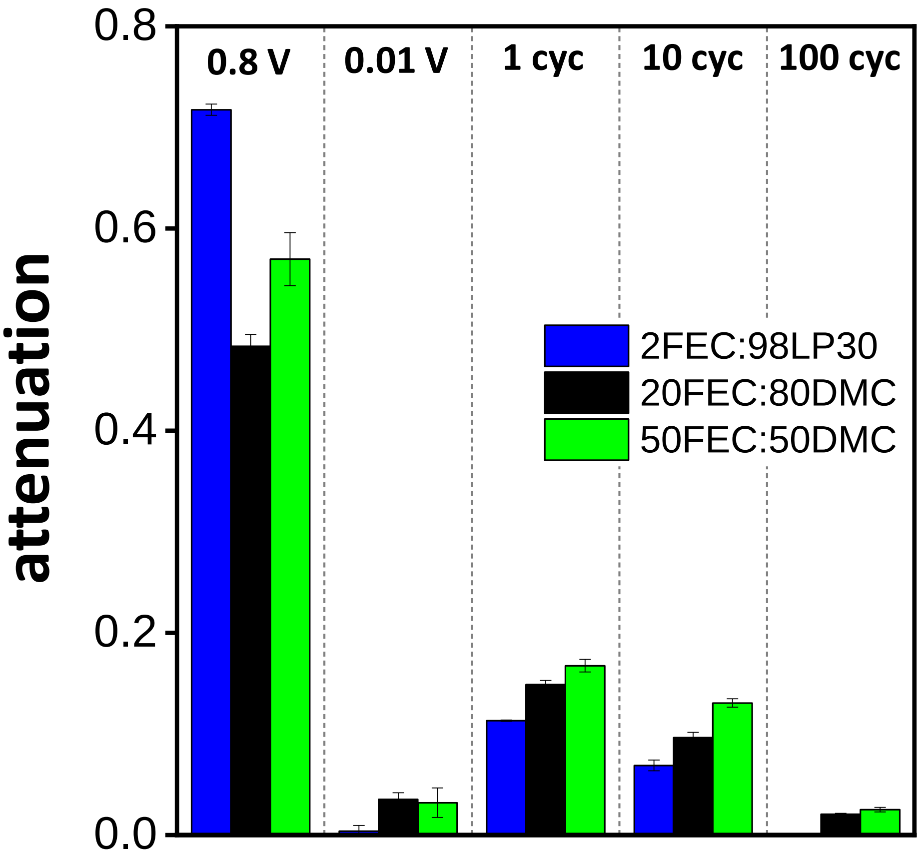

Figure 23: SEI thickness approximation on graphite particles of electrodes cycled in 2FEC:98LP30 (blue), 20FEC:80DMC (black), and 50FEC:50DMC electrolyte (green) at 0.8 V and 0.01 V during the first lithiation, and at 1.5 V after the 1st, the 10th, and the 100th cycle. The error bars indicate the standard deviation between two measurements on one electrode.

XPS fitting model of FEC decomposition

To gain an understanding of FEC decomposition products, the SEI formed by a pure FEC electrolyte (i.e., 1 mol $LiPF_6$ in 100% FEC) on Si/Gr electrodes is analyzed via XPS after cycling to 0.01 V. For more information about the XPS sample preparation see **Chapter 4.5**. The resulting C1s, F1s, and Si2p spectra are displayed in **Figure 24**. Detailed information about the used fitting parameters can be found in **Table A1** and the corresponding survey spectrum is given in **Figure A10**. Alongside hydrocarbon (285 eV) and graphite (283.4 eV), the following carbon-oxygen environments can be identified in the C1s spectrum: -**C**-O (286.8 eV), $\mathbf{C}_a$ (287.9 eV), -$\mathbf{C}O_2Li$ (289.2 eV), $Li_2\mathbf{C}O_3$ (290.2 eV), and $\mathbf{C}_b$ (291.1 eV). C_a and C_b represent the two carbon environments in 1,3-dioxolan-2-one (DO), see molecular structure in **Figure 24.** The fitting of this species was done based on previous data for these environments.[213] Further, FWHM and the area ratio between C_a and C_b were fixed to 2:1 during fitting. The detection of DO via XPS can be an indication for FEC de-fluorination, yielding LiF and VC. VC can subsequently polymerize and form poly(VC). To check whether VC forms a similar SEI, the decomposition products of an electrode cycled in pure VC are analyzed. The C1s spectrum in **Figure A3** displays two peaks corresponding to C_a and C_b in poly(VC).[213] Only little amounts of -C-O and -CO_2 and no Li_2CO_3 are detected. In contrast, FEC leads to an SEI with high -C-O, C_a/C_b, and -CO_2Li-content. This demonstrates that the SEI formed by FEC and VC is very different. As proposed in literature, it is very likely for DO or poly(VC), -C-O, and -CO_2Li units to form a heterogenous cross-linked polymer network.[23],[134],[137],[214],[215] For example, Jin *et al.* proposed a polymer consisting of cross-linked DO and PEO units.[137] The -C-O groups detected in the present XPS analysis could correspond to PEO species. It is important to note, that XPS cannot differentiate between poly(VC) and DO units as they display identical chemical environments at the same binding energies. It is also not possible to get information on the exact molecular structure of the polymer network with XPS, due to the highly inhomogeneous nature of the SEI. The F1s spectrum of **Figure 24** shows a peak at 685.3 eV corresponding to LiF and a broad peak at 687.7 eV most likely a mixture of $LiPF_6$ salt residues, Li_xPOF_y salt decomposition products, and silicon oxyfluorides SiO_xF_y.[216] Both F-P and F-Si environments can be found in the corresponding P2p (**Figure A3**) and Si2p spectra (**Figure 24**), respectively. It must be noted that a certain charging effect of the sample during XPS cannot be ruled out. A charge neutralizer could not be used because it damages the SEI, see **Chapter 4.5** for more information. Therefore, the broad peak at 687.7 eV could further contain -CF components which usually emerge at binding energies between 687-688 eV.[176] However, these -CF species are not included in the fitting model because their formation is still controversial.[137],[139] Different silicon environments can be found in the Si2p spectrum of **Figure 24**, namely Li_xSi (98.2 eV), Li_xSiO_y (101 eV), SiO_2 (103 eV), and SiO_xF_y (105.3 eV).[179],[180],[203] To ensure consistent data evaluation, this fitting model is used for the following XPS analyses.

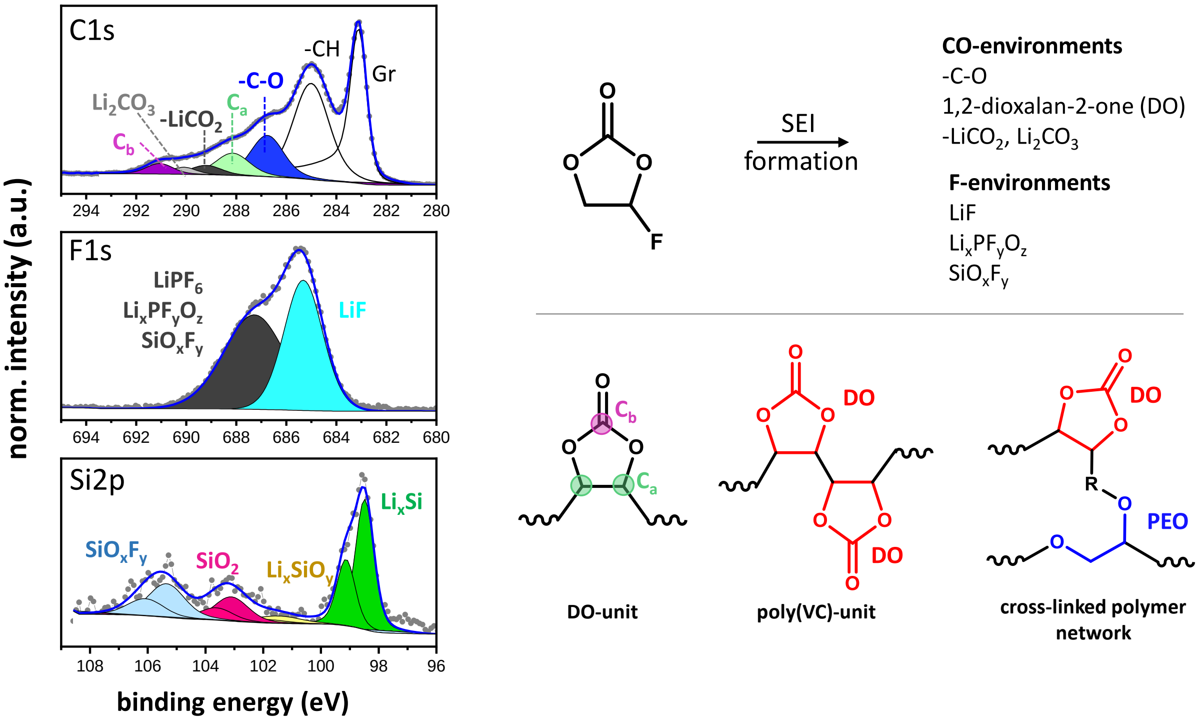

Figure 24: C1s, O1s, F1s, and Si2p photoelectron spectra of an electrode after the first lithiation cycled in 1 M $LiPF_6$ in FEC electrolyte. Decomposition products of FEC based on references.[23],[134],[137],[217]

SEI composition

C1s photoelectron spectra from electrodes cycled up to 0.8 V and 0.01 V during the first lithiation are displayed in **Figure 25**. Also shown are spectra of Si/Gr electrodes after 1, 10, and 100 cycles in delithiated states at 1.5 V. Derived atomic percentages of detected C1s species are shown in **Figure 26**. Also displayed in **Figure 26** are the atomic percentages of fluorine-containing decomposition products. F1s, O1s, and P2p spectra can be found in **Figure A4-Figure A6**. An overview of all detected species with their atomic percentages is shown in **Table A2-Table A4** and survey spectra are displayed in **Figure A10-Figure A11**. The surface species are assigned following the fitting model described above.

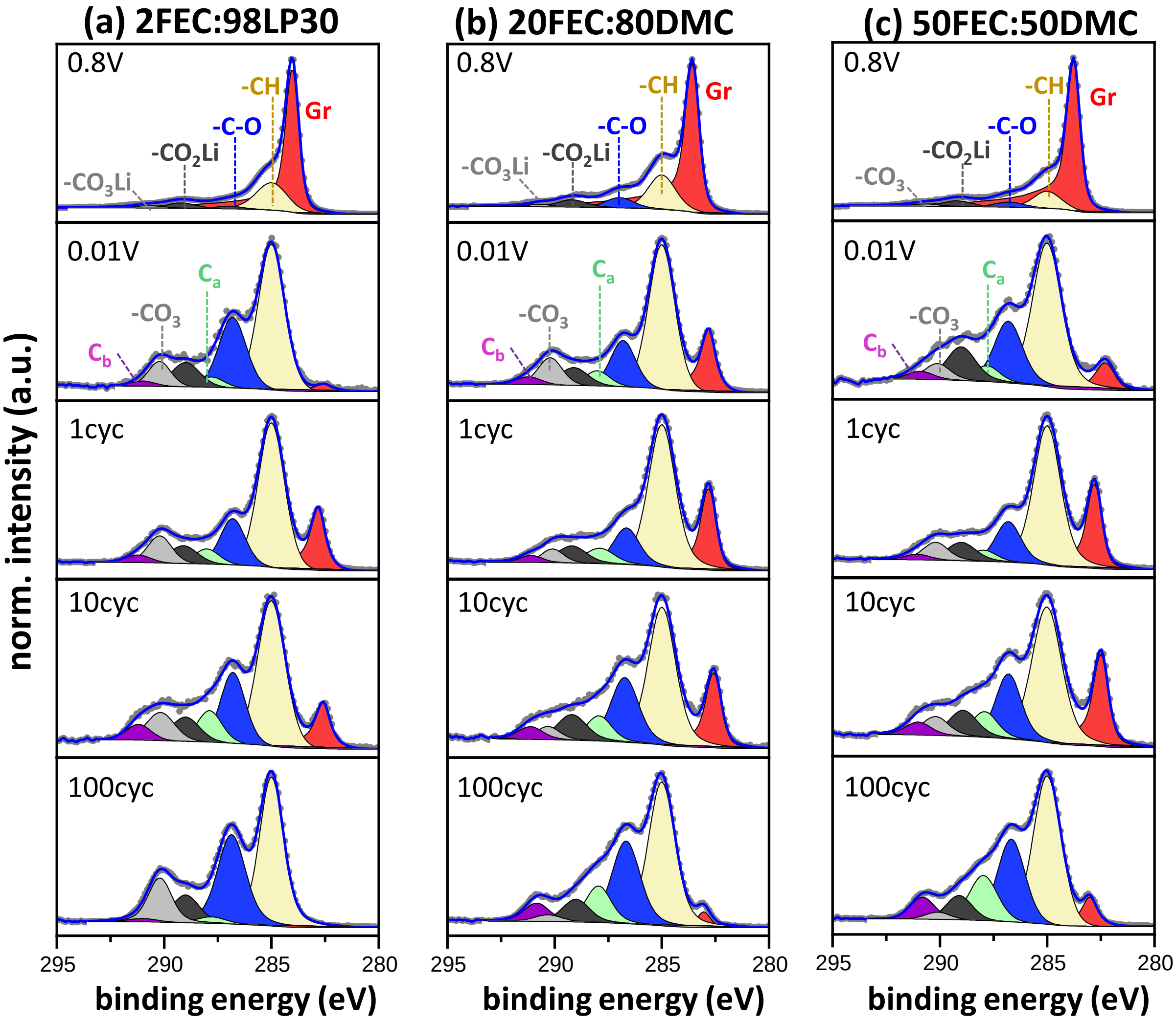

Figure 25: C 1s photoelectron spectra of electrodes cycled in (a) 2FEC:98LP30, (b) 20FEC:80DMC, and (c) 50FEC:50DMC electrolyte at 0.8 V and 0.01 V during the 1st lithiation, and at 1.5 V after the 1st, the 10th, and the 100th cycle.

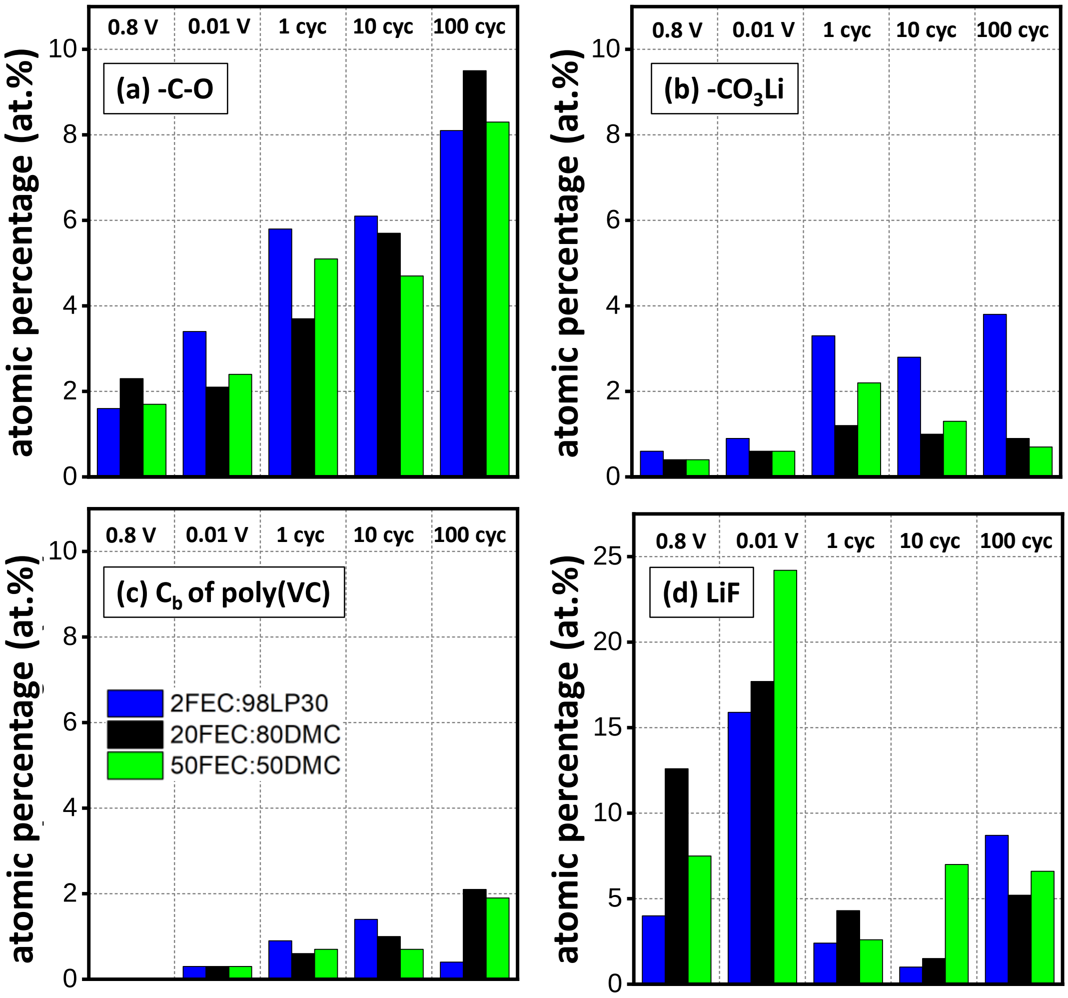

Figure 26: Atomic percentages of (a) -C-O, (b) $-CO_3$, (c) C_b in poly(VC), and (d) LiF. Displayed are the percentages at 0.01 V during the 1st lithiation, and at 1.5 V after the 1st, 10th, and 100th cycle for the respective electrolyte, i.e., 2FEC:98LP30, 20FEC:80DMC, and 50FEC:50DMC.

At 0.8 V, five peaks are observed for each electrolyte in the C1s spectra of **Figure 25**: graphite (~284.2 eV), hydrocarbons (285 eV), -C-O groups (~286.7 eV) $-CO_2Li$ species (289.2 eV), and $-CO_3Li$ species (~290.5 eV). Hydrocarbons can originate from surface contamination such as adventitious carbon as well as from -CH-containing SEI species. All -CO-containing compounds originate from starting electrolyte decomposition. Further voltage decrease to 0.01 V, leads to thickening of the SEI, as can be seen by a drop in graphite intensity. As previously seen, the SEI thickness depends on the amount of FEC in the electrolyte and follows the trend 2FEC > 20FEC > 50FEC. A shift to lower binding energies of the graphite peak (i.e., to 282.5 eV) can be explained by the formation of an electrical potential gradient at the buried interphase between the SEI and the electrode surface.[181] Additionally, two peaks emerge that can be ascribed to the two carbon environments in DO as has been previously discussed, namely C_a (287.9 eV) and C_b (291.0 eV). The intensity ratio of C_a and C_b is close to

1:2, suggesting that the peaks mainly consist of DO units. Compared to the C1s of the electrode cycled in pure FEC (see **Figure 24**), the same carbon species are detected. While -CH, -C-O, -CO_2Li, and -CO_3Li were observed with pure FEC electrolytes, these species typically also emerge in SEIs formed by DMC and EC containing electrolytes, see **Figure A8**. Only C_a and C_b emerge in presence of FEC. In the following discussion, these peaks are therefore used as an unambiguous indicator for the presence of FEC decomposition products in the SEI. (The emergence of LiF occurs for $LiPF_6$ and FEC, making it difficult to differentiate from which electrolyte component LiF is originating.) After the first delithiation to 1.5 V, the graphite intensity increases in all three cases, indicating a thinner SEI. The SEI thinning results from the dissolution or detachment of certain species, such as LiF which drops by 20 a.t.%, see **Figure 26**. A decrease in relative peak area is observed for -C-O and -CO_2Li compounds, see **Figure A7**, while carbonate and DO species only change to a negligible extent. After 10 cycles, a decrease in atomic percentages and relative peak areas of carbonate species is observed for all three electrolytes, see **Figure 25** and **Figure A7**. Electrodes cycled in 2FEC:98LP30 and 20FEC:80DMC display an increase in -C-O and DO abundance, while the detected LiF amount decreases. By contrast, the electrodes cycled in 50FEC:50DMC show no changes for -C-O and DO species, but an increase in LiF. After 100 cycles, a large decrease of C_a and C_b is observed with 2FEC:98LP30, while -C-O and -CO_3Li species increase in intensity and abundance, see **Figure 25** and **Figure 26**. In fact, the spectrum now looks very similar to a spectrum from an electrode cycled in pure LP30 electrolyte, see **Figure A8**. By contrast, the electrodes cycled in 20FEC:80DMC and 50FEC:50DMC still display intensive C_a and C_b peaks in their C1s spectrum. The decline of both peaks when cycling in the 2FEC:98LP30 formulation indicates decreasing FEC concentration in the electrolyte and the SEI. Because FEC makes up only 2 vol.% of the electrolyte, its depletion occurs much earlier than when it is used as a cosolvent. The increase in -C-O and -CO_3Li species indicates an increase in EC and DMC decomposition. Previously observed DO components (i.e., C_a and C_b) are now most likely buried under a new layer of these carbonate products. In contrast, when cycling in the FEC cosolvent electrolytes, namely 20FEC:80DMC and 50FEC:50DMC, the FEC reservoir is much larger. Therefore, DO species are still present in the SEI even after prolonged cycling.

Another interesting feature is the influence of the EC cosolvent on the SEI composition of Si/Gr electrodes cycled in 2FEC:98LP30. The amount of detected -CO_3Li is highest for this electrolyte in all analyzed states (i.e., 0.8 V, 0.01 V, 1 cyc, 10 cyc, and 100 cyc). The presence of EC seems to promote the formation of more carbonate-containing SEI species, suggesting that EC decomposition occurs, even in presence of FEC. Jung *et al.* could show that the presence of FEC reduces the decomposition of EC to a bare minimum.[140] Similarly, Jin *et al.* found that in presence of FEC, the formation of liquid decomposition products such as LEDC is suppressed.[23] That XPS still detects EC decomposition can be explained by its high chemical sensitivity. To evaluate the effect of EC in an FEC cosolvent electrolyte, electrodes were cycled in 20FEC:40EC:40DMC, with corresponding C1s spectra displayed in **Figure 27(a)**. The C1s spectra after the 1st lithiation (0.01 V) and the 1st delithiation (1cyc) show the same surface species as the spectra in **Figure 25**. A comparison between atomic percentages of an electrode cycled in 20FEC:80DMC (black) and 20FEC:40EC:40DMC (pink) is given in **Figure 27(b)**. The presence of EC leads to an increase in all carbon-oxygen species (i.e., -C-O, C_a, $-CO_2Li$, $-CO_3Li$, and C_b). The intensified electrolyte decomposition in presence of EC indicates that EC decomposition products negatively affect the SEI stability, promoting stronger electrolyte decomposition. Alkyl dicarbonates such as LEDC formed upon EC decomposition are known to be highly reactive.[107],[218] These species usually initiate all further reactions occurring in the SEI.[107],[218],[219] Additionally, the short-chained nature of LEDC leads to a poor ability to accommodate the silicon volume changes.[23]

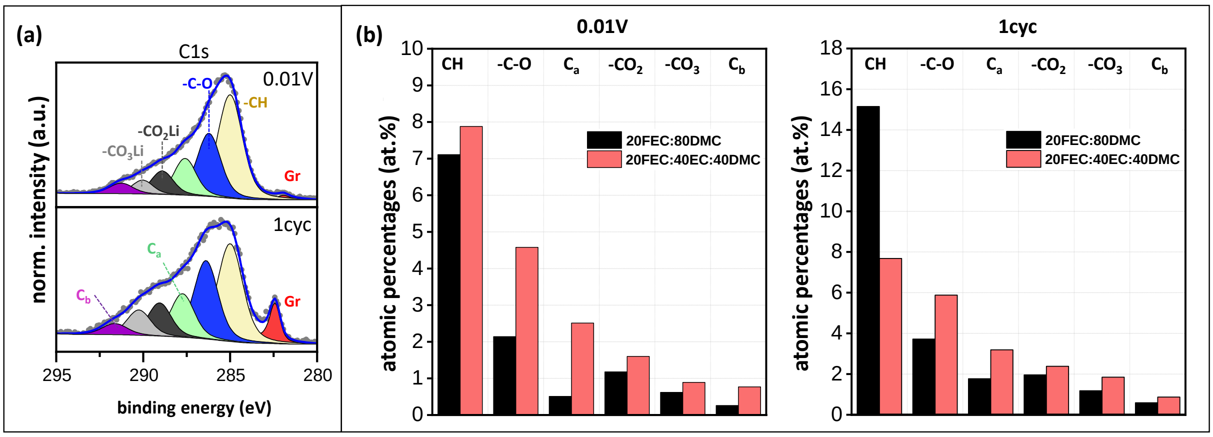

Figure 27: (a) C1s spectra of Si/Gr electrodes cycled in 1 M $LiPF_6$ 20FEC:40EC:40DMC after the first lithiation (0.01 V) and the first delithiation (1cyc). (b) Comparison of C1s atomic percentages of electrodes cycled in 20FEC:80DMC and 20FEC:40EC:40DMC.

Effect of FEC on silicon

Si2p spectra of 10%-Si/Gr electrodes cycled in the respective electrolytes are displayed in **Figure 28**. In general, some spectra show very noisy data, and the peak fits are included only as a guide to the eye. At 0.8 V, two silicon species are detected independent of the electrolyte formulation, namely Si^0 (99 eV) and SiO_2 (~103.3 eV). These signals are also found at the surface of silicon particles in pristine Si/Gr electrodes, see **Figure A9**. For electrodes cycled in 20FEC:80DMC and 50FEC:50DMC electrolytes, an additional component is seen, which corresponds to SiO_xF_y (~105.3 eV).[179],[180] This species was also observed in the 100 % FEC electrolyte previously discussed (see **Figure 24**). Upon lithiation to 0.01 V, the bulk silicon species, i.e., Si^0 and SiO_2, disappear in all three cases. By contrast, the SiO_xF_y species is still observed for 20FEC:80DMC and 50FEC:50DMC. After the first delithiation, the electrode cycled in the 2FEC:98LP30 electrolyte displays peaks corresponding to lithiated silicon species such as Li_xSi (98.2 eV) and Li_xSiO_y (101 eV). For this electrolyte, both species disappear after 10 cycles, but Li_xSiO_y is re-emerging after 100 cycles. Electrodes cycled in 20FEC:80DMC and 50FEC:50DMC display Li_xSi and SiO_xF_y species after the first delithiation. Additionally, Li_xSiO_y is detected when using the 50FEC:50DMC electrolyte. After 10 and 100 cycles, only SiO_xF_y species are observed, and no bulk-silicon re-emerges for both FEC cosolvent formulations.

As is evident from the data, the FEC concentration in the electrolyte plays a role in the silicon species detected. Two main differences are observed: 1) The re-emergence of Li_xSiO_y after 100 cycles for the 2FEC:98LP30 electrolyte, while this is not the case with the two FEC cosolvent electrolytes. Re-emergence of the Li_xSiO_y species could be due to cracks or a more porous SEI and be correlated to low FEC content in the electrolyte after 100 cycles. As seen in the analysis of the C1s spectra, the SEI is predominantly made of EC and DMC decomposition products which leads to a less flexible SEI.[137] 2) SiO_xF_y is detected in presence of 20FEC:80DMC and 50FEC:50DMC, while not being observed at any time with 2FEC:98LP30. Interestingly, no correlation is seen between the FEC amount in the electrolyte and the amount of SiO_xF_y detected. Also, depth profiles done by sputtering the electrode with low-energetic monoatomic argon-ions show this species to behave like an SEI species, as it disappears with etching time, while all bulk silicon species increase in intensity, see **Figure 29(a)**. However, it cannot be excluded that SiO_xF_y might be more sensitive to the sputtering and thus might be removed in the process.

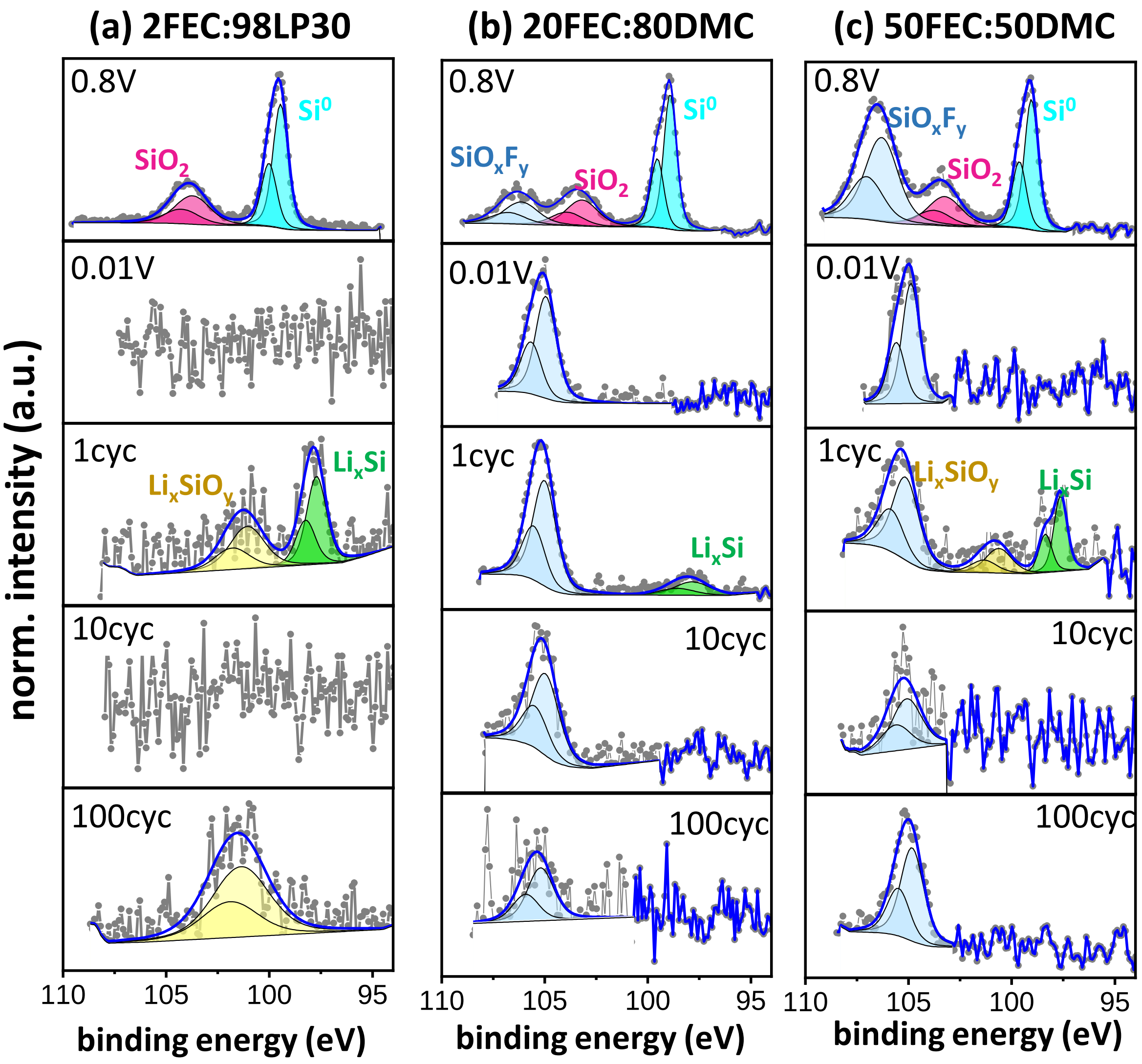

Figure 28: Si2p photoelectron spectra of 10%-Si/Gr half-cells cycled in (a) 2FEC:98LP30, (b) 20FEC:80DMC, and (c) 50FEC:50DMC.

The most extensive reporting of SiO_xF_y has been done by Philippe *et. al.* who observed this species when cycling electrodes containing 80 % silicon in pure LP40 electrolyte (i.e., 1 M $LiPF_6$ in 1:1 EC:DEC), with $LiPF_6$ as the sole fluorine source.[179] The authors could demonstrate this species to form during cycling as well as when storing the electrode in the electrolyte over a long period. HAXPES experiments showed SiO_xF_y to be more present in upper layers and diminishing when deeper layers were probed. These results agree with the sputtering depth profiling experiment conducted in the present work. Furthermore, the authors analyzed electrodes cycled in 1 M of LiFSI in 1:1 EC:DEC mixtures and could not detect any SiO_xF_y species.[180] They concluded $LiPF_6$ to play a major role in SiO_xF_y formation. To verify this hypothesis, $LiPF_6$ was replaced with LiTFSI for the 20FEC:80DMC electrolyte, and indeed, no SiO_xF_y is detected, see **Figure 29(b)**. As a remainder, the SEI formed by the $LiPF_6$

20FEC:80DMC formulation displays SiO_xF_y species. This emphasized that $LiPF_6$ is crucial for the SiO_xF_y formation. To verify whether EC influences the formation of this species, electrodes were cycled in a 1 M $LiPF_6$ 20FEC:40EC:40DMC electrolyte. Despite the presence of $LiPF_6$ and FEC, no SiO_xF_y species is detected, see **Figure 29(b)**. Based on these observations, the formation of SiO_xF_y is correlated with the amount of silicon in the electrode and with the presence or absence of $LiPF_6$, FEC, and EC in the electrolyte. With high silicon loadings, SiO_xF_y can still form even in presence of EC and absence of FEC – however, $LiPF_6$ should be the electrolyte salt. With lower silicon loadings (i.e., 9 wt%), SiO_xF_y is not detected if EC is present in the electrolyte – even if $LiPF_6$ and FEC are being used. However, in absence of EC, but the presence of FEC and $LiPF_6$, SiO_xF_y forms also at lower silicon contents.

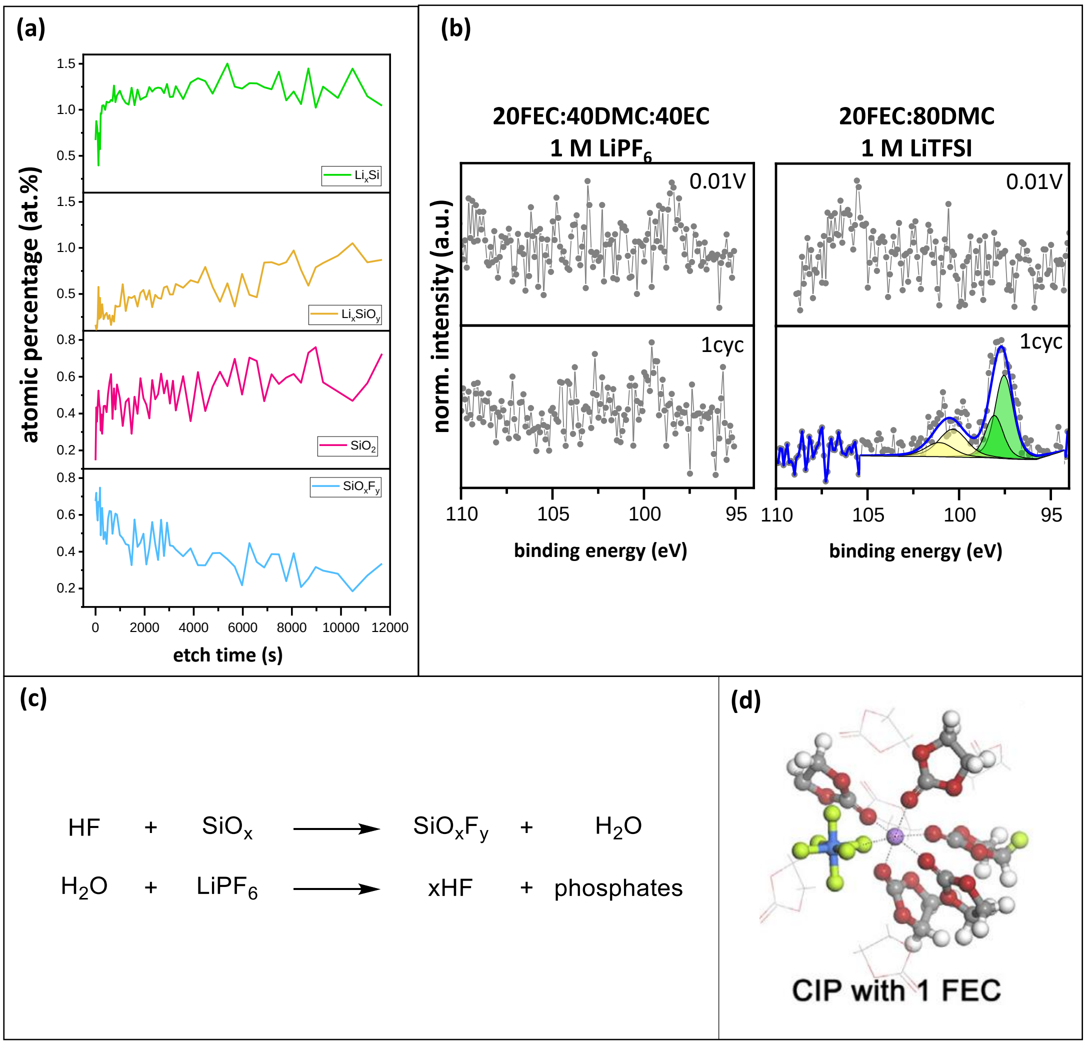

Figure 29: (a) Si2p spectra of Si/Gr electrodes cycled in 20FEC:40DMC:40EC-1 M $LiPF_6$ and 20FEC:40DMC-1 M LiTFSI, respectively, and (b) SEI depth profile of different silicon species of electrodes cycled in 20FEC:80DMC-$LiPF_6$, (c) Formation reaction of SiO_xF_y, (d) Contact ion pair (CIP) of Li^+, PF^-_6, EC, and FEC (lithium in purple, phosphor in blue, fluorine in yellow, oxygen in red, carbon in grey, and hydrocarbon in white).[220]

In literature, the formation of SiO_xF_y was hypothesized to be a result of the dissolution of silica by HF, see **Figure 29**. HF is known to form through the reaction of $LiPF_6$ with trace amounts of water.[221] The water content in all electrolytes was determined by Karl-Fischer titration to be below 10 ppm. Therefore, the amount of hydrolyzed $LiPF_6$, i.e. amount of HF formed, should be similar for 2FEC:98LP30, 20FEC:80DMC, and 50FEC:50DMC. However, FEC can act as a source of F^- anions, which form during FEC decomposition by cleavage of the C-F bond. These F^- anions can now either react with Li^+ ions to form LiF or with silicon-oxide to form SiO_xF_y compounds. However, in this case, SiO_xF_y could also be formed when cycling in 20FEC:80DMC with LiTFSI salt. This suggests that the interaction of FEC and $LiPF_6$ may play an important role in the formation of SiO_xF_y. While no experimental results can be found in literature, molecular dynamic calculations of FEC and $LiPF_6$ do exists.[220] They have shown that the presence of FEC leads to an increase in contact Li^+ - PF_6^- ion pairs. Contact ion pairs (CIP) are ions that are not separated by solvent molecules, see **Figure 29(d)**. This can increase the interaction between PF_6^- and Li^+ and promote the formation of PF_5, Li^+, and F^-, independent of the water content. In other words, the presence of FEC can increase the reactivity of the $LiPF_6$ salt. These CIPs may also affect the reactivity of FEC and $LiPF_6$ with respect to silicon. In presence of EC or EC decomposition products, this reactivity might be inhibited.

In summary, using FEC cosolvent seems to lead to a more stable SEI because no bulk Li_xSi or Li_xSiO_y species are re-emerging after cycling (which would indicate SEI dissolution or crack formation). Also, the presence of FEC and $LiPF_6$ and the absence of EC leads to the formation of SiO_xF_y at low silicon contents.

Electrode morphology

SEM micrographs of electrodes cycled in the respective electrolyte for 1 and 100 cycles are presented in **Figure 30**. After the first cycle, all three electrodes display graphite as large rectangular-shaped particles. Silicon can be seen in agglomerations of bright, small, and round particles, while carbon nanofibers emerge as long wires. Also, small bright dots are seen on the graphite and nanofibers. Whether they are also present on silicon particles is difficult to assess, because both emerge as bright white dots in the SEM images. After 100 cycles, substantial changes in morphology can be observed for all three cases. The surface of the electrode cycled in 2FEC:98LP30 exhibits large areas with charging effects as can be seen from the extremely bright borders of graphite particles and silicon agglomerations. It can be assumed that the SEI is thick and highly insulating. This observation agrees with the SEI thickness analysis. When cycled in the FEC cosolvent electrolytes the electrodes show less charging, and the overall morphology is much better resolved. This could indicate a thinner SEI as seen in the XPS measurements. The small dots observed on the graphite particles already observe after 1 cycle have grown to larger roundly shaped particles. This is especially the case with 50FEC:50DMC. With the help of EDS, these areas can be assigned to fluorine-containing species, see the elemental distribution maps **Figure 30**. Elemental distribution in **Figure 31** further shows that these particles emerge especially in the fluorine map and much less in the maps of the other elements. Similar shapes have been observed in literature and were suggested to be LiF.[222] Assignment to LiF might also apply here because other fluorine-containing compounds such as P-F and Si-F are not seen as clearly in the respective phosphorus and silicon map, see **Figure 31**. Furthermore, the elemental distribution of the electrode cycled in 20FEC:80DMC suggest, for the fluffy parts to belong to primarily oxygen species, with a small proportion of silicon and even less fluorine. As these fluffy parts are also present in the SEM micrographs of the electrodes cycled in 2FEC:98DMC and 50FEC:50DMC, it can be assumed that those areas contain similar elemental distribution, i.e., O > Si > F > C.

In spite of the difficulty of assigning specific compounds to the elements, the elemental distribution can be related to the atomic percentages measured by XPS. In the case of 2FEC:98LP30, high oxygen contents result mostly from inorganic oxygen species containing Li_2CO_3 as well as inorganic -C-O species. Silicon emerges due to Li_xSiO_y groups, while fluorine is mainly due to LiF and Li_xPF_y. For the two FEC cosolvent electrolytes, the high oxygen content could be related to -C-O and DO groups. Silicon is present as SiO_xF_y while fluorine species include LiF, SiO_xF_y, and Li_xPF_y.

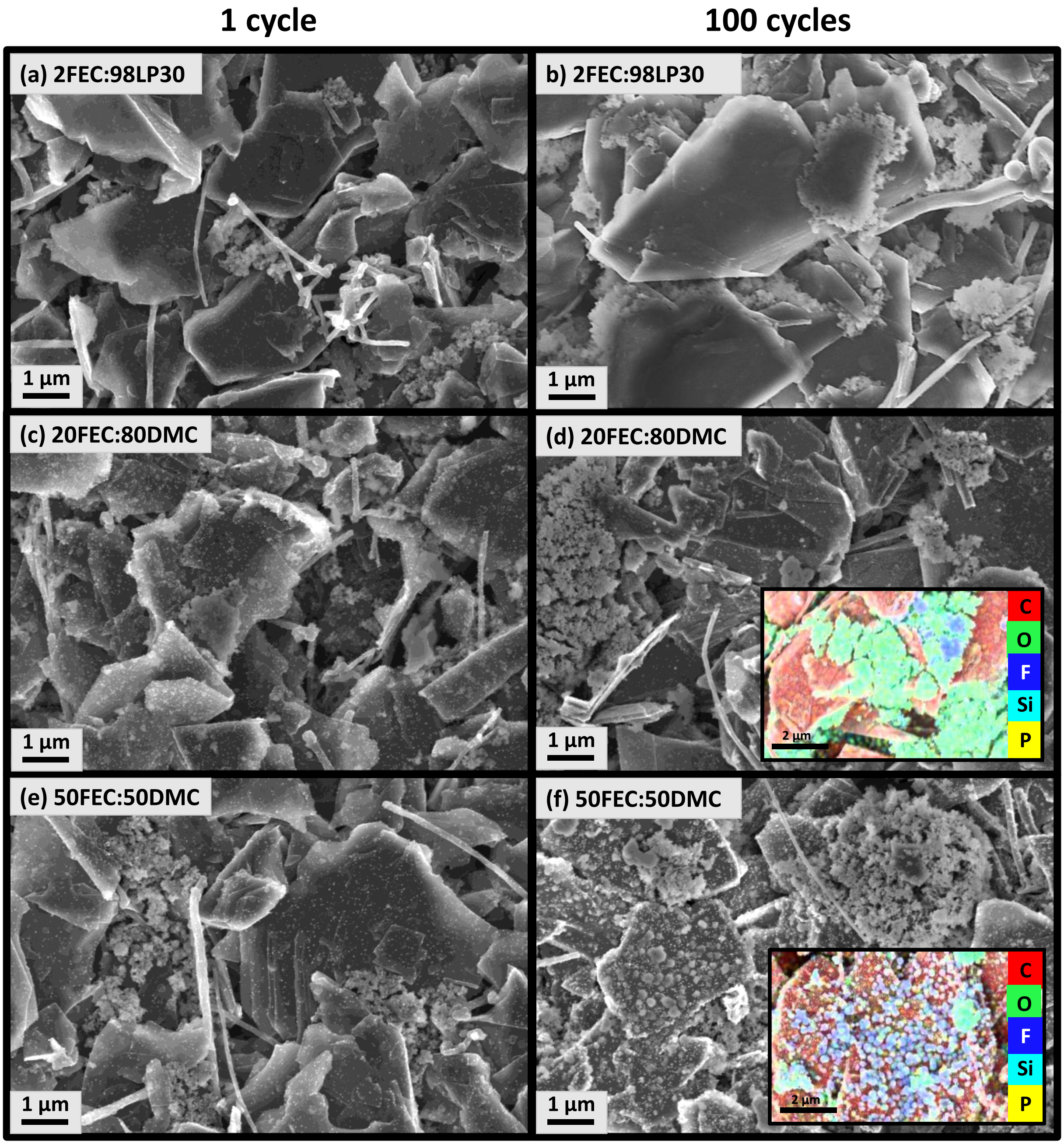

Figure 30: SEM micrographs of Si/Gr electrodes cycled in 2FEC:98LP30, 20FEC:80DMC, and 50FEC:50DMC after 1 and 100 cycles in the delithiated state at 1.5 V. Inset of elemental distribution for 20FEC:80DMC, and 50FEC:50DMC after 100 cycles.

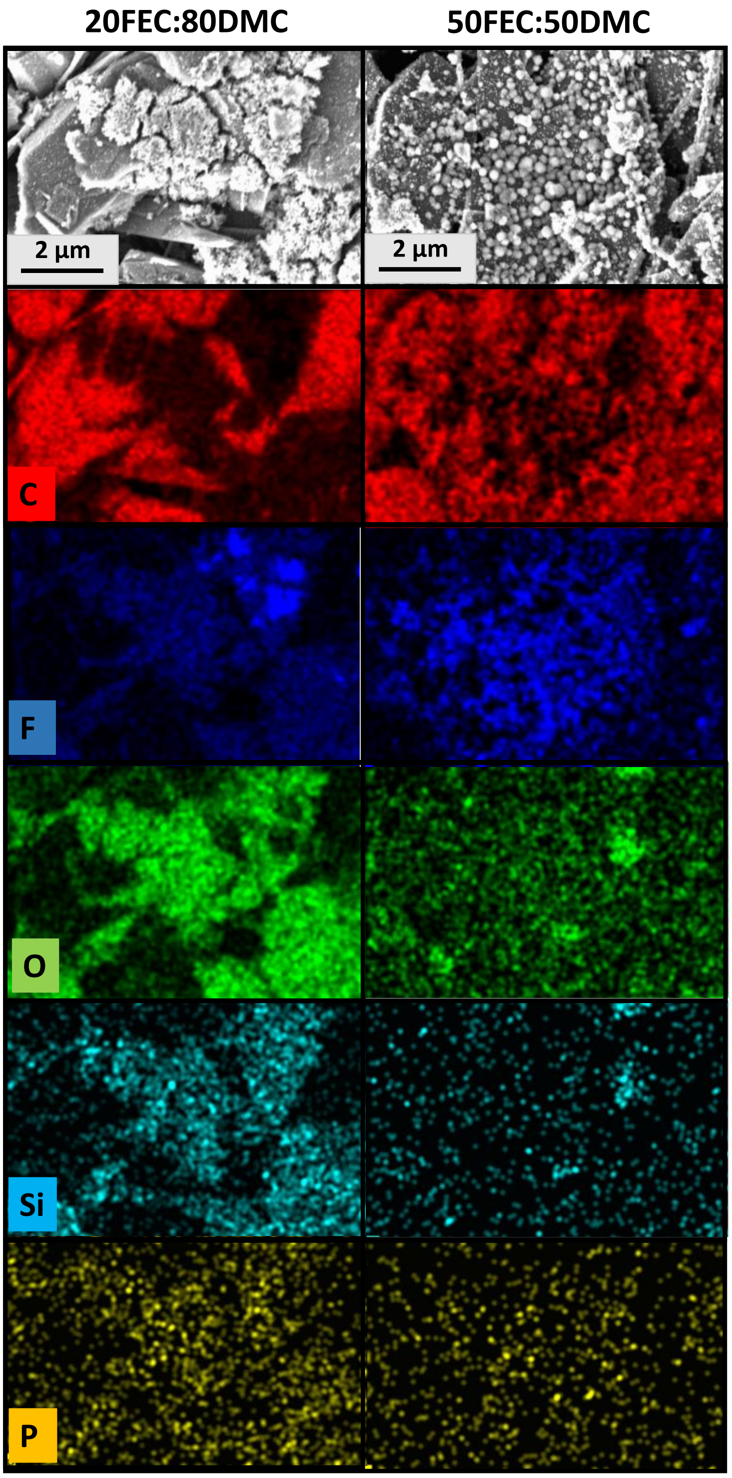

Figure 31: EDS elemental distribution maps of Si/Gr electrodes cycled for 100 times in 20FEC:80DMC and 50FEC:50DMC, respectively.

Correlating FEC concentrations to SEI properties and electrochemical performances

Previous parts of this chapter investigated the electrochemical performance, SEI properties, and electrode morphologies of three FEC-containing electrolytes with 10%-Si/Gr anodes. In this section, the different observations and findings are correlated. Similar electrochemical performances are seen for earlier cycles between 2FEC:98LP30, 20FEC:80DMC, and 50FEC:50DMC formulations. Significant differences emerge at later stages. After 100 cycles, Si/Gr anodes cycled in the 2FEC:98LP30 formulation display poor capacity retentions and a decrease in silicon and graphite activity. In contrast, the two FEC cosolvent formulations show much higher capacity retentions with higher silicon and graphite activities. SEI properties also display a dependence on the amount of FEC in the electrolyte. Compared to the FEC additive formulation, both FEC cosolvent electrolytes show a thinner SEI as determined by the XPS signal attenuation. While similar SEI compositions are observed in earlier cycling stages, differences emerge at later cycling numbers. SEM micrographs display a less charged electrode surface and the presence of large fluorine-containing particles when Si/Gr anodes are cycled in both FEC cosolvent formulations.

Based on the XPS analysis, the variance in electrochemical performance can be attributed to differences in the SEI composition. The developed XPS fitting model shows FEC to decompose to -C-O, DO, and $-CO_2Li$ containing products. Most likely, these species are incorporated in a cross-linked polymeric network. The formation of a cross-linked polymeric network has been suggested in literature many times.[23],[134],[137],[214],[215] The peaks corresponding to DO species (C_a and C_b) are an unambiguous indicator for the presence of FEC decomposition products in the SEI, as this species does not form with any other electrolyte component. DO environments are detected in the SEI when cycling in 20FEC:80DMC and 50FEC:50DMC electrolytes even after 100 cycles. However, while being present in earlier cycling stages, the amount of detected DO drastically decreases after longer cycling with 2FEC:98LP30. Instead, most of the observed peaks are related to -C-O and $-CO_3Li$ environments, which correspond to EC decomposition products (i.e, Li_2CO_3, LEDC, and PEO). Therefore, the good *initial* electrochemical performance of the electrode cycled in 2FEC:98LP30 is explained by the presence FEC decomposition products in the SEI. The formed polymeric network increases the ability of the SEI to better accommodate the silicon volume changes. However, this network might not form a perfectly elastic SEI as it still cracks and leads to recurrent FEC reduction. In the case of 2FEC:98LP30, the continuous consumption of FEC eventually depletes the electrolyte of the additive. Simultaneously, an increase in EC reduction occurs which ultimately leads to an SEI that is composed of short-chain LEDC and PEO components. These components are less fit to accommodate the silicon volume changes.[214] Hence, the SEI fractures and electrode material is re-exposed (see Li_xSiO_y peak for 2FEC:98LP30 case). Consequently, new SEI is formed on the re-exposed surfaces. This excessive SEI formation can ultimately lead to the isolation of silicon particles and reduced electrode integrity. The loss in graphite and silicon activity observed for the 2FEC:98LP30 electrolyte formulation could be explained by this phenomenon. In contrast, when cycling in 20FEC:80DMC and 50FEC:50DMC, FEC decomposition products (indicated by DO environments) are present in the SEI for a longer period, because the FEC reservoir in the electrolyte is larger. Also, since EC is not present in the electrolyte, its decomposition products are absent in the SEI. Consequently, the SEI is more stable, and less electrolyte is decomposed. The extended presence of the polymeric network buffers the silicon volume changes, reduces the amount of SEI formed, and helps to maintain the electrode integrity for a longer time. This would explain the smaller decrease in silicon and graphite activity when cycling in the FEC cosolvent electrolytes. Presence of this polymer in the SEI seems therefore crucial for a good electrochemical performance.

Another interesting observation is the emergence of SiO_xF_y species, which are detected when using the FEC cosolvent formulations but not the FEC additive electrolyte. Translating the findings from Philippe *et.al.* with pure silicon to Si/Gr anodes, SiO_xF_y may decrease the affinity between the binder and the surface of the active material.[180] This would result in poor electrochemical performance. However, the proposed negative impact of SiO_xF_y does not seem to be that detrimental to the performance, because cells cycled in 20FEC:80DMC and 50FEC:50DMC electrolytes show superior capacity retention. Therefore, the suggested negative effect of SiO_xF_y most probably has an inferior impact on the SEI stability. Instead, the volume accommodating effect of the polymeric network seems to have a much higher influence on the electrochemical performance of Si/Gr electrodes.

In conclusion, FEC cosolvent electrolytes offer two advantages: (1) the positive effect of a polymeric network containing -C-O, DO, and $-CO_2$ species is preserved for much longer, and (2) no EC decomposition products are present in the SEI, which leads to a more stable surface layer and lower overall electrolyte consumption.

5.3 Summary

This chapter examined how the use of FEC cosolvent influenced the electrochemical performance, SEI thickness, and composition, as well as electrode morphology Two electrolyte formulations (20FEC:80DMC and 50FEC:50DMC) were compared to a reference electrolyte with FEC as electrolyte additive (2FEC:98LP30). The developed XPS fitting model showed FEC to decompose to -C-O, DO, and -CO_2Li containing products. Most likely, these species were incorporated in a cross-linked polymeric network. The two chemical environments in DO (C_a and C_b) enabled unambiguously tracing the presence of FEC decomposition products in the SEI. Compared to the additive concentration, both FEC cosolvent mixtures showed:

1) thinner SEI as determined from XPS signal attenuation

2) high amount of FEC decomposition products (as indicated by C_a and C_b) are present in the SEI even after longer cycling, while these species strongly decreased for the FEC additive electrolyte

3) reduced decomposition of DMC cosolvents (and absence of EC decomposition products)

4) lower amount of carbonate species

5) formation of SiO_xF_y species, suggesting the presence of FEC and absence of EC to promote the formation of this species

The improved electrochemical performance of the FEC cosolvents formulations originates from the presence of FEC decomposition products in the SEI even after 100 cycles as shown with XPS. The presence of this polymeric network species is crucial in stabilizing the SEI upon the silicon volume changes. Most probably, it increases the flexibility of the surface layer which reduces the amount of new SEI formed and thereby enables a longer cell lifetime. The prolonged presence of this polymeric species is especially essential when moving toward applications with higher silicon content. The main drawback of FEC-containing electrolyte formulations is that FEC is consumed upon cycling and its positive effect is diminishing over time. Therefore, alternative electrolyte solvents can be of interest which might not be consumed to such a high extent. The next chapter of this thesis focuses on glyoxal-based electrolyte solvents.

6 Glyoxylic Acetals as Electrolyte Solvents

In this chapter, glyoxylic acetals are investigated with Si/Gr anodes. They previously showed promising results with graphite electrodes but have so far not been tested with silicon-containing anodes. Two glyoxylic acetals (TMG and TEG)[1] are analyzed in terms of their cycling stability and SEI formation. The choice of these two electrolyte formulations was motivated by their positive impact on the thermal stability of LIBs. For comparison, two reference electrolytes (LP30 and L-E/D)[2] are also investigated. The electrochemical behavior of these electrolytes is analyzed in a half-cell setup containing Si/Gr working electrodes and lithium metal counter electrodes. X-ray photoelectron spectroscopy (XPS) is used to evaluate changes in SEI thickness and composition upon formation and aging. In addition, the electrode morphology is analyzed via scanning electron microscopy (SEM). In a second part, an electrolyte formulation with PC as cosolvent is examined to increase ionic conductivity.

6.1 Pure TEG and TMG Solvents

6.1.1 Electrochemical Performance

Galvanostatic cycling of Si/Gr half-cells cycled in the respective electrolytes TMG (blue), TEG (black), L-E/D (green), and LP30 (pink) are shown in **Figure 32(a)**. Corresponding columbic efficiencies are displayed in **Figure 32(b)**. During the first cycle, the electrodes exhibit higher specific lithiation capacities than the theoretical values in all 4 investigated electrolytes. This is due to extensive SEI formation during this first cycle. The cell cycled in the L-E/D electrolyte displays the highest lithiation capacity with 964 mAh^{-1}. Also, the largest irreversibility appears for L-E/D as can be seen in the coulombic efficiency of only 71 %. Cells cycled in TMG, TEG, and LP30 display lower initial lithiation capacities of around 780 mAh g^{-1} and higher columbic efficiencies of around 80 %. Upon cycling, the cell with the TMG electrolyte displays the fastest capacity drop out of all electrolytes. Already after 10 cycles, a decline of around 100 mAh g^{-1} can be observed. This decrease is reflected by a decrease in coulombic efficiencies of 1.5 %, indicating a possible loss of active material and solid electrolyte interphase evolution. After 100 cycles, only 38 % of capacity can be retained from the 647 mAh g^{-1} observed in the 2nd cycle. In comparison, cells cycled in TEG show the smallest capacity decrease out of all electrolytes. After 100 cycles, 488 mAh g^{-1} are retained (i.e., 72 %).

---

[1] TMG: 1 M LiTFSI in 1,1,2,2-tetramethoxyethane; TEG: 1 M LiTFSI in 1,1,2,2-tetraethoxyethane

[2] LP30: 1 M $LiPF_6$ in 1:1 EC: DMC; L-E/D: 1 M LiTFSI in 1:1 EC: DMC

Coulombic efficiencies remain at around 98.9 % throughout the cycling experiment. When using the two reference electrolytes LP30 and L-E/D, better performances are achieved compared to the TMG case. However, the capacity retention is worse than in presence of TEG. A significant capacity drop can be seen after 15 cycles for both carbonate-based electrolytes, leading to a retention of 53 % and 56 % after 100 cycles, respectively.

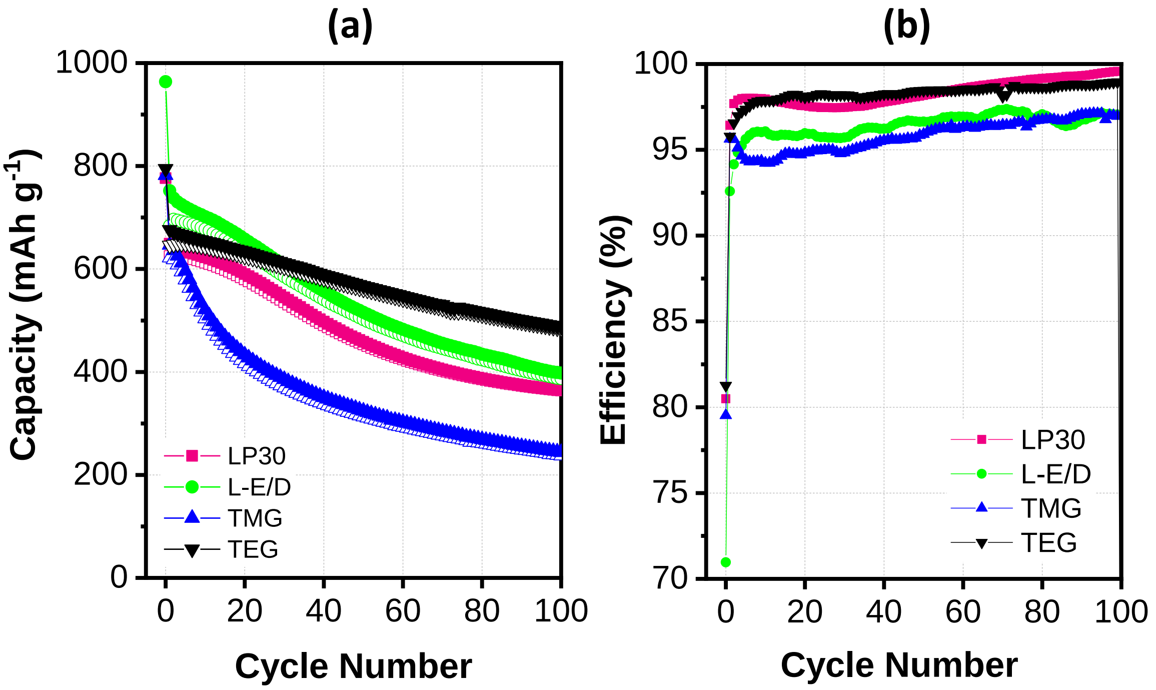

Figure 32: (a) Cycling stabilities and (b) coulombic efficiencies of Si/Gr electrodes cycled in TMG (blue), TEG (black), L-E/D (green), and LP30 (pink) electrolytes.

Figure 33(a) compares the evolution of the differential capacity (dQ/dE) of the Si/Gr electrodes for selected cycles over the first 100 cycles. Regardless of the used electrolyte, the Si/Gr electrodes generally display the same electrochemical processes, but with different rates of intensity decay for the characteristic intercalation/alloying peaks. Intercalation reactions of lithium-ions into graphite emerge at the following potentials: 0.2 V (stage IV), 0.13 V (stage III, LiC_{30}), 0.1 V (stage II, LiC_{12}), and 0.07 V (stage I, LiC_6).[201],[202] Lithiation of silicon extends over the whole lithiation profile. Crystalline silicon is lithiated via a two-phase mechanism resulting in amorphous silicon-lithium alloys (Li_xSi).[52]–[55] At the end of the first lithiation, this amorphous phase reacts to crystalline $Li_{15}Si_4$, corresponding to the minima at 0.04 V in the dQ/dE plot.[58]–[60] During delithiation, $Li_{15}Si_4$ transforms back to amorphous silicon in which state it remains during further cycling. In subsequent cycles, a new signal is observed at 0.3 V corresponding to the lithiation of this amorphous phase, see the 10th cycle (purple line).

In all systems, the first cycles display intense dQ/dE signals during both lithiation and delithiation. Cells cycled in the TMG electrolyte show the most pronounced intensity decrease upon cycling. Already after 10 cycles, a large amount of graphite and silicon activity is lost, reflecting the dramatic capacity drop observed in **Figure 32**. Both reference electrolytes L-E/D and LP30 show higher electrochemical activity than TMG, which results in the higher capacity retentions observed in **Figure 32**. Especially graphite intercalation reactions are better retained upon cycling. However, both silicon and graphite show losses in activity, mirroring the capacity drop in **Figure 32**. By contrast, when using TEG, only small losses in silicon activity are observed as can be seen in the signal at 0.3 V and 0.04 V from the 10th to the 100th cycle. Moreover, the electrochemical activity of graphite is completely retained throughout the GCPL experiment. This better retention in the activity of both silicon and graphite explains the improved electrochemical performance displayed in **Figure 32**.

At this stage, neither electrolyte viscosity nor ionic conductivity appears to play a role. For TMG and TEG, both parameters are very similar, however, their electrochemical performances are very different. Compared to L-E/D and LP30, TEG has much higher viscosities and lower ionic conductivities. However, much higher capacity retention is achieved during cycling with TEG. Different film-forming abilities might be one reason for the observed differences in electrochemical activity, as will be discussed in the following part of this thesis.

Figure 33(b) illustrates the differential capacities in the voltage range of initial SEI formation (between 2.5-0.4 V vs. Li/Li^+). Assignment of changes in the dQ/dE signal to specific electrochemical reactions has to be undertaken with caution because the signal also indirectly shows electrochemical reactions on the lithium counter electrode. Keeping this in mind, the electrode surface was analyzed with XPS at the indicated potentials (i.e., 2.5 V, 1.3 V, 0.9 V, and 0.5 V) to elucidate whether SEI formation is taking place.

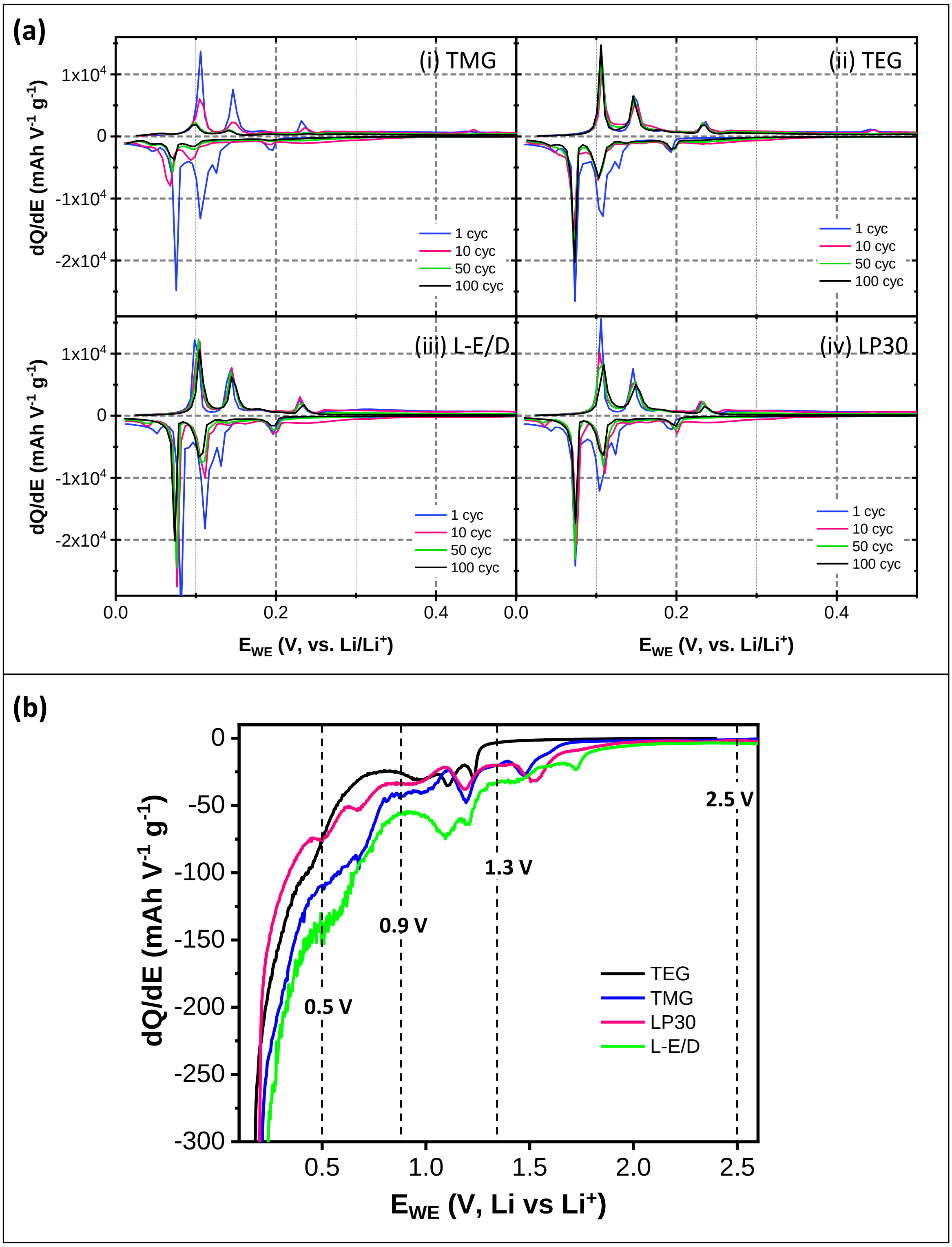

Figure 33: (a) Differential capacities of dQ/dE plot of Si/Gr electrodes cycled in TMG (i), TEG (ii), L-E/D (iii), and LP30 (iv) electrolytes and (b) dQ/dE in the voltage range of initial SEI formation.

6.1.2 SEI Analysis

SEI thickness approximation

Similar to **Chapter 5**, the SEI thickness is approximated by calculating an intensity attenuation, see Eq.(25). The obtained attenuation values at different potentials during the first lithiation (i.e., at 2.5 V, 1.3 V, 0.9 V, 0.5 V, and 0.01 V) as well as after the 1st, the 10th, and 100th cycle (all in the delithiated state at 1.5 V) are displayed in **Figure 35**. The formation potentials are motivated by specific minima in the differential capacity plots of **Figure 33(b)**.

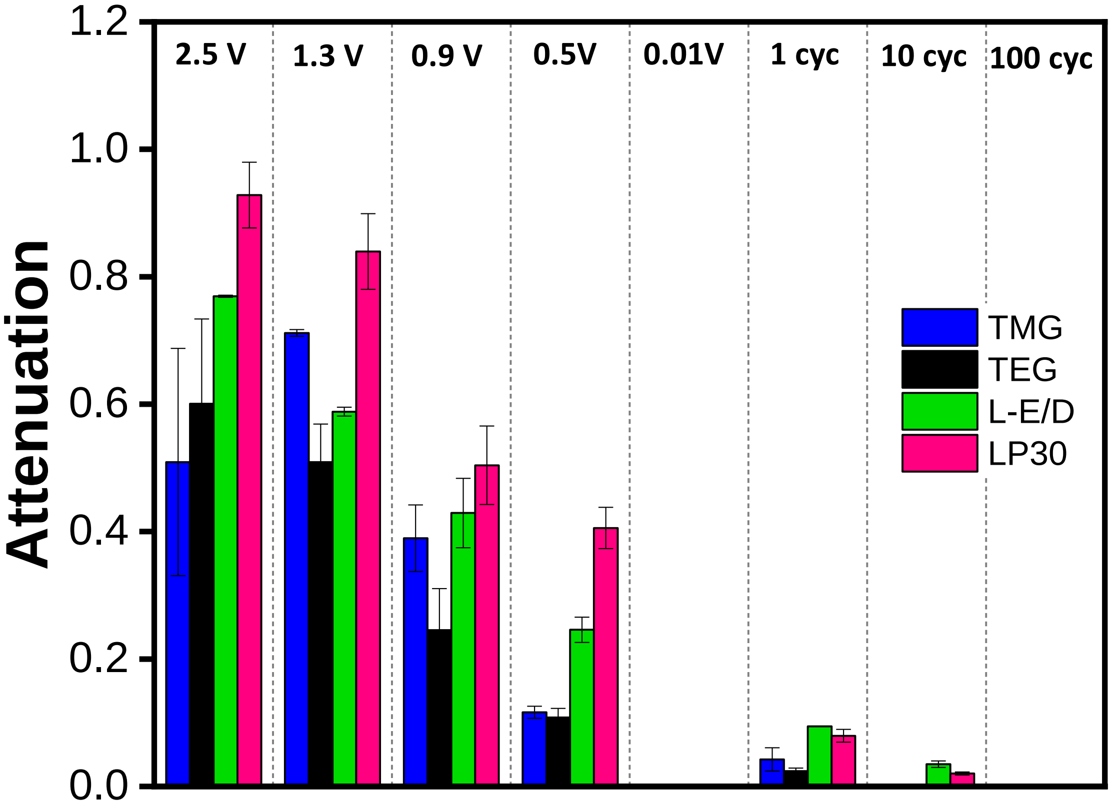

Figure 34: Thickness approximation of the SEI formed by TMG, TEG, L-E/D, and LP30 electrolyte decomposition. The error bars indicate the standard deviation between two measurements on one electrode.

During the first lithiation at 2.5 V and 1.3 V, less graphite is detected for cells containing LiTFSI-salt i.e., TMG, TEG, and L-E/D. In presence of $LiPF_6$ (i.e., LP30 electrolyte) the detected graphite intensity is higher. Only small changes are observed in the attenuation between 2.5 V and 1.3 V, which indicates similar surface layer thicknesses. At 0.9 V, the observed attenuation values decrease in all four cases from around 0.9 - 0.6 to 0.5 - 0.3 indicating an increase in layer thickness. This increase coincides with the electrochemically observed onset of electrolyte decomposition (i.e., 1.5-1.0 V vs. Li/Li^+) seen in **Figure 33(b)**.

The attenuation values continue to drop from 0.5 V to below 0.2 for TMG and TEG. In comparison, both carbonate-containing electrolytes, L-E/D, and LP30 display higher attenuation values and therefore a thinner SEI layer. At 0.01 V, no graphite is observed for any electrolyte. Thus, the SEI is thicker than 3λ, i.e., thicker than 9.6-11.7 nm (see 3λ for LiF and PMMA, respectively). After the first delithiation, graphite reappears in the case of TMG, TEG, L-E/D, and LP30. The SEI layer thickness increase during lithiation and decrease during delithiation is already known in literature. Especially in presence of silicon, the SEI layer is known for such a "breathing behavior".[211],[212],[223] It can be explained by the mechanical instability of the SEI during the silicon volume decrease from the lithiated to the delithiated state. Thereby, graphite is re-exposed and can be detected via XPS due to emerging cracks in the SEI or parts of it detaching or dissolving into the electrolyte. After 10 cycles, no graphite is observed for TMG and TEG while it is still being detected for L-E/D and LP30. There can be two reasons for this observation: 1) glyoxal-based electrolytes decompose to a stronger degree, which would lead to a faster SEI coverage of the electrode, or 2) glyoxal-based electrolytes accommodate the electrode volume changes to a higher degree. After 100 cycles, graphite is not observed in all cases suggesting a considerable SEI layer is built-up during extended cycling.

Overall, the electrolyte solvent seems to play a more important role in SEI thickness than the electrolyte salt. Higher similarities were detected between the same group of electrolyte solvents than for the same electrolyte salt. The SEI thicknesses of electrolytes containing carbonate solvents (i.e., LP30 and L-E/D) are more comparable to each other, as are the thicknesses between electrolytes containing glyoxal solvents (i.e., TMG and TEG). In contrast, the thicknesses of LiTFSI-containing TMG, TEG, and L-E/D are much less comparable. Also, TMG and TEG show similar absolute values and trends in attenuation, which would suggest similar SEI thicknesses during the first ten cycles. Possible changes in SEI thickness upon longer cycling, especially when the achievable capacities and thus the amount of active material being (de)lithiated differ significantly from each other, cannot be observed because of the high surface sensitivity of XPS.

Fitting model for glyoxylic acetal decomposition products

XPS is used to analyze the film forming properties of TMG and TEG. The electrode preparation procedure prior to XPS measurements is detailed in **Chapter 4.5**. To determine which surface species belong to TMG and TEG decomposition products, the surface of a pristine Si/Gr electrode is compared to the surface of a fully lithiated electrode. The resulting C1s and O1s spectra are shown in **Figure 35(a)** and obtained binding energies and atomic percentages of detected species are summarized in **Table 7**. The C1s spectrum of the pristine electrode displays three peaks corresponding to graphite (284.6 eV), hydrocarbons associated with both adventitious carbon, and the LiPAA binder (285 eV), and $-CO_2Li$-groups of the LiPAA binder (C1s: 288.3 eV). Corresponding peaks of the LiPAA binder emerge in the O1s spectrum at 531.6 eV and 533.2 eV).

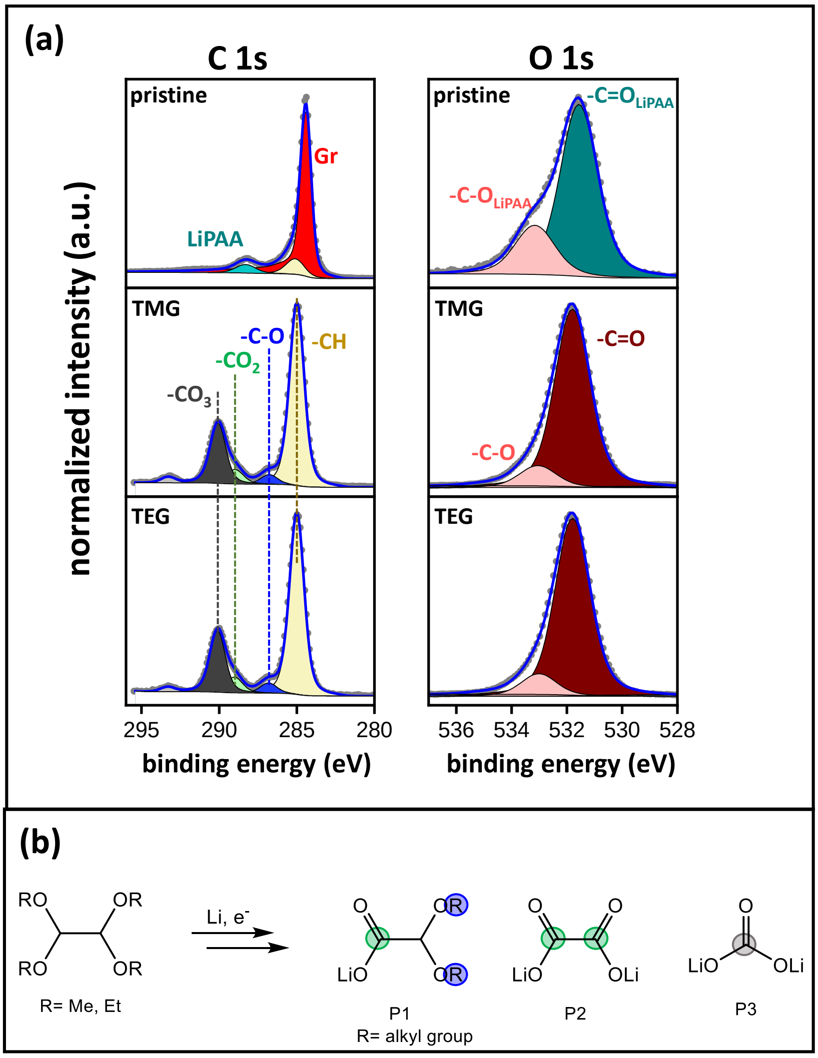

Figure 35: (a) C1s photoelectron spectra of pristine and cycled Si/Gr electrodes. The cycling was done in TMG and TEG electrolytes, respectively. (b) Hypothesized TMG and TEG decomposition products with highlighted functional groups were observed with XPS (-C-O (blue), $-CO_2Li$ (green), and $-CO_3$ (gray)).

After lithiation to 0.01 V in the respective glyoxal electrolytes, four peaks are observed in the C1s spectra: -CH (285 eV), -C-O (286.8 eV), -CO_2Li (i.e., carboxylic -C(=O)O environment at 289.0 eV), and -CO_3Li (i.e., carbonate -O(C=O)OLi environment at 290.1 eV). Respective peaks are detected in the O1s spectrum for -C=O species at 531.8 eV and -C-O at around 533.1 eV.

Table 7: Binding energies (BE) and atomic percentages (at.%) of carbon-oxygen species detected on Si/Gr electrodes before cycling (i.e., pristine) and after cycling in either TMG or TEG.

		Pristine		**TMG**		**TEG**	
		BE (eV)	At.%	BE (eV)	At.%	BE (eV)	At.%
C 1s	-C-O	-	-	286.8	1.4	286.8	1.4
	-CO_2Li	288.3	4.9	289.0	2.0	289.0	2.1
	-CO_3Li	-	-	290.1	7.7	290.1	7.8
O 1s	-C=O	531.6	12.7	531.8	29.0	531.8	29.6
	-C-O	533.2	3.9	533.1	3.8	533.0	3.8

XPS can give information about functional groups detected in the SEI. Due to the inhomogeneous nature of the surface layer, it is difficult to determine the actual molecular structure of TMG and TEG decomposition products. -C-O groups most probably result from the carbon atoms in ether position, see highlighted group in P1 of **Figure 35(b)**. Carboxylic -CO_2Li environments probably emerge in structures such as P1 and P2. Carbonates could emerge in form of Li_2CO_3, see P3. The formation of carbonates could result via the decomposition of TMG and TEG to CO_2, which can subsequently react with lithium to form lithium carbonate.[99] Another indicator that the peak at 290.1 eV can be assigned to carbonate species is a relation close to 1 between the atomic percentages of -C=O species detected in the C1s (as part of C(=O)O and -O(C=O)O environments) and the O1s spectrum, see **Table A5** for more information. Interestingly, the acetal environment (i.e., O-C-O) which should emerge at around 288 eV is not detected with XPS. Also, no ROLi compounds are detected at around 531 eV in the O1s spectra of TEG and TMG which would indicate the formation of lithium alkoxide species.

Evolution of the SEI composition during formation and aging

To understand the SEI formation in the investigated electrolytes, electrodes were cycled up to 2.5 V, 1.3 V, 0.9 V, 0.5 V, and 0.01 V in the first cycle, and subsequently analyzed via XPS. C 1s spectra are displayed in **Figure 36** and the atomic percentages derived from this data are summarized in **Figure 37**. The corresponding F1s spectra and the atomic percentage evaluation are presented in **Figure 38** and **Figure 39**, respectively. N1s, O1s, P2p, and S2p spectra can be found in **Figure A12-Figure A14**. An overview of all detected species can be found in **Table A6-Table A9**. Assignment of different surface species follows previous reports in the literature, see **Table 4**. Survey spectra are displayed in **Figure A22-Figure A25**.

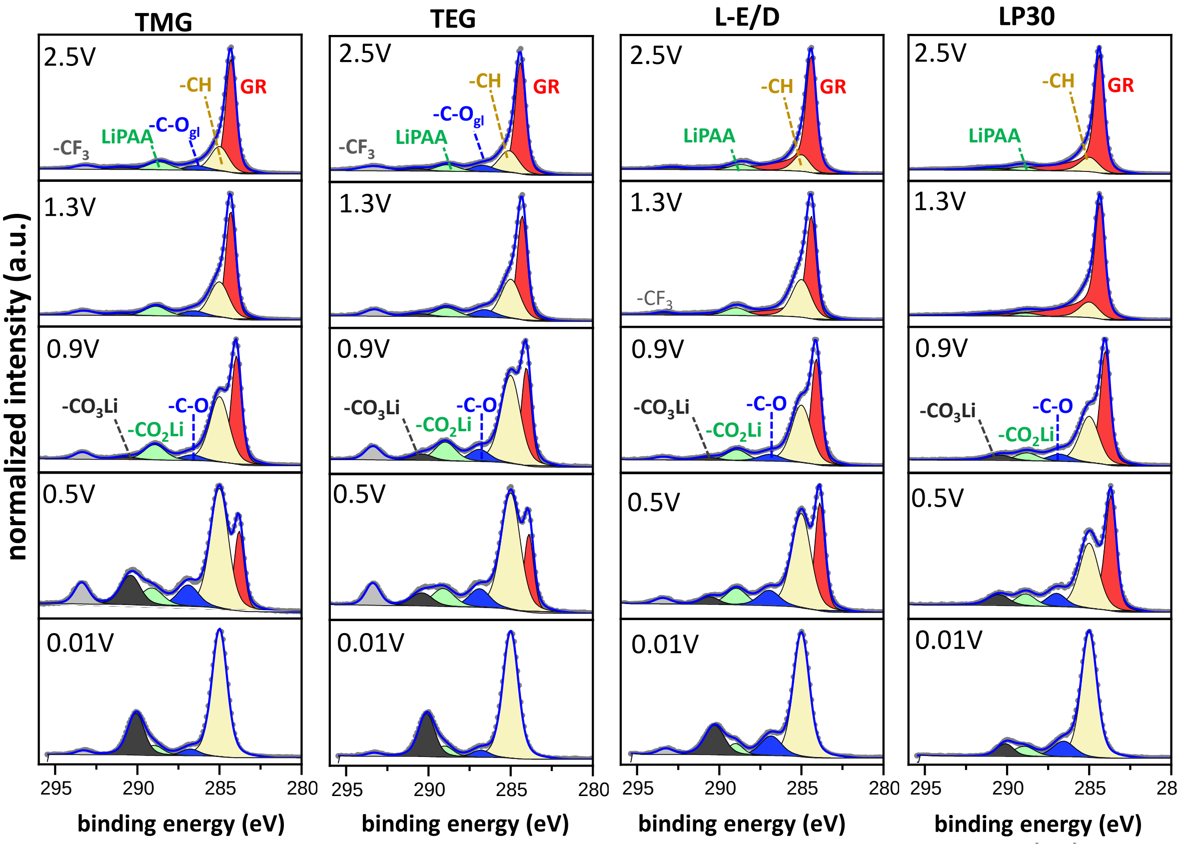

Figure 36: C 1s photoelectron spectra of electrodes cycled in TMG, TEG, L-E/D, and LP30 electrolyte respectively at 2.5 V, 1.3 V, 0. 9 V, 0.5 V, and 0.01 V during the first lithiation.

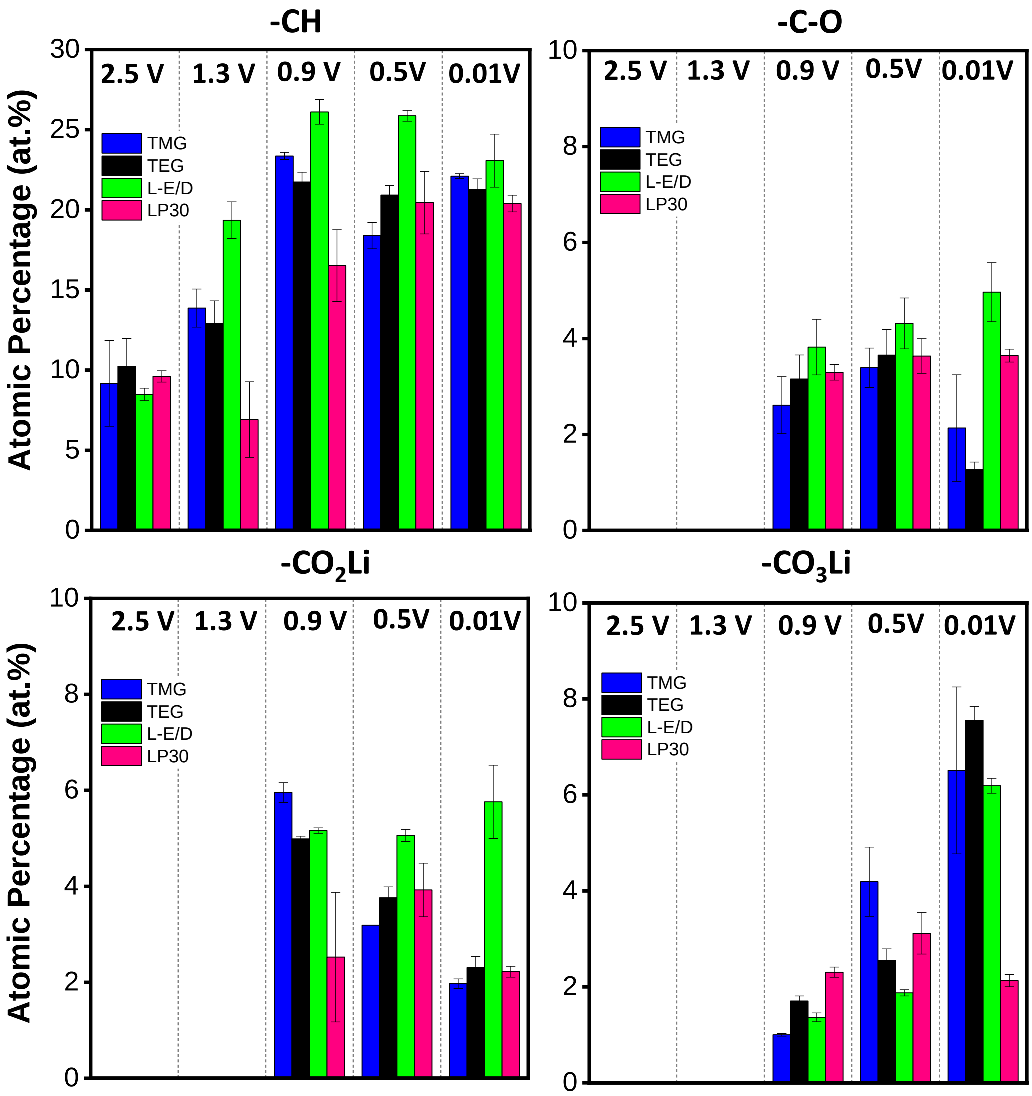

Figure 37: Atomic percentages of detected SEI species -CH, -C-O, $-CO_2$, and $-CO_3$ of electrodes cycled in TMG, TEG, L-E/D, and LP30 electrolyte at 2.5 V, 1.3 V, 0. 9 V, 0.5 V, and 0.01 V. The error bars indicate the standard deviation between two measurements on one electrode.

Solvent decomposition. Electrodes cycled in TMG and TEG electrolytes display very similar C 1s spectra at 2.5 V and 1.3 V, see **Figure 36**. Six peaks are observed in each spectrum: graphite (284.8 eV) with its corresponding $\pi \rightarrow \pi^*$ shake-up (290.8 eV), hydrocarbons (285 eV), -C-O groups (286.5 eV), $-CO_2Li$ groups (carboxylic environment at 289 eV), and $-CF_3$ groups of the LiTFSI salt (293.4 eV). At these voltages, it is reasonable to assume that the decomposition of TMG and TEG is not yet prominent. Differences in atomic percentages between both potentials are very low, see **Table A2** and **Table A3**. Also, no $-CO_3Li$ compounds are yet observed. Therefore, the -C-O peak could belong to TMG and TEG solvent residues and not to electrolyte decomposition products. Electrolyte solvent residues might derive from the electrode washing process in which TEG and TMG are used as washing solvents. As they have high vapor pressures, the respective solvent might not completely evaporate, and a small residue remains on the surface. Following this hypothesis, hydrocarbons can be assigned to adventitious carbon, LiPAA, and in the case of TEG also by -CH groups. -CO_2Li groups emerge due to the LiPAA binder. The -O-C-O-groups of TEG and TMG cannot be seen in the C1s spectra, which could be due to the low amount of TEG and TMG present on the surface. At 0.9 V, a distinct difference in surface composition is observed. A new peak emerges corresponding to -CO_3Li (290.4 eV), similar to the spectra in **Figure 22**. Hydrocarbons, -C-O, and -CO_2Li-containing compounds are increasing in intensity, while the graphite intensity is decreasing. These observations indicate the decomposition of the glyoxal solvents. When lowering the potential further down to 0.5 V and 0.01 V, the SEI components continue to increase, while graphite decreases in intensity. In the fully lithiated state, the SEI is so thick that no more graphite is detected. Here, the C1s spectra are dominated by hydrocarbons (~22 at.%) and -CO_3Li containing compounds (~7 at.%), see **Figure 37**. Overall, TMG and TEG display very similar C1s spectra as well as atomic percentages of the different carbon surface species.

C1s spectra of electrodes cycled in the two reference electrolytes LP30 and L-E/D show four peaks at 2.5 V, corresponding to graphite (284.4 eV) with the corresponding $\pi \rightarrow \pi^*$ shake-up (290.8 eV), adventitious carbon and -CC/CH groups at 285 eV, and -CO_2Li-groups of the LiPAA binder (288 eV). L-E/D shows an additional peak corresponding to -CF_3 groups of the LiTFSI salt (293.3 eV). Substantial changes in the C1s spectra can be observed for both reference electrolytes when the cell potential is lowered to 0.9 V. At this stage, a decrease in graphite intensity is detected, while the intensities for hydrocarbons and -CO_2Li-groups are increasing. The -CO_2Li-groups now correspond to EC:DMC decomposition products, rather than to the LiPAA binder. Furthermore, two new peaks are observed corresponding to -C-O (286.5 eV) and -CO_3Li-groups (290.3 eV) of EC:DMC decomposition products such as PEO and Li_2CO_3. The -C-O-component at 286.5 eV could also be attributed to carbon neighboring a carbonate group (i.e. -**C**-CO_3Li), as is the case for alkyl-carbonates.[224] Alkyl-carbonates such as lithium ethylene decarbonate (LEDC) are typical degradation products of carbonate-containing electrolytes.[99],[210] At 0.5 V and 0.01 V, all SEI components continue to increase in intensity, indicating ongoing electrolyte solvent decomposition. The amount of detected graphite further decreases and disappears completely in the fully lithiated state. A previous XPS study on graphite electrodes showed comparable SEI evolution over cycling for both L-E/D and LP30 electrolytes, respectively.[115]

Both glyoxal- and carbonate-based solvents show initial SEI formation between 1.5 V and 0.9 V, which is also supported by the dQ/dE plots in **Figure 33(b)**. In the fully lithiated state, they display similar amounts of hydrocarbons, while -C-O compounds are more abundant for L-E/D and LP30. The amount of -CO_2Li species is similar for TMG, TEG, and LP30, but higher for L-E/D. Carbonate-containing compounds are more abundant for the LiTFSI-containing electrolytes, i.e., TMG, TEG, and L-E/D but less present for the $LiPF_6$ containing LP30.

Salt components and decomposition. LiTFSI is suggested to be reduced via the intermediate product $LiSO_2CF_3$ to a combination of LiF, Li_2S, $Li_2S_2O_4$, Li_2SO_3, Li_2SO, and Li_3N.[117],[162],[225] It was further proposed for LiTFSI to form $C_2F_xLi_y$-like compounds.[117] In **Figure 38**, F1s spectra of cells cycled in TMG and TEG display two peaks corresponding to -CF_3 (689.1 eV) and LiF (685.1 eV). At higher potentials such as 2.5 V and 1.3 V, the -CF_3 peaks most probably correspond to residual LiTFSI electrolyte salt. At lower voltages, the LiTFSI-CF_3 peak overlaps with possible -CF_3-containing decomposition products. However, it is not possible to differentiate between -CF_3 groups which correspond to salt or salt decomposition products. As can be seen in **Table A6-Table A9** the ratio of -C**F**$_3$, -**N**-SO_2, and -**S**O_2 matches the ratio observed in LiTFSI. This increases the probability for the -CF_3 peak to belong to the LiTFSI salt. Because the intensity is normalized to a scale of 0 to 1, changes in the detected -CF_3 species cannot be readily analyzed from the shown graphs. Therefore, the absolute atomic percentages displayed in **Figure 39** are examined. At higher potentials (i.e., from 2.5 V to 0.5 V), both LiTFSI-containing TMG and TEG electrolytes demonstrate only small changes in atomic percentages of the -CF_3 species. In the fully lithiated state at 0.01 V, both display a decline in the detected -CF_3 amount of 10 at.%. This suggests a stronger reduction of LiTFSI to LiF. Indeed, the intensity of the LiF peak relative to -CF_3 increases from 2.5 V to 0.01 V for both TMG and TEG electrolytes. Compared to TEG, TMG displays higher LiF amounts at each investigated potential, indicating higher LiTFSI-salt decomposition with this electrolyte. S2p spectra in **Figure A14** of electrodes cycled in TMG and TEG display an intensive doublet at 169.3 eV which corresponds to the -SO_2 group in the LiTFSI-salt. The second doublet at 167 eV is ascribed to oxidized sulfur species such as -SO_x. Some works also assigned this species to Li_2SO_3 components.[117] During formation, no other sulfur decomposition products emerging below 167 eV such as Li_2S, $Li_2S_2O_4$, or Li_2SO are detected. N1s spectra in **Figure A13** display a peak at 399.8 eV corresponding to N-SO_2 groups of LiTFSI. At 0.01 V, cells cycled TEG show an additional peak at 397.5 eV corresponding to Li_3N. With TMG, no such component is observed.

Cells cycled in the L-E/D reference electrolyte display two peaks corresponding to -CF_3 (689 eV) and LiF (685.1 eV) see **Figure 38**. At 0.01 V, an additional peak emerges, which can be ascribed to groups in $C_2F_xLi_y$-like compounds.[117] Compared to the -CF_3 peak at 689.1 eV, these -CF$_x$ components emerge at much lower binding energies of 687 eV. This could be explained by the absence of neighboring -NSO$_2$ groups. In the C1s spectra, -CF$_x$ species are difficult to assign as they are hidden by prominent carbon-oxygen peaks. Interestingly, both glyoxal-based electrolytes do not display this species. Similar to TMG and TEG, L-E/D shows an increase in the relative intensity of LiF from 2.5 V to 0.01 V. Also, S2p spectra exhibit two doublets at 169.5 eV and 166 eV, corresponding to -SO$_2$ groups and -SO$_x$ or Li_2SO_3, respectively, see **Figure A14**. Contrary to TMG and TEG, no increase is observed for the -SO$_x$ or Li_2SO_3 species. N1s spectra show a peak at 399.9 eV ascribed to N-SO$_2$ groups. Like TEG, Li_3N emerges in the fully lithiated state at 0.01 V (see **Figure A13**).

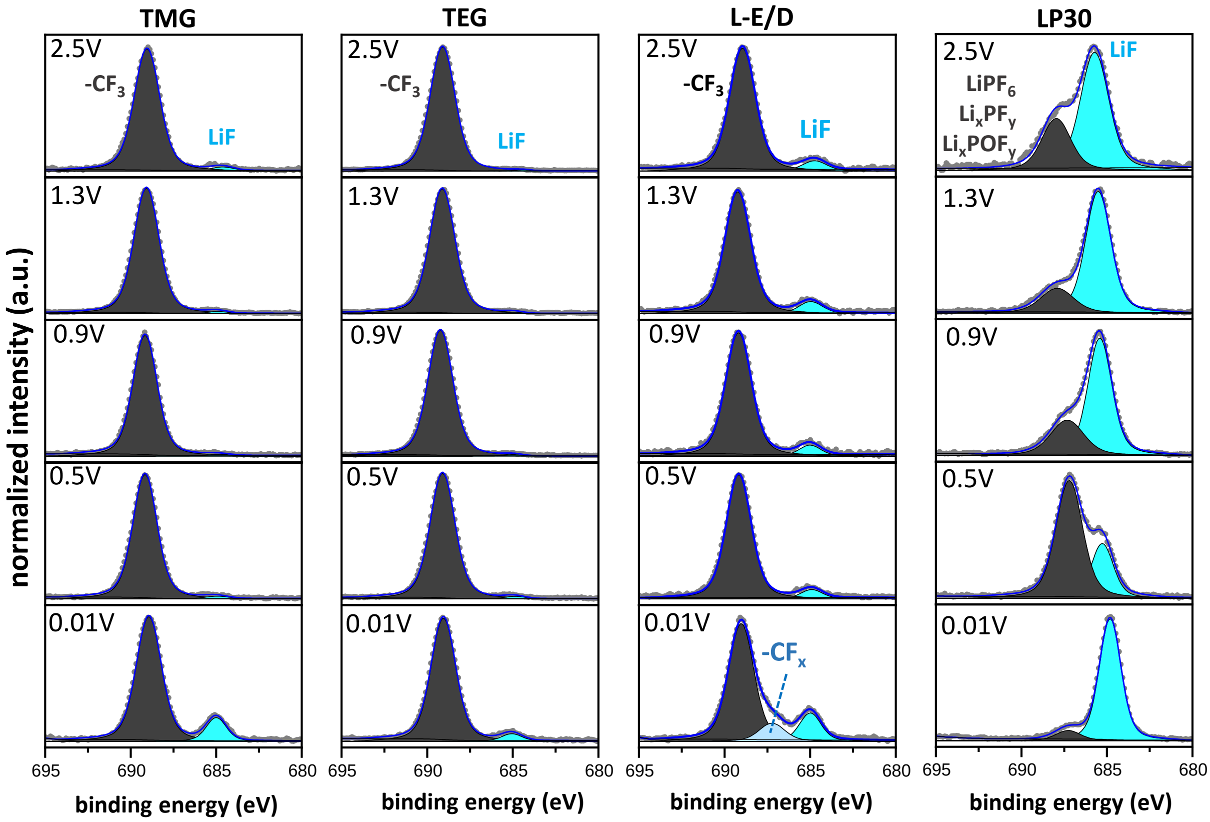

Figure 38: F 1s photoelectron spectra of electrodes cycled in TMG, TEG, L-E/D, and LP30 electrolyte at 2.5 V, 1.3 V, 0. 9 V, 0.5 V, and 0.01 V.

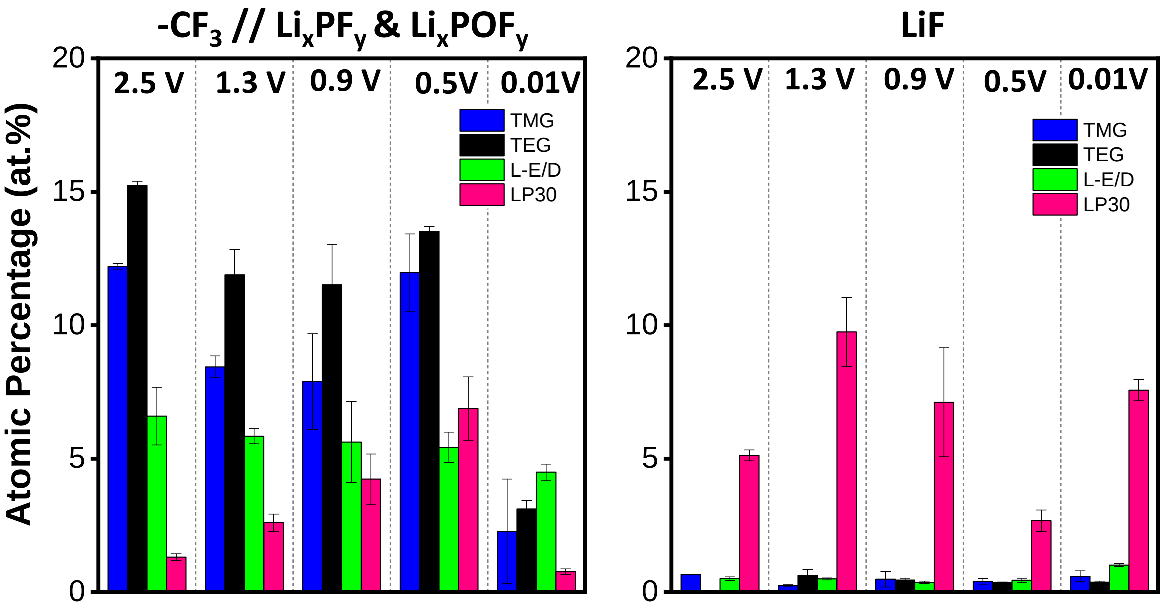

Figure 39: Atomic percentages of LiF and-CF$_3$/-CF$_x$ for electrodes cycled in TMG, TEG, and L-E/D at 2.5 V, 1.3 V, 0. 9 V, 0.5 V, and 0.01 V. For cells cycled in LP30, LiF and Li$_x$PF$_y$ are displayed, also at 2.5 V, 1.3 V, 0. 9 V, 0.5 V, and 0.01 V. The error bars indicate the standard deviation between two measurements on one electrode.

Cells cycled in the LP30 reference electrolyte show two peaks in **Figure 38** corresponding to LiF (685.1 eV) and a mixture of Li$_x$PF$_y$/Li$_x$POF$_y$ (687.2 eV). Both result from the decomposition of the electrolyte salt LiPF$_6$.[130],[226],[227] Interestingly, LiF is already detected at 2.5 V, indicating LiPF$_6$ to be decomposing at higher potentials, most probable via hydrolysis.[105],[130] An increase in LiF abundance can be observed from 2.5 V to 1.3 V, see **Figure 39**. From 1.3 V to 0.5 V the detected amount of LiF decreases, while more Li$_x$PF$_y$/Li$_x$POF$_y$ is observed. Such a decrease might be due to the starting EC and DMC reduction, as is seen in the C1s spectra. In the fully lithiated state, LiF again increases in intensity, which can occur due to the low potential and a more reactive SEI. P2p spectra of **Figure A14** display two doublets corresponding to Li$_x$PF$_y$ (137 eV) and Li$_x$POF$_y$ (134.5 eV). Upon lithiation, the amount of detected Li$_x$POF$_y$ behaves similar to LiF, as it shows a decrease from 2.5 V to 0.5 V but a subsequent increase from 0.5 V to 0.01 V.

Overall, all anodes cycled in LiTFSI-containing electrolytes display lower atomic percentages of LiF, while 4-9 at.% more of this component is seen when cycling in presence of LiPF$_6$.

Evolution of SEI composition during aging. To investigate SEI aging in the different electrolyte systems, XPS was conducted after 1, 10, and 100 cycles on electrodes in the delithiated state (i.e., at 1.5 V). **Figure 40** shows the C 1s spectra of electrodes cycled in TMG, TEG, L-E/D, and LP30 electrolyte, respectively. Derived atomic percentages from these data are summarized in **Figure 41**. F1s spectra are displayed in **Figure 42** with corresponding atomic percentages in **Figure 43**. Spectra of the remaining elements O1s, N1s, P2p, and S2p can be found in the appendix **Figure A15-Figure A17**. An overview of all detected species can be found in **Table A6-Table A9**.

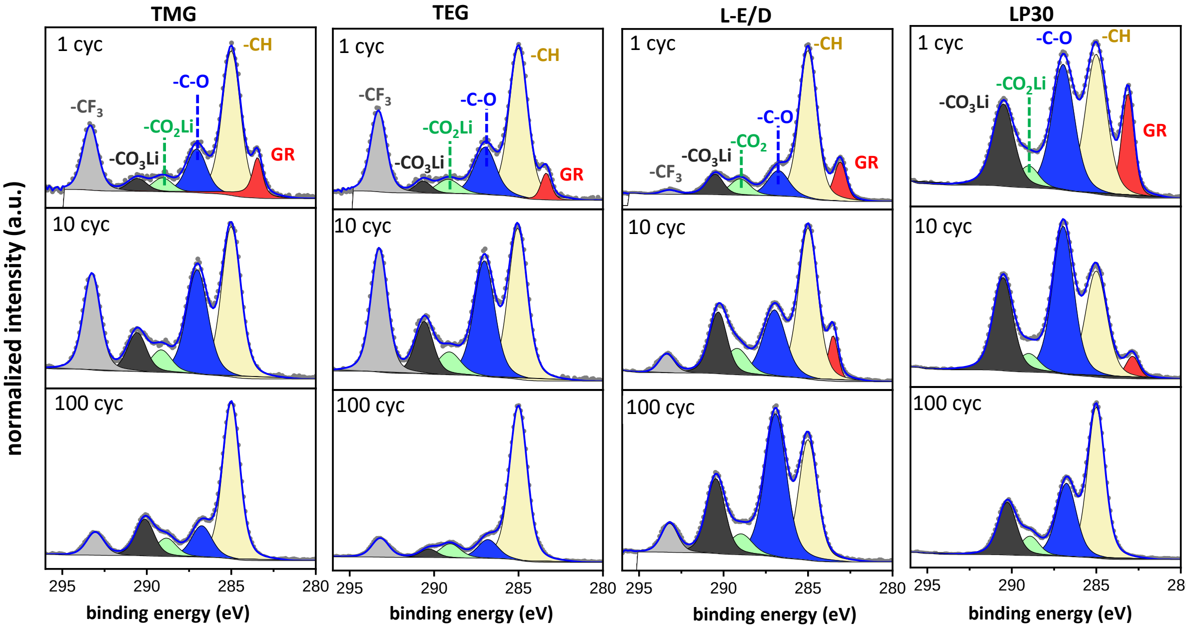

Figure 40: C1s spectra of Si/Gr electrodes cycled in TMG, TEG, L-E/D, and LP30 electrolyte at C/10. Photoelectron spectra were taken after the following cycles: 1, 10, and 100 cycles.

Solvent decomposition. The following species are found at the electrode surface for all four electrolytes, see **Figure 40**: hydrocarbons (285 eV), -C-O groups (286.5 eV), -CO$_2$Li groups (288.9 eV), and -CO$_3$Li groups (290.4 eV). Electrodes cycled in TMG, TEG, and L-E/D show an additional peak at 293.2 eV corresponding to -CF$_3$ groups resulting from the remaining LiTFSI salt as previously discussed in the formation analysis part. Upon cycling, TMG and TEG display very similar trends in atomic percentages. While -C-O components remain at around 4 at.% throughout all 100 cycles, hydrocarbons, -CO$_2$Li, and -CO$_3$Li groups increase in abundance. This suggests TMG and TEG solvents decompose to -CH, -CO$_2$Li, and -CO$_3$Li containing products upon prolonged cycling. When cycling in L-E/D, a decrease is observed for -CO$_2$Li, while the amount of -CO$_3$Li and -C-O components increases. Cells cycled in LP30 exhibit an increase in hydrocarbons and -CO$_2$Li compounds upon cycling. The amount of detected -C-O and -CO$_3$Li however stays very similar between the first and the 100th cycle.

However, the SEI formed by LP30 exhibits the highest abundance in -CO_3Li out of all electrolytes.

During aging, the composition of the organic part of the SEI is affected by the electrolyte solvent. SEIs formed in glyoxal-based electrolytes TMG and TEG display very similar compositions that are more abundant in hydrocarbons. By contrast, both SEI layers derived from carbonate-based electrolytes show higher contents of -C-O and -CO_3 species, which is expected for carbonate-based electrolytes as they form PEO, Li_2CO_3, and LEDC.[99]

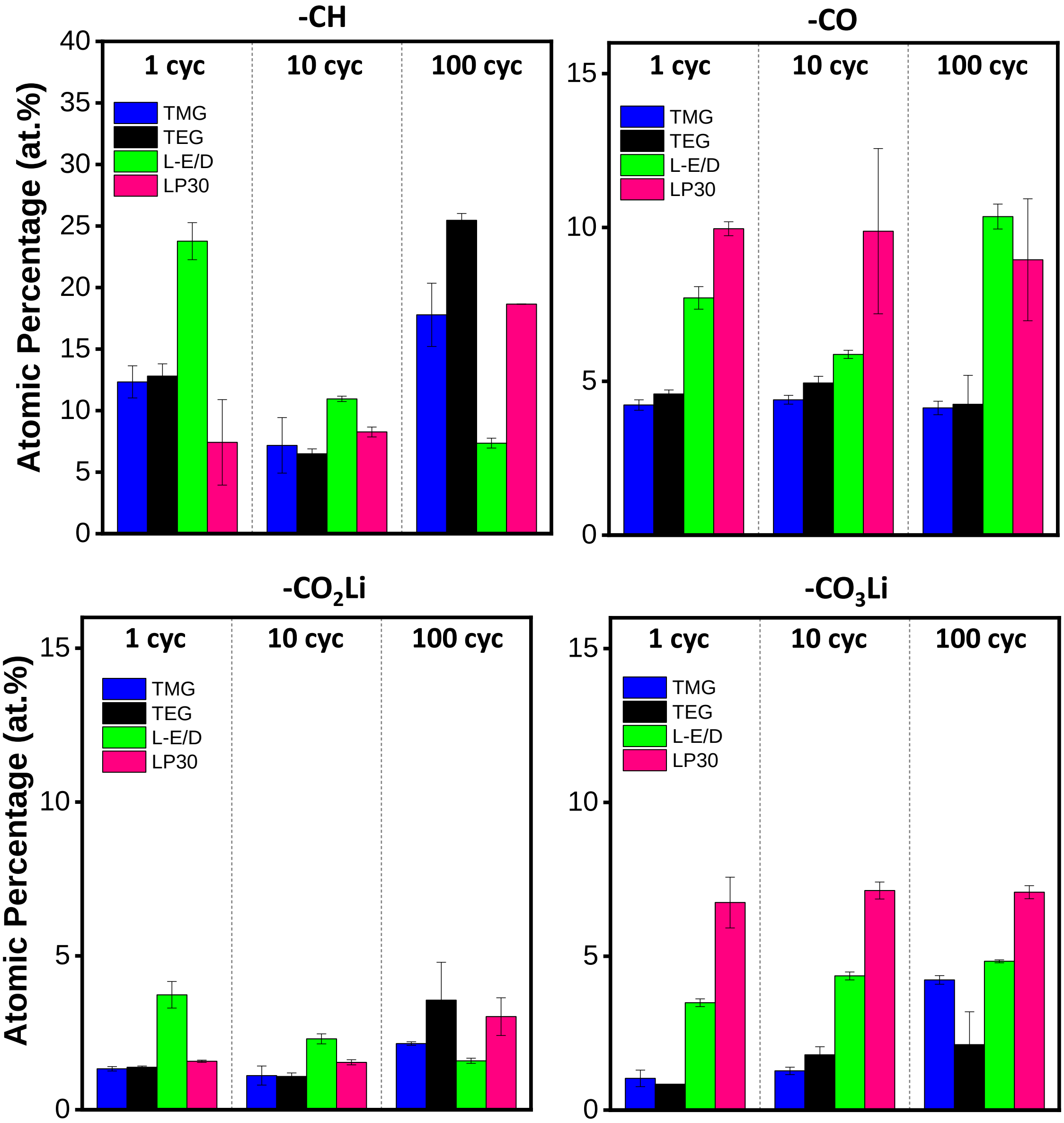

Figure 41: Atomic percentages of different carbon-containing species in the SEI of Si/Gr electrodes cycled in TMG, TEG, L-E/D, and LP30 electrolyte at C/10. Photoelectron spectra were taken after the following cycles: 1, 10, and 100 cycles. The error bars indicate the standard deviation between two measurements on one electrode.

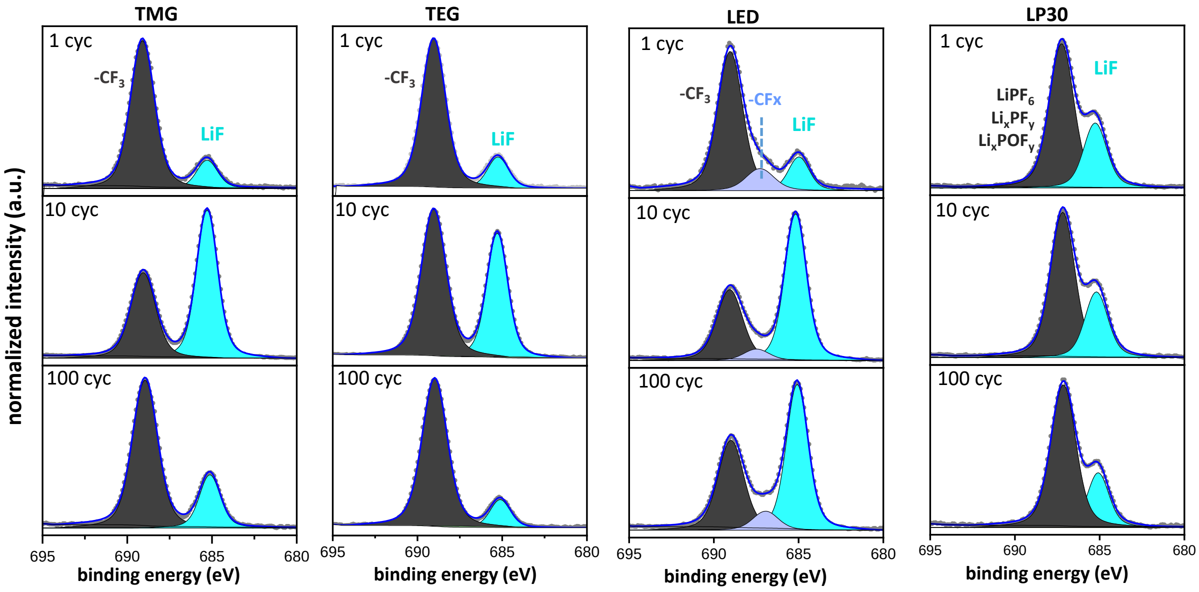

Figure 42: F1s spectra of Si/Gr electrodes cycled in TMG, TEG, L-E/D, and LP30 electrolyte at C/10. Photoelectron spectra were taken after the following cycles: 1, 10, and 100 cycles.

Salt decomposition. The decomposition products of the different electrolyte salts LiTFSI and $LiPF_6$ can be followed in the F1s spectra displayed in **Figure 42**. As seen during the SEI formation, two peaks are detected when cycling in TMG or TEG, namely LiF and $-CF_3$. While $-CF_3$ decreases upon cycling, the amount of detected LiF increases for both electrolytes from the first to the 10th cycle (i.e., 18 at.% for TMG and 10 at.% for TMG), see **Figure 43**. After 100 cycles, LiF decreases by 14 at.% for TMG and 9 at.% for TEG. In all cases, TMG displays higher LiF abundance than TEG, indicating higher salt decomposition for the TMG electrolyte. In addition to fluorine-containing decomposition species, TMG and TEG show emerging Li_3N (397.4 eV), $-SO_x$ or Li_2SO_3 (167.3 eV), and additional sulfur decomposition products (~163.9 eV and 161.8 eV), see **Figure A16** and **Figure A17**. These additional sulfur decomposition products are already present after the first cycle with TMG, while they only emerge after 100 cycles with TEG.

The F1s spectra of cells cycled in the L-E/D reference electrolyte display three peaks as already seen after 0.01 V, corresponding to $-CF_3$, $C_2F_xLi_y$, and LiF species. Upon cycling, the amount of detected LiF increases by 11 at.% from the first to the 10th cycle. Unlike TMG and TEG, the amount of LiF does not drop upon continued cycling but stays at around 12 at.%. The detected amount of $-CF_3$ compounds increases slightly upon cycling by 4 at.% from the first to the 100th cycle. Detected $C_2F_xLi_y$ species are decreasing upon cycling. Concerning N- and S- containing decomposition products, neither Li_3N nor $-SO_x/Li_2SO_3$ components are detected with L-E/D upon cycling. The SEI formed by LP30 demonstrates an increase of Li_xPF_y/Li_xPOF_y

species upon cycling, while the amount of LiF decreases. Intensities of detected Li_xPOF_y species in P2p spectra of **Figure A17** remain similar throughout cycling.

Compared to the C1s spectra, where an increase in solvent decomposition is observed, no dramatic increase in salt decomposition is detected after 100 cycles. While the amount of measured LiF even decreases for TMG, TEG, and LP30, no changes are seen for L-E/D. Also, differences in the composition of deeper layers cannot be identified due to the high surface sensitivity of XPS. Nevertheless, it can be concluded that for all four electrolyte formulations used, the inner SEI layer is mostly made of inorganic components while the outer layer is more organic in nature. While this is already known for carbonate-based electrolytes,[99],[164] the same is true for the SEI formed by glyoxal-based electrolytes.

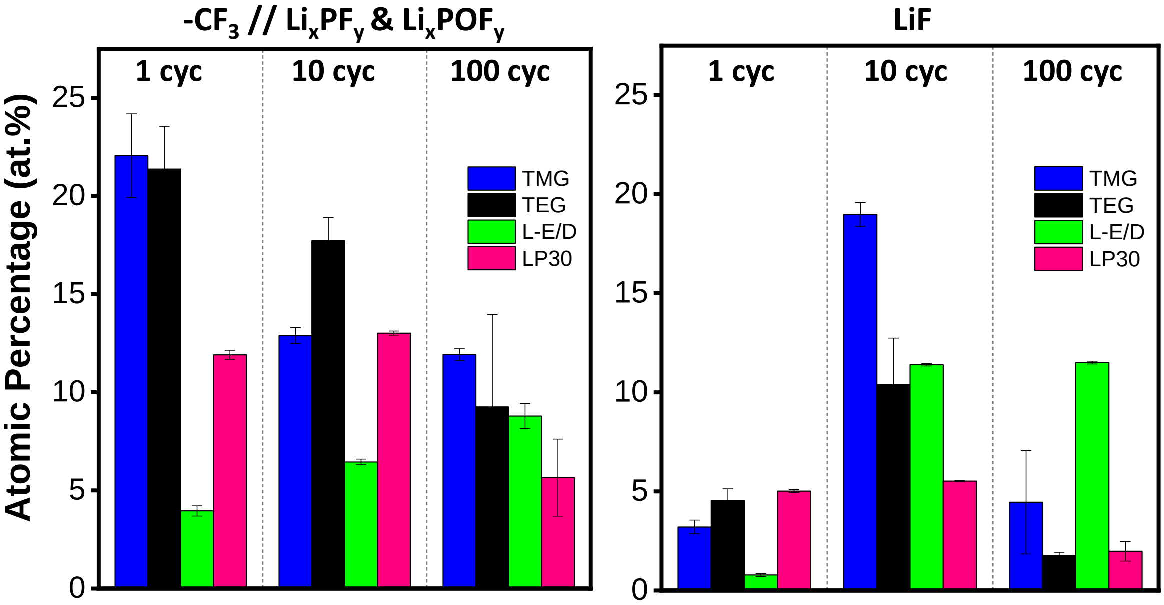

Figure 43: F1s atomic percentages of Si/Gr electrodes cycled in TMG, TEG, L-E/D, and LP30 electrolyte at C/10. Photoelectron spectra were taken after the following cycles: 1, 10, and 100 cycles. The error bars indicate the standard deviation between two measurements on one electrode.

SEI and electrode morphology

SEM micrographs of a pristine Si/Gr electrode and electrode surfaces after 100 cycles are presented in **Figure 44**. The uncycled electrode of **Figure 44(a)** displays graphite as large rectangular-shaped particles, silicon as small and round shapes, spread into different agglomerations, and carbon nanofibers as long wires. After 100 cycles, all surfaces display pronounced changes in electrode morphology. In the case of TMG, L-E/D, and LP30 graphite particles are covered with electrolyte decomposition products. The previously sharp graphite edges are concealed by bright and small particles, that are either closely sticking together or forming intricate networks. Corresponding magnifications show a strong SEI coverage of graphite, carbon nanofibers, and silicon particles. However, it is difficult to differentiate between silicon particles and electrolyte decomposition products such as LiF. For all three cases, the surface morphology is very rough, suggesting continuous breaking and reformation of the SEI layer.

By contrast, the surface of the electrode cycled in TEG is covered by a smooth SEI film, which makes it difficult to distinguish between separate graphite particles. This difference in electrode surface morphology is also observed in the magnification, suggesting an extensive coverage of the electrode material. Furthermore, the SEI film does not exhibit obvious cracks, suggesting that TEG forms an SEI with an increased ability to accommodate the volume changes of the Si/Gr electrode.

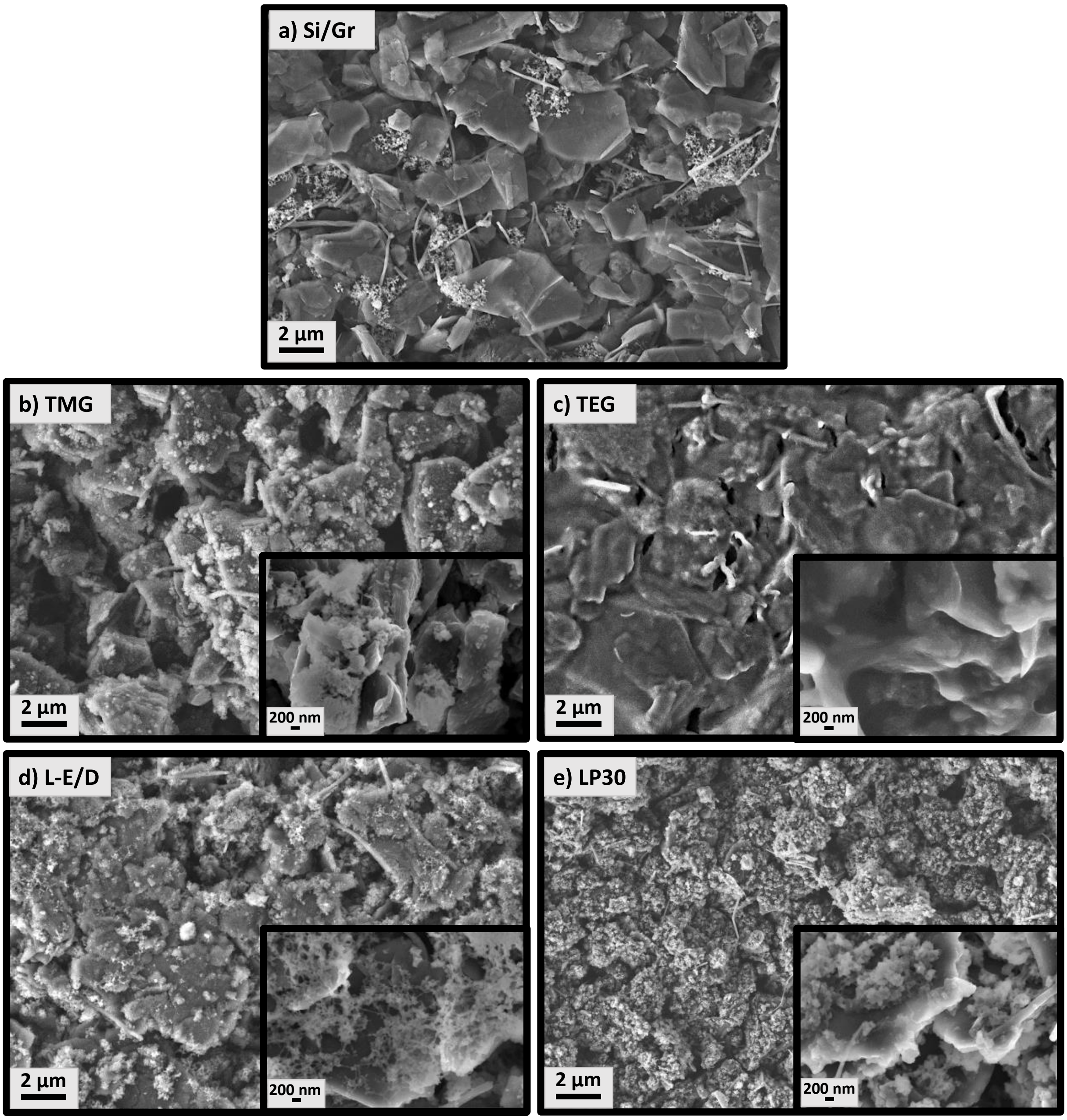

Figure 44: SEM pictures of a pristine Si/Gr electrode (a) and after 100 cycles in TMG (b), TEG (c), L-E/D (d), and LP30 (e) electrolyte.

Stability of TMG and TEG against Li-metal

Previous chapters analyzed the influence of TMG and TEG on the SEI thickness and composition, as well as the electrode morphology. In this part, a closer look is taken at the interaction of TMG and TEG electrolytes with the lithium metal counter electrode. **Figure 28** illustrates the lithium metal electrode after being cycled 100 times in the (a) TMG, and (b) TEG electrolytes. In the case of TMG, the middle area of the lithium-metal is completely black and almost no metallic lithium remains. This suggests a severe depletion of the lithium reservoir. Accordingly, it seems TMG cannot passivate the lithium metal well. When cycled in the TEG electrolyte, the lithium metal also displays black parts, however, enough metallic lithium remains, as can be seen in the front and back side pictures of the lithium electrode in **Figure 45**. The metal passivation appears to be greater for TEG.

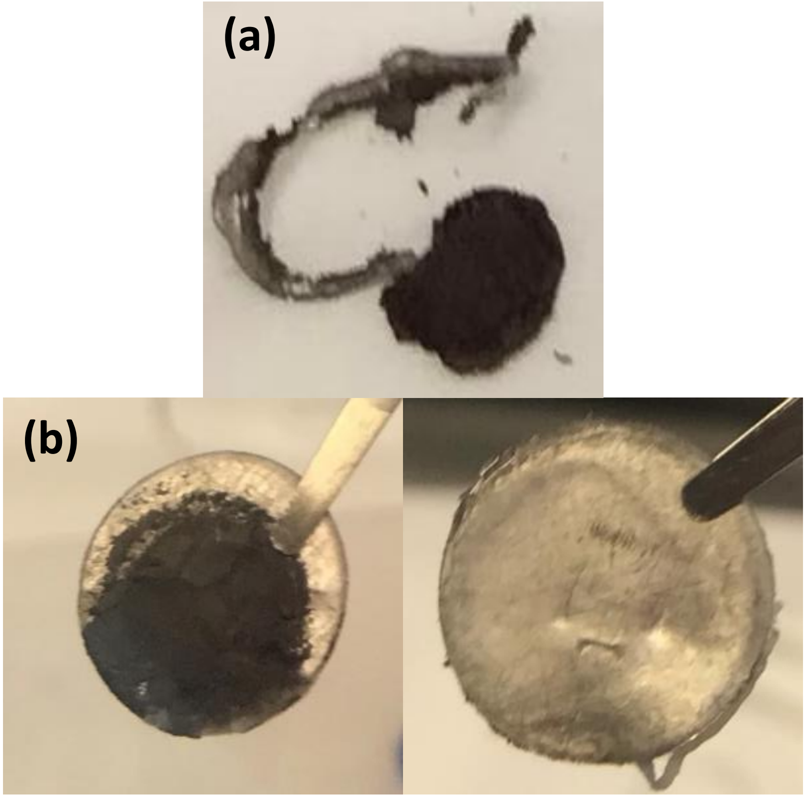

Figure 45: (a) Li-metal after 100 cycles in TMG electrolyte. (b) Li-metal after 100 cycles in TEG electrolyte front (left) and back (right).

Correlating film-forming properties to electrochemical performance

In this study, all experiments were conducted under similar parameters except for the electrolytes used. Therefore, the differences in cycling stability and SEI properties between Si/Gr electrodes can be related to the electrolyte formulations. The carbonate-based reference electrolytes L-E/D and LP30 show similar capacity profiles with a pronounced capacity decrease after 20 cycles. Also, very similar retentions are achieved after 100 cycles, indicating a loss in both silicon and graphite electrochemical activity. The organic part of the SEI is very similar, as can be expected of an SEI formed by the same carbonate-solvents (i.e., EC and DMC). The following species are detected: -CH, -C-O, -CO_2Li, and -CO_3Li. LiF is the main electrolyte salt decomposition product for both electrolytes, despite the two different salts (i.e., $LiPF_6$ and LiTFSI). Upon cycling, the amount of detected LiF decreases, while an increase is seen for -C-O, and -CO_3Li containing species. Also, changes in SEI thickness are comparable. SEM micrographs of electrode surfaces after 100 cycles show a very rough surface morphology, indicating high mechanical strain as well as pulverization of the electrode material. As previously motivated in this thesis, EC is not an ideal electrolyte solvent. The poor electrochemical performance of L-E/D and LP30 can be correlated to an SEI whose main organic species are decomposition products such as PEO and LEDC (seen in XPS as -C-O and -CO_3Li species). These components are known to poorly adapt to the silicon volume changes.[23] As a result, ongoing SEI formation occurs which leads to a loss of the electrode integrity and finally a decrease in electrochemical activity.

The investigated glyoxal-based electrolytes TMG and TEG only differ by a methyl group in the solvent molecule. Still, very different cycling profiles are observed. Cells cycled in TMG exhibit worse electrochemical performance than TEG and the two carbonate-based electrolytes. A dramatic decrease in both silicon and graphite activity is already observed in the first 10 cycles. By contrast, TEG outperforms TMG, L-E/D, and LP30. While small losses are observed in silicon activity, graphite can completely retain its electrochemical activity. TEG and TMG display similar trends in initial SEI thickness. However, it is difficult to accurately estimate the thickness after 10 cycles because the thickness reaches the limit of the XPS information depth of 3λ. Concerning SEI composition, the following functional groups are detected in the C1s spectra, namely -CH, -C-O, -CO_2, -CO_3. The inorganic SEI is in both cases made of LiF, -SO_x/ Li_2SO_3, and Li_3N compounds. While the amount of detected -CH, -C-O, and -CO_2 remains very similar for TEG and TMG upon cycling, the following differences are observed when cycling in TMG: 1) earlier LiTFSI salt decomposition, as seen in additional sulfur decomposition products are observed from the 1st cycle on. These are not observed for the SEI formed by the TEG electrolyte. 2) higher LiF amounts are detected after 10 and 100 cycles, 3) more carbonate species are detected after 100 cycles. The earlier and stronger salt decomposition with TMG may indicate poor SEI stability. SEM displays evident differences in the morphology of electrodes cycled in TEG and TMG. TMG displays a very brittle and rough surface morphology, suggesting repeated breaking of the SEI layer upon cycling. This further indicates a poor film forming ability of TMG on the Si/Gr anode. By contrast, TEG forms an SEI layer with a very interconnected coverage, which suggests a better ability to adjust to the volume changes of the Si/Gr electrode.

In conclusion, TMG shows poor film-forming abilities on both lithium-metal electrodes and Si/Gr electrodes, explaining its poor electrochemical performance. When using TEG, a more stable interphase is formed on the counter electrode and the Si/Gr anodes. The results further indicate that the good electrochemical performance of Si/Gr electrodes in TEG electrolytes can be related to the formation of an SEI that accommodates the silicon volume changes more easily.

6.1.3 Summary

Two electrolytes based on glyoxylic acetals were investigated as potential alternative electrolyte formulations for Si/Gr anodes. While TMG performed worse than cells cycled in the reference electrolytes L-E/D and LP30, a performance improvement could be achieved when using TEG. The latter exhibited a much more stable capacity profile with overall higher capacities. The poor performance of TMG could be related to a dramatic drop in both graphite and silicon activity after already 10 cycles. TEG, on the other hand, showed higher retention of silicon activity, with graphite activity remaining unchanged from the 1st to the 100th cycle. XPS showed that TMG formed an SEI with slightly higher carbonate content and also earlier and stronger LiTFSI salt decomposition, while -C-O and -CO_2Li concentrations were similar when compared to the TEG SEI. Further findings suggest that the SEI might not be the only reason for the observed different cycling stabilities. The high reactivity of the TME solvent with the lithium-metal counter-electrode can negatively affect the overall electrochemical performance and partially explain the poor capacity retention with the TMG electrolyte. Thus, future work will have to evaluate TMG's effect on the cell performance without unwanted side reactions by using less reactive counter electrodes. Analysis of the electrode morphology revealed TEG to form a smoother and continuously connected SEI. This surface layer most probably has a higher ability to accommodate the silicon volume changes upon cycling, rendering TEG a very promising electrolyte candidate for realizing silicon-containing anodes with high capacity and high stability. Even without SEI stabilizing electrolyte additive or ionic conductivity enhancing cosolvent, TEG showed enhanced electrochemical performance with Si/Gr anodes compared to the standard LP30.

6.2 TEG:PC as electrolyte solvent

In **Chapter 6.1** of this thesis, Si/Gr electrodes cycled in pure TEG electrolyte showed promising cycling stability. However, pure TEG electrolytes exhibit high viscosities and low ionic conductivities, when compared to carbonate-based electrolytes. By adding cosolvents such as EC, PC, or DMC, these properties can be improved. Out of these candidates, the mixture 1 M LiTFSI in 30TEG:70PC has been identified as the most promising when used with graphite.[153] The following part investigates electrolyte mixtures based on this 30:70 ratio with 10%-Si/Gr electrodes.

6.2.1 Electrochemical Performance

Figure 46(a) shows the galvanostatic cycling of Si/Gr electrodes cycled in 30TEG:70PC (dark cyan) and 30TEG:70PC-10FEC (navy). Also shown are electrodes cycled under the same conditions in the reference electrolytes TEG (black) and 10FEC:90LP30 (pink). All TEG-containing formulations contain LiTFSI as electrolyte salt, while the LP30-containing electrolyte uses $LiPF_6$.

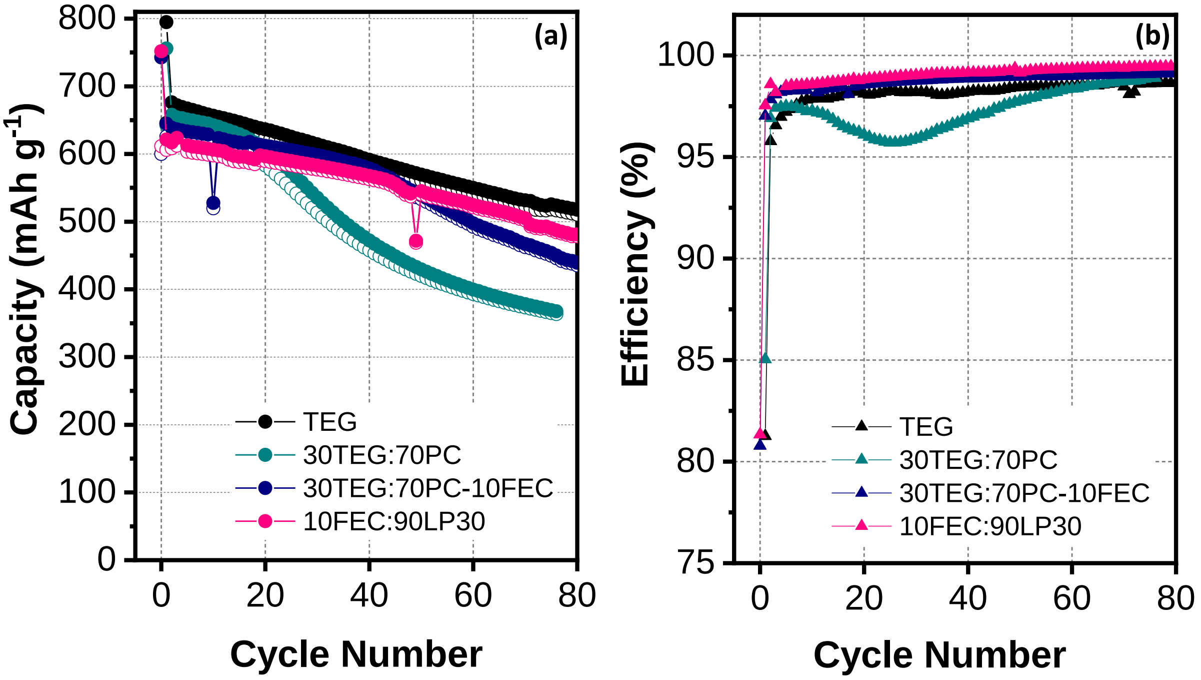

Figure 46: a) Long-term cycling stability and (b) efficiencies of Si/Gr electrodes cycled in TEG, 30TEG:70PC, 30TEG:70PC-10FEC, and 10FEC:90LP30.

In the first cycle, electrodes cycled in 30TEG:70PC, 30TEG:70PC-10FEC, and 10FEC:90LP30 show a lithiation capacity of around 750 mAh g^{-1}. With TEG a capacity of around 800 mAh g^{-1} is achieved. The capacity is much higher than the theoretical one, due to excessive SEI formation during the first cycle. Coulombic efficiencies amount to 81-85 %, see **Figure 46(b)**. When cycling in 30TEG:70PC, a drop in capacity is observed after the first 20 cycles and after around 78 cycles, only 57 % of the capacity observed in the second cycle can be retained. This is the lowest capacity out of all four electrolyte formulations. Interestingly, the cycling stability with 30TEG:70PC is very similar to that observed with LP30 or L-E/D. If 10 vol.% FEC is added to the 30TEG:70PC formulation, the capacity is improved for the first 40 cycles. Upon further cycling, however, a drop is seen and after 80 cycles only 70 % of the capacity can be retained. In contrast, cells cycled in either reference TEG or 10FEC:90LP30 electrolyte display much better electrochemical performance. The cell cycled in TEG displays overall higher capacities, but lower coulombic efficiencies than with LP30. This results in a capacity retention of only 77 % after 80 cycles. With LP30 this value is slightly higher and amounts to 78 %.

GCPL and dQ/dE profiles are displayed in **Figure 47**. Every plateau in the GCPL diagram corresponds to a peak in the dQ/dE profiles. Similar to **Chapter 5** and **Chapter 6.1**, the same electrochemical processes are observed: Intercalation reactions of lithium-ions into graphite at 0.2 V (stage IV), 0.13 V (stage III, LiC_{30}), 0.1 V (stage II, LiC_{12}), and 0.07 V (stage I, LiC_6).[201],[202] Lithiation of silicon starts at 0.4 V and extends over the whole lithiation profile. During the first lithiation, crystalline silicon forms amorphous silicon-lithium alloys (Li_xSi).[52]–[55] At 0.04 V, the amorphous phase reacts to crystalline $Li_{15}Si_4$.[58]–[60] During delithiation, $Li_{15}Si_4$ transforms back to amorphous silicon in which state it remains during further cycling. In subsequent cycles, a new signal is observed at 0.3 V corresponding to the lithiation of this amorphous phase, see inset of **Figure 47(b)**.

The cycling profile of PC:TEG in **Figure 47(a)** is not displaying overly large lithiation/delithiation plateaus, therefore, co-intercalation of the PC solvent into graphite particles can be ruled out. In the case of solvent co-intercalation, much higher lithiation capacities would occur than theoretically possible.[155] In fact, the obtained capacity profile is characteristic of pure lithium-intercalation. It seems, that similar to the works done on graphite anodes, TEG is hindering the co-intercalation of PC into the graphite particles. However, the positive effect pure TEG displays on the electrochemical performance cannot be replicated by the 30TEG:70PC formulation. Si/Gr electrodes cycled in 30TEG:70PC display the highest capacity drop out of all electrolytes, which can be correlated to a complete decrease in silicon activity after 100 cycles, see dQ/dE inset **Figure 47(b)**. Cycling in 30TEG:70PC-10FEC and 10FEC:90LP30 formulations leads to higher retention of the silicon activity. However, graphite peaks decrease in intensity as well as a shift towards higher potentials (during delithiation) and lower potentials (during lithiation). This behavior was also obtained for the FEC-containing electrolytes analyzed in **Chapter 5**. It was suggested to result from increasing electrical isolation of the graphite particles and a loss in electrode integrity. When cycling in pure TEG, Si/Gr electrodes display the highest retention in graphite activity. With regard to the silicon activity, higher values are obtained when compared to 30TEG:70PC and 30TEG:70PC-10FEC but lower values are achieved when compared to 10FEC:90LP30.

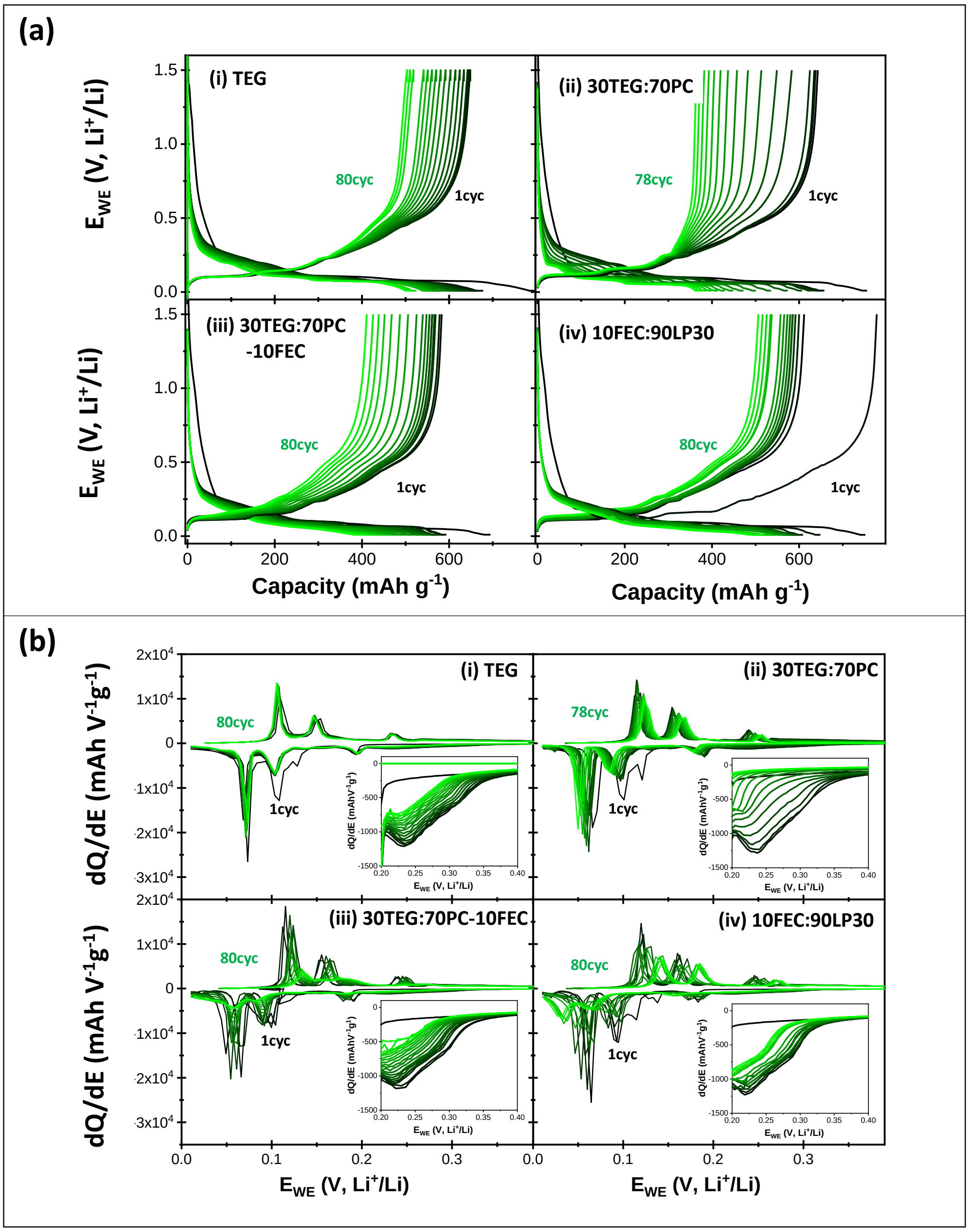

Figure 47: (a) GCPL profiles and (b) dQ/dE profiles of Si/Gr electrodes cycled in TEG, 30TEG:70PC, 30TEG:70PC-10FEC, and LP30-FEC, respectively.

6.2.2 SEI Analysis

X-Ray photoelectron spectroscopy was used to determine the effect of the SEI on the electrochemical performance. Cells were cycled to 0.8 V and 0.01 V during the first lithiation, as well as to 1.5 V after the 1st, 10th, and 78-80th delithiation. All electrodes were washed in 500 µL of DMC for 1 min, see **Chapter 4**. The obtained C1s spectra are displayed in **Figure 48**. C1s spectra for electrodes cycled in pure TEG can be found in **Figure 36** and **Figure 40**. Atomic percentages of different carbon-oxygen compounds and LiF are displayed in **Figure 49**. F1s, N1s, O1s, P2p, and S2p spectra can be found in the appendix **Figure A18-Figure A21**. A summary of all atomic percentages can be found in **Table A10-Table A12**. Survey spectra are displayed in **Figure A25-Figure A26**.

Solvent decomposition. The following carbon peaks are observed independent of the electrolyte, see **Figure 48**: graphite (~282-283 eV), hydrocarbons (285 eV), -C-O (286.5 eV), -CO_2Li (288-289 eV), and -CO_3Li (290-290.5 eV). Two additional peaks emerge when electrodes are cycled in 30TEG:70PC-10FEC and 10FEC:90LP30. They correspond to the two chemical environments C_a and C_b in DO resulting from FEC decomposition, see **Figure 49**. A detailed discussion of FEC decomposition products is presented in **Chapter 5.2** of this thesis. As seen in **Figure 49**, electrodes cycled in the 30TEG:70PC electrolyte show the highest abundance in -C-O containing species. This is especially true after 80 cycles. With 30TEG:70PC10FEC and 10FEC:90LP30 fewer -C-O groups are detected, while the electrode cycled in TEG shows the lowest amount. From the 10th cycle onwards, when using 30TEG:70PC and 30TEG:70PC-10FEC the highest abundance of -CO_3Li species is achieved. Regarding FEC decomposition, electrodes cycled in 10FEC:90LP30 display an earlier FEC reduction than the ones cycled in 30TEG:70PC-10FEC. Already after 0.8 V, 0.6 at.% of the C_b component in poly(VC)/DO can be detected. With 30TEG:70PC-10FEC, this component is barely observed with 0.1 at.% after the first delithiation and is present with similarly low abundance (i.e., 0.7 at.%) only after 10 cycles.

Salt decomposition. While electrodes cycled in the TEG and 30TEG:70PC electrolytes show the lowest amount in LiF (<4 at.%), higher abundance is observed in presence of 30TEG:70PC-10FEC (4-9 at.%). All three electrolytes contain LiTFSI as electrolyte salt. However, FEC also forms LiF upon reduction, which could explain the higher LiF content observed for the 30TEG:70PC-10FEC formulation. The highest concentration of LiF is observed with 10FEC:90LP30 (10-21 at.%). It has already been seen in **Chapter 5.1** that the presence of $LiPF_6$ results in more LiF formation. The addition of FEC further increases the levels of LiF in the SEI for 10FEC:90LP30.

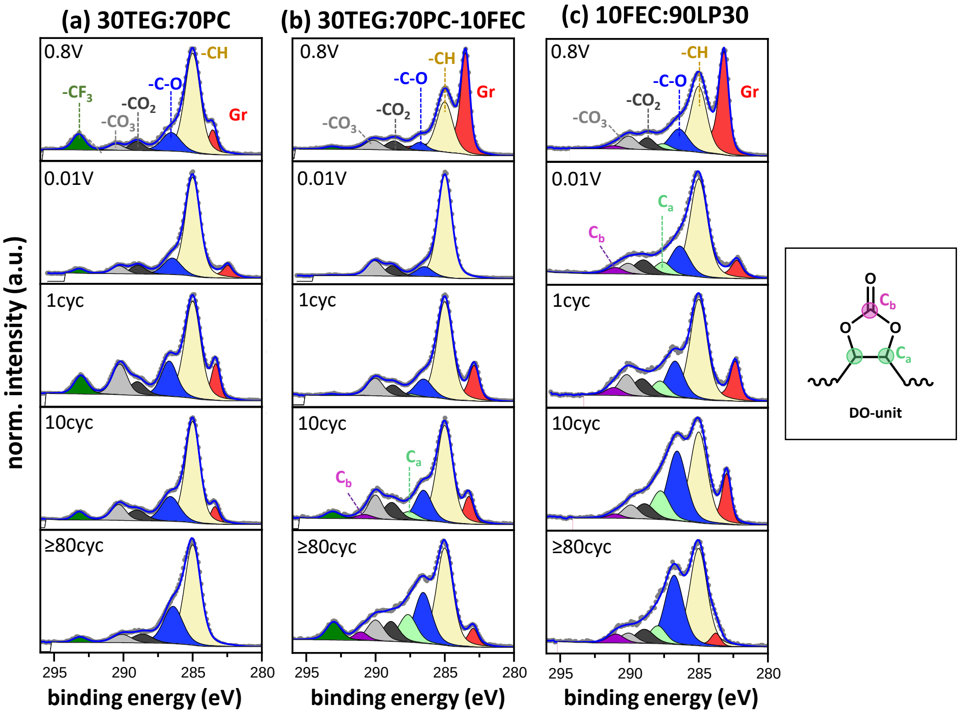

Figure 48: C1s spectra of Si/Gr electrodes cycled in 30TEG-70PC, 30TEG-70PC-10FEC, and 10FEC:90LP30, respectively.

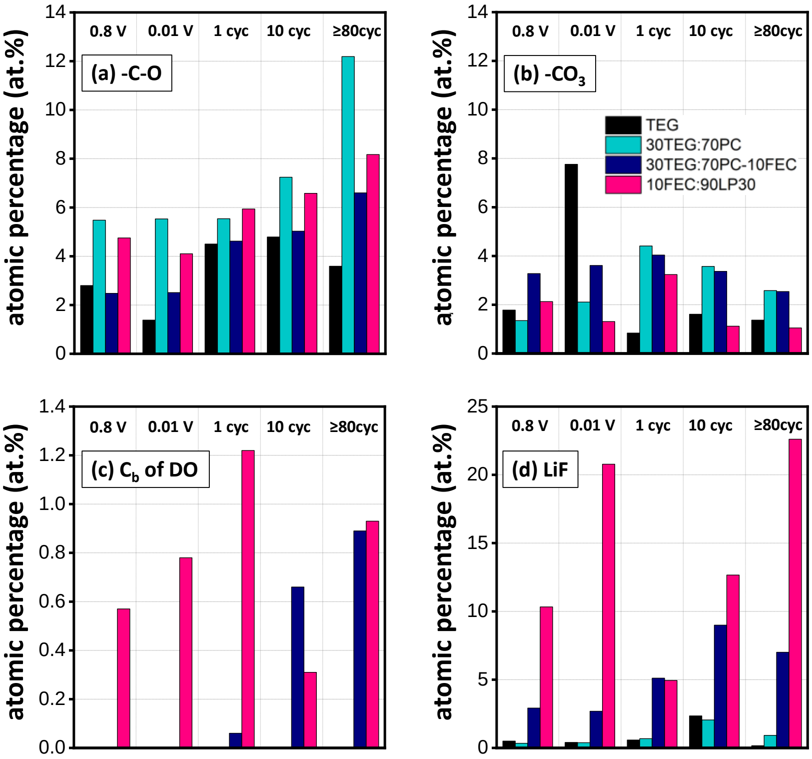

Figure 49: Atomic percentages of Si/Gr electrodes cycled in TEG, 30TEG-70PC, 30TEG-70PC-10FEC, and 10FEC:90LP30.

6.2.3 Correlating SEI properties to electrochemical performance

While the 30TEG:70PC electrolyte formulation shows enhanced transport properties[152],[153], no improvement in the electrochemical performance of Si/Gr anodes was observed in **Chapter 6.2.1**. Especially the silicon activity decreases strongly upon cycling. Adding 10 vol.% of FEC increases the cycling stability for 20 more cycles, however, a subsequent decline in performance is observed after longer cycling. When cycled in the 10FEC:90LP30 formulation, Si/Gr anodes display the highest capacity retention and also the highest silicon activity after 100 cycles, out of all four electrolytes. However, the capacity is still lower than when cells are cycled in pure TEG. This mostly results from better retention in graphite activity with TEG than with 10FEC:90LP30.

The poor performance of Si/Gr anodes with 30TEG:70PC most probably arises due to the high presence of PC (70%) in the electrolyte. Similar to EC, PC decomposes to inorganic and organic lithium carbonates such as LPDC.[228] These species are detected as -C-O and -CO_3 groups with XPS. The SEI formed by 30TEG:70PC displays a much higher abundance of these two compounds than the SEI formed by the pure TEG formulation. A high abundance of these PC decomposition products in the SEI seems to negate the positive influence of TEG on the SEI stability. Therefore, the SEI formed by 30TEG:70PC is most likely unable to accommodate the silicon volume changes. This leads to higher SEI formation and a loss in electrode integrity, which ultimately explains the drop in silicon activity and poor electrochemical performance. Improved cycling stability is achieved by adding FEC to the 30TEG:70PC formulation. As seen in **Chapter 5**, FEC decomposes to a polymer network containing -C-O, DO, and -CO_2Li units. This polymer is hypothesized to stabilize the SEI upon the silicon volume changes. However, as FEC is being depleted upon cycling, the stabilizing effect of this polymer is dampened. This would explain the decrease in capacity observed for the 30TEG:70PC-10FEC formulation. However, FEC decomposition products are still measured in the SEI after 80 cycles, as indicated by the detection of DO in the C1s. Also, the SEI is still thinner than the XPS information depth of 3λ, as graphite is still being detected. This indicates that there is still enough FEC present in the electrolyte for its decomposition products to be detected with XPS and for it to still have a positive impact on the cycling stability. In fact, Si/Gr electrodes cycled in the 30TEG:70PC-10FEC formulation display around 100 mAh g^{-1} more capacity than when cycled in 30TEG:70PC. Comparing the electrochemical performance of Si/Gr anodes in the 30TEG:70PC-10FEC formulation to the one in 10FEC:90LP30, much lower capacity retention is obtained. While both formulations use the same FEC concentration in the electrolyte, the cosolvents are different, namely TEG:PC and EC:DMC. EC and PC form carbonates upon decomposition such as LEDC and LPDC, respectively. However, Melin *et al.* could show that PC is reduced much more extensively than EC and forms a thicker SEI.[182] They could also demonstrate by EQCM measurements that the SEI derived from EC remains on the graphite electrode, while PC reduction products dissolve more easily in the electrolyte. Another work also observed that LPDC is more soluble than LEDC in DEC solvent.[113] However, taking these results and applying them to the present observations requires caution, because the solubility of LPDC is different for 30TEG:70PC and DEC. XPS shows that FEC decomposition products are already found after 0.8 V during the first lithiation with 10FEC:90LP30. In contrast, with 30TEG:70PC-10FEC the same amount of this DO species is not detected until the 10th cycle. Differences in initial FEC reactivity might be due to different interactions between FEC and the respective electrolyte salt (i.e., $LiPF_6$ or LiTFSI). Also, the presence of the 30TEG:70PC solvent mixture could reduce the initial FEC decomposition. It can be hypothesized that this early SEI composition will have an effect on the cycling stability and explain why 10FEC:90LP30 shows an improved electrochemical performance. Overall, the results show that using PC as electrolyte solvent is unfavorable for silicon-containing anodes.

6.2.3 Summary

This chapter investigated the electrochemical performance and SEI properties of a mixture of TEG and PC. Contrary to the pure TEG electrolytes, the 30TEG:70PC electrolyte showed very poor capacity retention with Si/Gr anodes. This could be correlated to an SEI that was mainly composed of PC decomposition products such as LPDC and Li_2CO_3. Consequently, it was hypothesized that these species were not able to accommodate the silicon volume changes, which results in the poor electrochemical performance observed. An improvement could be achieved when adding 10 vol.% FEC to the electrolyte formulation. While an increase in cycling stability was observed during the first 40 cycles, the capacity dropped upon subsequent cycling. Analysis of the SEI indicated that FEC decomposition products were still present in the SEI after 80 cycles. Hence, the positive effect of FEC on the SEI stability should still be present. A negative influence of the PC cosolvents was therefore proposed. In contrast, Si/Gr electrodes cycled in 10FEC:90LP30 displayed better electrochemical performance. Interestingly, when using the pure TEG formulation, a similar performance was achieved. This further highlighted the potential of TEG as an electrolyte solvent for silicon-containing anodes. To maintain the positive effects of the TEG solvent, further work must be done to optimize electrolyte formulations.

7 Electrolyte Comparison

In the previous two chapters, six electrolyte formulations were described as alternatives to EC-containing electrolytes. The first two formulations were based on FEC as cosolvent with 1 M LiPF6 in either 20FEC:80DMC or 50FEC:50DMC, see **Chapter 5**. Two other formulations consisted of 1 M LiTFSI in glyoxylic acetals TMG or TEG, see **Chapter 6.1**. TEG was further mixed with PC, yielding the electrolytes 30TEG:70PC and 30TEG:70PC-10FEC, see **Chapter 6.2**. Because all experiments were conducted under similar parameters (e.g., ~2.8-3.1 mg cm-2 of active material, lithium counter electrode, cell set-up, XPS washing procedure) differences in electrochemical performance and SEI properties can be correlated to the electrolyte formulation. While formulations with the best electrochemical performance were identified at the end of every chapter, no overall comparison has been conducted so far. This chapter aims to identify the formulations that have the highest impact on the cycle life of Si/Gr anodes. Therefore, all electrolytes used in this thesis are compared in **Figure 50**, which includes the six formulations mentioned above as well as all reference electrolytes. In this comparison, LP30 is taken as the overall reference electrolyte.

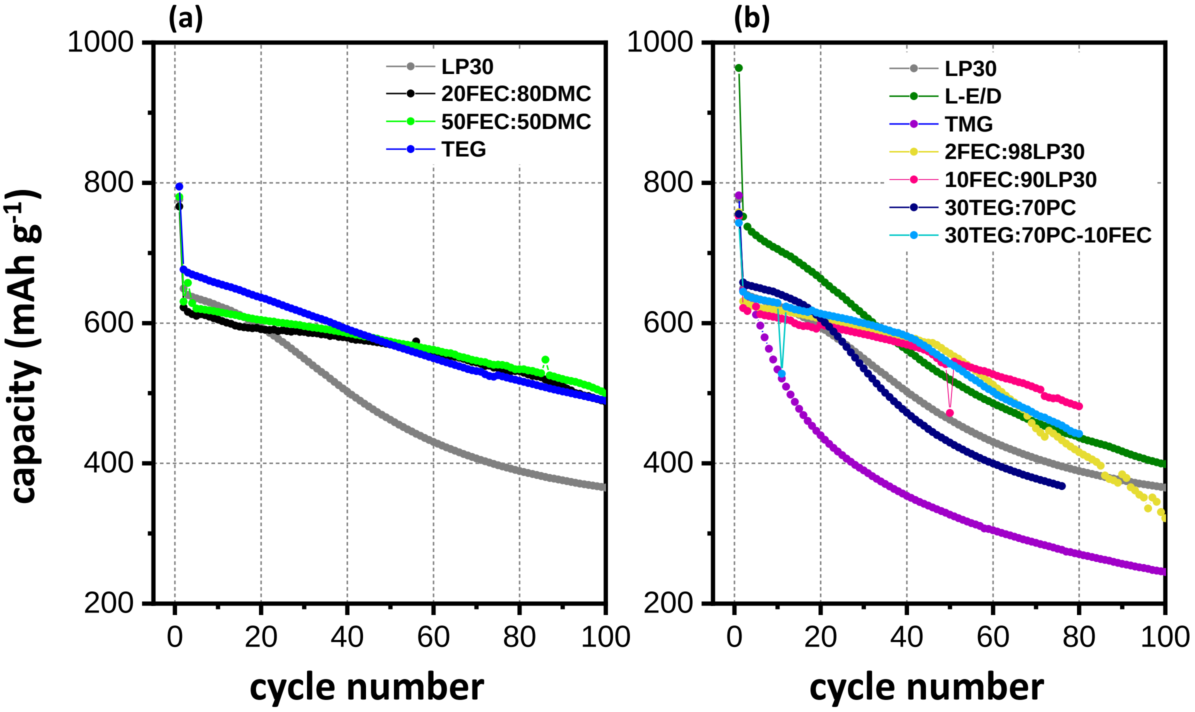

Figure 50: Cycling stability of Si/Gr electrodes cycled in electrolyte formulations resulting in (a) high capacity retention (i.e., ≥ 80 % after 80 cycles), and (b) poor capacity retention (i.e., ≤ 79 % after 80 cycles). LP30 is shown in each graph as the reference electrolyte. Displayed is the lithiation capacity.

For clarity of presentation, the electrolyte formulations enabling high electrochemical performance of Si/Gr anodes are shown in **Figure 50(a)**. These include 20FEC:80DMC, 50FEC:50DMC, and TEG. LP30 is plotted as the reference electrolyte. Formulations that displayed poorer capacity retentions are depicted in **Figure 50(b)**. In particular: L-E/D, TMG, 2FEC:98LP30, 10FEC:90LP30, 30TEG:70PC, and 30TEG:70PC-10FEC. Capacities and capacity retentions are displayed in **Table 8**.

Table 8: Lithiation capacities of Si/Gr electrodes cycled in the respective electrolytes after 2, 80, and 100 cycles. Also shown are capacity retentions after 80 and 100 cycles. Electrolytes are listed in decreasing order of capacity retention with LP30 as the reference.

Electrolyte	Lithiation capacity 2^{nd} cycle (mAh g^{-1})	Lithiation capacity 80 cycles (mAh g^{-1})	Capacity retention 80 cycles (%)	Lithiation capacity 100 cycles (mAh g^{-1})	Capacity retention 100 cycles (%)
LP30	**625**	**389**	**62**	**365**	**58**
50FEC:50DMC	622	534	86	503	81
20FEC:80DMC	617	532	86	488	79
TEG	646	518	80	489	76
10FEC:90LP30	611	481	79		
30TEG:70PC-10FEC	600	442	74		
2FEC:98LP30	624	416	67	322	52
L-E/D	751	437	64	399	47
30TEG:70PC	643	368	57		
TMG	647	270	42	245	38

The summarized data indicates that the electrochemical performance is not influenced by the transport properties of the electrolyte at this point. Formulations with similarly high viscosities and low ionic conductivities such as TMG and TEG show very different performances. TMG displays extremely poor cycling stability, while cycling with TEG achieves very good performance. Formulations based on EC, DMC, PC, and FEC have lower viscosities and higher ionic conductivities than both glyoxal electrolytes.[150],[157] However, Si/Gr electrodes cycled with <10 vol.% of FEC show poor cycling stability, while in presence of ≥20 vol.% FEC the best performance is achieved. Therefore, no correlation can be found between conductivities or viscosities and electrochemical performance. This is likely due to the fact, that the cycling was performed at slow rates (C/10 for lithiation reaction; C/10, or C/3 for the delithiation).

The reference electrolyte LP30 displayed in both **Figure 50(a)** and **Figure 50(b)** shows a decrease in capacity after around 10-20 cycles and after 100 cycles only 58 % of the capacity of the 2nd cycle can be retained, see **Table 8**. **Chapter 6.1** shows that the capacity drop is mainly due to a decrease in silicon activity. The decreasing activity can be attributed to poor SEI properties formed by EC and DMC solvent in LP30. Electrodes cycled in L-E/D, which contains the same solvents but different salt (i.e., LiTFSI instead of $LiPF_6$), displays similar capacity retention after 100 cycles and similar decrease in silicon activity. It has been shown that EC decomposition leads to the formation of LEDC and PEO.[23] With XPS, LEDC is detected as $-CO_3Li$ peak. The SEIs derived from LP30 and L-E/D show the highest amount of this species out of electrolytes, see **Figure 51**. LEDC and PEO are known to not sufficiently stabilize the SEI upon silicon volume changes.[23] As a result, cracks form in the SEI, revealing previously covered active material. Consequently, continuous side reactions occur at the electrode/electrolyte interface, depleting the electrolyte of lithium, increasing the resistance of the SEI, and electrically isolating the silicon particles.

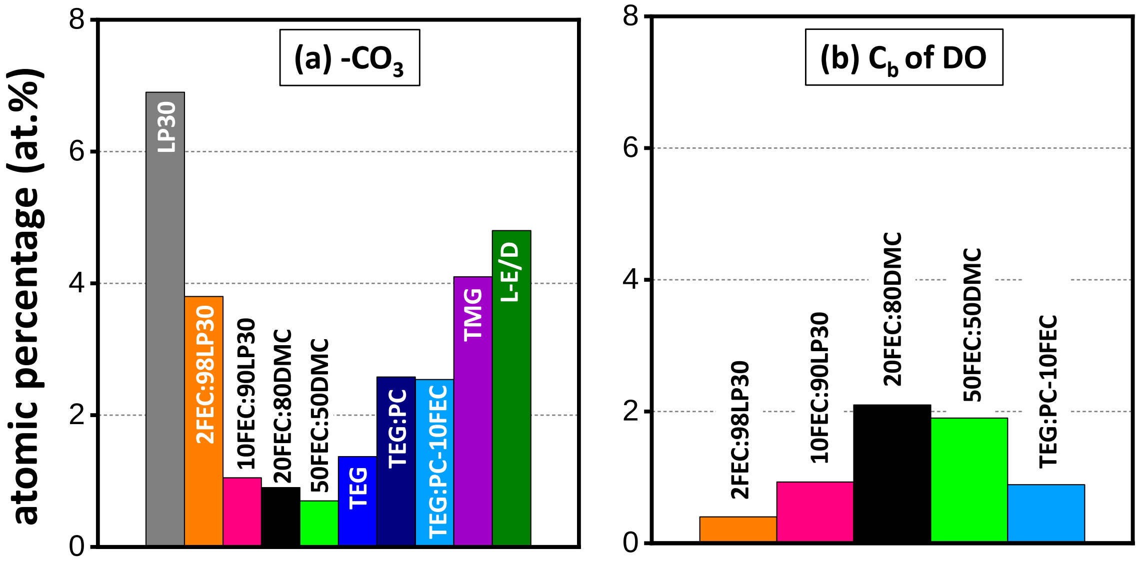

Figure 51: Atomic percentages of $-CO_3Li$ and DO (C_b peak) SEI species after 80 cycles for 10FEC:90LP30, 30TEG:70PC, and 30TEG:70PC-10FEC, as well as after 100 cycles for LP30, 2FEC:98LP30, 20FEC:80DMC, 50FEC:50DMC, TEG, TMG, and L-E/D.

In comparison to the LP30 reference, Si/Gr anodes perform less well using TMG as an electrolyte. In fact, when cycling in TMG, the poorest performance out of all electrolytes is achieved, see **Figure 50(b)**. After 100 cycles, the cell only delivered 245 mAh g^{-1}, see **Table 8**. This corresponds to a capacity retention of only 38 %. Such a low capacity was related to a huge drop in both graphite and silicon activity when Si/Gr anodes were cycled in TMG. Ultimately, the poor electrochemical performance was attributed to the ineffective film-forming capabilities of TMG on both the Si/Gr anode and the lithium counter electrode, see **Chapter 6.1**. The 30TEG:70PC electrolyte is the second formulation in which Si/Gr anodes perform worse than the LP30 reference, see **Figure 50(b)**. After 80 cycles, only 368 mAh g^{-1} of capacity remains which corresponds to 57 % of the capacity of the 2nd cycle. Again, the poor electrochemical performance can be correlated to bad SEI properties. PC decomposes to LPDC species which are detected as $-CO_3Li$ groups with XPS, see **Figure 51**. Just like LEDC, LPDC species might also be unable to adjust to the silicon volume changes. With 70 vol.% of PC, it is likely that these species are abundant in the SEI and will negate the positive effects of TEG.

Adding 2-10 vol.% FEC in the electrolyte formulation leads to an increase in cycling stability for LP30, see **Figure 50(b)**. Similarly, Si/Gr electrodes cycled in 30TEG:70PC-10FEC display improved electrochemical performance compared to pure 30TEG:70PC. Consequently, with 2FEC:98LP30, 10FEC:90LP30, and 30TEG:70PC-10FEC formulations, higher capacities and capacity retentions are observed after 80 cycles, see **Table 8**. However, FEC is being consumed upon cycling, leading to the depletion of its concentration in the electrolyte. In the SEI, this depletion can be traced by a decrease in DO (1,3-dioxolan-2-one) species. These compounds are unambiguously linked to the presence of FEC decomposition products, since no other electrolyte component forms this species upon reduction, see **Chapter 5.2**. As less DO is formed, the SEI's capacity to adjust the volume changes is diminished. This results in continued re-exposure of active material and ongoing SEI formation. Consequently, silicon particles are electrically isolated, the electrolyte gets depleted of lithium, and the SEI resistance increases.[7],[10]–[15] Ultimately the capacity decreases. The depletion of FEC could explain the drop in capacity observed for 2FEC:98LP30 where the least DO species are observed, see **Figure 51**. Interestingly, DO is still well observed in the SEI for 30TEG:70PC-10FEC after 80 cycles, while its presence decreased dramatically in the case of 2FEC:98LP30 after 100 cycles. The high drop in abundance in the latter case could be explained by 8 vol.% less FEC in the electrolyte formulation and the fact that 20 more cycles were conducted before analyzing the SEI with XPS. 10FEC:90LP30 and 30TEG:70PC-10FEC use 10 vol.% FEC and display similar amounts of the FEC decomposition marker DO in the SEI, see **Figure 51**. However, both show different electrochemical performances. This could be explained by the amount of respective PC and EC cosolvent in the electrolyte. In the glyoxal-based formulation, 70 vol.% of PC is present in the electrolyte, while only 50 vol.% of EC exists in the LP30 formulation. Therefore, PC likely decomposes to a higher degree than EC, resulting in a more pronounced SEI instability. The abundance of $-CO_3Li$ species is also higher for 30TEG:70PC-10FEC than it is for 10FEC:90LP30, see **Figure 51**. This could indicate the formation of more SEI species which are unable to accommodate the volume changes. Additionally, the interactions between FEC and the respective salt (i.e., $LiPF_6$ or LiTFSI) might also influence the electrochemical performance. **Figure 52** proposes schematic figures of the SEI composition of Si/Gr electrodes cycled in 30TEG:70PC, 30TEG:70PC-10FEC, and 10FEC:90LP30, respectively.

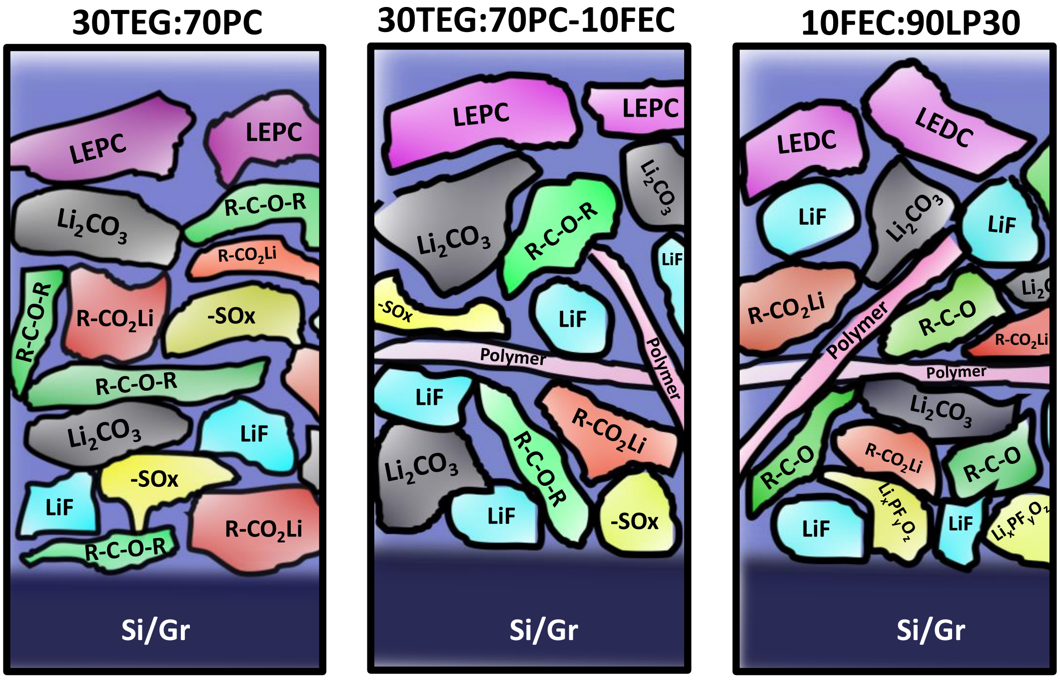

Figure 52: Proposed schematic figures of SEI composition of Si/Gr anodes after 80 cycles in 30TEG:70PC, 30TEG:70PC-10FEC, and 10FEC:90LP30, respectively. The polymer contains C-O, DO, and $-CO_2Li$ units.

The best electrochemical performances are achieved when using electrolyte formulations containing ≥20 vol.% FEC that are EC-free (i.e., 20FEC:80FEC and 50FEC:50DMC), see **Figure 50(a)**. Both formulations achieve around 86 % and 80 % of capacity retention after 80 and 100 cycles, respectively. For the 50FEC:50DMC formulation, 500 mAh g^{-1} of capacity is achieved after 100 cycles, which is 20 mAh g^{-1} more than with 20FEC:80DMC. The improved cycling stability can be attributed to an extended presence of FEC decomposition products in the SEI. In fact, the measured FEC decomposition marker DO is highest after 100 cycles for 20FEC:80FEC and 50FEC:50DMC, see **Figure 51**. The presence of higher amounts of DO species suggests that the SEI is formed largely from FEC degradation products, indicating that it retains its ability to adjust to volume changes even after extended cycling. **Figure 53** proposes schematic figures of the SEI composition formed in the FEC cosolvent and reference formulations. While the polymer containing C-O, DO, and $-CO_2Li$ units are visible in the SEI for FEC cosolvents, the FEC additive SEI is displaying much less of this species. At the same time, more carbonates such as Li_2CO_3 or LEDC are observed. Also, SiO_xF_y species are observed with the cosolvent but not with the additive formulations.

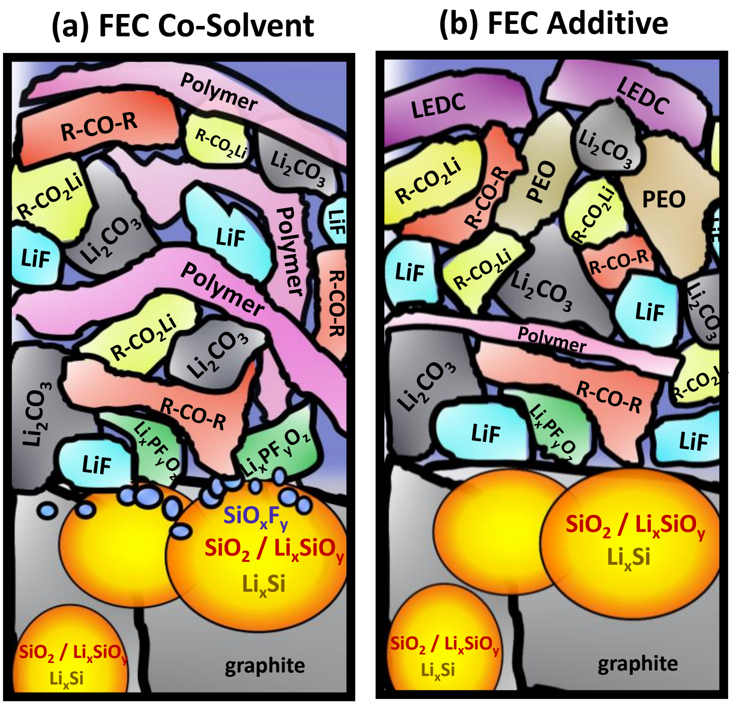

Figure 53: Proposed schematic figures of SEI composition of Si/Gr anodes after 100 cycles in (a) FEC cosolvents (20FEC:80DMC or 50FEC:50DMC) and (b) FEC additive (2FEC:98LP30). The polymer contains C-O, DO, and $-CO_2Li$ units.

Cells cycled in TEG perform much better than the EC-containing LP30 reference and similarly well to the FEC cosolvent formulations, see **Figure 50(a)**. After 100 cycles, the cell delivers 489 mAh g^{-1} of capacity with retention amounting to 76 %. In terms of absolute capacities, TEG is similar to 20FEC:80DMC after 100 cycles with 490 mAh g^{-1}. However, cells cycled in TEG display lower capacity retention after 100 cycles when compared to the retentions obtained with the 20FEC:80FEC and 50FEC:50DMC formulations. As a result, while the capacity is comparable between the three formulations, the rate at which the capacity decreases in future cycles may be faster for TEG. The reason for the improved cycling stability of Si/Gr anodes cycled in TEG could also be correlated to good film-forming properties. While TEG and TMG displayed similar SEI composition in terms of functional groups detected, the actual molecular structures of TEG and TMG decomposition products might be different for each solvent. Furthermore, SEM showed the formation of a smooth and interconnected surface layer when TEG is used as an electrolyte solvent. This suggests that TEG forms a layer or polymer, which can adapt more easily to the silicon volume changes. **Figure 54** suggests schematic figures for the SEI composition with TEG and TMG. TMG displays higher salt decomposition products such as -SO_x, LiF, and Li_3N, as well as Li_2CO_3. Furthermore, TMG might form more short-chained C-O-containing polymers, which are not able to adjust to the silicon volume changes. TEG decomposition shows much less salt decomposition and carbonates. It might also form longer chained C-O-containing polymers, which can better stabilize the SEI.

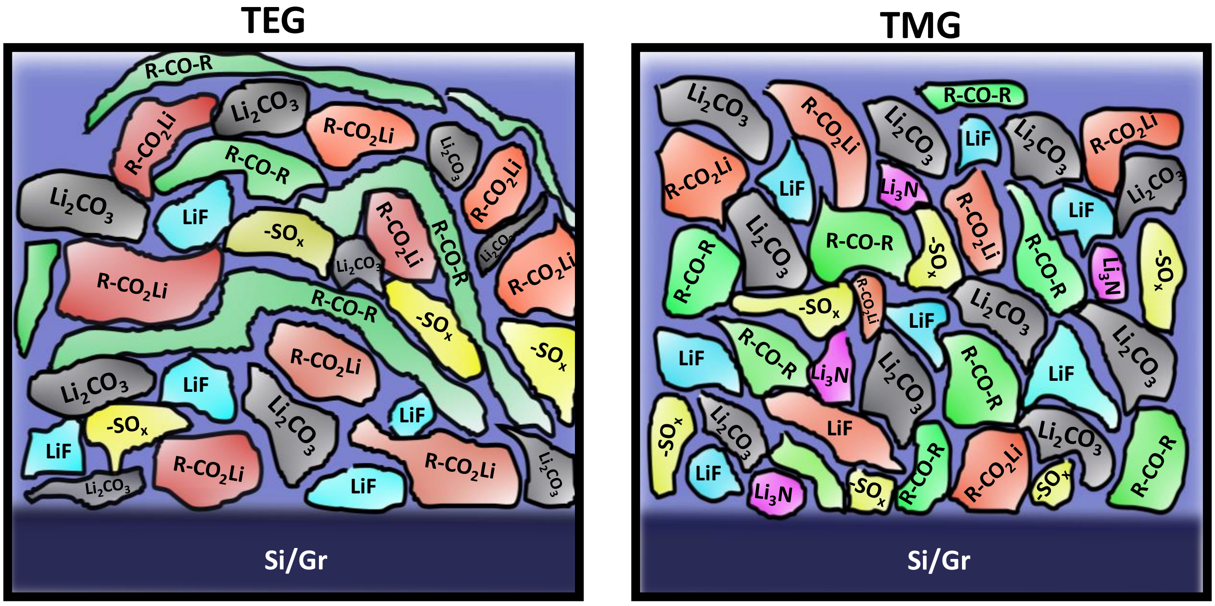

Figure 54: Proposed schematic figures of SEI composition of Si/Gr anodes after 100 cycles in (a) TEG and (b) TMG.

In summary, the results show that Si/Gr anodes perform best with electrolyte formulations containing ≥20 vol.% FEC. Also, TEG seems to be a promising electrolyte candidate for Si/Gr anodes. The improved cycling stability could be correlated in both cases to the formation of an SEI layer, which seems to better accommodate the silicon volume changes. Unlike TEG, where the molecular structure of decomposition products must be investigated further, the cycling stability of FEC is correlated to the presence of a polymer containing C-O, DO, and -CO_2Li species in the SEI.

8 Conclusion and Outlook

The purpose of this thesis was to identify alternative electrolyte solvents which improve the SEI's ability to adapt to volume changes in silicon, enhancing the performance of Si/Gr anodes. To evaluate this ability, SEI properties and electrochemical performance were correlated. XPS was used to characterize the SEI thickness and composition. Electrode morphology was analyzed via SEM. Three out of the six evaluated EC-free electrolytes showed improved cycling stability when compared to EC-containing formulations. In each case, this was associated with the formation of a favorable SEI layer.

The first two electrolytes with improved performance used FEC as a cosolvent instead of as an additive: 1 M $LiPF_6$ in 20FEC:80DMC or 50FEC:50DMC. When using each formulation, Si/Gr anodes showed an enhancement in cycling stability of around 36-39 % after 100 cycles compared to electrodes cycled in an EC-containing reference electrolyte (2FEC:98LP30). Contrary to the reference electrolyte, FEC cosolvent formulations showed the following SEI properties:

1) less electrolyte decomposition and a thinner SEI

2) high presence of FEC decomposition products (as indicated by DO species) in the SEI even after 100 cycles, while this species was present only in low amounts for 2FEC:98LP30

3) lower amount of carbonate species (such as Li_2CO_3)

4) formation of SiO_xF_y

The improved cycling stability of the 20FEC:80DMC and 50FEC:50DMC formulations were primarily attributed to the presence of a polymeric species containing -C-O, DO (1,3-dioxolan-2-one), and $-CO_2Li$ units, originating from FEC decomposition. Due to its distinct chemical environments, the detection of DO was unambiguously linked to the presence of FEC decomposition products in the SEI. After cycling Si/Gr electrodes in 20FEC:80DMC or 50FEC:50DMC, DO was still detected in high amounts in the SEI. After cycling in the reference electrolyte, only very small concentrations of DO were present. At the same time, very poor electrochemical performance was achieved. This indicated the presence of FEC decomposition products in the SEI to be a crucial factor for the good electrochemical performance of Si/Gr anodes. Most probably, the polymer increased the flexibility of the surface layer, which reduces the amount of new SEI formed and enables a longer cell lifetime. A major advantage of FEC cosolvents was that FEC decomposition products were still present in the SEI after a long time.

Additionally, much less electrolyte decomposition was observed when replacing EC with FEC. The results obtained in this thesis can be further utilized to develop an artificial SEI layer made of flexible polymers. A starting point for such a polymer could be poly(VC).

The third EC-free electrolyte with improved performance consisted of 1 M LiTFSI in TEG. Upon cycling in this formulation, Si/Gr anodes showed an improvement in capacity retention of 31 % after 100 cycles compared to the EC-containing reference LP30 electrolyte. This could be correlated to better film-forming properties of the TEG solvent, as it formed a smoother, and more interconnected SEI, which could better adapt to the volume changes of the silicon. Because of the high viscosities of TEG, a real-life implementation requires a formulation with improved lithium-ion transport properties. Therefore, PC was investigated as ionic conductivity increasing solvent. However, a decrease in electrochemical performance of Si/Gr anodes was observed for the 30TEG:70PC formulation. Further improvement of the electrolyte by the addition of FEC additive, did not meet the outstanding performance of pure TEG electrolytes. Both PC-based formulations showed high electrolyte decomposition with a large abundance of carbonate species in the SEI. This suggested the formation of a surface layer with poor ability to adjust to the silicon volume changes. The glyoxal electrolyte TMG showed the worst electrochemical performance of all electrolytes analyzed, which could be explained by poor film-forming properties on both the anode and the lithium-metal counter electrode. Overall, TEG is a very promising candidate as an alternative to well-established, carbonate-based electrolyte solvents. While this thesis suggested for TEG to form a more interconnected SEI that can better accommodate the silicon volume changes upon cycling, it is important to understand more about the structure of its decomposition products. Answers to the nature of those products would explain why TEG performs so well with Si/Gr anodes. Chemical reduction of TEG and subsequential NMR analysis may reveal the chemical structure of TEG reduction products. Time of flight secondary ion mass spectrometry (TOF-SIMS) could be used to determine whether TEG forms long-chained polymers. Online electrochemical mass spectrometry (OEMS) and high-performance liquid chromatography (HPLC) can be used as complementary techniques to analyze gaseous and liquid TEG decomposition products. Currently, TEG electrolytes cannot be used in full-cells due to the inability of the LiTFSI salt to passivate the aluminum current collector. Preliminary measurements have shown lithium difluoro(oxalato)borate (LDFOB) to be a good candidate as an aluminum passivating additive.

In conclusion, this thesis provided insights into the relationship between electrolyte formulation, SEI stability, and electrochemical performance, thus contributing to the development of future silicon-based anodes.

Bibliography

[1] Commission, E. 2030 climate & energy framework https://ec.europa.eu/clima/eu-action/climate-strategies-targets/2030-climate-energy-framework_de.

[2] Roland, Z. https://www.orovel.net/insights/li-on-battery-gigafactories-in-europe-january-2021.

[3] Qi, W.; Shapter, J. G.; Wu, Q.; Yin, T.; Gao, G.; Cui, D. Nanostructured Anode Materials for Lithium-Ion Batteries: Principle, Recent Progress and Future Perspectives. *J. Mater. Chem. A* **2017**, *5* (37), 19521–19540. https://doi.org/10.1039/c7ta05283a.

[4] Ma, D.; Cao, Z.; Hu, A. Si-Based Anode Materials for Li-Ion Batteries: A Mini Review. *Nano-Micro Lett.* **2014**, *6* (4), 347–358. https://doi.org/10.1007/s40820-014-0008-2.

[5] Obrovac, M. N.; Christensen, L.; Le, D. B.; Dahn, J. R. Alloy Design for Lithium-Ion Battery Anodes. *J. Electrochem. Soc.* **2007**, *154* (9), A849. https://doi.org/10.1149/1.2752985.

[6] Obrovac, M. N.; Chevrier, V. L. Alloy Negative Electrodes for Li-Ion Batteries. *Chem. Rev.* **2014**, *114* (23), 11444–11502. https://doi.org/10.1021/cr500207g.

[7] Huang, W.; Wang, J.; Braun, M. R.; Zhang, Z.; Li, Y.; Boyle, D. T.; McIntyre, P. C.; Cui, Y. Dynamic Structure and Chemistry of the Silicon Solid-Electrolyte Interphase Visualized by Cryogenic Electron Microscopy. *Matter* **2019**, *1* (5), 1232–1245. https://doi.org/10.1016/j.matt.2019.09.020.

[8] Iaboni, D. S. M.; Obrovac, M. N. Li 15 Si 4 Formation in Silicon Thin Film Negative Electrodes . *J. Electrochem. Soc.* **2016**, *163* (2), A255–A261. https://doi.org/10.1149/2.0551602jes.

[9] Wetjen, M.; Pritzl, D.; Jung, R.; Solchenbach, S.; Ghadimi, R.; Gasteiger, H. A. Differentiating the Degradation Phenomena in Silicon-Graphite Electrodes for Lithium-Ion Batteries. *J. Electrochem. Soc.* **2017**, *164* (12), A2840–A2852. https://doi.org/10.1149/2.1921712jes.

[10] Petibon, R.; Chevrier, V. L.; Aiken, C. P.; Hall, D. S.; Hyatt, S. R.; Shunmugasundaram, R.; Dahn, J. R. Studies of the Capacity Fade Mechanisms of LiCoO 2 /Si-Alloy: Graphite Cells . *J. Electrochem. Soc.* **2016**, *163* (7), A1146–A1156. https://doi.org/10.1149/2.0191607jes.

[11] Wetjen, M.; Trunk, M.; Werner, L.; Gernhäuser, R.; Märkisch, B.; Révay, Z.; Gilles, R.; Gasteiger, H. A. Quantifying the Distribution of Electrolyte Decomposition Products in Silicon-Graphite Electrodes by Neutron Depth Profiling. *J. Electrochem. Soc.* **2018**, *165* (10), A2340–A2348. https://doi.org/10.1149/2.1341810jes.

[12] Benning, S.; Chen, C.; Eichel, R. A.; Notten, P. H. L.; Hausen, F. Direct Observation of SEI Formation and Lithiation in Thin-Film Silicon Electrodes via in Situ Electrochemical Atomic Force Microscopy. *ACS Appl. Energy Mater.* **2019**, *2* (9), 6761–6767. https://doi.org/10.1021/acsaem.9b01222.

[13] Kumar, R.; Tokranov, A.; Sheldon, B. W.; Xiao, X.; Huang, Z.; Li, C.; Mueller, T. In Situ and Operando Investigations of Failure Mechanisms of the Solid Electrolyte Interphase on Silicon Electrodes. *ACS Energy Lett.* **2016**, *1* (4), 689–697. https://doi.org/10.1021/acsenergylett.6b00284.

[14] Tokranov, A.; Kumar, R.; Li, C.; Minne, S.; Xiao, X.; Sheldon, B. W. Control and Optimization of the Electrochemical and Mechanical Properties of the Solid Electrolyte Interphase on Silicon Electrodes in Lithium Ion Batteries. *Adv. Energy Mater.* **2016**, *6* (8), 1–12. https://doi.org/10.1002/aenm.201502302.

[15] Yang, J.; Solomatin, N.; Kraytsberg, A.; Ein-Eli, Y. In-Situ Spectro–Electrochemical Insight Revealing Distinctive Silicon Anode Solid Electrolyte Interphase Formation in a Lithium–Ion Battery. *ChemistrySelect* **2016**, *1* (3), 572–576. https://doi.org/10.1002/slct.201600119.

[16] Jeschull, F.; Surace, Y.; Zürcher, S.; Lari, G.; Spahr, M. E.; Novák, P.; Trabesinger, S. Graphite Particle-Size Induced Morphological and Performance Changes of Graphite–Silicon Electrodes. *J. Electrochem. Soc.* **2020**, *167* (10), 100535. https://doi.org/10.1149/1945-7111/ab9b9a.

[17] Jeschull, F.; Surace, Y.; Zürcher, S.; Spahr, M. E.; Novák, P.; Trabesinger, S. Electrochemistry and Morphology of Graphite Negative Electrodes Containing Silicon as Capacity-Enhancing Electrode Additive. *Electrochim. Acta* **2019**, *320*, 1–12. https://doi.org/10.1016/j.electacta.2019.134602.

[18] Schott, T.; Robert, R.; Ulmann, P. A.; Lanz, P.; Zürcher, S.; Spahr, M. E.; Novák, P.; Trabesinger, S. Cycling Behavior of Silicon-Containing Graphite Electrodes, Part A: Effect of the Lithiation Protocol. *J. Phys. Chem. C* **2017**, *121* (34), 18423–18429. https://doi.org/10.1021/acs.jpcc.7b05919.

[19] Schott, T.; Robert, R.; Pacheco Benito, S.; Ulmann, P. A.; Lanz, P.; Zürcher, S.; Spahr, M. E.; Novák, P.; Trabesinger, S. Cycling Behavior of Silicon-Containing Graphite Electrodes, Part B: Effect of the Silicon Source. *J. Phys. Chem. C* **2017**, *121* (46), 25718–25728. https://doi.org/10.1021/acs.jpcc.7b08457.

[20] Mazouzi, D.; Karkar, Z.; Hernandez, C. R.; Manero, P. J.; Guyomard, D.; Roué, L.; Lestriez, B. Critical Roles of Binders and Formulation at Multiscales of Silicon-Based Composite Electrodes. *J. Power Sources* **2015**, *280*, 533–549. https://doi.org/10.1016/j.jpowsour.2015.01.140.

[21] Karkar, Z.; Mazouzi, D.; Hernandez, C. R.; Guyomard, D.; Roué, L.; Lestriez, B. Threshold-like Dependence of Silicon-Based Electrode Performance on Active Mass Loading and Nature of Carbon Conductive Additive. *Electrochim. Acta* **2016**, *215*, 276–288. https://doi.org/10.1016/j.electacta.2016.08.118.

[22] Lestriez, B.; Desaever, S.; Danet, J.; Moreau, P.; Plée, D.; Guyomard, D. Hierarchical and Resilient Conductive Network of Bridged Carbon Nanotubes and Nanofibers for High-Energy Si Negative Electrodes. *Electrochem. Solid-State Lett.* **2009**, *12* (4). https://doi.org/10.1149/1.3074312.

[23] Jin, Y.; Kneusels, N. J. H.; Magusin, P. C. M. M.; Kim, G.; Castillo-Martínez, E.; Marbella, L. E.; Kerber, R. N.; Howe, D. J.; Paul, S.; Liu, T.; Grey, C. P. Identifying the Structural Basis for the Increased Stability of the Solid Electrolyte Interphase Formed on Silicon with the Additive Fluoroethylene Carbonate. *J. Am. Chem. Soc.* **2017**, *139* (42), 14992–15004. https://doi.org/10.1021/jacs.7b06834.

[24] Dunn, B.; Kamath, H.; Tarascon, J. M. Electrical Energy Storage for the Grid: A Battery of Choices. *Science (80-.).* **2011**, *334* (6058), 928–935. https://doi.org/10.1126/science.1212741.

[25] Xiao, J.; Li, Q.; Bi, Y.; Cai, M.; Dunn, B.; Glossmann, T.; Liu, J.; Osaka, T.; Sugiura, R.; Wu, B.; Yang, J.; Zhang, J. G.; Whittingham, M. S. Understanding and Applying Coulombic Efficiency in Lithium Metal Batteries. *Nat. Energy* **2020**, *5* (8), 561–568. https://doi.org/10.1038/s41560-020-0648-z.

[26] Uddin, K.; Perera, S.; Widanage, W. D.; Somerville, L.; Marco, J. Characterising Lithium-Ion Battery Degradation through the Identification and Tracking of Electrochemical Battery Model Parameters. *Batteries* **2016**, *2* (2). https://doi.org/10.3390/batteries2020013.

[27] Woody, M.; Arbabzadeh, M.; Lewis, G. M.; Keoleian, G. A.; Stefanopoulou, A. Strategies to Limit Degradation and Maximize Li-Ion Battery Service Lifetime - Critical Review and Guidance for Stakeholders. *J. Energy Storage* **2020**, *28* (January), 101231. https://doi.org/10.1016/j.est.2020.101231.

[28] Li, H. Practical Evaluation of Li-Ion Batteries. *Joule* **2019**, *3* (4), 911–914. https://doi.org/10.1016/j.joule.2019.03.028.

[29] Tarascon, J.-M.; Armand, M. Issues and Challenges Facing Rechargeable Lithium Batteries. *Nature* **2001**, *414* (November), 359–367.

[30] Janek, J.; Zeier, W. G. A Solid Future for Battery Development. *Nat. Energy* **2016**, *1* (9), 1–4. https://doi.org/10.1038/nenergy.2016.141.

[31] Ohzuku, T.; Ueda, A. Solid-State Redox Reactions of LiCoO2 (R3m) for 4 Volt Secondary Lithium Cells. *J. Electrochem. Soc.* **1994**, *141* (11), 2972–2977. https://doi.org/10.1149/1.2059267.

[32] *Chemical Energy Storage*; Schlögl, R., Ed.; De Gruyer, 2013. https://doi.org/10.1515/9783110266320.

[33] Thackeray, M. M.; de Picciotto, L. A.; de Kock, A.; Johnson, P. J.; Nicholas, V. A.; Adendorff, K. T. Spinel Electrodes for Lithium Batteries - A Review. *J. Power Sources* **1987**, *21* (1), 1–8. https://doi.org/10.1016/0378-7753(87)80071-X.

[34] Thackeray, M. M. Manganese Oxides for Lithium Batteries. *Prog. Solid State Chem.* **1997**, *25* (1–2), 1–71. https://doi.org/10.1016/S0079-6786(97)81003-5.

[35] Somo, T. R.; Mabokela, T. E.; Teffu, D. M.; Sekgobela, T. K.; Ramogayana, B.; Hato, M. J.; Modibane, K. D. A Comparative Review of Metal Oxide Surface Coatings on Three Families of Cathode Materials for Lithium Ion Batteries. **2021**, 1–22.

[36] Goriparti, S.; Miele, E.; Angelis, F. De; Di, E.; Proietti, R.; Capiglia, C. Review on Recent Progress of Nanostructured Anode Materials for Li-Ion Batteries. *J. Power Sources* **2014**, *257*, 421–443. https://doi.org/10.1016/j.jpowsour.2013.11.103.

[37] A. Manthiram; G.-A. Nazri; G. Pistoia. *Lithium Batteries: Science and Technology*; Springer US, 2003.

[38] Franklin, R. E. Crystallite Growth in Graphitizing and Non-Graphitizing Carbons. *Proc. R. Soc. London. Ser. A. Math. Phys. Sci.* **1951**, *209* (1097), 196–218. https://doi.org/10.1098/rspa.1951.0197.

[39] Damm, S.; Qizhong, Z. *Supply and Demand of Natural Graphite*; 2020.

[40] Nitta, N.; Wu, F.; Lee, J. T.; Yushin, G. Li-Ion Battery Materials: Present and Future. *Mater. Today* **2015**, *18* (5), 252–264. https://doi.org/10.1016/j.mattod.2014.10.040.

[41] Winter, M.; Besenhard, J. O.; Spahr, M. E.; Novák, P. Insertion Electrode Materials for Rechargeable Lithium Batteries. *Adv. Mater.* **1998**, *10* (10), 725–763.

[42] Asenbauer, J.; Eisenmann, T.; Kuenzel, M.; Kazzazi, A.; Chen, Z.; Bresser, D. The Success Story of Graphite as a Lithium-Ion Anode Material-Fundamentals, Remaining Challenges, and Recent Developments Including Silicon (Oxide) Composites. *Sustain. Energy Fuels* **2020**, *4* (11), 5387–5416. https://doi.org/10.1039/d0se00175a.

[43] Chung, D. D. L. Review: Graphite. *J. Mater. Sci.* **2002**, *37* (8), 1475–1489. https://doi.org/10.1023/A:1014915307738.

[44] Bernal, J. D. The Structure of Graphite. 7 49. *Proc. R. Soc. A* **1924**, *106*, 749–773.

[45] H. Lipson.; A. R. Stokes. A New Structure of Carbon. *Nature* **1942**, *149* (1), 328.

[46] Shi, H.; Barker, J.; Saïdi, M. Y.; Koksbang, R. Structure and Lithium Intercalation Properties of Synthetic and Natural Graphite. *J. Electrochem. Soc.* **1996**, *143* (11), 3466–3472. https://doi.org/10.1149/1.1837238.

[47] Rüdorff, W.; Hofmann, U. Über Graphitsalze. *Zeitschrift für Anorg. und Allg. Chemie* **1938**, *238* (1), 1–50. https://doi.org/10.1002/zaac.19382380102.

[48] Schlögl, R. Graphite - A Unique Host Lattice. In *Progress in Intercalation Research*; Müller-

Warmuth, W., Schöllhorn, R., Eds.; Springer-Science+Business Media, B.V., 1994; pp 83–176.

[49] Besenhard, J. O.; Fritz, H. P. Elektrochemie Schwarzer Kohlenstoffe. *Angew. Chemie* **2006**, *95* (12), 954–980. https://doi.org/10.1002/ange.19830951204.

[50] Heß, M.; Novák, P. Shrinking Annuli Mechanism and Stage-Dependent Rate Capability of Thin-Layer Graphite Electrodes for Lithium-Ion Batteries. *Electrochim. Acta* **2013**, *106*, 149–158. https://doi.org/10.1016/j.electacta.2013.05.056.

[51] Nitta, N.; Yushin, G. High-Capacity Anode Materials for Lithium-Ion Batteries: Choice of Elements and Structures for Active Particles. *Part. Part. Syst. Charact.* **2014**, *31* (3), 317–336. https://doi.org/10.1002/ppsc.201300231.

[52] Wen, C. J.; Huggins, R. A. Chemical Diffusion in Intermediate Phases in the Lithium-Silicon System. *J. Solid State Chem.* **1981**, *37* (3), 271–278. https://doi.org/10.1016/0022-4596(81)90487-4.

[53] Limthongkul, P.; Jang, Y. Il; Dudney, N. J.; Chiang, Y. M. Electrochemically-Driven Solid-State Amorphization in Lithium-Silicon Alloys and Implications for Lithium Storage. *Acta Mater.* **2003**, *51* (4), 1103–1113. https://doi.org/10.1016/S1359-6454(02)00514-1.

[54] Chon, M. J.; Sethuraman, V. A.; McCormick, A.; Srinivasan, V.; Guduru, P. R. Real-Time Measurement of Stress and Damage Evolution during Initial Lithiation of Crystalline Silicon. *Phys. Rev. Lett.* **2011**, *107* (4), 1–4. https://doi.org/10.1103/PhysRevLett.107.045503.

[55] Key, B.; Morcrette, M.; Tarascon, J. M.; Grey, C. P. Pair Distribution Function Analysis and Solid State NMR Studies of Silicon Electrodes for Lithium Ion Batteries: Understanding the (de)Lithiation Mechanisms. *J. Am. Chem. Soc.* **2011**, *133* (3), 503–512. https://doi.org/10.1021/ja108085d.

[56] McDowell, M. T.; Lee, S. W.; Nix, W. D.; Cui, Y. 25th Anniversary Article: Understanding the Lithiation of Silicon and Other Alloying Anodes for Lithium-Ion Batteries. *Adv. Mater.* **2013**, *25* (36), 4966–4985. https://doi.org/10.1002/adma.201301795.

[57] Liu, X. H.; Wang, J. W.; Huang, S.; Fan, F.; Huang, X.; Liu, Y.; Krylyuk, S.; Yoo, J.; Dayeh, S. A.; Davydov, A. V.; Mao, S. X.; Picraux, S. T.; Zhang, S.; Li, J.; Zhu, T.; Huang, J. Y. In Situ Atomic-Scale Imaging of Electrochemical Lithiation in Silicon. *Nat. Nanotechnol.* **2012**, *7* (11), 749–756. https://doi.org/10.1038/nnano.2012.170.

[58] Li, J.; Dahn, J. R. An In Situ X-Ray Diffraction Study of the Reaction of Li with Crystalline Si. *J. Electrochem. Soc.* **2007**, *154* (3), A156. https://doi.org/10.1149/1.2409862.

[59] Hatchard, T. D.; Dahn, J. R. In Situ XRD and Electrochemical Study of the Reaction of Lithium with Amorphous Silicon. *J. Electrochem. Soc.* **2004**, *151* (6), A838. https://doi.org/10.1149/1.1739217.

[60] Netz, A.; Huggins, R. A. Amorphous Silicon Formed in Situ as Negative Electrode Reactant in Lithium Cells. *Solid State Ionics* **2004**, *175* (1–4), 215–219. https://doi.org/10.1016/j.ssi.2003.11.048.

[61] Key, B.; Bhattacharyya, R.; Morcrette, M.; Seznéc, V.; Tarascon, J. M.; Grey, C. P. Real-Time NMR Investigations of Structural Changes in Silicon Electrodes for Lithium-Ion Batteries. *J. Am. Chem. Soc.* **2009**, *131* (26), 9239–9249. https://doi.org/10.1021/ja8086278.

[62] Chevrier, V. L.; Dahn, J. R. First Principles Model of Amorphous Silicon Lithiation. *J. Electrochem. Soc.* **2009**, *156* (6), A454. https://doi.org/10.1149/1.3111037.

[63] Christensen, J.; Newman, J. Stress Generation and Fracture in Lithium Insertion Materials. *J. Solid State Electrochem.* **2006**, *10* (5), 293–319. https://doi.org/10.1007/s10008-006-0095-1.

[64] Deshpande, R.; Cheng, Y. T.; Verbrugge, M. W. Modeling Diffusion-Induced Stress in Nanowire Electrode Structures. *J. Power Sources* **2010**, *195* (15), 5081–5088.

https://doi.org/10.1016/j.jpowsour.2010.02.021.

[65] Cheng, Y.-T.; Verbrugge, M. W. Diffusion-Induced Stress, Interfacial Charge Transfer, and Criteria for Avoiding Crack Initiation of Electrode Particles. *J. Electrochem. Soc.* **2010**, *157* (4), A508. https://doi.org/10.1149/1.3298892.

[66] Verbrugge, M. W.; Cheng, Y.-T. Stress and Strain-Energy Distributions within Diffusion-Controlled Insertion-Electrode Particles Subjected to Periodic Potential Excitations. *J. Electrochem. Soc.* **2009**, *156* (11), A927. https://doi.org/10.1149/1.3205485.

[67] Cheng, Y. T.; Verbrugge, M. W. The Influence of Surface Mechanics on Diffusion Induced Stresses within Spherical Nanoparticles. *J. Appl. Phys.* **2008**, *104* (8). https://doi.org/10.1063/1.3000442.

[68] Cheng, Y. T.; Verbrugge, M. W. Evolution of Stress within a Spherical Insertion Electrode Particle under Potentiostatic and Galvanostatic Operation. *J. Power Sources* **2009**, *190* (2), 453–460. https://doi.org/10.1016/j.jpowsour.2009.01.021.

[69] Liu, X. H.; Zhong, L.; Huang, S.; Mao, S. X.; Zhu, T.; Huang, J. Y. Size-Dependent Fracture of Silicon Nanoparticles during Lithiation. *ACS Nano* **2012**, *6* (2), 1522–1531. https://doi.org/10.1021/nn204476h.

[70] Deshpande, R.; Cheng, Y.-T.; Verbrugge, M. W.; Timmons, A. Diffusion Induced Stresses and Strain Energy in a Phase-Transforming Spherical Electrode Particle. *J. Electrochem. Soc.* **2011**, *158* (6), A718. https://doi.org/10.1149/1.3565183.

[71] Lee, S. W.; McDowell, M. T.; Berla, L. A.; Nix, W. D.; Cui, Y. Fracture of Crystalline Silicon Nanopillars during Electrochemical Lithium Insertion. *Proc. Natl. Acad. Sci. U. S. A.* **2012**, *109* (11), 4080–4085. https://doi.org/10.1073/pnas.1201088109.

[72] Kalnaus, S.; Rhodes, K.; Daniel, C. A Study of Lithium Ion Intercalation Induced Fracture of Silicon Particles Used as Anode Material in Li-Ion Battery. *J. Power Sources* **2011**, *196* (19), 8116–8124. https://doi.org/10.1016/j.jpowsour.2011.05.049.

[73] Rhodes, K.; Dudney, N.; Lara-Curzio, E.; Daniel, C. Understanding the Degradation of Silicon Electrodes for Lithium-Ion Batteries Using Acoustic Emission. *J. Electrochem. Soc.* **2010**, *157* (12), A1354. https://doi.org/10.1149/1.3489374.

[74] Sethuraman, V. A.; Srinivasan, V.; Bower, A. F.; Guduru, P. R. In Situ Measurements of Stress-Potential Coupling in Lithiated Silicon. *J. Electrochem. Soc.* **2010**, *157* (11), 1253–1261. https://doi.org/10.1149/1.3489378.

[75] McDowell, M. T.; Ryu, I.; Lee, S. W.; Wang, C.; Nix, W. D.; Cui, Y. Studying the Kinetics of Crystalline Silicon Nanoparticle Lithiation with in Situ Transmission Electron Microscopy. *Adv. Mater.* **2012**, *24* (45), 6034–6041. https://doi.org/10.1002/adma.201202744.

[76] Loveridge, M. J.; Malik, R.; Paul, S.; Manjunatha, K. N.; Gallanti, S.; Tan, C.; Lain, M.; Roberts, A. J.; Bhagat, R. Binder-Free Sn-Si Heterostructure Films for High Capacity Li-Ion Batteries. *RSC Adv.* **2018**, *8* (30), 16726–16737. https://doi.org/10.1039/c7ra13489d.

[77] Goodenough, J. B.; Kim, Y. Challenges for Rechargeable Li Batteries †. *Chem. Mater.* **2010**, *22* (3), 587–603. https://doi.org/10.1021/cm901452z.

[78] Xu, K. Nonaqueous Liquid Electrolytes for Lithium-Based Rechargeable Batteries. *Chem. Rev.* **2004**, *104* (10), 4303–4417. https://doi.org/10.1021/cr030203g.

[79] Aurbach, D.; Talyosef, Y.; Markovsky, B.; Markevich, E.; Zinigrad, E.; Asraf, L.; Gnanaraj, J. S.; Kim, H. J. Design of Electrolyte Solutions for Li and Li-Ion Batteries: A Review. *Electrochim. Acta* **2004**, *50* (2-3 SPEC. ISS.), 247–254. https://doi.org/10.1016/j.electacta.2004.01.090.

[80] Aravindan, V.; Gnanaraj, J.; Madhavi, S.; Liu, H. K. Lithium-Ion Conducting Electrolyte Salts

for Lithium Batteries. *Chem. - A Eur. J.* **2011**, *17* (51), 14326–14346. https://doi.org/10.1002/chem.201101486.

[81] Henderson, W. A. Nonaqueous Electrolytes: Advances in Lithium Salts. In *Electrolytes for Lithium and Lithium- Ion Batteries*; Jow, T. R., Xu, K., Borodin, O., Ue, M., Eds.; Springer Science+Business Media, 2014; pp 1–92. https://doi.org/10.1007/978-1-4939-0302-3.

[82] Ue, M.; Sasaki, Y.; Tanaka, Y.; Morita, M. Nonaqueous Electrolytes with Advances in Solvents. In *Electrolytes for Lithium and Lithium- Ion Batteries*; Jow, T. R., Xu, K., Borodin, O., Ue, M., Eds.; Springer Science+Business Media, 2014; pp 93–165. https://doi.org/10.1007/978-1-4939-0302-3.

[83] Hubbard, J.; Onsager, L. Dielectric Dispersion and Dielectric Friction in Electrolyte Solutions. I. *J. Chem. Phys.* **1977**, *67* (11), 4850–4857. https://doi.org/10.1063/1.434664.

[84] Hyung, Y. E.; Vissers, D. R.; Amine, K. Flame-Retardant Additives for Lithium-Ion Batteries. *J. Power Sources* **2003**, *119–121*, 383–387. https://doi.org/10.1016/S0378-7753(03)00225-8.

[85] Ciosek Högström, K.; Lundgren, H.; Wilken, S.; Zavalis, T. G.; Behm, M.; Edström, K.; Jacobsson, P.; Johansson, P.; Lindbergh, G. Impact of the Flame Retardant Additive Triphenyl Phosphate (TPP) on the Performance of Graphite/LiFePO4 Cells in High Power Applications Dedication: Professor per Jacobsson in Memoriam. *J. Power Sources* **2014**, *256*, 430–439. https://doi.org/10.1016/j.jpowsour.2014.01.022.

[86] von Aspern, N.; Leissing, M.; Wölke, C.; Diddens, D.; Kobayashi, T.; Börner, M.; Stubbmann-Kazakova, O.; Kozel, V.; Röschenthaler, G. V.; Smiatek, J.; Nowak, S.; Winter, M.; Cekic-Laskovic, I. Non-Flammable Fluorinated Phosphorus(III)-Based Electrolytes for Advanced Lithium-Ion Battery Performance. *ChemElectroChem* **2020**, *7* (6), 1499–1508. https://doi.org/10.1002/celc.202000386.

[87] Haregewoin, A. M.; Wotango, A. S.; Hwang, B. J. Electrolyte Additives for Lithium Ion Battery Electrodes: Progress and Perspectives. *Energy Environ. Sci.* **2016**, *9* (6), 1955–1988. https://doi.org/10.1039/c6ee00123h.

[88] Jankowski, P.; Lindahl, N.; Weidow, J.; Wieczorek, W.; Johansson, P. Impact of Sulfur-Containing Additives on Lithium-Ion Battery Performance: From Computational Predictions to Full-Cell Assessments. *ACS Appl. Energy Mater.* **2018**, *1* (6), 2582–2591. https://doi.org/10.1021/acsaem.8b00295.

[89] Zhao, H.; Yu, X.; Li, J.; Li, B.; Shao, H.; Li, L.; Deng, Y. Film-Forming Electrolyte Additives for Rechargeable Lithium-Ion Batteries: Progress and Outlook. *J. Mater. Chem. A* **2019**, *7* (15), 8700–8722. https://doi.org/10.1039/c9ta00126c.

[90] Eshetu, G. G.; Figgemeier, E. Confronting the Challenges of Next-Generation Silicon Anode-Based Lithium-Ion Batteries: Role of Designer Electrolyte Additives and Polymeric Binders. *ChemSusChem* **2019**, *12* (12), 2515–2539. https://doi.org/10.1002/cssc.201900209.

[91] Ma, X.; Young, R. S.; Ellis, L. D.; Ma, L.; Li, J.; Dahn, J. R. 1,2,6-Oxadithiane 2,2,6,6-Tetraoxide as an Advanced Electrolyte Additive for Li[Ni 0.5 Mn 0.3 Co 0.2]O 2 /Graphite Pouch Cells . *J. Electrochem. Soc.* **2019**, *166* (12), A2665–A2672. https://doi.org/10.1149/2.1401912jes.

[92] Xia, L.; Lee, S.; Jiang, Y.; Li, S.; Liu, Z.; Yu, L.; Hu, D.; Wang, S.; Liu, Y.; Chen, G. Z. Physicochemical and Electrochemical Properties of 1,1,2,2-Tetrafluoroethyl-2,2,3,3-Tetrafluoropropyl Ether as a Cosolvent for High-Voltage Lithium-Ion Electrolytes. *ChemElectroChem* **2019**, *6* (14), 3747–3755. https://doi.org/10.1002/celc.201900729.

[93] Liu, L.; Wang, S.; Zhang, Z.; Fan, J.; Qi, W.; Chen, S. Fluoroethylene Carbonate as an Electrolyte Additive for Improving Interfacial Stability of High-Voltage LiNi 0.6 Co 0.2 Mn 0.2 O 2 Cathode. *Ionics (Kiel).* **2019**, *25* (3), 1035–1043. https://doi.org/10.1007/s11581-018-2641-0.

[94] Klein, S.; Harte, P.; van Wickeren, S.; Borzutzki, K.; Röser, S.; Bärmann, P.; Nowak, S.; Winter, M.; Placke, T.; Kasnatscheew, J. Re-Evaluating Common Electrolyte Additives for High-Voltage Lithium Ion Batteries. *Cell Reports Phys. Sci.* **2021**, *2* (8). https://doi.org/10.1016/j.xcrp.2021.100521.

[95] Ma, L.; Ellis, L.; Glazier, S. L.; Ma, X.; Liu, Q.; Li, J.; Dahn, J. R. LiPO 2 F 2 as an Electrolyte Additive in Li[Ni 0.5 Mn 0.3 Co 0.2]O 2 /Graphite Pouch Cells . *J. Electrochem. Soc.* **2018**, *165* (5), A891–A899. https://doi.org/10.1149/2.0381805jes.

[96] Hong, S.; Hong, B.; Song, W.; Qin, Z.; Duan, B.; Lai, Y.; Jiang, F. Communication—Lithium Difluorophosphate as an Electrolyte Additive to Improve the High Voltage Performance of LiNi 0.5 Co 0.2 Mn 0.3 O 2 /Graphite Cell . *J. Electrochem. Soc.* **2018**, *165* (2), A368–A370. https://doi.org/10.1149/2.0991802jes.

[97] Wang, S.; Hu, H.; Yu, P.; Yang, H.; Cai, X.; Wang, X. Effect of Electrolyte Additives on High-Temperature Cycling Performance of Spinel LiMn2O4 Cathode. *J. Appl. Electrochem.* **2018**, *48* (11), 1221–1230. https://doi.org/10.1007/s10800-018-1244-9.

[98] Wu, Z.; Li, S.; Zheng, Y.; Zhang, Z.; Umesh, E.; Zheng, B.; Zheng, X.; Yang, Y. The Roles of Sulfur-Containing Additives and Their Working Mechanism on the Temperature-Dependent Performances of Li-Ion Batteries. *J. Electrochem. Soc.* **2018**, *165* (11), A2792–A2800. https://doi.org/10.1149/2.0331811jes.

[99] Heiskanen, S. K.; Kim, J.; Lucht, B. L. Generation and Evolution of the Solid Electrolyte Interphase of Lithium-Ion Batteries. *Joule* **2019**, *3* (10), 2322–2333. https://doi.org/10.1016/j.joule.2019.08.018.

[100] Peled, E. The Electrochemical Behavior of Alkali and Alkaline Earth Metals in Nonaqueous Battery Systems—The Solid Electrolyte Interphase Model. *J. Electrochem. Soc.* **1979**, *126* (12), 2047–2051. https://doi.org/10.1149/1.2128859.

[101] Peled, E.; Menkin, S. Review—SEI: Past, Present and Future. *J. Electrochem. Soc.* **2017**, *164* (7), A1703–A1719. https://doi.org/10.1149/2.1441707jes.

[102] Peljo, P.; Girault, H. H. Electrochemical Potential Window of Battery Electrolytes: The HOMO-LUMO Misconception. *Energy Environ. Sci.* **2018**, *11* (9), 2306–2309. https://doi.org/10.1039/c8ee01286e.

[103] Horstmann, B.; Single, F.; Latz, A. Review on Multi-Scale Models of Solid-Electrolyte Interphase Formation. *Curr. Opin. Electrochem.* **2019**, *13*, 61–69. https://doi.org/10.1016/j.coelec.2018.10.013.

[104] Verma, P.; Maire, P.; Novák, P. A Review of the Features and Analyses of the Solid Electrolyte Interphase in Li-Ion Batteries. *Electrochim. Acta* **2010**, *55* (22), 6332–6341. https://doi.org/10.1016/j.electacta.2010.05.072.

[105] Kitz, P. G.; Novák, P.; Berg, E. J. Influence of Water Contamination on the SEI Formation in Li-Ion Cells: An Operando EQCM-D Study. *ACS Appl. Mater. Interfaces* **2020**, *12* (13), 15934–15942. https://doi.org/10.1021/acsami.0c01642.

[106] Herstedt, M.; Abraham, D. P.; Kerr, J. B.; Edström, K. X-Ray Photoelectron Spectroscopy of Negative Electrodes from High-Power Lithium-Ion Cells Showing Various Levels of Power Fade. *Electrochim. Acta* **2004**, *49* (28), 5097–5110. https://doi.org/10.1016/j.electacta.2004.06.021.

[107] Parimalam, B. S.; MacIntosh, A. D.; Kadam, R.; Lucht, B. L. Decomposition Reactions of Anode Solid Electrolyte Interphase (SEI) Components with LiPF6. *J. Phys. Chem. C* **2017**, *121* (41), 22733–22738. https://doi.org/10.1021/acs.jpcc.7b08433.

[108] Cresce, A. V.; Russell, S. M.; Baker, D. R.; Gaskell, K. J.; Xu, K. In Situ and Quantitative Characterization of Solid Electrolyte Interphases. *Nano Lett.* **2014**, *14* (3), 1405–1412.

https://doi.org/10.1021/nl404471v.

[109] Peled, E.; Golodnitsky, D.; Ulus, A.; Yufit, V. Effect of Carbon Substrate on SEI Composition and Morphology. *Electrochim. Acta* **2004**, *50* (2-3 SPEC. ISS.), 391–395. https://doi.org/10.1016/j.electacta.2004.01.130.

[110] Chung, G.-C.; Kim, H.-J.; Yu, S.-I.; Jun, S.-H.; Choi, J.; Kim, M.-H. Origin of Graphite Exfoliation An Investigation of the Important Role of Solvent Cointercalation. *J. Electrochem. Soc.* **2000**, *147* (12), 4391. https://doi.org/10.1149/1.1394076.

[111] Tsubouchi, S.; Domi, Y.; Doi, T.; Ochida, M.; Nakagawa, H.; Yamanaka, T.; Abe, T.; Ogumi, Z. Spectroscopic Characterization of Surface Films Formed on Edge Plane Graphite in Ethylene Carbonate-Based Electrolytes Containing Film-Forming Additives. *J. Electrochem. Soc.* **2012**, *159* (11), A1786–A1790. https://doi.org/10.1149/2.028211jes.

[112] Aurbach, D.; Markovsky, B.; Weissman, I.; Levi, E.; Ein-Eli, Y. On the Correlation between Surface Chemistry and Performance of Graphite Negative Electrodes for Li Ion Batteries. *Electrochim. Acta* **1999**, *45* (1), 67–86. https://doi.org/10.1016/S0013-4686(99)00194-2.

[113] Xu, K. Whether EC and PC Differ in Interphasial Chemistry on Graphitic Anode and How. *J. Electrochem. Soc.* **2009**, *156* (9), A751. https://doi.org/10.1149/1.3166182.

[114] Aurbach, D.; Gofer, Y.; Langzam, J. The Correlation Between Surface Chemistry, Surface Morphology, and Cycling Efficiency of Lithium Electrodes in a Few Polar Aprotic Systems. *J. Electrochem. Soc.* **1989**, *136* (11), 3198–3205. https://doi.org/10.1149/1.2096425.

[115] Leroy, S.; Martinez, H.; Dedryvère, R.; Lemordant, D.; Gonbeau, D. Influence of the Lithium Salt Nature over the Surface Film Formation on a Graphite Electrode in Li-Ion Batteries: An XPS Study. *Appl. Surf. Sci.* **2007**, *253* (11), 4895–4905. https://doi.org/10.1016/j.apsusc.2006.10.071.

[116] Leroy, S.; Blanchard, F.; Dedryvère, R.; Dedryvère, D.; Martinez, H.; Carré, B.; Carré, C.; Lemordant, D.; Gonbeau, D. Surface Film Formation on a Graphite Electrode in Li-Ion Batteries: AFM and XPS Study. *Surf. INTERFACE Anal. Surf. Interface Anal* **2005**, *37*, 773–781. https://doi.org/10.1002/sia.2072.

[117] Xu, C.; Sun, B.; Gustafsson, T.; Edström, K.; Brandell, D.; Hahlin, M. Interface Layer Formation in Solid Polymer Electrolyte Lithium Batteries: An XPS Study. *J. Mater. Chem. A* **2014**, *2* (20), 7256–7264. https://doi.org/10.1039/c4ta00214h.

[118] An, S. J.; Li, J.; Daniel, C.; Mohanty, D.; Nagpure, S.; Wood, D. L. The State of Understanding of the Lithium-Ion-Battery Graphite Solid Electrolyte Interphase (SEI) and Its Relationship to Formation Cycling. *Carbon N. Y.* **2016**, *105*, 52–76. https://doi.org/10.1016/j.carbon.2016.04.008.

[119] Moulder, J. F.; Stickle, W. F.; Sobol, P. E.; Bomben, K. D. *Handbook of X-Ray Photoelectron Spectroscopy*; Perkin-Elmer Corporation, 1992.

[120] Matthew R. Linford. Understanding One of the Governing Equiations of XPS and Highlights from a Recent Paper by Akagawa and Fujiwara. *Vac. Coat. Technol.* **2014**, No. March, 1–7.

[121] Scientific, T. F. Angle Resolved XPS. *Appl. Nore 31014* **2008**.

[122] Ratner, B. D.; Castner, D. C. Electron Spectroscopy for Chemical Analysis. In *Surface Analysis - The Principle Techniques*; Vickerman, J. C., Gilmore, I. S., Eds.; 9 John Wiley & Sons, Ltd, 2009; pp 47–112.

[123] Smith, G. C. *Surface Analysis by Electron Spectroscopy*; Springer Science+Businnes Media, LLC: New York, 1994. https://doi.org/10.1007/978-1-4899-0967-1.

[124] Boukamp, B. A.; Lesh, G. C.; Huggins, R. A.; Soc, J. E. All − Solid Lithium Electrodes with Mixed − Conductor Matrix Tetra Acknowledgment All-Solid Lithium Electrodes with Mixed-

Conductor Matrix. *J. Electrochem. Soc.* **1981**, *128* (4), 725–729.

[125] Chan, C. K.; Peng, H.; Liu, G.; McIlwrath, K.; Zhang, X. F.; Huggins, R. A.; Cui, Y. High-Performance Lithium Battery Anodes Using Silicon Nanowires. *Nat. Nanotechnol.* **2008**, *3* (1), 31–35. https://doi.org/10.1038/nnano.2007.411.

[126] Chae, S.; Ko, M.; Kim, K.; Ahn, K.; Cho, J. Confronting Issues of the Practical Implementation of Si Anode in High-Energy Lithium-Ion Batteries. *Joule* **2017**, *1* (1), 47–60. https://doi.org/10.1016/j.joule.2017.07.006.

[127] Son, I. H.; Park, J. H.; Kwon, S.; Park, S.; Rümmeli, M. H.; Bachmatiuk, A.; Song, H. J.; Ku, J.; Choi, J. W.; Choi, J. M.; Doo, S. G.; Chang, H. Silicon Carbide-Free Graphene Growth on Silicon for Lithium-Ion Battery with High Volumetric Energy Density. *Nat. Commun.* **2015**, *6* (May), 1–8. https://doi.org/10.1038/ncomms8393.

[128] Hwang, T. H.; Lee, Y. M.; Kong, B. S.; Seo, J. S.; Choi, J. W. Electrospun Core-Shell Fibers for Robust Silicon Nanoparticle-Based Lithium Ion Battery Anodes. *Nano Lett.* **2012**, *12* (2), 802–807. https://doi.org/10.1021/nl203817r.

[129] Huang, S.; Ren, J.; Liu, R.; Yue, M.; Huang, Y.; Yuan, G. The Progress of Novel Binder as a Non-Ignorable Part to Improve the Performance of Si-Based Anodes for Li-Ion Batteries. *Int. J. Energy Res.* **2018**, *42* (3), 919–935. https://doi.org/10.1002/er.3826.

[130] Aurbach, D.; Markovsky, B.; Shechter, A.; Ein-Eli, Y.; Cohen, H. A Comparative Study of Synthetic Graphite and Li Electrodes in Electrolyte Solutions Based on Ethylene Carbonate-Dimethyl Carbonate Mixtures. *J. Electrochem. Soc.* **1996**, *143* (12), 3809–3820. https://doi.org/10.1149/1.1837300.

[131] Jaumann, T.; Balach, J.; Langklotz, U.; Sauchuk, V.; Fritsch, M.; Michaelis, A.; Teltevskij, V.; Mikhailova, D.; Oswald, S.; Klose, M.; Stephani, G.; Hauser, R.; Eckert, J.; Giebeler, L. Lifetime vs. Rate Capability: Understanding the Role of FEC and VC in High-Energy Li-Ion Batteries with Nano-Silicon Anodes. *Energy Storage Mater.* **2017**, *6* (September 2016), 26–35. https://doi.org/10.1016/j.ensm.2016.08.002.

[132] Pan, J.; Zhang, Q.; Xiao, X.; Cheng, Y.-T.; Qi, Y. Design of Nanostructured Heterogeneous Solid Ionic Coatings through a Multiscale Defect Model. **2016**. https://doi.org/10.1021/acsami.5b12030.

[133] Choi, J. W.; Aurbach, D. Promise and Reality of Post-Lithium-Ion Batteries with High Energy Densities. *Nat. Rev. Mater.* **2016**, *1*. https://doi.org/10.1038/natrevmats.2016.13.

[134] Michan, A. L.; Parimalam, B. S.; Leskes, M.; Kerber, R. N.; Yoon, T.; Grey, C. P.; Lucht, B. L. Fluoroethylene Carbonate and Vinylene Carbonate Reduction: Understanding Lithium-Ion Battery Electrolyte Additives and Solid Electrolyte Interphase Formation. *Chem. Mater.* **2016**, *28* (22), 8149–8159. https://doi.org/10.1021/acs.chemmater.6b02282.

[135] Rezqita, A.; Sauer, M.; Foelske, A.; Kronberger, H.; Trifonova, A. The Effect of Electrolyte Additives on Electrochemical Performance of Silicon/Mesoporous Carbon (Si/MC) for Anode Materials for Lithium-Ion Batteries. *Electrochim. Acta* **2017**, *247*, 600–609. https://doi.org/10.1016/j.electacta.2017.06.128.

[136] Jaumann, T.; Balach, J.; Langklotz, U.; Sauchuk, V.; Fritsch, M.; Michaelis, A.; Teltevskij, V.; Mikhailova, D.; Oswald, S.; Klose, M.; Stephani, G.; Hauser, R.; Eckert, J.; Giebeler, L. Lifetime vs. Rate Capability: Understanding the Role of FEC and VC in High-Energy Li-Ion Batteries with Nano-Silicon Anodes. *Energy Storage Mater.* **2017**, *6*, 26–35. https://doi.org/10.1016/j.ensm.2016.08.002.

[137] Jin, Y.; Kneusels, N. J. H.; Marbella, L. E.; Castillo-Martínez, E.; Magusin, P. C. M. M.; Weatherup, R. S.; Jónsson, E.; Liu, T.; Paul, S.; Grey, C. P. Understanding Fluoroethylene Carbonate and Vinylene Carbonate Based Electrolytes for Si Anodes in Lithium Ion Batteries with NMR Spectroscopy. *J. Am. Chem. Soc.* **2018**, *140* (31), 9854–9867.

https://doi.org/10.1021/jacs.8b03408.

[138] Xu, C.; Lindgren, F.; Philippe, B.; Gorgoi, M.; Björefors, F.; Edström, K.; Gustafsson, T. Improved Performance of the Silicon Anode for Li-Ion Batteries: Understanding the Surface Modification Mechanism of Fluoroethylene Carbonate as an Effective Electrolyte Additive. *Chem. Mater.* **2015**, *27* (7), 2591–2599. https://doi.org/10.1021/acs.chemmater.5b00339.

[139] Michan, A. L.; Divitini, G.; Pell, A. J.; Leskes, M.; Ducati, C.; Grey, C. P. Solid Electrolyte Interphase Growth and Capacity Loss in Silicon Electrodes. *J. Am. Chem. Soc.* **2016**, *138* (25), 7918–7931. https://doi.org/10.1021/jacs.6b02882.

[140] Jung, R.; Metzger, M.; Haering, D.; Solchenbach, S.; Marino, C.; Tsiouvaras, N.; Stinner, C.; Gasteiger, H. A. Consumption of Fluoroethylene Carbonate (FEC) on Si-C Composite Electrodes for Li-Ion Batteries. *J. Electrochem. Soc.* **2016**, *163* (8), A1705–A1716. https://doi.org/10.1149/2.0951608jes.

[141] Lin, Y. M.; Klavetter, K. C.; Abel, P. R.; Davy, N. C.; Snider, J. L.; Heller, A.; Mullins, C. B. High Performance Silicon Nanoparticle Anode in Fluoroethylene Carbonate-Based Electrolyte for Li-Ion Batteries. *Chem. Commun.* **2012**, *48* (58), 7268–7270. https://doi.org/10.1039/c2cc31712e.

[142] Etacheri, V.; Haik, O.; Goffer, Y.; Roberts, G. A.; Stefan, I. C.; Fasching, R.; Aurbach, D. Effect of Fluoroethylene Carbonate (FEC) on the Performance and Surface Chemistry of Si-Nanowire Li-Ion Battery Anodes. *Langmuir* **2012**, *28* (1), 965–976. https://doi.org/10.1021/la203712s.

[143] Schiele, A.; Breitung, B.; Hatsukade, T.; Berkes, B. B.; Hartmann, P.; Janek, J.; Brezesinski, T. The Critical Role of Fluoroethylene Carbonate in the Gassing of Silicon Anodes for Lithium-Ion Batteries. *ACS Energy Lett.* **2017**, *2* (10), 2228–2233. https://doi.org/10.1021/acsenergylett.7b00619.

[144] Breitung, B.; Schneider, A.; Chakravadhanula, V. S. K.; Suchomski, C.; Janek, J.; Sommer, H.; Brezesinski, T. Artificial Composite Anode Comprising High-Capacity Silicon and Carbonaceous Nanostructures for Long Cycle Life Lithium-Ion Batteries. *Batter. Supercaps* **2018**, *1* (1), 27–32. https://doi.org/10.1002/batt.201700004.

[145] Jaumann, T.; Balach, J.; Klose, M.; Oswald, S.; Eckert, J.; Giebeler, L. Role of 1,3-Dioxolane and LiNO3 Addition on the Long Term Stability of Nanostructured Silicon/Carbon Anodes for Rechargeable Lithium Batteries. *J. Electrochem. Soc.* **2016**, *163* (3), A557–A564. https://doi.org/10.1149/2.1011603jes.

[146] Chen, J.; Fan, X.; Li, Q.; Yang, H.; Khoshi, M. R.; Xu, Y.; Hwang, S.; Chen, L.; Ji, X.; Yang, C.; He, H.; Wang, C.; Garfunkel, E.; Su, D.; Borodin, O.; Wang, C. Electrolyte Design for LiF-Rich Solid–Electrolyte Interfaces to Enable High-Performance Microsized Alloy Anodes for Batteries. *Nat. Energy* **2020**, *5* (5), 386–397. https://doi.org/10.1038/s41560-020-0601-1.

[147] Pohl, B.; Grünebaum, M.; Drews, M.; Passerini, S.; Winter, M.; Wiemhöfer, H. D. Nitrile Functionalized Silyl Ether with Dissolved LiTFSI as New Electrolyte Solvent for Lithium-Ion Batteries. *Electrochim. Acta* **2015**. https://doi.org/10.1016/j.electacta.2015.09.001.

[148] Horowitz, Y.; Ben-Barak, I.; Schneier, D.; Goor-Dar, M.; Kasnatscheew, J.; Meister, P.; Grünebaum, M.; Wiemhöfer, H.; Winter, M.; Golodnitsky, D.; Peled, E. Study of the Formation of a Solid Electrolyte Interphase (SEI) on a Silicon Nanowire Anode in Liquid Disiloxane Electrolyte with Nitrile End Groups for Lithium-Ion Batteries. *Batter. Supercaps* **2019**, *2* (3), 213–222. https://doi.org/10.1002/batt.201800123.

[149] Pohl, B.; Hiller, M. M.; Seidel, S. M.; Grünebaum, M.; Wiemhöfer, H. D. Nitrile Functionalized Disiloxanes with Dissolved LiTFSI as Lithium Ion Electrolytes with High Thermal and Electrochemical Stability. *J. Power Sources* **2015**, *274*, 629–635. https://doi.org/10.1016/j.jpowsour.2014.10.080.

[150] Heß, L. H.; Balducci, A. Glyoxal-Based Solvents for Electrochemical Energy-Storage Devices. *ChemSusChem* **2018**, *11* (12), 1919–1926. https://doi.org/10.1002/cssc.201800375.

[151] Hess, L. H.; Wankmüller, S.; Köps, L.; Bothe, A.; Balducci, A. Stable Acetals of Glyoxal as Electrolyte Solvents for Lithium-Ion Batteries. *Batter. Supercaps* **2019**, *2* (10), 852–857. https://doi.org/10.1002/batt.201900051.

[152] Leibing, C.; Balducci, A. Glyoxylic-Acetal-Based Electrolytes in Combination with Soft and Hard Carbon Electrodes for Lithium-Ion Batteries: An Evaluation of Room and High Temperature Performance. *J. Electrochem. Soc.* **2021**, *168* (9), 090533. https://doi.org/10.1149/1945-7111/ac23a2.

[153] Köps, L.; Leibing, C.; Hess, L. H.; Balducci, A. Mixtures of Glyoxylic Acetals and Organic Carbonates as Electrolytes for Lithium-Ion Batteries. *J. Electrochem. Soc.* **2021**, *168* (1), 010513. https://doi.org/10.1149/1945-7111/abd604.

[154] Atik, J.; Röser, S.; Wagner, R.; Berghus, D.; Winter, M.; Cekic-Laskovic, I. Acyclic Acetals in Propylene Carbonate-Based Electrolytes for Advanced and Safer Graphite-Based Lithium Ion Batteries. *J. Electrochem. Soc.* **2020**, *167* (4), 040509. https://doi.org/10.1149/1945-7111/ab72dc.

[155] Aurbach, D.; Koltypin, M.; Teller, H. In Situ AFM Imaging of Surface Phenomena on Composite Graphite Electrodes during Lithium Insertion. *Langmuir* **2002**, *18* (23), 9000–9009. https://doi.org/10.1021/la020306e.

[156] Song, H.-Y.; Fukutsuka, T.; Miyazaki, K.; Abe, T. Suppression of Co-Intercalation Reaction of Propylene Carbonate and Lithium Ion into Graphite Negative Electrode by Addition of Diglyme. *J. Electrochem. Soc.* **2016**, *163* (7), A1265–A1269. https://doi.org/10.1149/2.0831607jes.

[157] Hofmann, A.; Migeot, M.; Thißen, E.; Schulz, M.; Heinzmann, R.; Indris, S.; Bergfeldt, T.; Lei, B.; Ziebert, C.; Hanemann, T. Electrolyte Mixtures Based on Ethylene Carbonate and Dimethyl Sulfone for Li-Ion Batteries with Improved Safety Characteristics. *ChemSusChem* **2015**, *8* (11), 1892–1900. https://doi.org/10.1002/cssc.201500263.

[158] Verma, P.; Maire, P.; Novák, P. A Review of the Features and Analyses of the Solid Electrolyte Interphase in Li-Ion Batteries. *Electrochim. Acta* **2010**, *55* (22), 6332–6341. https://doi.org/10.1016/j.electacta.2010.05.072.

[159] Aurbach, D.; Daroux, M. L.; Faguy, P. W.; Yeager, E. Identification of Surface Films Formed on Lithium in Propylene Carbonate Solutions. *J. Electrochem. Soc.* **1987**, *134* (7), 1611–1620. https://doi.org/10.1149/1.2100722.

[160] Aurbach, D.; Gofer, Y.; Ben-Zion, M.; Aped, P. The Behaviour of Lithium Electrodes in Propylene and Ethylene Carbonate: Te Major Factors That Influence Li Cycling Efficiency. *J. Electroanal. Chem.* **1992**, *339* (1–2), 451–471. https://doi.org/10.1016/0022-0728(92)80467-I.

[161] Edström, K.; Herstedt, M.; Abraham, D. P. A New Look at the Solid Electrolyte Interphase on Graphite Anodes in Li-Ion Batteries. *J. Power Sources* **2006**, *153* (2), 380–384. https://doi.org/https://doi.org/10.1016/j.jpowsour.2005.05.062.

[162] Aurbach, D.; Weissman, I.; Schechter, A.; Cohen, H. X-Ray Photoelectron Spectroscopy Studies of Lithium Surfaces Prepared in Several Important Electrolyte Solutions. A Comparison with Previous Studies by Fourier Transform Infrared Spectroscopy. *Langmuir* **1996**, *12* (16), 3991–4007. https://doi.org/10.1021/la9600762.

[163] Dedryvère, R.; Laruelle, S.; Grugeon, S.; Gireaud, L.; Tarascon, J. M.; Gonbeau, D. XPS Identification of the Organic and Inorganic Components of the Electrode/Electrolyte Interface Formed on a Metallic Cathode. *J. Electrochem. Soc.* **2005**, *152* (4). https://doi.org/10.1149/1.1861994.

[164] Peled, E.; Bar Tow, D.; Merson, A.; Gladkich, A.; Burstein, L.; Golodnitsky, D. Composition, Depth Profiles and Lateral Distribution of Materials in the SEI Built on HOPG-TOF SIMS and XPS Studies. In *Journal of Power Sources*; 2001. https://doi.org/10.1016/S0378-7753(01)00505-5.

[165] Ota, H.; Akai, T.; Namita, H.; Yamaguchi, S.; Nomura, M. XAFS and TOF-SIMS Analysis of SEI Layers on Electrodes. *J. Power Sources* **2003**, *119–121*, 567–571. https://doi.org/10.1016/S0378-7753(03)00291-X.

[166] Veryovkin, I. V.; Tripa, C. E.; Zinovev, A. V.; Baryshev, S. V.; Li, Y.; Abraham, D. P. TOF SIMS Characterization of SEI Layer on Battery Electrodes. *Nucl. Instruments Methods Phys. Res. Sect. B Beam Interact. with Mater. Atoms* **2014**, *332*, 368–372. https://doi.org/10.1016/j.nimb.2014.02.098.

[167] Chan, C. K.; Ruffo, R.; Hong, S. S.; Cui, Y. Surface Chemistry and Morphology of the Solid Electrolyte Interphase on Silicon Nanowire Lithium-Ion Battery Anodes. *J. Power Sources* **2009**, *189* (2), 1132–1140. https://doi.org/10.1016/j.jpowsour.2009.01.007.

[168] Unocic, R. R.; Sun, X. G.; Sacci, R. L.; Adamczyk, L. A.; Alsem, D. H.; Dai, S.; Dudney, N. J.; More, K. L. Direct Visualization of Solid Electrolyte Interphase Formation in Lithium-Ion Batteries with in Situ Electrochemical Transmission Electron Microscopy. *Microsc. Microanal.* **2014**, *20* (4), 1029–1037. https://doi.org/10.1017/S1431927614012744.

[169] Yao, W.; Shahbazian-Yassar, R. Application of In Situ Electrochemical-Cell Transmission Electron Microscopy for the Study of Rechargeable Batteries. *Encycl. Inorg. Bioinorg. Chem.* **2019**, 1–10. https://doi.org/10.1002/9781119951438.eibc2684.

[170] Zhuang, G. V.; Yang, H.; Blizanac, B.; Ross, P. N. A Study of Electrochemical Reduction of Ethylene and Propylene Carbonate Electrolytes on Graphite Using ATR-FTIR Spectroscopy. *Electrochem. Solid-State Lett.* **2005**, *8* (9). https://doi.org/10.1149/1.1979327.

[171] Piernas-Muñoz, M. J.; Tornheim, A.; Trask, S.; Zhang, Z.; Bloom, I. Surface-Enhanced Raman Spectroscopy (SERS): A Powerful Technique to Study the SEI Layer in Batteries. *Chem. Commun.* **2021**, *57* (18), 2253–2256. https://doi.org/10.1039/d0cc08001b.

[172] Nanda, J.; Yang, G.; Hou, T.; Voylov, D. N.; Li, X.; Ruther, R. E.; Naguib, M.; Persson, K.; Veith, G. M.; Sokolov, A. P. Unraveling the Nanoscale Heterogeneity of Solid Electrolyte Interphase Using Tip-Enhanced Raman Spectroscopy. *Joule* **2019**, *3* (8), 2001–2019. https://doi.org/10.1016/j.joule.2019.05.026.

[173] Schranzhofer, H.; Bugajski, J.; Santner, H. J.; Korepp, C.; Möller, K. C.; Besenhard, J. O.; Winter, M.; Sitte, W. Electrochemical Impedance Spectroscopy Study of the SEI Formation on Graphite and Metal Electrodes. *J. Power Sources* **2006**, *153* (2), 391–395. https://doi.org/10.1016/j.jpowsour.2005.05.034.

[174] Dedryvère, R.; Gireaud, L.; Grugeon, S.; Laruelle, S.; Tarascon, J. M.; Gonbeau, D. Characterization of Lithium Alkyl Carbonates by X-Ray Photoelectron Spectroscopy: Experimental and Theoretical Study. *J. Phys. Chem. B* **2005**, *109* (33), 15868–15875. https://doi.org/10.1021/jp051626k.

[175] Pavlin, N.; Hribernik, S.; Kapun, G.; Talian, S. D.; Njel, C.; Dedryvère, R.; Dominko, R. The Role of Cellulose Based Separator in Lithium Sulfur Batteries. *J. Electrochem. Soc.* **2019**, *166* (3), A5237–A5243. https://doi.org/10.1149/2.0401903jes.

[176] G. Beamson, D. B. *High Resolution XPS of Organic Polymers: The Scienta ESCA300 Database*; John Wiley & Son Ltd.: West Sussex, England, 1992.

[177] Powell, C. J. Recommended Auger Parameters for 42 Elemental Solids. *J. Electron Spectros. Relat. Phenomena* **2012**, *185* (1–2), 1–3. https://doi.org/10.1016/j.elspec.2011.12.001.

[178] Ciosek Högström, K.; Malmgren, S.; Hahlin, M.; Gorgoi, M.; Nyholm, L.; Rensmo, H.;

Edström, K. The Buried Carbon/Solid Electrolyte Interphase in Li-Ion Batteries Studied by Hard x-Ray Photoelectron Spectroscopy. *Electrochim. Acta* **2014**, *138*, 430–436. https://doi.org/10.1016/j.electacta.2014.06.129.

[179] Philippe, B.; Dedryveère, R.; Gorgoi, M.; Rensmo, H.; Gonbeau, D.; Edström, K. Role of the LiPF6 Salt for the Long-Term Stability of Silicon Electrodes in Li-Ion Batteries - A Photoelectron Spectroscopy Study. *Chem. Mater.* **2013**, *25* (3), 394–404. https://doi.org/10.1021/cm303399v.

[180] Philippe, B.; Dedryveìre, R.; Gorgoi, M.; Rensmo, H.; Gonbeau, D.; Edström, K. Improved Performances of Nanosilicon Electrodes Using the Salt LiFSI: A Photoelectron Spectroscopy Study. *J. Am. Chem. Soc.* **2013**, *135* (26), 9829–9842. https://doi.org/10.1021/ja403082s.

[181] Maibach, J.; Lindgren, F.; Eriksson, H.; Edströ, K.; Hahlin, M. Electric Potential Gradient at the Buried Interface between Lithium-Ion Battery Electrodes and the SEI Observed Using Photoelectron Spectroscopy. *J. Phys. Chem. Lett* **2016**, *7*, 40. https://doi.org/10.1021/acs.jpclett.6b00391.

[182] Melin, T.; Lundström, R.; Berg, E. J. Revisiting the Ethylene Carbonate–Propylene Carbonate Mystery with Operando Characterization. *Adv. Mater. Interfaces* **2022**, *9* (8). https://doi.org/10.1002/admi.202101258.

[183] Jung, R.; Metzger, M.; Maglia, F.; Stinner, C.; Gasteiger, H. A. Oxygen Release and Its Effect on the Cycling Stability of LiNi x Mn y Co z O 2 (NMC) Cathode Materials for Li-Ion Batteries . *J. Electrochem. Soc.* **2017**, *164* (7), A1361–A1377. https://doi.org/10.1149/2.0021707jes.

[184] Lundström, R.; Berg, E. J. Design and Validation of an Online Partial and Total Pressure Measurement System for Li-Ion Cells. *J. Power Sources* **2021**, *485* (December 2020). https://doi.org/10.1016/j.jpowsour.2020.229347.

[185] Aurbach, D.; Zaban, A. The Application of EQCM to the Study of the Electrochemical Behavior of Propylene Carbonate Solutions. *J. Electroanal. Chem.* **1995**, *393* (1–2), 43–53. https://doi.org/10.1016/0022-0728(95)04014-F.

[186] Saqib, N.; Ganim, C. M.; Shelton, A. E.; Porter, J. M. On the Decomposition of Carbonate-Based Lithium-Ion Battery Electrolytes Studied Using Operando Infrared Spectroscopy. *J. Electrochem. Soc.* **2018**, *165* (16), A4051–A4057. https://doi.org/10.1149/2.1051816jes.

[187] Tremolet de Villers, B. J.; Bak, S. M.; Yang, J.; Han, S. D. In Situ ATR-FTIR Study of the Cathode–Electrolyte Interphase: Electrolyte Solution Structure, Transition Metal Redox, and Surface Layer Evolution. *Batter. Supercaps* **2021**, *4* (5), 778–784. https://doi.org/10.1002/batt.202000259.

[188] Krause, A.; Tkacheva, O.; Omar, A.; Langklotz, U.; Giebeler, L.; Dörfler, S.; Fauth, F.; Mikolajick, T.; Weber, W. M. In Situ Raman Spectroscopy on Silicon Nanowire Anodes Integrated in Lithium Ion Batteries. *J. Electrochem. Soc.* **2019**, *166* (3), A5378–A5385. https://doi.org/10.1149/2.0541903jes.

[189] Flores, E.; Novák, P.; Berg, E. J. In Situ and Operando Raman Spectroscopy of Layered Transition Metal Oxides for Li-Ion Battery Cathodes. *Front. Energy Res.* **2018**, *6* (AUG), 1–16. https://doi.org/10.3389/fenrg.2018.00082.

[190] Zhu, C.; Fan, C.; Cortés, E.; Xie, W. In Situsurface-Enhanced Raman Spectroelectrochemistry Reveals the Molecular Conformation of Electrolyte Additives in Li-Ion Batteries. *J. Mater. Chem. A* **2021**, *9* (35), 20024–20031. https://doi.org/10.1039/d1ta04218a.

[191] Maibach, J.; Xu, C.; Eriksson, S. K.; Åhlund, J.; Gustafsson, T.; Siegbahn, H.; Rensmo, H.; Edström, K.; Hahlin, M. A High Pressure X-Ray Photoelectron Spectroscopy Experimental Method for Characterization of Solid-Liquid Interfaces Demonstrated with a Li-Ion Battery System. *Rev. Sci. Instrum.* **2015**, *86* (4). https://doi.org/10.1063/1.4916209.

[192] Maibach, J.; Källquist, I.; Andersson, M.; Urpelainen, S.; Edström, K.; Rensmo, H.; Siegbahn, H.; Hahlin, M. Probing a Battery Electrolyte Drop with Ambient Pressure Photoelectron Spectroscopy. *Nat. Commun.* **2019**, *10* (1), 1–7. https://doi.org/10.1038/s41467-019-10803-y.

[193] Källquist, I.; Lindgren, F.; Lee, M. T.; Shavorskiy, A.; Edström, K.; Rensmo, H.; Nyholm, L.; Maibach, J.; Hahlin, M. Probing Electrochemical Potential Differences over the Solid/Liquid Interface in Li-Ion Battery Model Systems. *ACS Appl. Mater. Interfaces* **2021**, *13* (28), 32989–32996. https://doi.org/10.1021/acsami.1c07424.

[194] Dietrich, P. M.; Gehrlein, L.; Maibach, J.; Thissen, A. Probing Lithium-Ion Battery Electrolytes with Laboratory Near-Ambient Pressure XPS. **2020**.

[195] Parry, K. L.; Shard, A. G.; Short, R. D.; White, R. G.; Whittle, J. D.; Wright, A. ARXPS Characterisation of Plasma Polymerised Surface Chemical Gradients. *Surf. INTERFACE Anal. Surf. Interface Anal* **2006**, *38*, 1497–1504. https://doi.org/10.1002/sia.2400.

[196] Williard, N.; Sood, B.; Osterman, M.; Pecht, M. Disassembly Methodology for Conducting Failure Analysis on Lithium-Ion Batteries. *J. Mater. Sci. Mater. Electron.* **2011**, *22* (10), 1616–1630. https://doi.org/10.1007/s10854-011-0452-4.

[197] Orsini, F.; Du Pasquier, A.; Beaudoin, B.; Tarascon, J. M.; Trentin, M.; Langenhuizen, N.; De Beer, E.; Notten, P. In Situ Scanning Electron Microscopy (SEM) Observation of Interfaces within Plastic Lithium Batteries. *J. Power Sources* **1998**, *76* (1), 19–29. https://doi.org/10.1016/S0378-7753(98)00128-1.

[198] Malmgren, S.; Ciosek, K.; Lindblad, R.; Plogmaker, S.; Kühn, J.; Rensmo, H.; Edström, K.; Hahlin, M. Consequences of Air Exposure on the Lithiated Graphite SEI. *Electrochim. Acta* **2013**, *105*, 83–91. https://doi.org/10.1016/j.electacta.2013.04.118.

[199] Somerville, L.; Bareño, J.; Jennings, P.; McGordon, A.; Lyness, C.; Bloom, I. The Effect of Pre-Analysis Washing on the Surface Film of Graphite Electrodes. *Electrochim. Acta* **2016**, *206*, 70–76. https://doi.org/10.1016/j.electacta.2016.04.133.

[200] Xin, N.; Sun, Y.; He, M.; Radke, C. J.; Prausnitz, J. M. Solubilities of Six Lithium Salts in Five Non-Aqueous Solvents and in a Few of Their Binary Mixtures. **2018**. https://doi.org/10.1016/j.fluid.2017.12.034.

[201] Didier, C.; Pang, W. K.; Guo, Z.; Schmid, S.; Peterson, V. K. Phase Evolution and Intermittent Disorder in Electrochemically Lithiated Graphite Determined Using in Operando Neutron Diffraction. *Chem. Mater.* **2020**, *32* (6), 2518–2531. https://doi.org/10.1021/acs.chemmater.9b05145.

[202] Sole, C.; Drewett, N. E.; Hardwick, L. J. Insitu Raman Study of Lithium-Ion Intercalation into Microcrystalline Graphite. *Faraday Discuss.* **2014**, *172*, 223–237. https://doi.org/10.1039/c4fd00079j.

[203] Jaumann, T.; Balach, J.; Klose, M.; Oswald, S.; Langklotz, U.; Michaelis, A.; Eckert, J.; Giebeler, L. SEI-Component Formation on Sub 5 Nm Sized Silicon Nanoparticles in Li-Ion Batteries: The Role of Electrode Preparation, FEC Addition and Binders. *Phys. Chem. Chem. Phys.* **2015**, *17* (38), 24956–24967. https://doi.org/10.1039/c5cp03672k.

[204] Schroder, K.; Alvarado, J.; Yersak, T. A.; Li, J.; Dudney, N.; Webb, L. J.; Meng, Y. S.; Stevenson, K. J. The Effect of Fluoroethylene Carbonate as an Additive on the Solid Electrolyte Interphase on Silicon Lithium-Ion Electrodes. *Chem. Mater.* **2015**, *27* (16), 5531–5542. https://doi.org/10.1021/acs.chemmater.5b01627.

[205] Chen, X.; Li, X.; Mei, D.; Feng, J.; Hu, M. Y.; Hu, J.; Engelhard, M.; Zheng, J.; Xu, W.; Xiao, J.; Liu, J.; Zhang, J. G. Reduction Mechanism of Fluoroethylene Carbonate for Stable Solid-Electrolyte Interphase Film on Silicon Anode. *ChemSusChem* **2014**, *7* (2), 549–554. https://doi.org/10.1002/cssc.201300770.

[206] Ghamlouche, A.; Müller, M.; Jeschull, F.; Maibach, J. Degradation Phenomena in Silicon/Graphite Electrodes with Varying Silicon Content. *J. Electrochem. Soc.* **2022**, *169* (2), 020541. https://doi.org/10.1149/1945-7111/ac4cd3.

[207] Tanuma, S.; Shinotsuka, H.; Powell, C. J.; Penn, D. R. Electron Inelastic Mean Free Paths in Compounds. *Surf. Coatings Technol.* **1993**, *21*, 165–176. https://doi.org/10.1384/jsa.26.106.

[208] Boutboul, T.; Akkerman, A.; Breskin, A.; Chechik, R. Electron Inelastic Mean Free Path and Stopping Power Modelling in Alkali Halides in the 50 EV-10 KeV Energy Range. *J. Appl. Phys.* **1996**, *79* (9), 6714–6721. https://doi.org/10.1063/1.361491.

[209] NIST Electron Inelastic-Mean-Free-Path Database 71. NIST 1999. https://doi.org/http://dx.doi.org/10.18434/T48C78.

[210] An, S. J.; Li, J.; Daniel, C.; Mohanty, D.; Nagpure, S.; Wood, D. L. The State of Understanding of the Lithium-Ion-Battery Graphite Solid Electrolyte Interphase (SEI) and Its Relationship to Formation Cycling. *Carbon N. Y.* **2016**, *105*, 52–76. https://doi.org/10.1016/j.carbon.2016.04.008.

[211] Cao, C.; Steinrück, H. G.; Shyam, B.; Toney, M. F. The Atomic Scale Electrochemical Lithiation and Delithiation Process of Silicon. *Adv. Mater. Interfaces* **2017**, *4* (22), 1–7. https://doi.org/10.1002/admi.201700771.

[212] Fears, T. M.; Doucet, M.; Browning, J. F.; Baldwin, J. K. S.; Winiarz, J. G.; Kaiser, H.; Taub, H.; Sacci, R. L.; Veith, G. M. Evaluating the Solid Electrolyte Interphase Formed on Silicon Electrodes: A Comparison of: Ex Situ X-Ray Photoelectron Spectroscopy and in Situ Neutron Reflectometry. *Phys. Chem. Chem. Phys.* **2016**, *18* (20), 13927–13940. https://doi.org/10.1039/c6cp00978f.

[213] El Ouatani, L.; Dedryvère, R.; Siret, C.; Biensan, P.; Reynaud, S.; Iratçabal, P.; Gonbeau, D. The Effect of Vinylene Carbonate Additive on Surface Film Formation on Both Electrodes in Li-Ion Batteries. *J. Electrochem. Soc.* **2009**, *156* (2), A103. https://doi.org/10.1149/1.3029674.

[214] Kamikawa, Y.; Amezawa, K.; Terada, K. First-Principles Study on the Mechanical Properties of Polymers Formed by the Electrochemical Reduction of Fluoroethylene Carbonate and Vinylene Carbonate. *J. Phys. Chem. C* **2020**, *124* (37), 19937–19944. https://doi.org/10.1021/acs.jpcc.0c04878.

[215] Shkrob, I. A.; Wishart, J. F.; Abraham, D. P. What Makes Fluoroethylene Carbonate Different? *J. Phys. Chem. C* **2015**, *119* (27), 14954–14964. https://doi.org/10.1021/acs.jpcc.5b03591.

[216] Bosman, H. J. M.; Pijpers, A. P.; Jaspers, A. W. M. A. An X-Ray Photoelectron Spectroscopy Study of the Acidity of SiO2-ZrO2 Mixed Oxides. *J. Catal.* **1996**, *161* (2), 551–559. https://doi.org/10.1006/jcat.1996.0217.

[217] Markevich, E.; Salitra, G.; Aurbach, D. Fluoroethylene Carbonate as an Important Component for the Formation of an Effective Solid Electrolyte Interphase on Anodes and Cathodes for Advanced Li-Ion Batteries. *ACS Energy Lett.* **2017**, *2* (6), 1337–1345. https://doi.org/10.1021/acsenergylett.7b00163.

[218] Yoon, T.; Milien, M. S.; Parimalam, B. S.; Lucht, B. L. Thermal Decomposition of the Solid Electrolyte Interphase (SEI) on Silicon Electrodes for Lithium Ion Batteries. *Chem. Mater.* **2017**, *29* (7), 3237–3245. https://doi.org/10.1021/acs.chemmater.7b00454.

[219] Soto, F. A.; Ma, Y.; Martinez De La Hoz, J. M.; Seminario, J. M.; Balbuena, P. B. Formation and Growth Mechanisms of Solid-Electrolyte Interphase Layers in Rechargeable Batteries. *Chem. Mater.* **2015**, *27* (23), 7990–8000. https://doi.org/10.1021/acs.chemmater.5b03358.

[220] Hou, T.; Yang, G.; Rajput, N. N.; Self, J.; Park, S. W.; Nanda, J.; Persson, K. A. The Influence of FEC on the Solvation Structure and Reduction Reaction of LiPF6/EC Electrolytes and Its Implication for Solid Electrolyte Interphase Formation. *Nano Energy* **2019**, *64* (November

2018), 103881. https://doi.org/10.1016/j.nanoen.2019.103881.

[221] Ha, Y.; Stetson, C.; Harvey, S. P.; Teeter, G.; Tremolet De Villers, B. J.; Jiang, C. S.; Schnabel, M.; Stradins, P.; Burrell, A.; Han, S. D. Effect of Water Concentration in LiPF6-Based Electrolytes on the Formation, Evolution, and Properties of the Solid Electrolyte Interphase on Si Anodes. *ACS Appl. Mater. Interfaces* **2020**, *12* (44), 49563–49573. https://doi.org/10.1021/acsami.0c12884.

[222] Surace, Y.; Leanza, D.; Mirolo, M.; Kondracki, L.; Vaz, C. A. F.; Kazzi, M. El; Novák, P.; Trabesinger, S. Evidence for Stepwise Formation of Solid Electrolyte Interphase in a Li-Ion Battery. *Energy Storage Mater.* **2021**, *44* (September 2021), 156–167. https://doi.org/10.1016/j.ensm.2021.10.013.

[223] Veith, G. M.; Doucet, M.; Baldwin, J. K.; Sacci, R. L.; Fears, T. M.; Wang, Y.; Browning, J. F. Direct Determination of Solid-Electrolyte Interphase Thickness and Composition as a Function of State of Charge on a Silicon Anode. *J. Phys. Chem. C* **2015**, *119* (35), 20339–20349. https://doi.org/10.1021/acs.jpcc.5b06817.

[224] Ota, H.; Sakata, Y.; Inoue, A.; Yamaguchi, S. Analysis of Vinylene Carbonate Derived SEI Layers on Graphite Anode. *J. Electrochem. Soc.* **2004**, *151* (10), A1659. https://doi.org/10.1149/1.1785795.

[225] Parimalam, B. S.; Lucht, B. L. Reduction Reactions of Electrolyte Salts for Lithium Ion Batteries: LiPF 6 , LiBF 4 , LiDFOB, LiBOB, and LiTFSI. *J. Electrochem. Soc.* **2018**, *165* (2), 251–255. https://doi.org/10.1149/2.0901802jes.

[226] Eriksson, T.; Andersson, A. M.; Bishop, A. G.; Gejke, C.; Gustafsson, T.; Thomas, J. O. Surface Analysis of LiMn[Sub 2]O[Sub 4] Electrodes in Carbonate-Based Electrolytes. *J. Electrochem. Soc.* **2002**, *149* (1), A69. https://doi.org/10.1149/1.1426398.

[227] Aurbach, D. Review of Selected Electrode-Solution Interactions Which Determine the Performance of Li and Li Ion Batteries. *J. Power Sources* **2000**, *89* (2), 206–218. https://doi.org/10.1016/S0378-7753(00)00431-6.

[228] Nie, M.; Abraham, D. P.; Seo, D. M.; Chen, Y.; Bose, A.; Lucht, B. L. Role of Solution Structure in Solid Electrolyte Interphase Formation on Graphite with LiPF 6 in Propylene Carbonate. *J. Phys. Chem. C* **2013**, 117–25381. https://doi.org/10.1021/jp409765w.

[229] Vos, M.; Marmitt, G. G.; Finkelstein, Y.; Moreh, R.; Vos, M.; Marmitt, G. G.; Finkelstein, Y.; Moreh, R. Determining the Band Gap and Mean Kinetic Energy of Atoms from Reflection Electron Energy Loss Spectra Determining the Band Gap and Mean Kinetic Energy of Atoms from Reflection Electron Energy Loss Spectra. **2015**, *104203*. https://doi.org/10.1063/1.4929911.

Appendix

Fluoroethylene Carbonate as Electrolyte Solvent

Raman spectra. The raman spectra of all cycled electrode show the graphite G band at ~1584 cm^{-1}, D band at ~1349 cm^{-1} and the 2D band at ~2714 cm^{-1} indicating that graphite is not damaged and is still able to take place in the electrochemical process. Raman spectra were recorded with a LabRAM HR Evolution spectrometer (HORIBA Scientific), using a HeNe laser with a wavelength of 632.8 nm (Elaser=1.9876 eV).

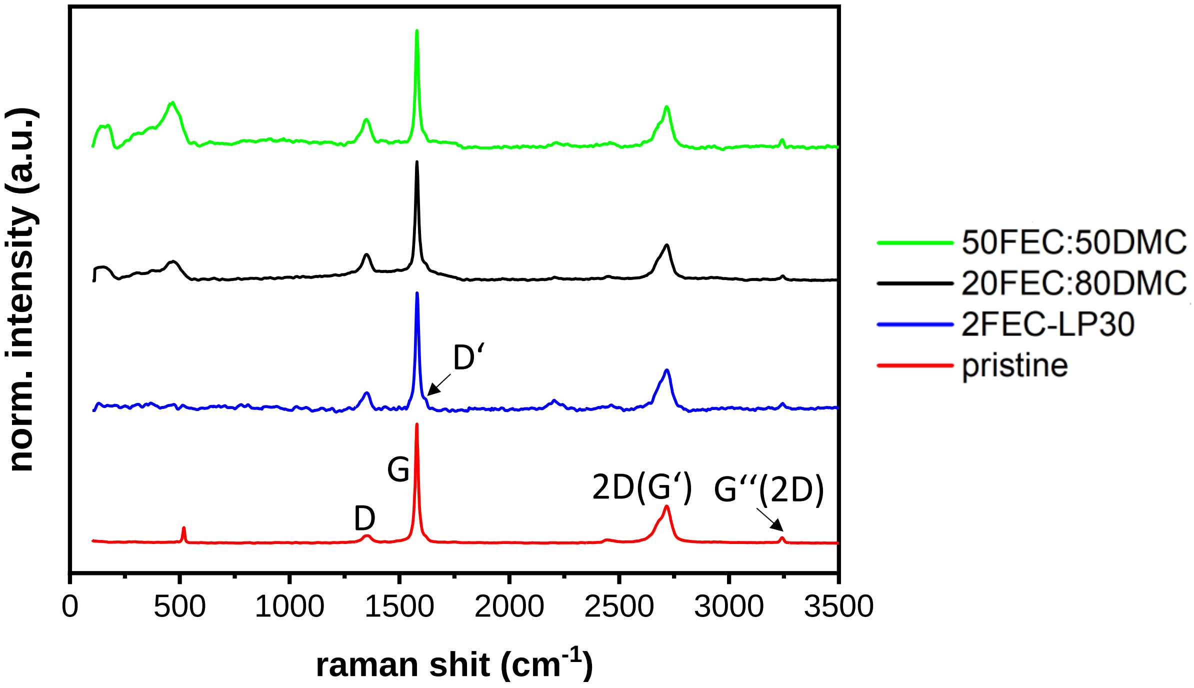

Figure A1: Raman spectra of Si/Gr electrodes cycled in (a) 2FEC-LP30, (b) 20FEC:80DMC, (c) 50FEC:50DMC electrolytes after 100 cycles and of a pristine Si/Gr electrode.

Spectra of pure FEC solvent: Photoelectron spectra of pure FEC solvent were obtained by casting the solution on a gold plate. **Figure A2** displays C1s, O1s, and F1s spectra of pure FEC. Three peaks are observed in the C1s spectrum resulting from the three different chemical environments of carbon: -C-O (C_a, 286.7 eV), -C-F (C_b, 288.6 eV), and -O-C(=O)-O (C_c, 290.4 eV). Corresponding oxygen species emerge in the O1s spectrum for -C-O (O_a, 533.2 eV), F-C-O (O_b, 534.3 eV), and -C=O (O_c, 532 eV). The -C-F peak arises at 687.7 eV in the F1s spectrum.

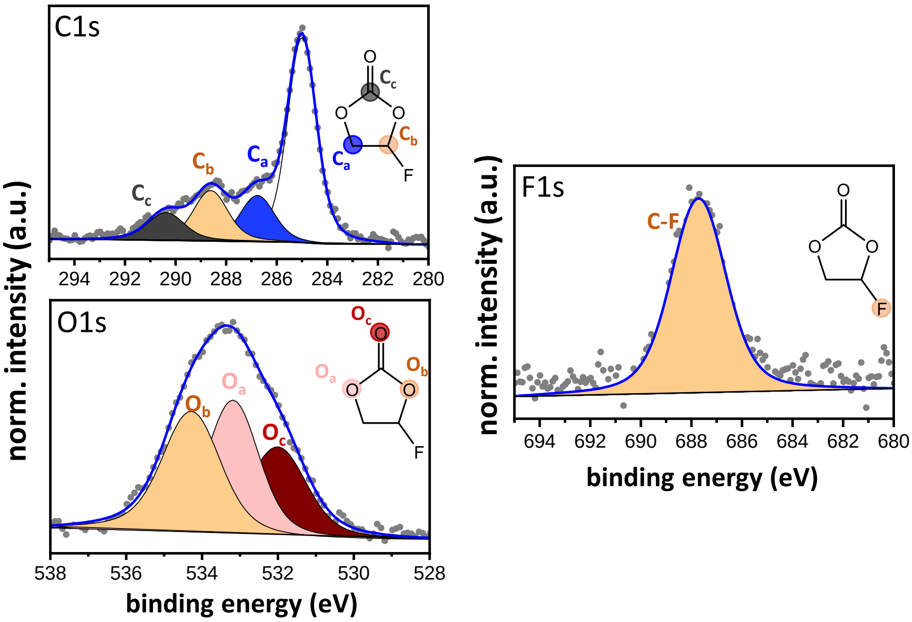

Figure A2: C1s, O1s, and F1s photoelectron spectra of pure FEC.

FEC electrolyte: P2p spectrum of an electrode cycled in pure FEC electrolyte is displayed in **Figure A3**.

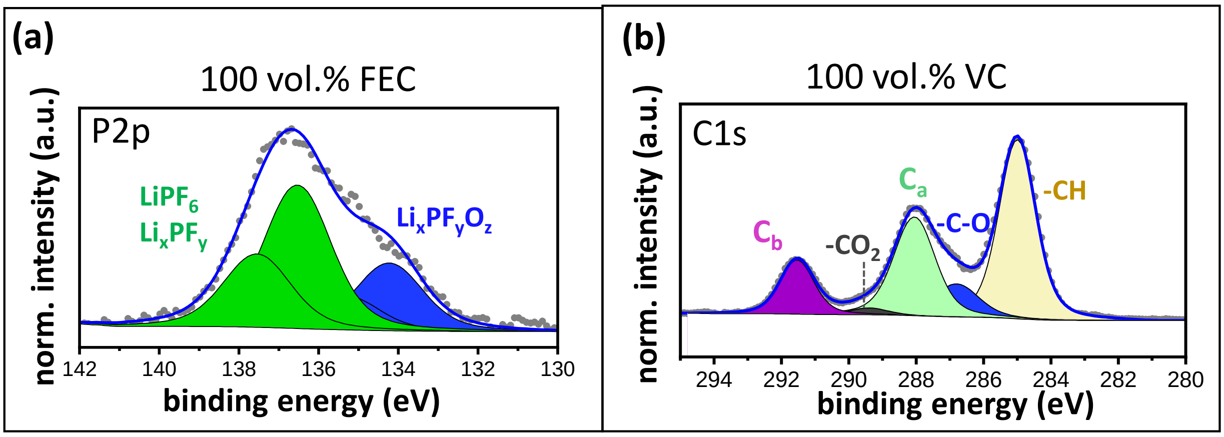

Figure A3: (a) P2p photoelectron spectra of Si/Gr electrode cycled in pure FEC electrolyte. (b) C1s of electrode cycled in pure VC.

Figure A4-Figure A6 display the F1s, O1s, and P2p photoelectron spectra from electrodes cycled up to 0.8 V, 0.01 V during the first lithiation, as well as spectra of Si/Gr electrodes after 1, 10, and 100 cycles in delithiated states at 1.5 V.

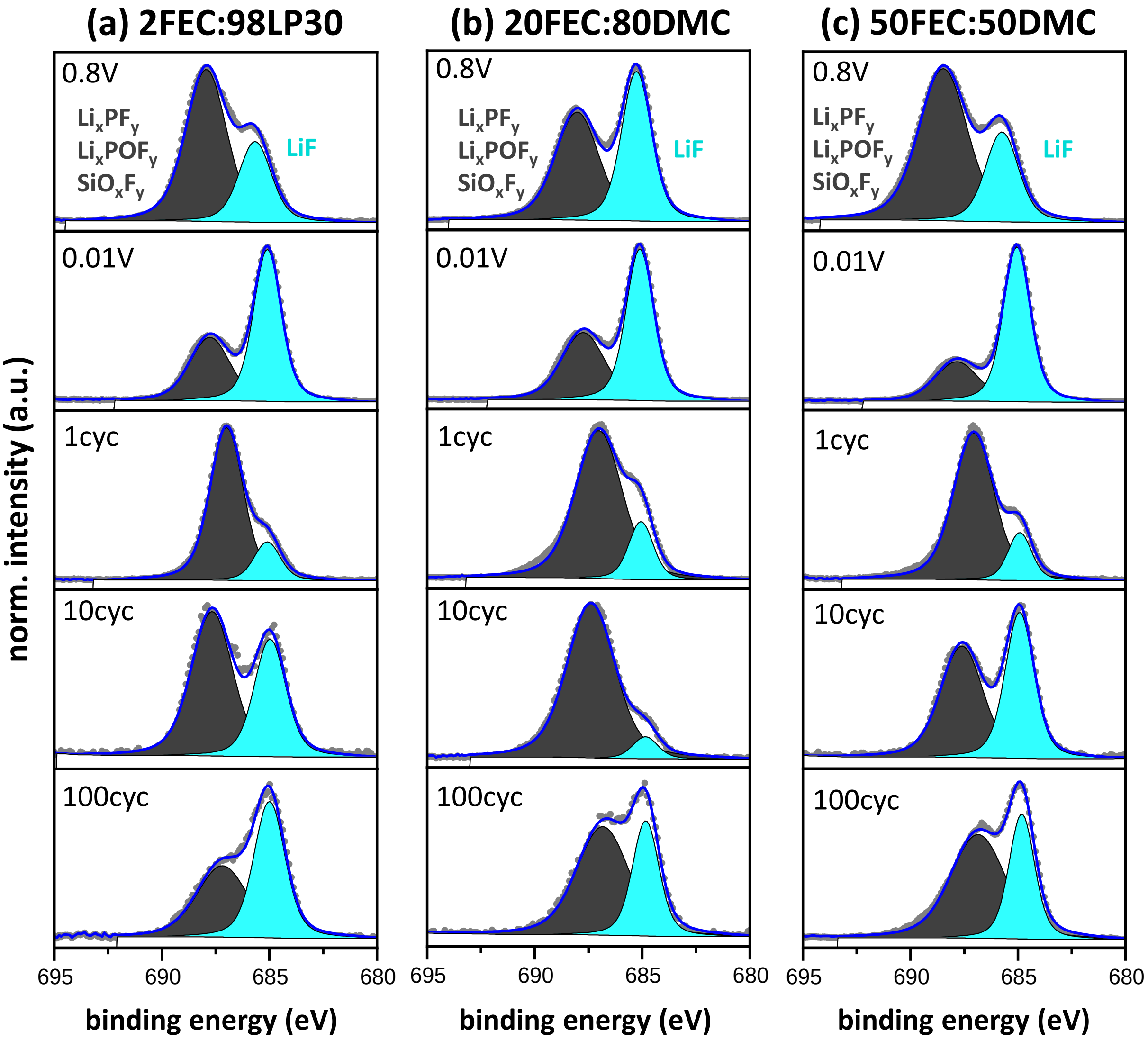

Figure A4: F 1s photoelectron spectra of electrodes cycled in 2FEC:98LP30, 80DMC-20FEC, and 50DMC:50FEC electrolyte at 0.8 V and 0.01 V during the first lithiation, and at 1.5 V after the first, the 10th, and the 100th cycle.

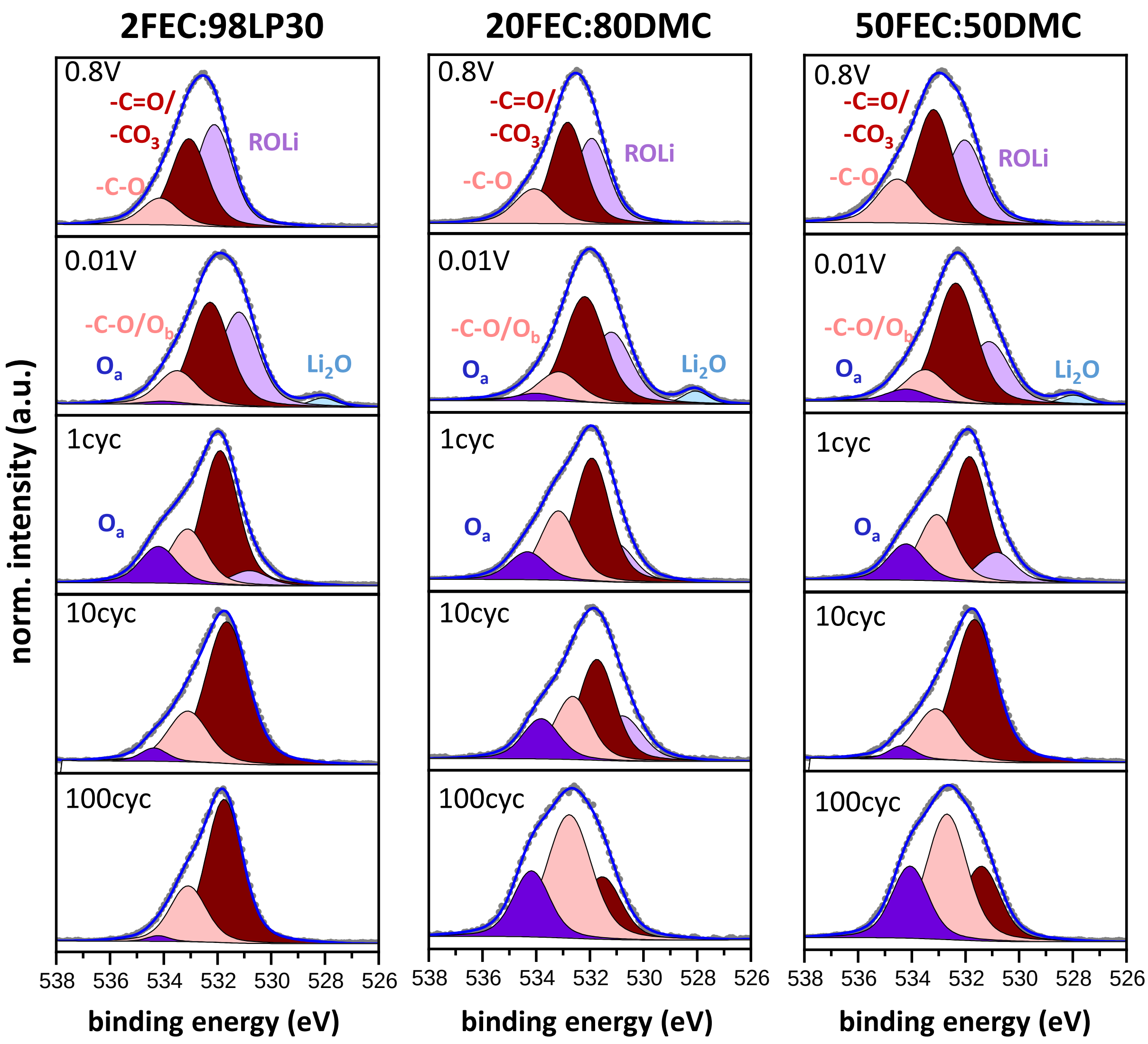

Figure A5: O 1s photoelectron spectra of electrodes cycled in 2FEC:98LP30, 80DMC-20FEC, and 50DMC:50FEC electrolyte at 0.8 V and 0.01 V during the first lithiation, and at 1.5 V after the first, the 10th, and the 100th cycle.

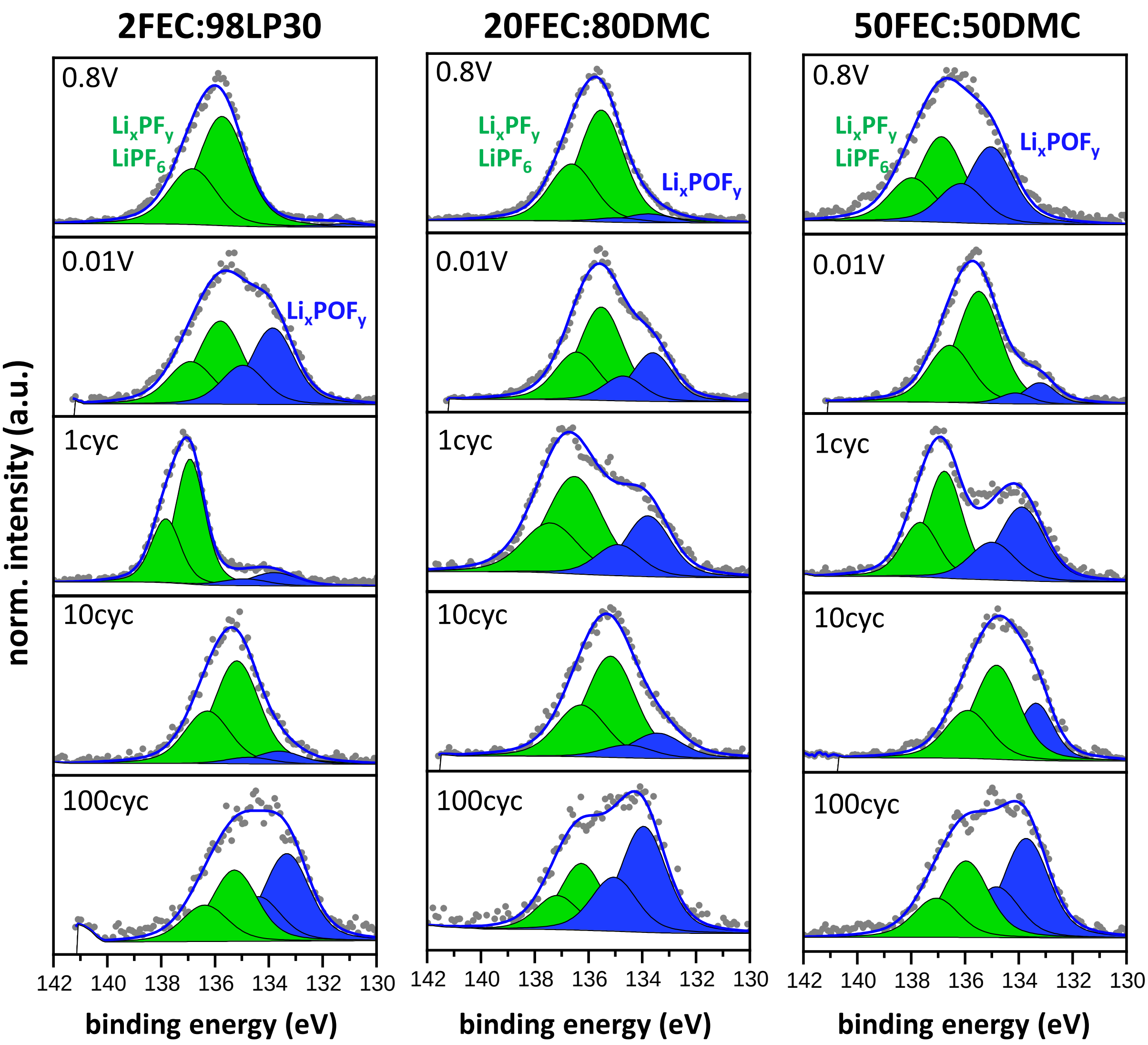

Figure A6: P2p photoelectron spectra of electrodes cycled in 2FEC:98LP30, 80DMC-20FEC, and 50DMC:50FEC electrolyte at 0.8 V and 0.01 V during the first lithiation, and at 1.5 V after the first, the 10th, and the 100th cycle.

Relative peak areas are displayed in **Figure A7**.

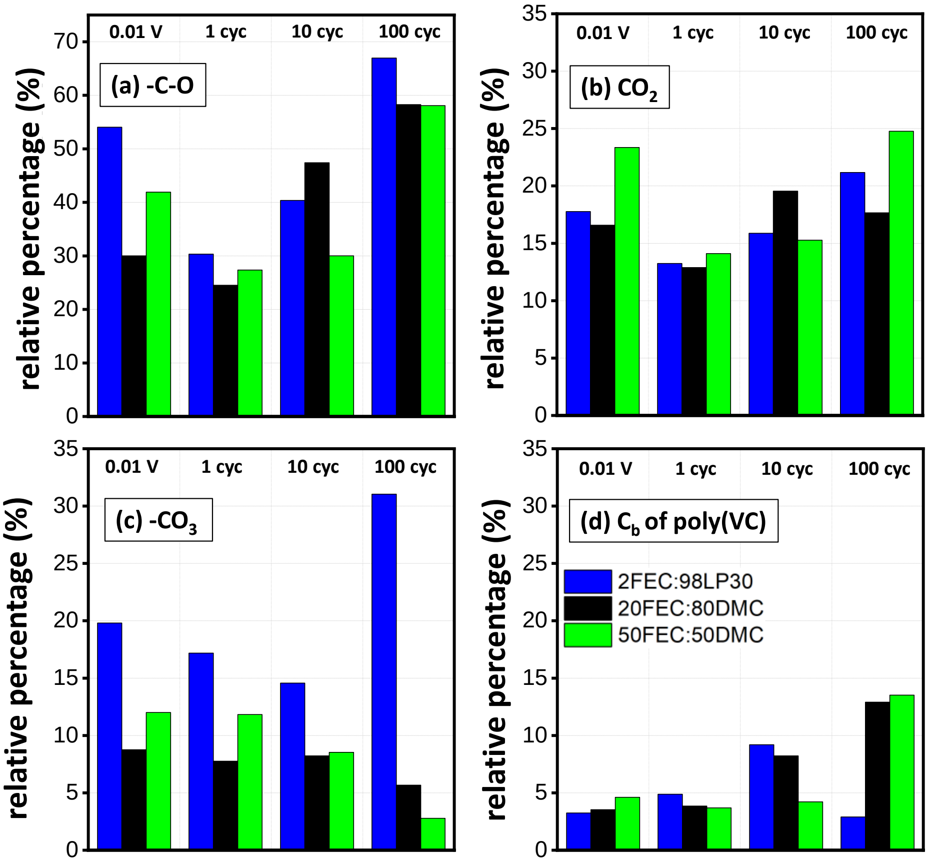

Figure A7: Relative peak areas of (a) -C-O, (b) $-CO_2$, (c) $-CO_3$, and (d) poly(VC) of Si/Gr electrodes cycled in 2FEC:98LP30, 20FEC:80DMC, and 50FEC:50DMC. The relative peak areas were calculated relative to the hydrocarbon peak area.

Figure A8: displays the C1s spectrum of Si/Gr electrode cycled in pure LP30 electrolyte.

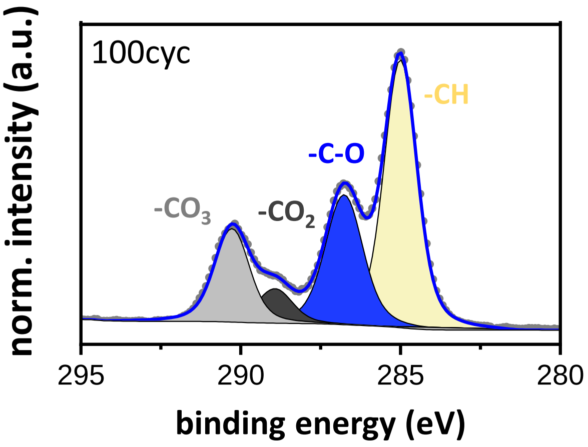

Figure A8: C1s spectrum of Si/Gr electrode cycled in pure LP30 electrolyte.

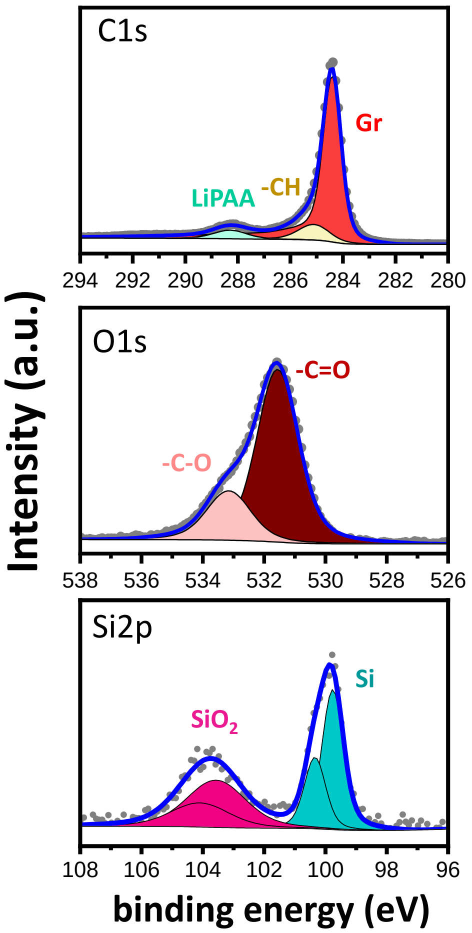

Figure A9: C1s, O1s, and Si2p spectra of pristine Si/Gr electrodes.

Table A1: Fitting parameters for FEC decomposition

Peak	Chemical shift	Constrains FWHM	Constrains Height & Area
-CH	285	1.2:1.4	none
-C-O	-CH + 1.5 (±0.1)	1.4:1.6	none
C_a	-CH + 3.0 (±0.1)	1.4:1.6	none
$-CO_2$	-CH + 4.1 (±0.1)	1.4:1.6	none
$-CO_3$	-CH + 5.3 (±0.1)	1.4:1.6	none
C_b	C_a + 3.3 (±0.1)	1.4:1.6	C_a * 0.5 (±0.1)

Table A2: Binding energies, full widths half maximums, and atomic percentages of SEI components detected on electrodes cycled in 2FEC-LP30 electrolyte at different cycling stages.

2FEC:98LP30		**0.8V**			**0. 01V**			**1cyc**			**10cyc**			**100cyc**		
Element	Component	Peak BE eV	FWHM eV	Atomic %	Peak BE eV	FWHM eV	Atomic %	Peak BE eV	FWHM eV	Atomic %	Peak BE eV	FWHM eV	Atomic %	Peak BE eV	FWHM eV	Atomic %
C1s	graphite	283.8	0.77	32.6	282.6	1.08	0.4	282.8	0.85	7.3	282.6	0.88	3.9			
	-CH	285	1.5	5.2	285	1.44	6.8	285	1.43	19.0	285.0	1.51	14.0	285.0	1.44	12.1
	-C-O	286.8	1.55	1.6	286.8	1.49	3.4	286.8	1.36	5.8	286.8	1.35	6.1	286.7	1.6	8.1
	C_a, C=O, OCO				287.8	1.35	0.5	288.0	1.35	1.9	287.9	1.35	2.7	287.8	1.43	0.8
	$-CO_2$	289.2	1.6	1.8	289.1	1.54	1.3	289.1	1.54	2.5	289.0	1.53	2.4	289.1	1.5	2.6
	$-CO_3$	290.7	1.46	0.6	290.3	1.16	0.9	290.2	1.31	3.3	290.2	1.54	2.8	290.2	1.38	3.8
	$ROCO_2R$, C_b				291	1.35	0.3	291.2	1.35	0.9	291.2	1.35	1.4	291.0	1.43	0.4
F1s	LiF	685.7	1.79	4.0	685.1	1.59	15.9	685.1	1.44	2.4	684.9	1.46	1.0	685.0	1.71	8.7
	$Li_xPF_yO_z$ & SiO_xF_y	687.9	2.25	9.4	687.7	2.28	10.1	687	1.83	12.2	687.4	2.49	16.8	687.2	2.78	7.4
Li1s	Li-X				55.8	1.68	27.1	55.7	2	18.2	55.6	2	16.7	54.5	1.8	26.0
	Li-Y				54.4	1.6	6.6									
O1s	Li_2O				528.2	1.55	1									
	ROLi				531.2	1.73	8.3	530.8	1.92	2.2	530.8	1.83	2.4	530.8	1.83	1.8
	-C=O	532.4	1.92	10.4	532.3	1.73	9	532	1.73	13.8	532.1	1.61	13.0	531.8	1.55	16.5
	-C-O	533.8	1.92	3.4	533.5	1.73	2.8	533.4	1.73	4.1	533.1	1.59	7.2	533.2	1.65	7.2
	O				534.3	1.92	0.8	534.2	1.91	3.8	534.3	1.7	5.3	534.5	1.98	0.9
Si2p	Si^0 2p3	99.1	0.77	1												
	Li_xSi							97.7	1.13	0.2						
	Li_xSiO_y							101.1	2	0.1				101.4	3.26	0.4
	SiO_2 2p3	103.4	1.44	0.4												
	SiO_xF_y	106.6	2.23	1.3												
P2p	Li_xPF_y	136.9	2	1.67	135.8	2	2.55	136.9	1.29	1.6	135.5	1.86	3.2	135.3	2	1.4
	$Li_xPF_yO_z$	135	2	1.5	133.9	1.91	2.24	133.8	2	0.3	136.9	1.44	0.8	133.3	2	1.7

Table A3: Binding energies, full widths half maximums, and atomic percentages of SEI components detected on electrodes cycled in 20FEC-80DMC electrolyte at different cycling stages

20FEC:80DMC		0.8V			0. 01V			1cyc			10cyc			100cyc		
Element	Component	Peak BE eV	FWHM eV	Atomic %	Peak BE eV	FWHM eV	Atomic %	Peak BE eV	FWHM eV	Atomic %	Peak BE eV	FWHM eV	Atomic %	Peak BE eV	FWHM eV	Atomic %
C1s	graphite	283.6	0.81	24.5	282.4	1.09	2	282.8	0.85	6.7	282.6	0.88	5.1	283.0	0.76	1.2
	-CH	285	1.5	7.5	285	1.64	7.1	285	1.49	15.1	285	1.52	12.1	285	1.43	16.3
	-C-O	287.0	1.55	2.3	286.8	1.49	2.1	286.7	1.42	3.7	286.7	1.53	5.7	286.6	1.6	9.5
	C_a, C=O, OCO				287.8	1.44	0.5	287.9	1.6	1.8	287.9	1.4	2.0	287.8	1.52	4.2
	$-CO_2$	289.2	1.6	1.7	289	1.54	1.2	289.2	1.6	2.0	289.2	1.6	2.4	288.9	1.49	2.9
	$-CO_3$	290.7	1.2	0.4	290.1	1.15	0.6	290.1	1.2	1.2	290.3	1.29	1.0	290.3	1.38	0.9
	$ROCO_2R$, C_b				290.9	1.44	0.3	291.1	1.2	0.6	291.1	1.4	1.0	291.0	1.52	2.1
F1s	LiF	685.3	1.64	12.6	685.1	1.52	17.7	685.1	1.36	4.3	684.9	1.4	1.5	684.8	1.46	5.2
	$Li_xPF_yO_z$ & SiO_xF_y	688.0	2.38	13.2	687.8	2.34	12.1	687.0	2.56	20.7	687.4	2.65	20.3	686.8	2.88	10.1
Li1s	Li-X	56.1	1.79	16.7	55.8	1.79	28.5	56	2.43	21.9	55.8	2.58	19.3	55.7	2	19.3
	Li-Y				54.0	1.6	4.1									
O1s	Li_2O				528.1	1.2	0.7									
	ROLi				531.2	1.8	6.3	531.2	1.8	2.5	531.2	1.8	4.1	531.1	1.7	1.5
	-C=O	532.3	1.81	11.3	532.3	1.8	9.8	531.9	1.8	9.0	532.3	1.8	12.9	532	1.8	9.7
	-C-O	533.7	2	4.2	533.5	1.8	2.3	533.2	1.8	4.6	533.4	1.8	3.8	533.2	1.8	8.5
	O				534.2	1.8	0.1	534.2	1.8	2	534.2	1.8	3.3	534.2	1.8	5.6
Si2p	Si^0 2p3	98.9	0.79	1.0												
	Li_xSi							97.8	2	0.2						
	Li_xSiO_y															
	SiO_2 2p3	103. 3	1.99	0.5												
	SiO_xF_y	106.2	1.92	0.4	105.0	1.42	0.7	105.0	1.35	1	105.0	1.54	0.7	105.2	2.6	0.5
P2p	Li_xPF_y	135.5	2	3.3	135.5	1.94	2.6	136.5	2.45	1.8	135.6	2.2	3.7	136.3	1.86	1.0
	$Li_xPF_yO_z$	133.8	2	0.3	133.6	1.75	1.2	133.8	2	0.9	133.9	2.2	0.9	134.0	2	1.7

Table A4: Binding energies, full widths half maximums, and atomic percentages of SEI components detected on electrodes cycled in 50FEC:50DMC electrolyte at different cycling stages

50FEC:50DCM		0.8V			0. 01V			1cyc			10cyc			100cyc		
Element	Component	Peak BE eV	FWHM eV	Atomic %	Peak BE eV	FWHM eV	Atomic %	Peak BE eV	FWHM eV	Atomic %	Peak BE eV	FWHM eV	Atomic %	Peak BE eV	FWHM eV	Atomic %
C1s	graphite	283.7	0.79	28.2	282.3	1.07	0.9	282.8	0.85	8.5	282.9	0.89	6.6	283.0	0.87	2.3
	-CH	285	1.5	5.0	285.0	1.59	5.6	285	1.49	18.4	285	1.5	15.5	285	1.51	15.1
	-C-O	286.7	1.55	1.7	286.8	1.55	2.4	286.8	1.4	5.1	286.7	1.6	4.7	286.7	1.49	8.3
	C_a, C=O, OCO	287.9	1.53	0	287.8	1.4	0.6	288.0	1.4	1.4	287.6	1.52	1.3	288.1	1.54	4.7
	$-CO_2$	289.2	1.6	1.6	289.0	1.6	1.3	289	1.6	2.6	288.9	1.5	2.4	289.1	1.42	2.3
	$-CO_3$	290.7	1.23	0.4	290.1	1.4	0.6	290.2	1.4	2.2	290.2	1.38	1.3	290.1	1.35	0.7
	$ROCO_2R$, C_b				290.9	1.4	0.3	291.1	1.4	0.7	290	1.52	0.7	290.8	1.33	1.9
F1s	LiF	685.8	1.82	7.5	685.1	1.49	24.2	684.9	1.3	2.6	684.9	1.58	7.0	684.8	1.41	6.6
	$Li_xPF_yO_z$ & SiO_xF_y	688.5	2.67	18.6	687.8	2.38	9.8	687.1	2.23	13.8	687.6	2.32	7.9	686.9	3	11.6
Li1s	Li-X	56.4	2	11.9	55.8	1.64	31.5	55.7	2.06	18.1	55.6	1.68	20.8	55.6	2	19.2
	Li-Y	58.6	2	4.4	53.9	1.6	4.5									
O1s	Li_2O				528.0	1.21	0.4									
	ROLi				531.1	1.8	4.0	531.1	1.8	3.8	531.1	1.8	3.4	531.1	1.7	2.5
	-C=O	532.3	1.9	7.6	532.4	1.8	7.7	532	1.8	12.1	531.8	1.8	16.6	531.9	1.8	8.6
	-C-O	533.7	2.2	6.9	533.5	1.8	2.1	533.4	1.8	4.9	533.2	1.8	5.7	533.1	1.8	8.9
	O				534.2	1.8	0.8	534.1	1.8	2.5	534.2	1.8	1.6	534.2	1.7	4.5
Si2p	Si^0 2p3	99.1	0.8	1.0												
	Li_xSi							97.6	1.71	0.2						
	Li_xSiO_y							100.7	1.5	0.1						
	SiO_2 2p3	103.2	1.9	0.5												
	SiO_xF_y	106.4	1.97	1.5	104.9	1.02	0.3	105.1	1.5	0.3	105.1	1.5	0.3	104.8	1.49	0.5
P2p	Li_xPF_y	136.5	2	2.1	135.5	1.94	2.7	136.8	1.6	1.4	134.8	2	2.9	136.0	2	1.0
	$Li_xPF_yO_z$	134.9	2	1.4	133.2	1.38	0.4	133.9	2	1.2	133.4	1.53	1.4	133.7	2	1.3

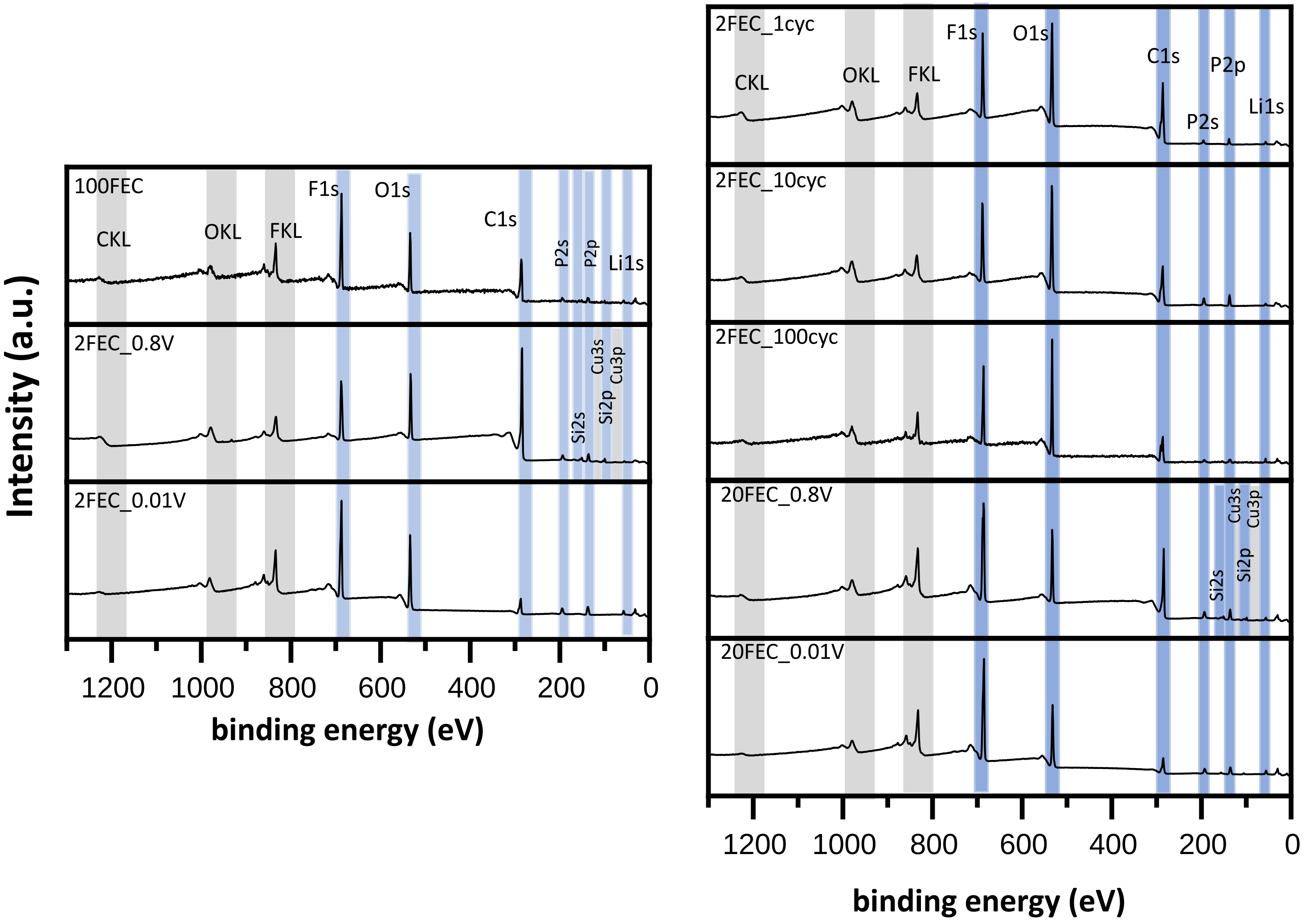

Figure A10: Survey spectra of Si/Gr electrodes cycled in 100FEC to 0.01 V. As well as in 2FEC:98LP30 to 0.8 V, 0.01 V during the 1st lithiation and to 1.5 V after the 1st, 10th, and 100th cycle. Also shown are survey spectra of Si/Gr electrodes cycled in 20FEC:80LP30 to 0.8 V and 0.01 V during the 1st lithiation.

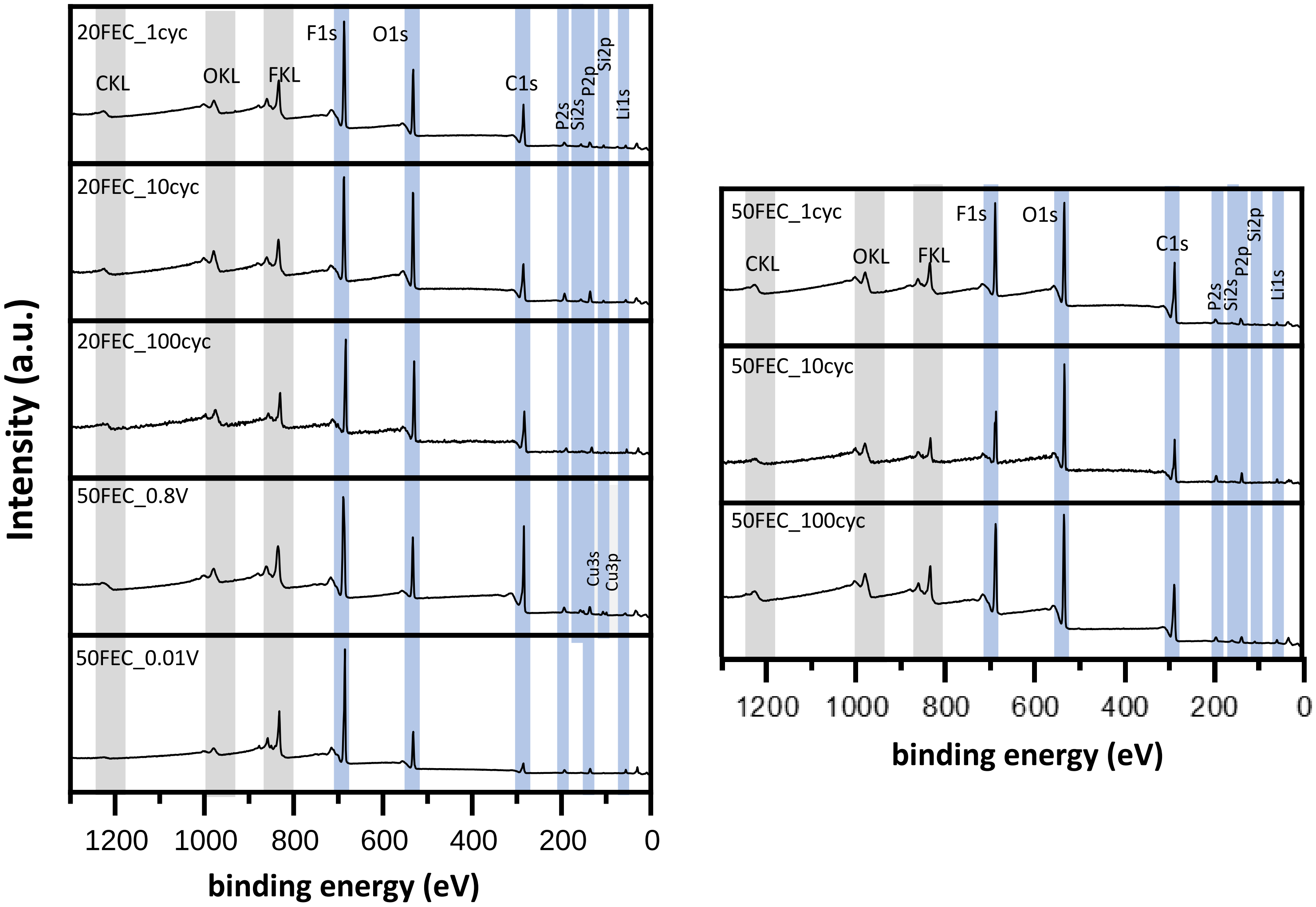

Figure A11: Survey spectra of Si/Gr electrodes cycled in 20FEC:80LP30 to 1.5 V after the 1st, 10th, and 100th cycle. As well as survey spectra of Si/Gr electrodes cycled in 50FEC:50LP30 to 0.8 V and 0.01 V during the 1st lithiation and to 1.5 V after the 1st, 10th, and 100th cycle.

Glyoxylic Acetals as Electrolyte Solvents

Evolution of SEI composition during formation. **Figure A12-Figure A14** displays the O1s, N1s, P2p, and S2p spectra at 2.5, 1.3 V, 0.9 V, 0.5 V, and 0.01 V.

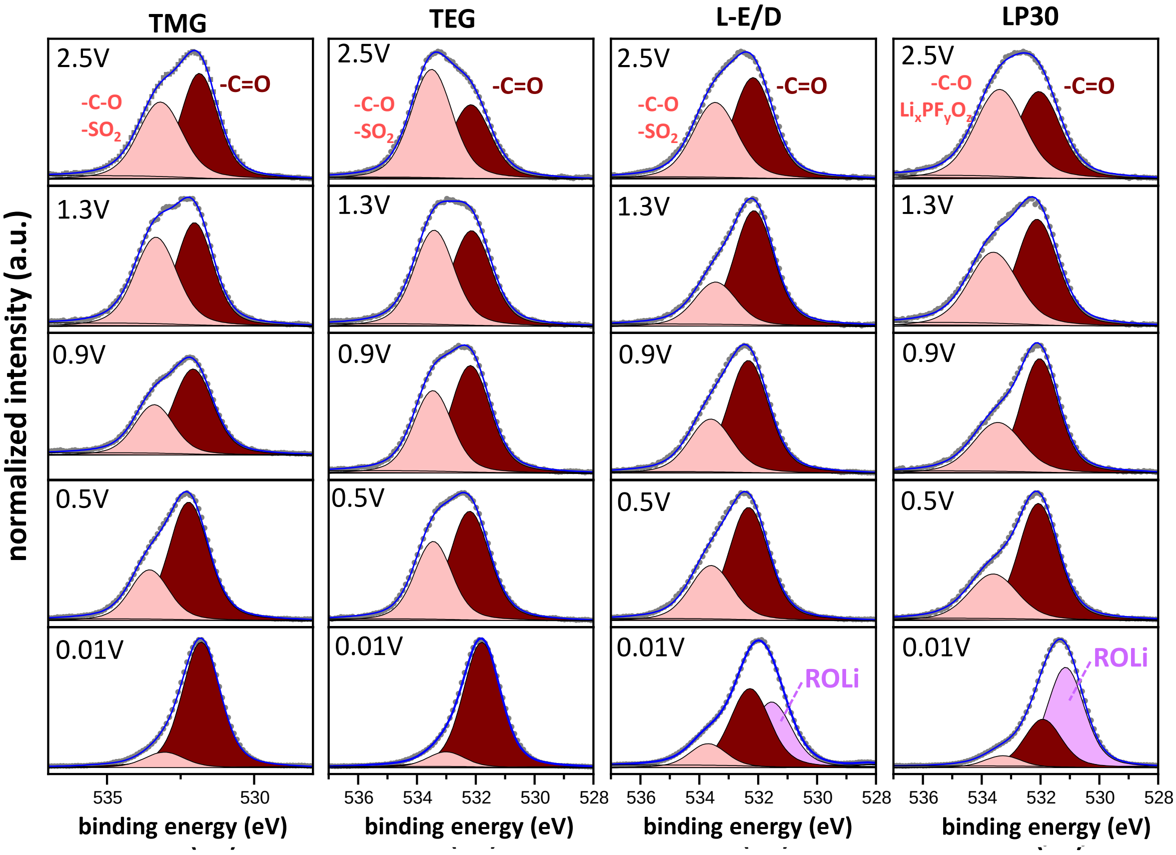

Figure A12: O1s photoelectron spectra of electrodes cycled in TMG, TEG, L-E/D, and LP30 electrolyte at 2.5 V, 1.3 V, 0. 9 V, 0.5 V, and 0.01 V.

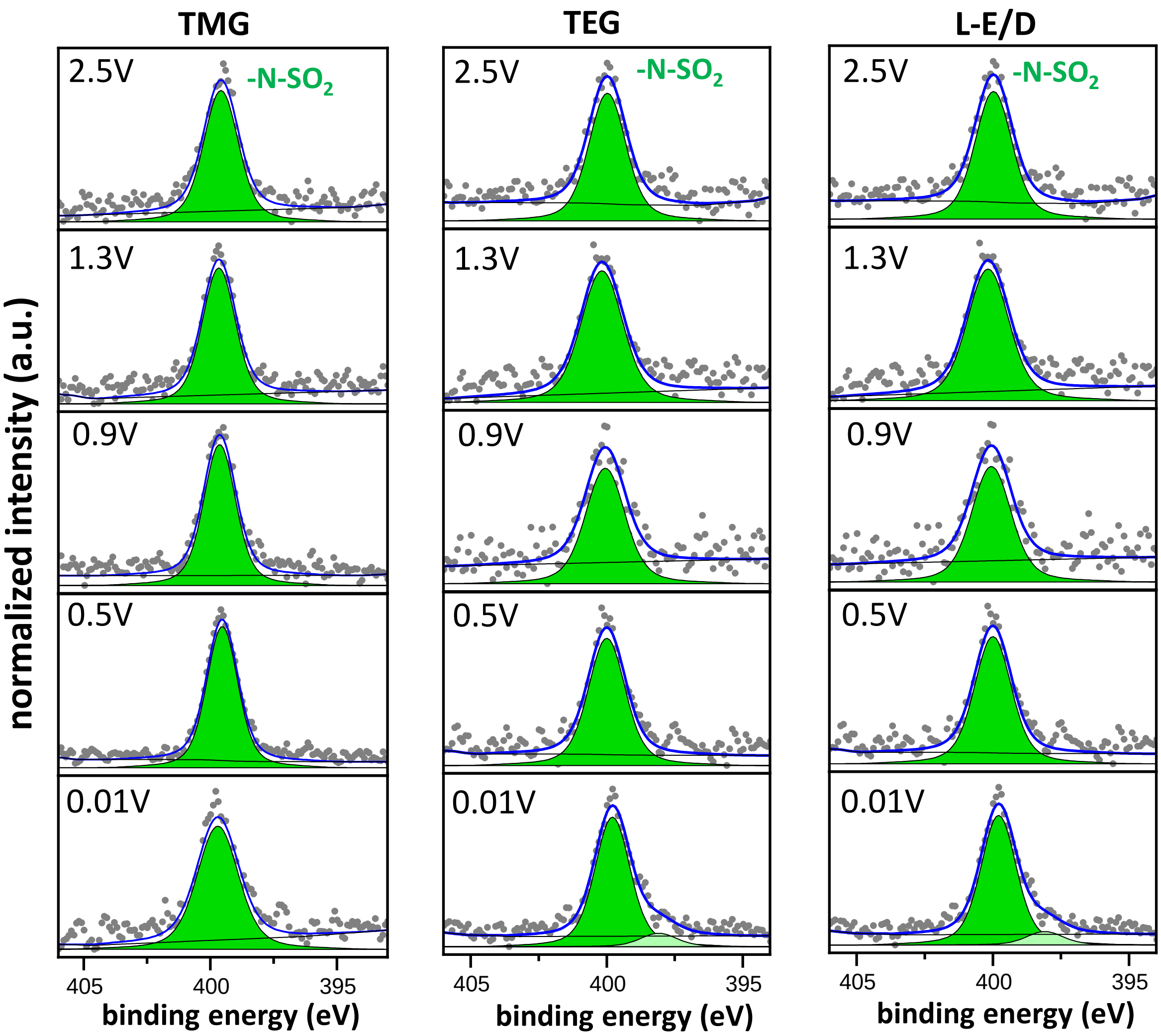

Figure A13: N1s photoelectron spectra of electrodes cycled in TMG, TEG, and L-E/D electrolyte at 2.5 V, 1.3 V, 0. 9 V, 0.5 V, and 0.01 V.

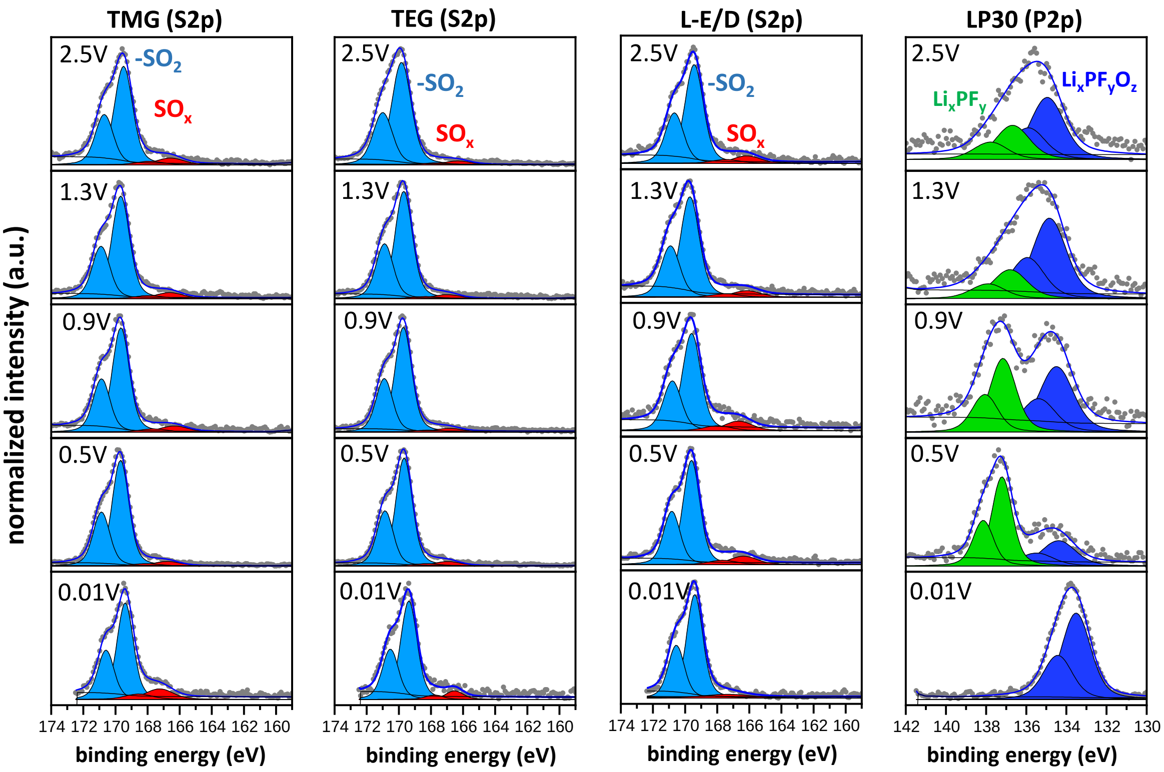

Figure A14: S2p photoelectron spectra of electrodes cycled in TMG, TEG, and L-E/D electrolyte at 2.5 V, 1.3 V, 0. 9 V, 0.5 V, and 0.01 V. As well as P2p photoelectron spectra of electrodes cycled in LP30 electrolyte at 2.5 V, 1.3 V, 0. 9 V, 0.5 V, and 0.01 V.

Evolution of SEI composition during aging. **Figure A15-Figure A17** displays the O1s, N1s, P2p, and S2p spectra after 1, 10, and 100 cycles in fully delithiated state (i.e., 1.5 V).

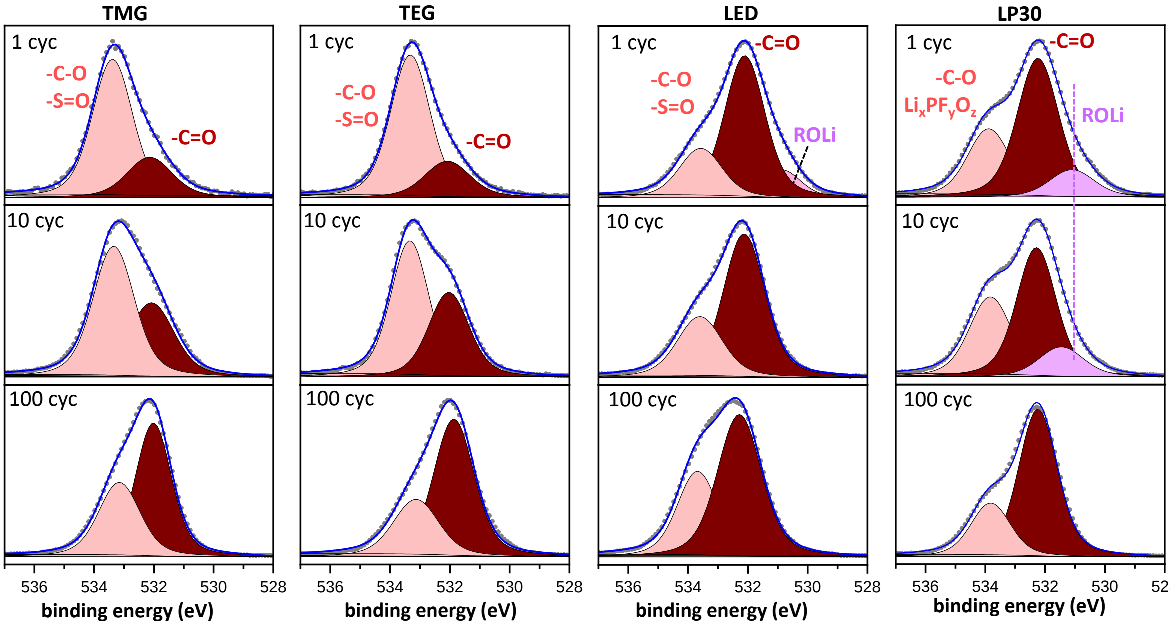

Figure A15: O1s photoelectron spectra of electrodes cycled in TMG, TEG, L-E/D, and LP30 electrolyte after 1, 10, and 100 cycles.

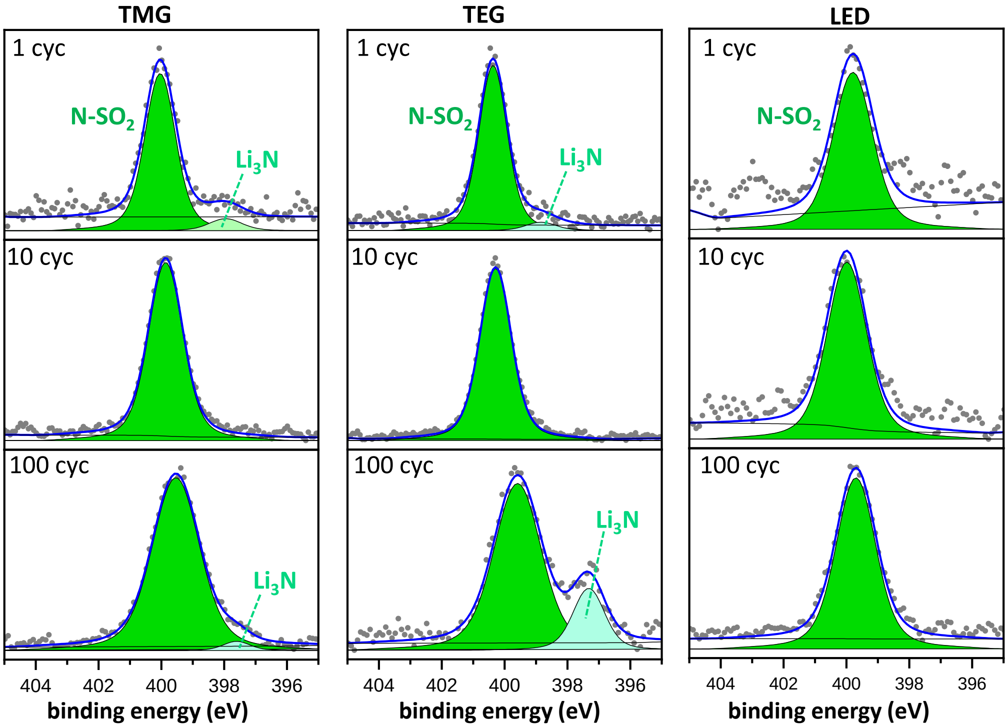

Figure A16: N1s photoelectron spectra of electrodes cycled in TMG, TEG, and L-E/D electrolyte after 1, 10, and 100 cycles.

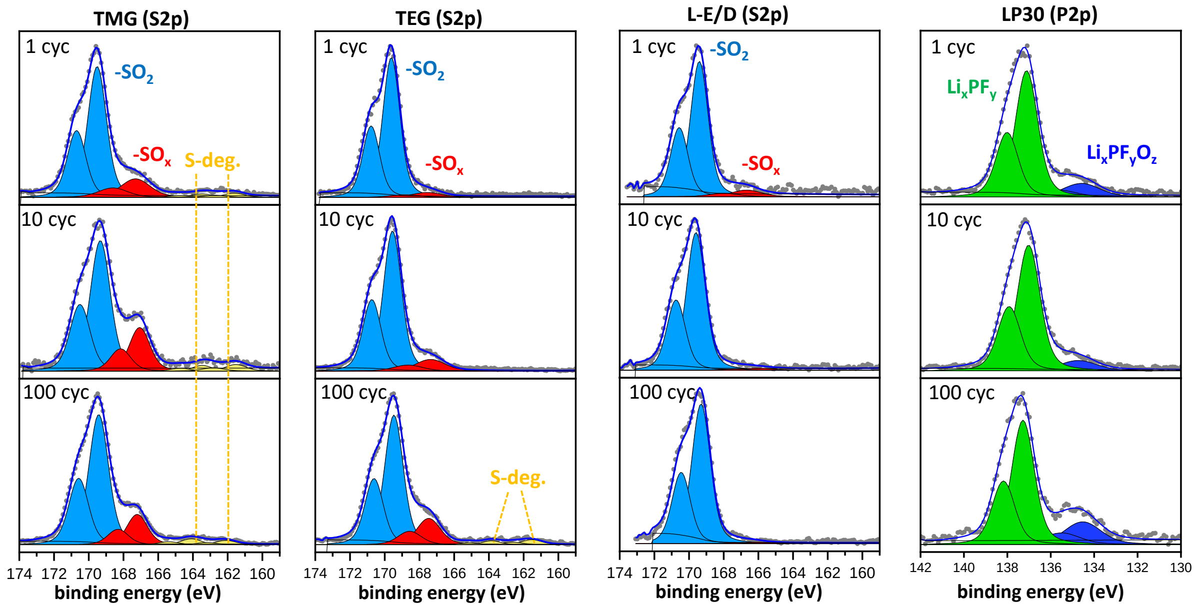

Figure A17: S2p photoelectron spectra of electrodes cycled in TMG, TEG, and L-E/D electrolyte after 1, 10, and 100 cycles. As well as P2p photoelectron spectra of electrodes cycled in LP30 electrolyte after 1, 10, and 100 cycles.

F1s, N1s, O1s, and S2p spectra of Si/Gr electrodes cycled in 30TEG:70PC and 30TEG:70PC-10FEC are shown in **Figure A18-Figure A21**.

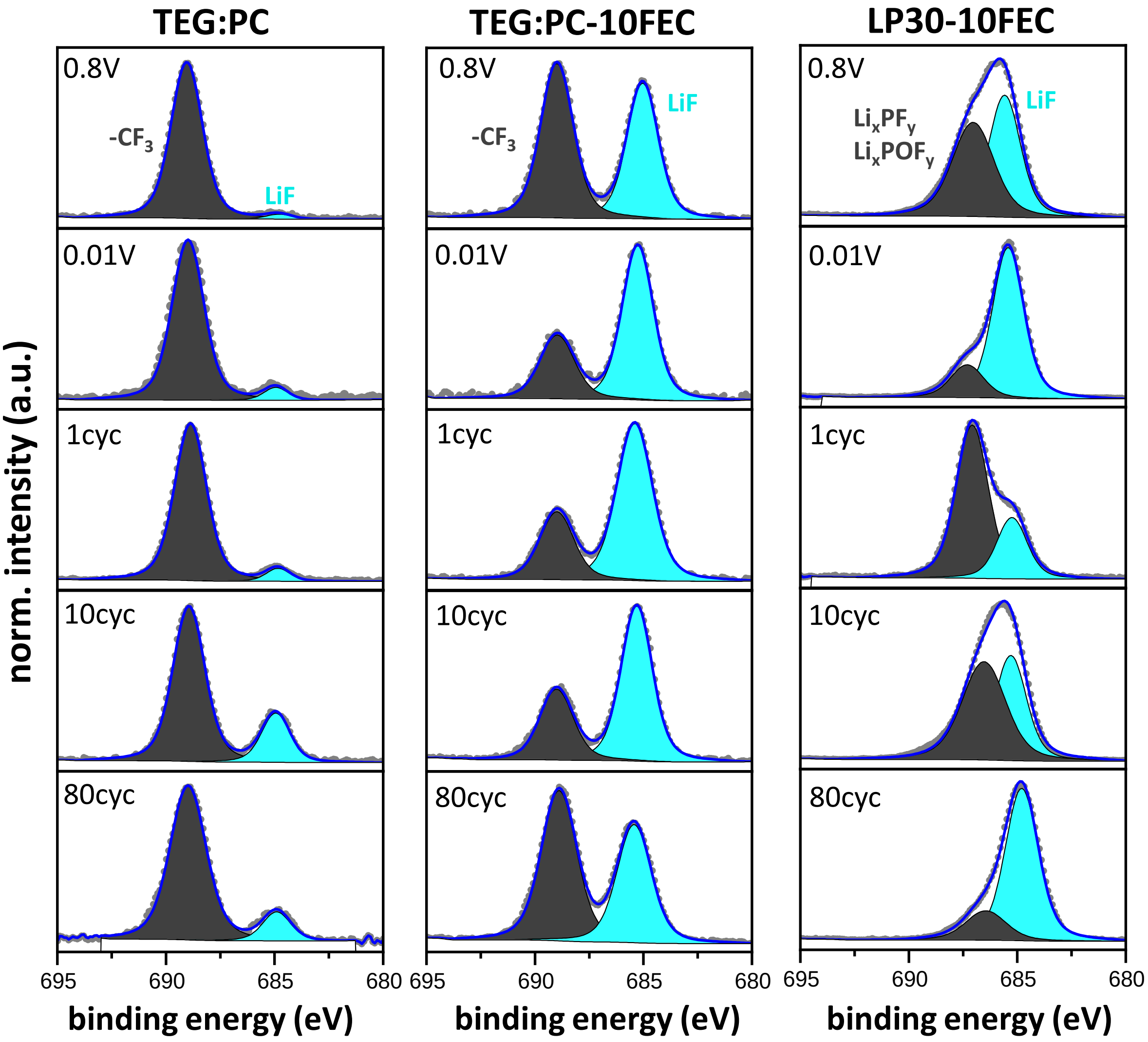

Figure A18: F1s spectra of Si/Gr electrodes cycled in 30TEG:70PC, 30TEG:70PC-10FEC, and 10FEC:90LP30, respectively.

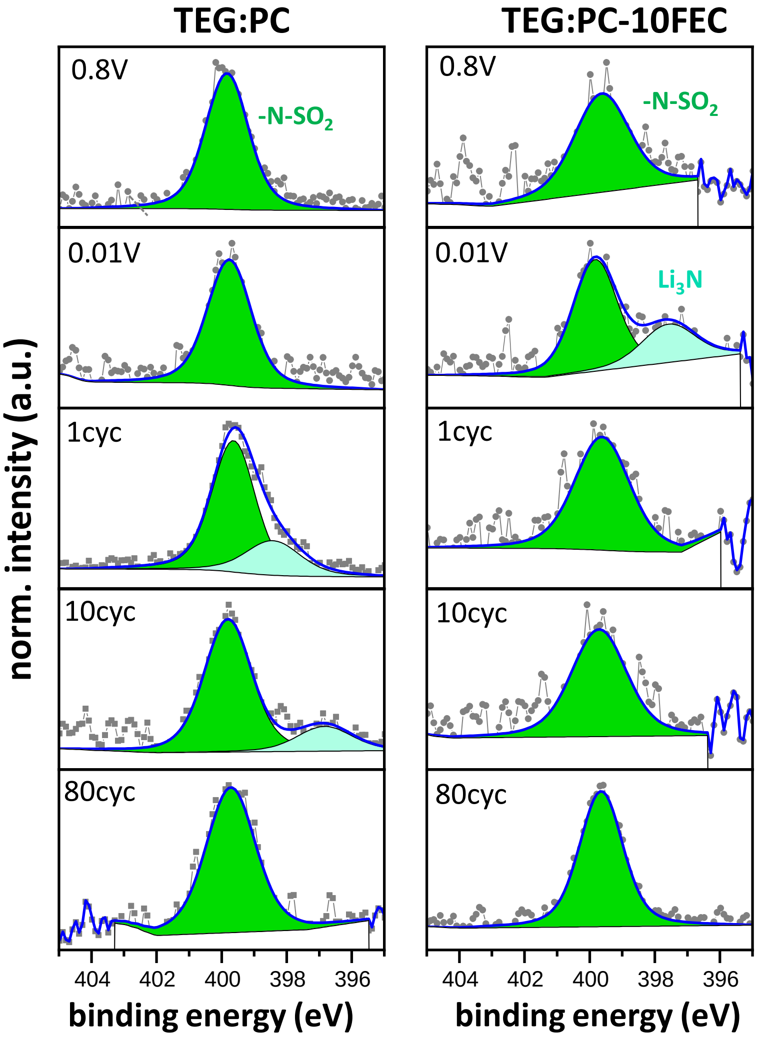

Figure A19: N1s spectra of Si/Gr electrodes cycled in 30TEG:70PC and 30TEG:70PC-10FEC, respectively.

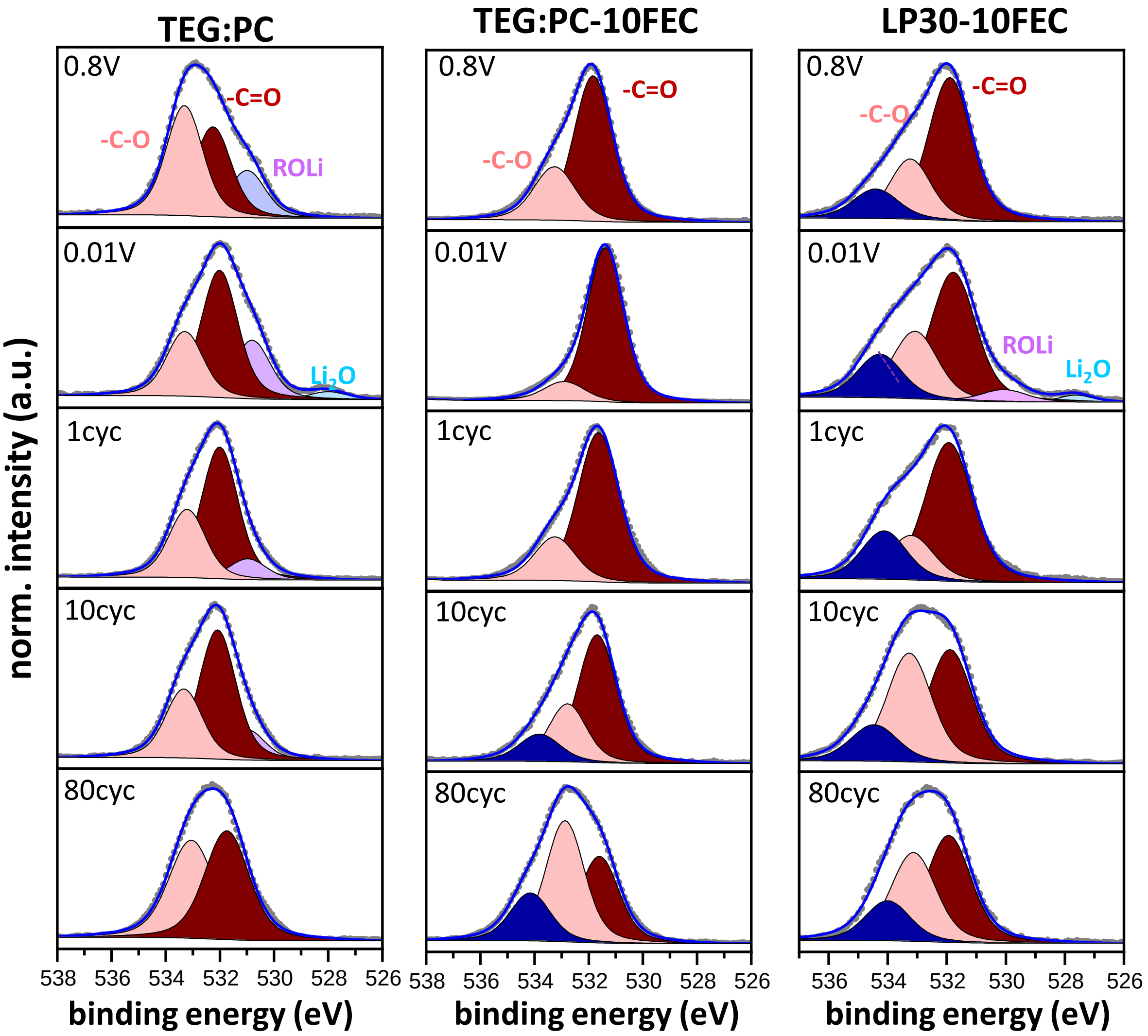

Figure A20: O1s spectra of Si/Gr electrodes cycled in 30TEG:70PC, 30TEG:70PC-10FEC, and 10FEC:90LP30, respectively.

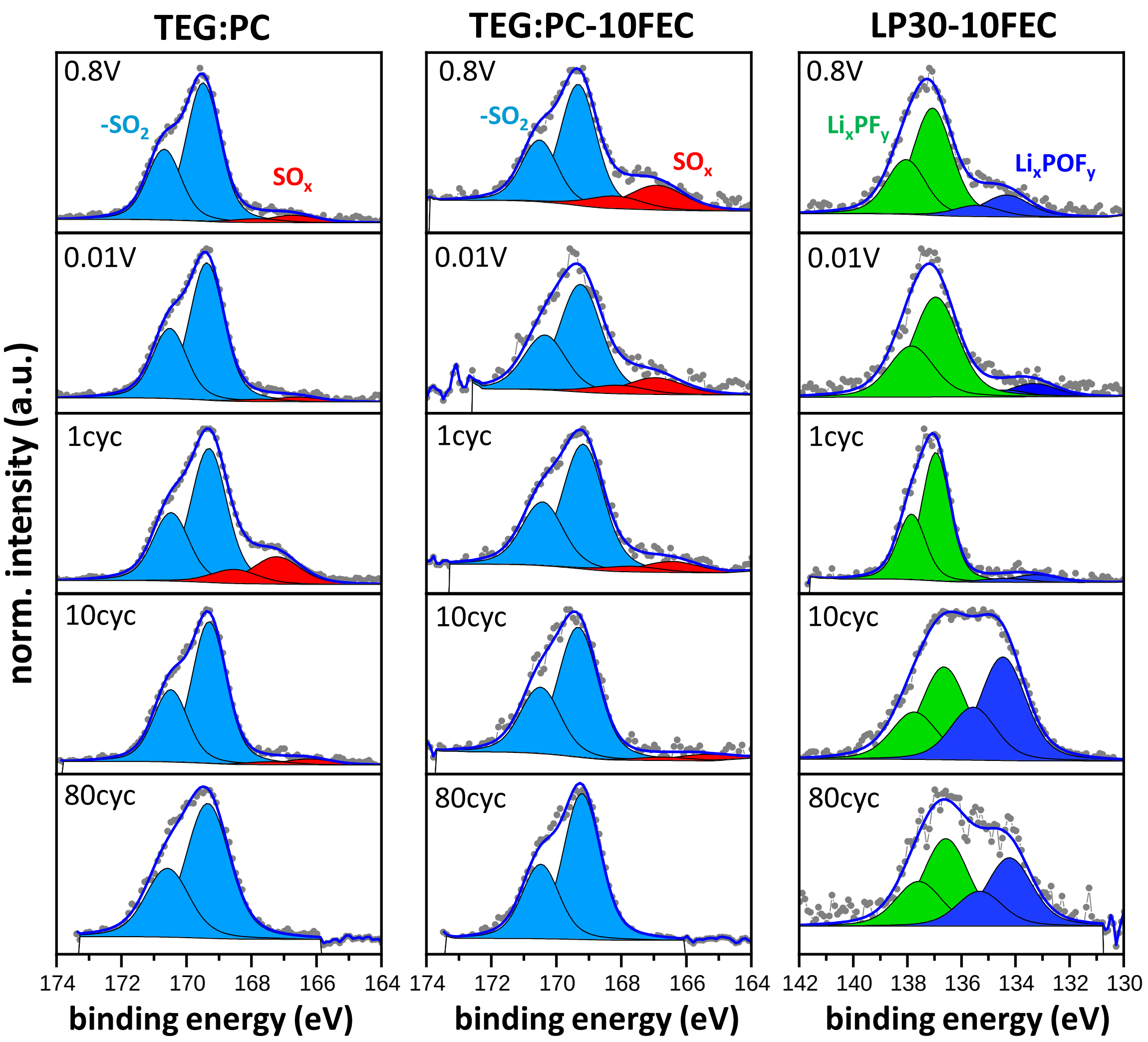

Figure A21: S2p spectra of Si/Gr electrodes cycled in 30TEG:70PC, and 30TEG:70PC-10FEC respectively. P2p spectra of Si/Gr electrodes cycled in 10FEC:90LP30.

Table A5: Calculation of the ratio between C=O species detected in the C1s and O1s spectra.

	C1s (at.%)	Sum (at.%)	O1s (at.%)	C1s/O1s
TMG	-CO$_2$: 2*2 = 4 -CO$_3$: 7.7*3 = 23.1	SUM: 27.1	-C=O: 29.0	1.1
TEG	-CO$_2$: 2.1*2 = 4.2 -CO$_3$: 7.8*3 = 23.4	SUM: 27.6	-C=O: 29.6	1.1

Table A6: Binding energies, full widths at half maximum, and atomic percentages of SEI components detected on electrodes cycled in TMG electrolyte at different cycling stages.

TEG		TEG_2.5V			TEG_1.3V			TEG_0.9V			TEG_05V			TEG_0.01V			TEG_1cyc_deli			TEG_10cyc_deli			TEG_100cyc_deli		
Element	Component	Peak BE	FWHM eV	Atomic %	Peak BE	FWHM eV	Atomic %	Peak BE	FWHM eV	Atomic %	Peak BE	FWHM eV	Atomic %	Peak BE	FWHM eV	Atomic %	Peak BE	FWHM eV	Atomic %	Peak BE	FWHM eV	Atomic %	Peak BE	FWHM eV	Atomic %
C1s	graphite	284.27	0.75	37.3	284.3	0.77	32.6	284.04	0.73	13.7	283.89	0.7	7.2				283.37	0.72	1.2						
	-CH	285	1.4	9.1	285	1.4	14.1	285.01	1.4	21.3	285	1.4	21.4	285	1.12	21.7	285	1.3	12.1	285	1.34	6.3	285	1.25	25.8
	-C-O	286.6	1.6	1.4	286.8	1.5	1.9	286.93	1.37	2.8	286.96	1.31	3.3	286.82	1.27	1.4	286.98	1.52	4.5	287.02	1.49	4.9	286.81	1.42	3.6
	-CO$_2$	288.97	1.6	2.8	288.97	1.5	3.9	288.97	1.52	4.9	289.1	1.6	3.9	289.02	1.27	2.1	289.17	1.6	1.4	289.15	1.44	1.0	289.05	1.42	2.7
	-CO$_3$							290.41	1.5	1.6	290.4	1.3	2.4	290.11	1.18	7.8	290.65	1.13	0.8	290.58	1.31	1.6	290.3	1.2	1.4
	-CF$_3$	293.31	1.5	4.2	293.3	1.32	2.8	293.37	1.15	2.8	293.38	1.05	3.0	293.33	1.1	0.6	293.3	1.1	5.6	293.25	1.2	3.6	293.19	1.2	3.1
F1s	-CF$_3$	689.1	1.73	15.2	689.21	1.76	11.4	689.22	1.71	12.6	689.19	1.7	13.7	689.02	1.75	3.3	689.05	1.68	22.9	689.04	1.73	17.1	688.98	1.77	12.6
	LiF	684.36	1.16	0.1	685.16	1.68	0.8	685.01	1.42	0.4	684.96	1.43	0.4	684.86	1.6	0.34	685.25	1.46	4.1	685.29	1.46	12.2	685.12	1.41	1.9
Li1s	Li-X	56.31	2.68	7.2	56.24	1.83	8.2	56.04	1.83	10.6	56.02	1.79	13.0	55.51	1.56	27.9	56.26	1.6	11.4	56.27	1.53	19.7	55.92	1.78	18.0
	Li-Y																54.36	1.6	2.2	55.37	1.55	2.5			
N1s	N-SO$_2$	400.03	1.53	2.2	400.11	1.57	1.7	400.09	1.49	1.8	400.03	1.42	2.0	399.67	1.75	0.5	399.98	1.38	3.6	399.87	1.54	2.6	399.77	1.5	2.0
	Li$_3$N																397.99	1.5	0.2			0.2	397.72	1.94	0.7
O1s	-C=O	531.87	1.5	4.0	532.15	1.6	9.2	532.18	1.6	12.9	532.21	1.6	14.7	531.79	1.5	29.6	532.09	1.8	5.1	532.08	1.53	5.5	532.02	1.6	13.1
	-C-O	533.31	1.6	11.3	533.43	1.62	9.4	533.46	1.56	9.7	533.45	1.5	10.0	533.01	1.53	3.8	533.32	1.57	17.7	533.27	1.73	16.7	533.19	1.57	10.2
S2p	-SO$_2$ 2p3	169.65	1.27	3.9	169.7	1.31	2.7	169.72	1.23	3.1	169.67	1.22	3.5	169.38	1.21	0.8	169.62	1.16	6.4	169.55	1.24	4.9	169.47	1.27	3.8
	-SO$_2$ 2p1	170.85	1.27	0	170.89	1.31	0	170.91	1.23	0	170.86	1.22	0	170.53	1.21	0	170.79	1.16	0	170.74	1.24	0	170.62	1.27	0
	-SO$_x$ 2p3	166.7	2	0.2	167	1.4	0.1	166.87	2	0.2	166.96	2	0.2	166.53	1.3	0.1	167.56	2	0.4	167.36	2	0.7	167.46	1.6	0.9
	-SO$_x$ 2p1	168	2	0	168.11	1.4	0	168.17	2	0	168.26	2	0	167.79	1.3	0	168.83	2	0	168.66	2	0	168.56	1.6	0
	sulfur deg.																						163.85	1.24	0.1
	sulfur deg.																						165.15	1.24	0
	sulfur deg.																						161.54	1.4	0.2
	sulfur deg.																						162.64	1.4	0
Si2p	Si^0 2p3	99.65	0.91	0.5	99.7	0.73	0.6	99.37	0.88	0.5	99.29	0.71	0.4												
	Si^0 2p1	100.22	0.92	0	100.41	0.73	0	100.01	0.88	0	99.92	0.71	0												
	SiO$_2$ 2p3	104.69	1.9	0.3	103.5	2.34	0.6	103.13	2.27	0.5	102.87	2.39	0.4												
	SiO$_2$ 2p1	105.42	1.9	0	104.03	2.34	0	103.66	2.27	0	103.4	2.39	0												

Table A7: Binding energies, full widths at half maximum, and atomic percentages of SEI components detected on electrodes cycled in TEG electrolyte at different cycling stages.

TMG		TMG_2.5V			TMG_1.3V			TMG_0.9V			TMG_05V			TMG_0.01V			TMG_1cyc_deli			TMG_10cyc_deli			TMG_100cyc_deli		
Element	Component	Peak BE	FWHM eV	Atomic %	Peak BE	FWHM eV	Atomic %	Peak BE	FWHM eV	Atomic %	Peak BE	FWHM eV	Atomic %	Peak BE	FWHM eV	Atomic %	Peak BE	FWHM eV	Atomic %	Peak BE	FWHM eV	Atomic %	Peak BE	FWHM eV	Atomic %
C1s	graphite	284.3	0.75	39.6	284.3	0.72	38.5	283.97	0.73	21.6	283.8	0.71	6.4				283.48	0.75	4.3						
	-CH	285	1.31	13.7	285.02	1.3	14.8	285	1.4	23.2	285	1.31	17.8	285	1.12	22.0	285	1.23	28.1	285	1.34	5.3	285	1.2	15.9
	-C-O	286.4	1.6	3.2	286.48	1.5	1.8	286.68	1.53	2.2	286.9	1.52	3.7	286.78	1.31	1.4	286.79	1.5	3.1	287.02	1.49	4.1	286.76	1.5	4.0
	-CO_2	288.65	1.6	5.4	288.89	1.43	4.7	288.93	1.5	5.8	289.12	1.6	3.2	288.98	1.31	2.0	289.08	1.5	3.4	289.15	1.44	0.9	288.91	1.5	2.2
	-CO_3							290.67	1.6	1.0	290.4	1.4	4.7	290.08	1.2	7.7	290.29	1.4	2.3	290.58	1.31	1.4	290.15	1.4	4.1
	-CF_3	293.2	1.49	2.3	293.28	1.48	2.3	293.34	1.2	2.1	293.39	1.05	2.5	293.3	1.1	0.7	293.26	1.09	2.3	293.25	1.2	3.1	293.12	1.18	3.1
F1s	-CF_3	689.02	1.78	8.6	689.19	1.74	8.8	689.2	1.72	9.5	689.21	1.71	10.9	688.99	1.7	3.7	689.06	1.74	10.0	689.06	1.73	12.6	688.98	1.74	11.7
	LiF	684.75	1.42	0.5	684.84	1.5	0.2	684.9	1.46	0.3	684.99	1.35	0.3	684.88	1.58	0.5	685.03	1.44	0.9	685.29	1.48	18.6	685.17	1.45	2.6
Li1s	Li-X	56.08	2.01	6.0	56.18	1.88	6.3	56.04	2.01	9.7	56.02	1.69	16.5	55.44	1.59	27.6	55.79	1.71	15.9	56.18	1.42	22.2	56.08	1.7	21.1
	Li-Y																			54.81	2	3.2			
N1s	N-SO_2	400.06	1.46	1.1	400.16	1.68	1.4	400.14	1.61	1.6	400.03	1.57	1.8	399.7	1.94	0.7	399.83	1.46	1.5	399.84	1.55	2.1	399.62	1.77	2.6
	Li_3N	398.35	1	0.1													397.56	2	0.4				397.46	1.09	0.1
O1s	-C=O	531.92	1.6	8.8	532.02	1.5	8.2	532.08	1.6	12.1	532.23	1.6	19.9	531.8	1.53	29.0	531.99	1.68	15.7	532.08	1.8	6.8	532.09	1.46	17.5
	-C-O	533.28	1.65	7.1	533.33	1.7	7.9	533.4	1.59	7.0	533.56	1.57	8.4	533.05	1.6	3.8	533.25	1.69	8.2	533.35	1.64	11.0	533.28	1.53	9.9
S2p	-SO_2 2p3	169.51	1.4	1.8	169.66	1.31	2.0	169.66	1.26	2.1	169.69	1.24	3.1	169.39	1.19	0.9	169.52	1.27	2.7	169.53	1.24	3.6	169.42	1.35	3.9
	-SO_2 2p1	170.62	1.7	0	170.89	1.31	0	170.87	1.26	0	170.87	1.24	0	170.59	1.19	0	170.7	1.27	0	170.72	1.24	0	170.58	1.35	0
	-SO_x 2p3	165.79	2.5	0.1	166.62	2	0.2	166.34	2	0.2	166.76	2	0.2	167.26	2	0.2	167.3	2	0.6	167.54	1.97	0.7	167.21	1.4	0.9
	-SO_x 2p1	167.09	2.5	0	167.92	2	0	167.64	2	0	168.06	2	0	168.56	2	0	168.6	2	0	168.84	1.97	0	168.31	1.4	0
	sulfur deg.																163.5	1.4	0.1	164.1	1.79	0.1	164.1	1.4	0.2
	sulfur deg.																164.8	1.4	0	165.21	1.5	0	165.4	1.4	0
	sulfur deg.																161.62	1.4	0.1	162.2	1.5	0.7	162.1	1.4	0.1
	sulfur deg.																162.72	1.4	0	163.38	1.5	0	163.2	1.4	0
Si2p	Si^0 2p3	99.73	0.84	0.9	99.73	0.72	0.8	99.35	0.83	0.8	99.21	0.63	0.3				98.42	1.94	0.3						
	Si^0 2p1	100.37	0.84	0	100.34	0.72	0	99.92	0.83	0	99.86	0.63	0				98.95	1.94	0						
	SiO_2 2p3	103.68	1.9	0.8	103.66	1.83	0.7	103.33	2.05	0.7	102.78	2	0.4				101.48	2	0.2						
	SiO_2 2p1	104.21	1.9	0	104.19	1.82	0	103.86	2.05	0	103.51	2	0				102.21	2	0						

Table A8: Binding energies, full widths at half maximum, and atomic percentages of SEI components detected on electrodes cycled in L-E/D electrolyte at different cycling stages.

LED		LED_2.5V			LED_1.3V			LED_0.9V			LED_05V			LED_0.01V			LED_1cyc_deli			LED_10cyc_deli			LED_100cyc_deli		
Element	Component	Peak BE	FWHM eV	Atomic %	Peak BE	FWHM eV	Atomic %	Peak BE	FWHM eV	Atomic %	Peak BE	FWHM eV	Atomic %	Peak BE	FWHM eV	Atomic %	Peak BE	FWHM eV	Atomic %	Peak BE	FWHM eV	Atomic %	Peak BE	FWHM eV	Atomic %
C1s	graphite	284.4	0.78	52.4	284.39	0.74	38.8	284.09	0.72	27.5	283.87	0.72	15.7				283.09	0.87	6.4	283.53	0.8	1.9			
	-CH	285	1.2	8.8	285	1.4	20.2	285	1.4	25.6	285	1.38	26.1	285	1.13	24.4	285	1.23	27.9	285.01	1.35	11.2	285	1.29	7.6
	-C-O							286.93	1.6	3.4	286.97	1.52	4.7	286.82	1.38	5.1	286.76	1.48	5.8	286.99	1.5	5.6	286.92	1.51	10.6
	-CO$_2$	288.67	1.5	3.7	288.97	1.5	4.4	288.93	1.5	5.1	288.96	1.5	5.0	289.07	1.3	2.6	289.02	1.42	3.6	289.06	1.5	2.0	288.97	1.6	1.6
	-CO$_3$							290.7	1.58	1.4	290.57	1.27	1.9	290.41	1.21	4.9	290.5	1.16	3.7	290.28	1.29	4.6	290.46	1.31	4.8
	-CF$_3$	292.88	1.6	1.4	293.38	1.16	1.1	293.42	1.36	1.3	293.44	1.22	1.5	293.27	1.1	0.8	293.23	1.1	0.7	293.37	1.2	1.2	293.19	1.15	1.6
F1s	-CF$_3$	688.95	1.78	6.0	689.23	1.78	5.7	689.19	1.77	4.6	689.17	1.73	5.8	688.99	1.75	4.3	689.05	1.76	4.1	689.05	1.83	6.1	688.99	1.8	8.3
	-CF$_x$													687.08	1.55	0.6	687.1	1.55	0.8	687.41	1.86	1.0	686.95	1.79	1.7
	LiF	684.75	1.68	0.5	684.97	1.64	0.5	685.01	1.5	0.3	684.91	1.54	0.4	684.99	1.71	1.1	684.98	1.52	0.7	685.17	1.51	11.3	685.08	1.53	11.4
Li1s	Li-X	55.98	1.94	6.7	56.11	1.9	6.8	55.96	1.6	7.2	55.91	1.84	11.0	55.4	1.9	24.6	55.58	1.83	17.2	55.97	1.7	24.4	55.85	1.61	21.0
	Li-Y																								
N1s	N-SO$_2$	399.98	1.6	0.9	400.18	1.83	1.1	400.05	1.71	0.7	400	1.6	0.9	399.74	1.54	0.7	399.8	1.5	0.6	400.04	1.5	0.8	399.7	1.5	1.2
	Li$_3$N																			398.6	1.5	0.1			
O1s	ROLi																530.87	1.5	3.3						
	-C=O	531.84	1.5	8.6	532.08	1.52	10.3	532.12	1.75	13.4	532.11	1.78	15.6	531.88	1.85	23.9	532.11	1.6	18.0	532.07	1.57	16.4	532.29	1.74	17.2
	-C-O	533.18	2	7.9	533.4	2	7.7	533.7	2	6.6	533.59	1.96	8.0	533.46	1.75	5.7	533.58	1.7	6.7	533.47	1.93	10.1	533.69	1.6	9.6
S2p	-SO$_2$ 2p3	169.44	1.36	1.4	169.7	1.38	1.3	169.59	1.35	1.1	169.6	1.23	1.5	169.42	1.2	1.1	169.4	1.2	1.1	169.62	1.32	1.4	169.31	1.26	2.1
	-SO$_2$ 2p1	170.67	1.36	0	170.91	1.38	0	170.79	1.35	0	170.83	1.23	0	170.62	1.2	0	170.56	1.2	0	170.79	1.32	0	170.45	1.27	0
	-SO$_x$ 2p3	166.16	2	0.2	166.16	2	0.1	166.67	2	0.2	166.36	2	0.2	167.37	1.97	0.1	166.67	2	0.1	166.01	2	0.02	166.08	2	0.04
	-SO$_x$ 2p1	167.46	2	0	167.46	2	0	167.97	2	0	167.66	2	0	168.67	1.97	0	167.97	2	0	167.11	2	0	167.38	2	0
Si2p	Si^0 2p3	99.91	0.87	0.8	99.88	0.76	0.9	99.52	0.8	0.7	99.26	0.72	0.8												
	Si^0 2p1	100.49	0.87	0	100.5	0.76	0	100.19	0.79	0	99.89	0.72	0												
	SiO$_2$ 2p3	103.65	2	0.7	103.79	2	0.7	103.36	2	0.5	102.93	2	0.7												
	SiO$_2$ 2p1	104.38	2	0	104.32	2	0	103.98	2	0	103.66	2	0												

Table A9: Binding energies, full widths at half maximum, and atomic percentages of SEI components detected on electrodes cycled in LP30 electrolyte at different cycling stages.

LP30		LP30_2.5V			LP30_1.3V			LP30_0.9V			LP30_05V			LP30_0.01V			LP30_1cyc_deli			LP30_10cyc_deli			LP30_100cyc_deli		
Element	Component	Peak BE	FWHM eV	Atomic %	Peak BE	FWHM eV	Atomic %	Peak BE	FWHM eV	Atomic %	Peak BE	FWHM eV	Atomic %	Peak BE	FWHM eV	Atomic %	Peak BE	FWHM eV	Atomic %	Peak BE	FWHM eV	Atomic %	Peak BE	FWHM eV	Atomic %
C1s	graphite	284.38	0.73	58.7	284.35	0.75	48.9	284.01	0.74	28.8	283.67	0.8	23.8				283.12	0.86	5.0	282.86	0.93	1.3			
	-CH	285	1.4	9.4	285	1.4	8.6	285	1.4	18.1	285	1.4	19.1	285	1.14	20.8	285	1.5	10.4	285	1.5	8.6	285	1.22	18.7
	-C-O							286.8	1.6	3.2	286.99	1.4	3.9	286.56	1.57	3.6	286.96	1.57	9.8	286.96	1.48	11.8	286.76	1.39	10.4
	-CO_2	290.88	2	3.3	288.87	1.6	2.0	288.8	1.58	3.5	288.86	1.4	3.5	288.96	1.54	2.3	289	1.42	1.6	289	1.48	1.5	288.93	1.31	2.6
	-CO_3				290.85	2	1.0	290.42	1.6	2.4	290.51	1.51	3.4	290.1	1.2	2.2	290.5	1.5	6.2	290.52	1.38	6.9	290.27	1.29	6.9
F1s	$Li_xPF_yO_z$	687.96	2	1.2	687.91	2.3	2.4	687.17	2.11	4.9	687.2	1.86	7.7	687.27	1.71	0.7	687.24	1.71	11.8	687.18	1.7	12.9	687.14	1.74	7.0
	LiF	685.72	1.97	5.0	685.51	1.75	8.8	685.27	1.6	5.7	685.27	1.53	3.0	684.81	1.5	7.3	685.26	1.62	5.0	685.19	1.6	5.5	685.09	1.5	2.3
Li1s	Li-X	56.44	2	5.0	56.35	1.78	10.7	56.15	1.75	12.6	56.06	1.78	12.2	55.26	1.65	33.1	55.82	1.98	19.9	55.87	1.86	20.0	56.23	1.62	19.4
	Li-Y																						54.68	2	0.7
O1s	ROLi													531.15	1.5	17.4	531.1	1.78	3.5	531.1	1.6	1.5			
	-C=O	532.06	1.75	6.9	532.12	1.68	7.0	532.03	1.53	11.0	532.07	1.6	13.7	531.92	1.5	8.4	532.24	1.64	16.3	532.25	1.71	18.7	532.24	1.53	22.2
	-C-O	533.39	2	5.8	533.61	2	5.8	533.45	2	6.4	533.61	1.96	6.7	533.28	1.5	2.1	533.89	1.68	8.3	533.88	1.6	9.2	533.82	1.57	8.3
P2p	Li_xPF_y 2p3	136.68	2	0.4	136.81	2	0.3	137.16	1.53	0.6	137.21	1.21	0.9				137.11	1.22	1.6	137.02	1.25	1.9	137.28	1.24	1.3
	Li_xPF_y 2p1	137.78	2	0	137.91	2	0	138.06	1.53	0	138.14	1.21	0				138.01	1.22	0	137.92	1.25	0	138.18	1.24	0
	Li_xPOF_y 2p3	135.9	2	0.1	134.85	2	0.9	134.49	2	0.7	134.39	2	0.4	133.52	1.71	2.2	134.59	2	0.3	134.73	2	0.3	134.53	2	0.4
	Li_xPOF_y 2p1	134.95	2	0	135.95	2	0	135.39	2	0	135.49	2	0	134.43	1.71	0	135.69	2	0	135.83	2	0	135.51	2	0
Si2p	Si^0 2p3	99.82	0.74	1.1	99.85	0.88	0.9	99.44	0.83	0.9	99.09	0.79	0.8				98.1	1.53	0.3						
	Si^0 2p1	100.47	0.74	0	100.48	0.88	0	100.09	0.83	0	99.71	0.79	0				98.63	1.53	0						
	SiO_2 2p3	103.87	2	0.1	103.97	2	0.8	103.59	2	0.8	103.26	2	0.7				101.02	2	0.2						
	SiO_2 2p1	104.4	2	0	104.7	2	0	104.32	2	0	103.98	2	0				101.75	2	0						

Table A10: Binding energies, full widths at half maximum, and atomic percentages of SEI components detected on electrodes cycled in 30TEG:70PC electrolyte at different cycling stages.

30TEG:70PC		0.8V			0. 01V			1cyc			10cyc			100cyc		
Element	Component	Peak BE	FWHM eV	Atomic %	Peak BE	FWHM eV	Atomic %	Peak BE	FWHM eV	Atomic %	Peak BE	FWHM eV	Atomic %	Peak BE	FWHM eV	Atomic %
C1s	graphite	283.55	0.76	4.9	282.45	0.9	4.1	283.33	0.76	4.4	283.39	0.73	2.9			
	-CH	285	1.33	24.4	285	1.27	28.0	285	1.38	15.2	285	1.24	22.8	285	1.37	27.4
	-C-O	286.54	1.6	5.5	286.47	1.5	5.5	286.69	1.38	5.5	286.6	1.6	7.2	286.41	1.64	12.2
	$-CO_2$	289.04	1.2	2.0	288.95	1.26	2.5	288.98	1.38	2.2	289.03	1.56	3.0	288.62	1.7	3.0
	$-CO_3$	290.51	1.2	1.4	290.3	1.2	2.1	290.25	1.27	4.4	290.33	1.24	3.6	290.1	1.57	2.6
	$-CF_3$	293.22	1.1	3.2	293.18	1	1.0	293.07	1.14	2.4	293.19	1.03	1.6	293.14	1.15	1.2
F1s	$-CF_3$	689.04	1.71	13.6	688.99	1.74	6.4	688.87	1.74	11.1	688.94	1.75	7.4	688.98	1.97	6.4
	LiF	684.8	1.38	0.3	684.94	1.27	0.4	684.84	1.29	0.7	684.95	1.54	2.1	684.9	1.53	0.9
Li1s	Li-X	55.8	2.01	12.2	55.01	1.99	18.3	55.61	1.67	17.4	55.65	1.75	17.9	55.52	2.02	16.7
	Li-Y				56.09	1.53	3.1									
N1s	$N-SO_2$	399.84	1.57	2.3	399.76	1.6	1.2	399.63	1.57	1.5	399.81	1.71	1.4	399.72	1.82	1.3
	Li_3N							398.42	2	0.5	396.83	2	0.3			
O1s	Li_2O				528	1.6	0.8									
	ROLi	530.99	1.6	4.7	530.81	1.6	5.8	530.97	1.6	2.9	531.01	1.6	3.7			
	-C=O	532.26	1.6	8.9	532.01	1.6	12.6	532.01	1.6	18.4	532.09	1.6	15.6	531.74	1.94	13.7
	-C-O	533.31	1.6	10.8	533.29	1.6	6.4	533.21	1.6	9.6	533.33	1.6	8.4	533.05	1.97	12.6
S2p	$-SO_2$ 2p3	169.49	1.24	4.2	169.37	1.25	1.8	169.31	1.31	2.8	169.3	1.25	2.2	169.35	1.6	2.1
	$-SO_x$ 2p3	166.72	1.7	0.3	166.58	1.7	1.0	167.22	1.7	0.8	166.21	1.7	0.1			
Si2p	Si^0 2p3	98.93	0.72	0.9												
	Li_xSi 2p3							98.34	1.09	0.2						
	SiO_x 2p3	102.85	2	0.6				101.2	2	0.1						
	SiO_2 2p3															

Table A11: Binding energies, full widths at half maximum, and atomic percentages of SEI components detected on electrodes cycled in 30TEG:70PC-10FEC electrolyte at different cycling stages.

30TEG:70PC-10FEC		0.8V			0. 01V			1cyc			10cyc			100cyc		
Element	Component	Peak BE	FWHM eV	Atomic %	Peak BE	FWHM eV	Atomic %	Peak BE	FWHM eV	Atomic %	Peak BE	FWHM eV	Atomic %	Peak BE	FWHM eV	Atomic %
C1s	graphite	283.5	0.8	28.1				282.88	0.89	7.2	283.27	0.83	3.2	282.95	0.91	2.1
	-CH	285	1.38	17.3	285	1.2	22.8	285	1.34	22.2	285	1.36	15.3	285	1.4	11.9
	-C-O	286.8	1.2	2.5	286.47	1.38	2.5	286.53	1.5	4.6	286.53	1.42	5.0	286.55	1.49	6.6
	C_a							287.6	1.49	0.7	287.6	1.49	1.5	287.66	1.5	3.6
	$-CO_2$	288.66	1.4	3.2	288.8	1.2	2.3	288.75	1.31	2.5	288.83	1.4	2.8	288.88	1.4	2.4
	$-CO_3$	290.16	1.4	3.3	290.06	1.28	3.6	290.02	1.34	4.0	290	1.2	3.4	290	1.4	2.5
	C_b							290.8	1.2	0.1	290.8	1.35	0.7	291.06	1.2	0.9
	$-CF_3$	293.16	1.2	0.7	293.17	1	0.1	293.18	1	0.2	293.11	1.21	0.9	293.02	1.25	1.9
F1s	LiF	685.04	1.71	2.9	685.26	1.7	2.7	685.4	1.94	5.1	685.31	1.7	9.0	685.43	1.86	7.0
	$-CF_3$	688.99	1.77	3.5	688.97	1.87	1.2	688.99	1.84	2.1	689	1.81	4.4	688.89	1.93	9.3
Li1s	Li-X	55.69	1.68	12.9	54.85	1.35	21.2	55.53	2.03	23.6	55.81	2.16	26.7	55.79	2.45	22.4
	Li-Y				55.66	1.6	11.8									
N1s	$N-SO_2$	399.63	2	0.6	399.83	1.6	0.2	399.62	2	0.5	399.71	2	0.9	399.65	1.57	1.3
	Li_3N				397.58	1.97	0.1									
O1s	-C=O	531.84	1.68	15.9	531.39	1.6	27.3	531.64	1.8	20.2	531.69	1.68	14.9	531.61	1.71	8.8
	-C-O	533.26	1.8	6.3	532.91	1.79	3.8	533.25	1.8	5.9	532.78	1.64	6.6	532.87	1.68	12.0
	O_b										533.82	1.8	3.4	534.15	1.75	5.0
S2p	$-SO_2$ 2p3	169.32	1.31	0.9	169.26	1.53	0.3	169.18	1.5	0.6	169.33	1.46	1.2	169.22	1.35	2.4
	$-SO_x$ 2p3	166.9	2	0.3	166.95	2.01	0.1	166.44	2	0.1	165.37	2	0.1			
Si2p	Si^0 2p3	98.88	0.76	1.2												
	Li_xSi 2p3							97.74	1.72	0.3						
	SiO_x 2p3							100.52	2	0.2						
	SiO_2 2p3	102.82	1.84	0.7												

Table A12: Binding energies, full widths at half maximum, and atomic percentages of SEI components detected on electrodes cycled in 30TEG:70PC electrolyte at different cycling stages.

10FEC:90LP30		0.8V			0. 01V			1cyc			10cyc			100cyc		
Element	Component	Peak BE eV	FWHM eV	Atomic %	Peak BE eV	FWHM eV	Atomic %	Peak BE eV	FWHM eV	Atomic %	Peak BE eV	FWHM eV	Atomic %	Peak BE eV	FWHM eV	Atomic %
C1s	graphite	283.17	0.86	16.2	282.25	1.03	2.7	282.36	0.87	5.3	282.98	0.79	3.3	283.76	0.88	1.2
	-CH	285	1.4	12.6	285	1.5	12.8	285	1.46	15.9	285	1.5	8.0	285.01	1.5	10.8
	-C-O	286.43	1.6	4.8	286.37	1.6	4.1	286.71	1.49	5.9	286.56	1.6	6.6	286.77	1.6	8.2
	C_a, C=O, OCO	287.6	1.31	1.1	287.6	1.4	1.6	287.8	1.4	2.4	287.76	1.49	2.5	287.96	1.4	1.9
	$-CO_2$	288.71	1.3	2.1	289	1.6	2.0	289.1	1.6	3.1	288.9	1.6	1.4	288.91	1.6	1.7
	$-CO_3$	290.06	1.44	2.6	290.1	1.4	1.3	290.2	1.4	3.2	289.9	1.4	1.1	290.08	1.4	1.1
	$ROCO_2R$, C_b	291.13	1.31	0.6	291.02	1.4	0.8	291.12	1.4	1.2	291.02	1.2	0.3	290.98	1.4	0.9
F1s	LiF	685.59	1.72	10.3	685.42	1.70	20.8	685.25	1.64	4.9	685.3	1.7	12.7	684.8	1.81	22.6
	$Li_xPF_yO_z$ & SiO_xF_y	687.03	2.27	10.5	687.31	1.79	4.8	687.08	1.75	13.2	686.53	2.38	16.6	686.45	2.19	5.3
Li1s	Li-X	56.23	2.01	19.8	56.13	1.74	28.7	55.79	2.22	19.4	56.34	2.43	30.9	55.88	1.73	28.3
	Li-Y	-	-	-	53.70	2.00	4.8									
O1s	Li_2O	-			527.64	1.3	0.3									
	ROLi	-			530.06	1.8	0.7									
	-C=O	531.91	1.72	10.4	531.78	1.8	7.0	531.93	1.9	14.4	531.89	1.8	6.3	531.94	1.8	7.6
	-C-O	533.23	1.64	4.2	533.08	1.8	3.7	533.2	1.8	4.4	533.27	1.8	6.1	533.13	1.8	6.3
	O_b	534.41	1.8	2.2	534.26	1.8	2.4	534.12	1.8	4.8	534.46	1.9	2.2	534	1.8	2.8
Si2p	Si^0 2p3	98.54	0.72	0.8	-	-	-									
	Li_xSi															
	Li_xSiO_y	101.67	0.83	0.1												
	SiO_2 2p3	103	0.84	0.3												
	SiO_xF_y				104.75	2	0.4									
P2p	Li_xPF_y	137.07	1.72	1.1	136.95	1.97	1.0	136.95	1.23	1.8	136.65	2	1.0	136.58	2	0.8
	$Li_xPF_yO_z$	134.33	2	0.3	133.34	2	0.1	133.27	2	0.2	134.47	2	1.1	134.22	2	0.6

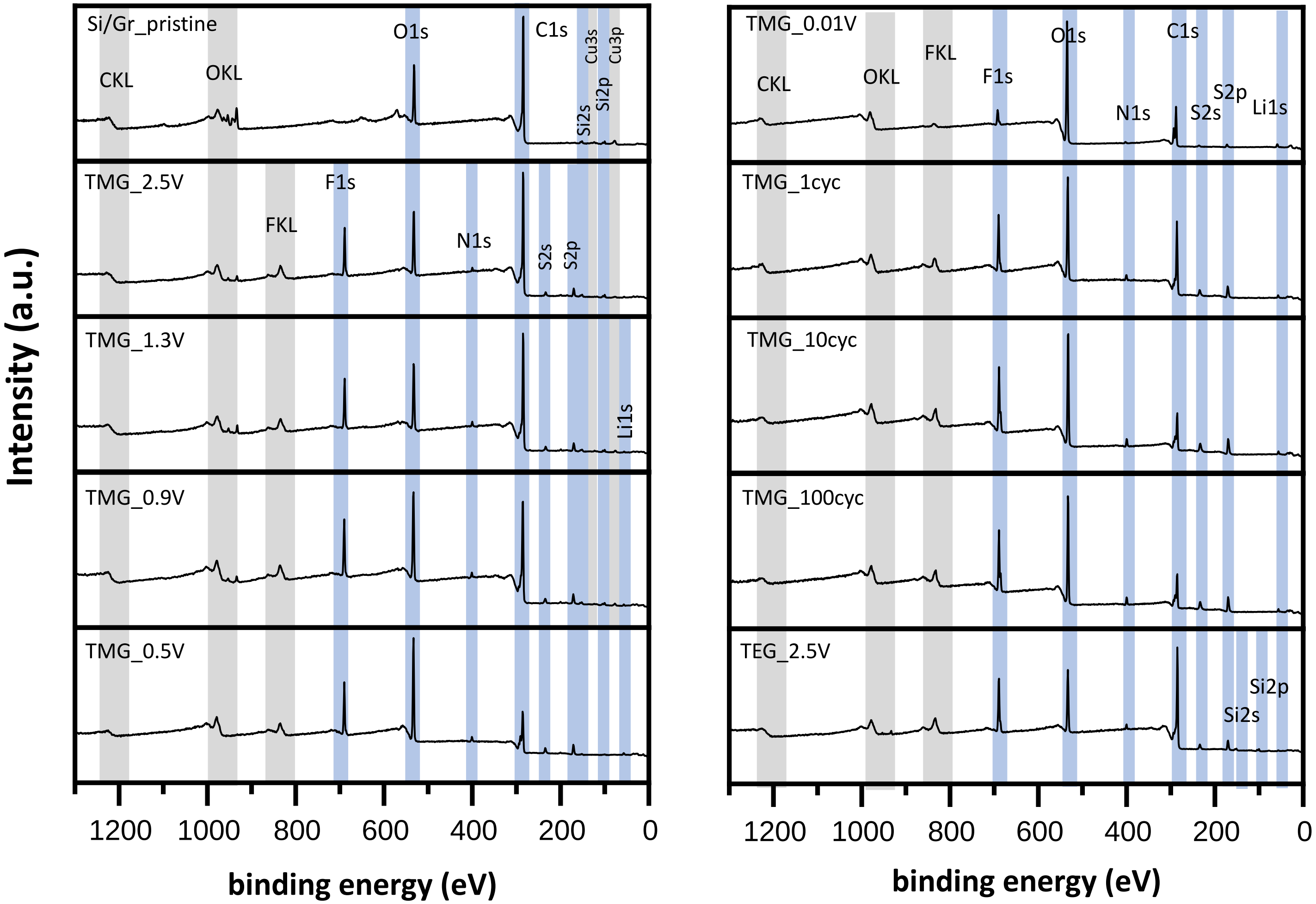

Figure A22: Survey spectra of Si/Gr electrodes cycled in TMG to 2.5 V, 1.3 V, 0.9 V, 0.5 V, and 0.01 V during the 1st lithiation and to 1.5 V after the 1st, 10th, and 100th cycle. As well as survey spectra of Si/Gr electrodes cycled in TEG to 2.5 V during the 1st lithiation.

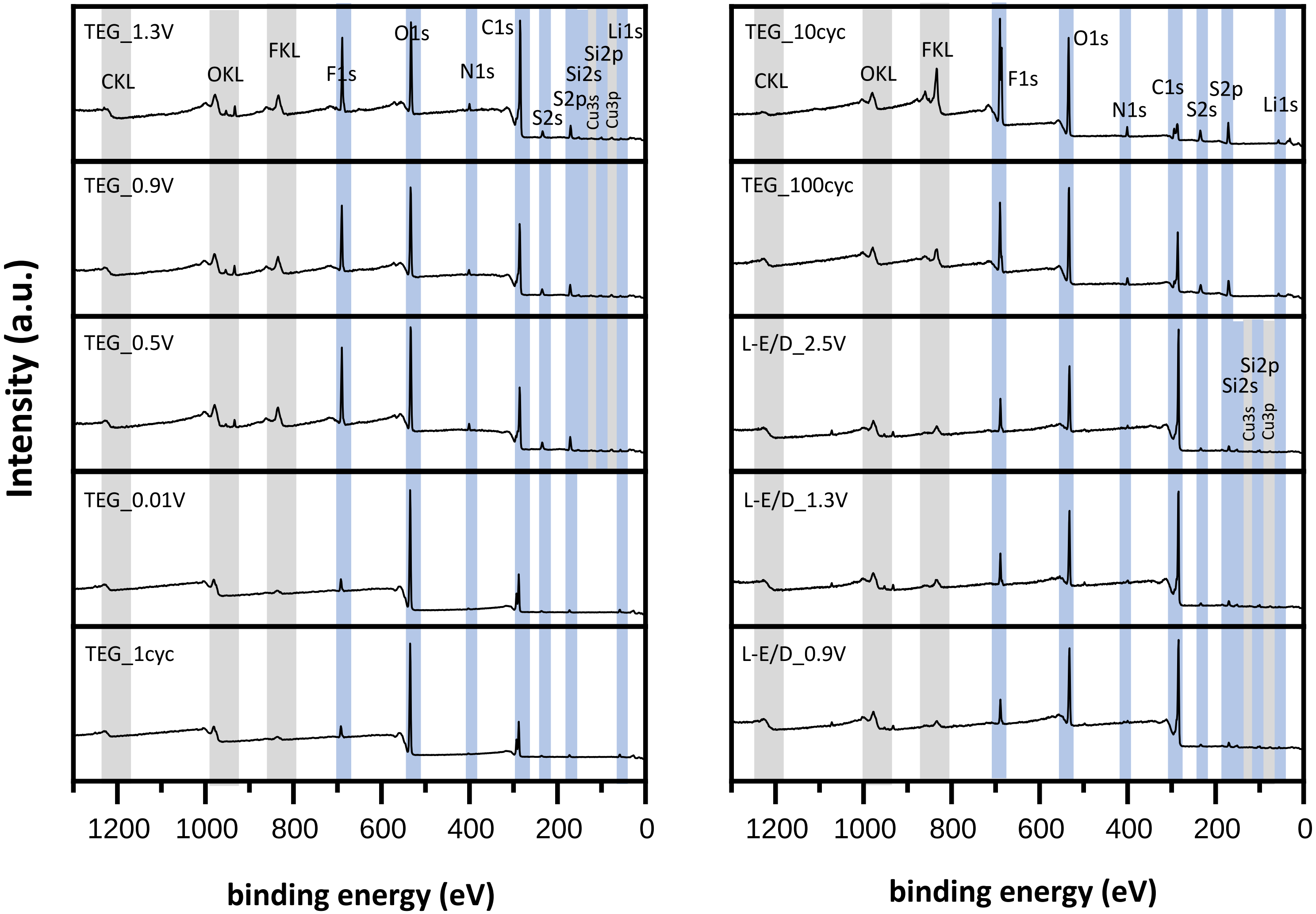

Figure A23: Survey spectra of Si/Gr electrodes cycled in TEG to 1.3 V, 0.9 V, 0.5 V, and 0.01 V during the 1st lithiation and to 1.5 V after the 1st, 10th, and 100th cycle. As well as survey spectra of Si/Gr electrodes cycled in L-E/D to 2.5 V, 1.3 V, and 0.9 V during the 1st lithiation.

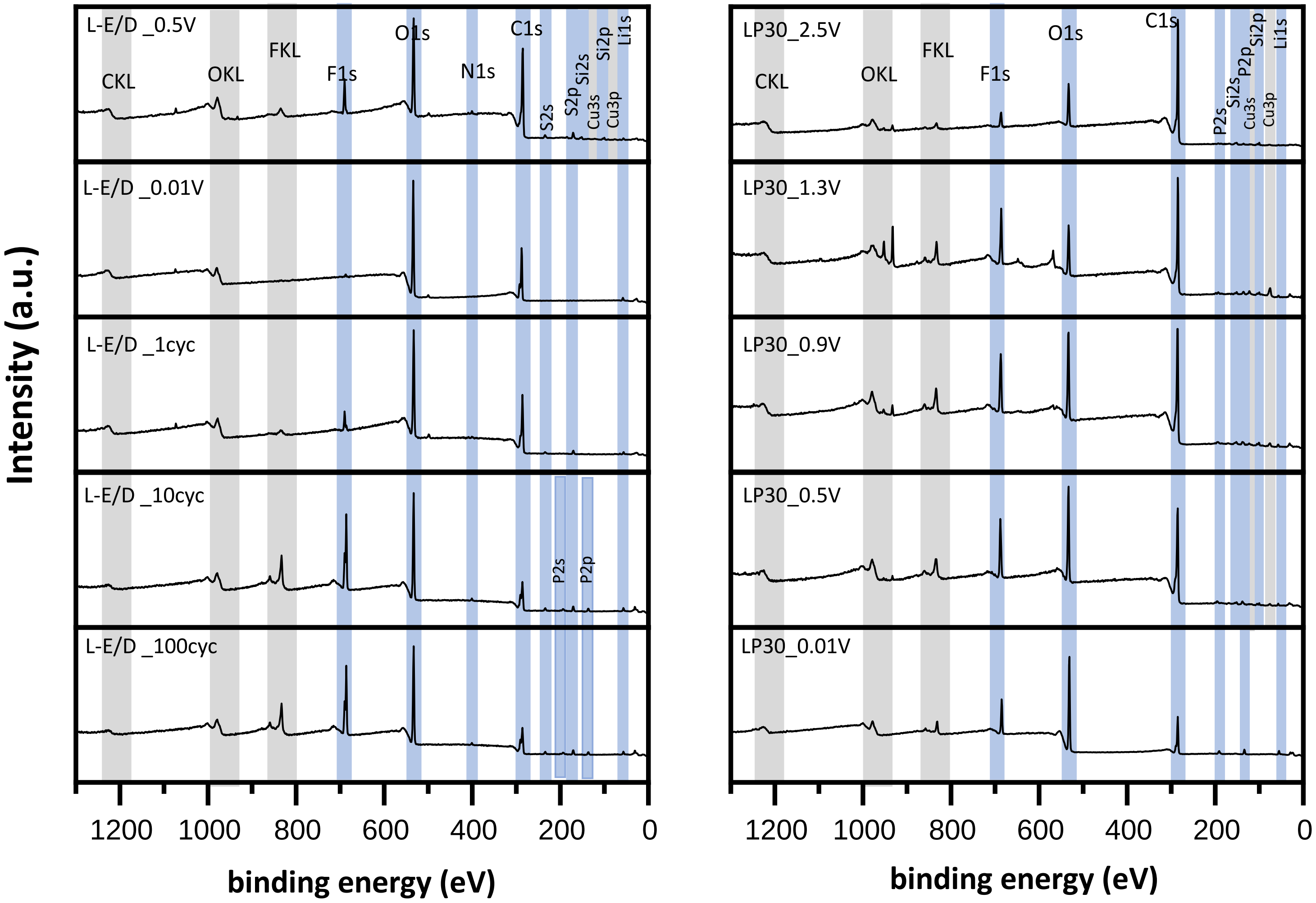

Figure A24: Survey spectra of Si/Gr electrodes cycled in L-E/D to 0.5 V and 0.01 V during the 1st lithiation and to 1.5 V after the 1st, 10th, and 100th cycle. As well as survey spectra of Si/Gr electrodes cycled in LP30 to 2.5 V, 1.3 V, 0.9 V, 0.5 V, and 0.01 V during the 1st lithiation.

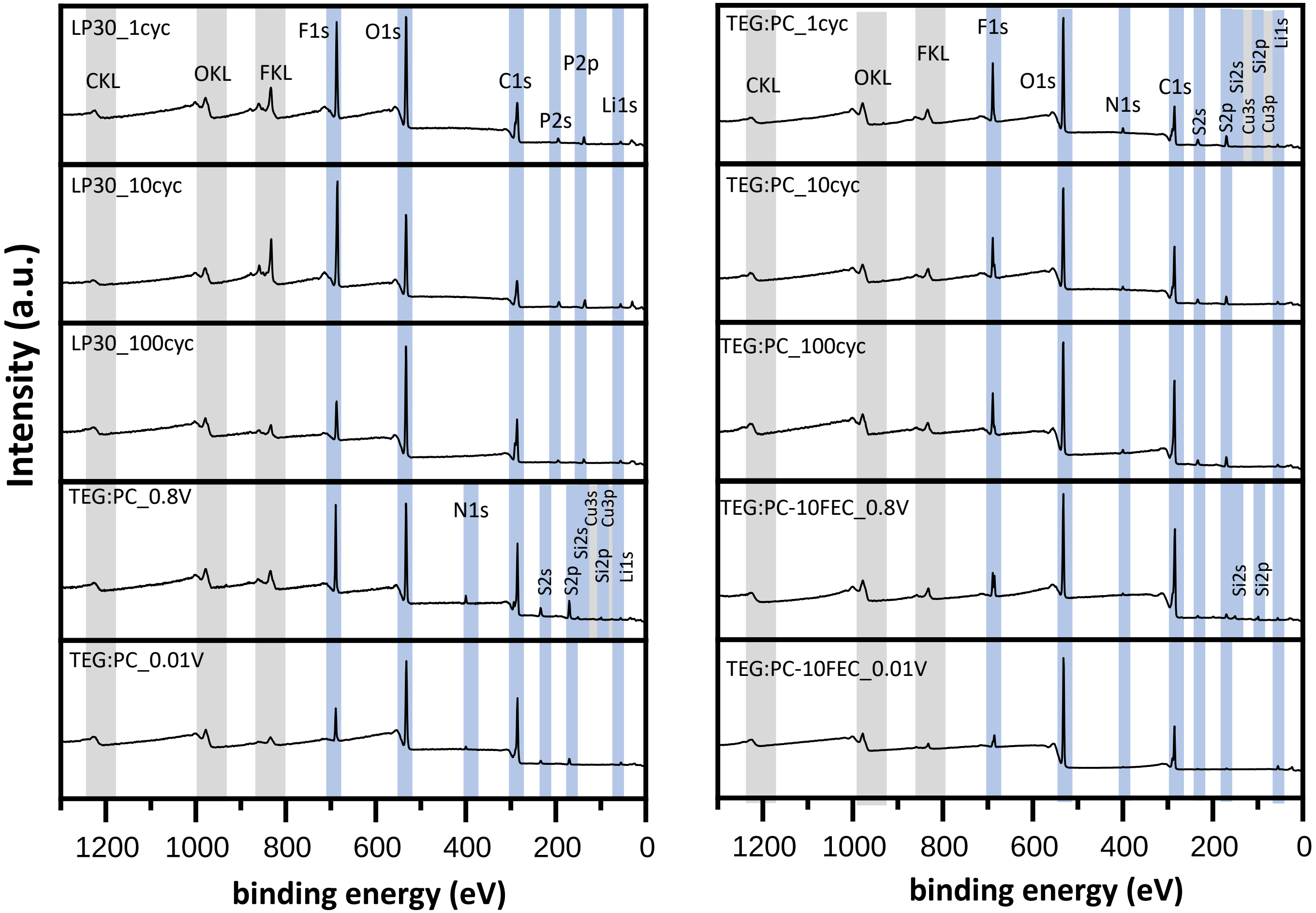

Figure A25: Survey spectra of Si/Gr electrodes cycled in LP30 to 1.5 V after the 1st, 10th, and 100th cycle. As well as survey spectra of Si/Gr electrodes cycled in 30TEG:70PC to 0.8 V, 0.01 V during the 1st lithiation and to 1.5 V after the 1st, 10th, and 100th cycle. Survey of Si/Gr electrode cycled in 30TEG:70PC-10FEC to 0.8 V and 0.01 V during the 1st lithiation are also shown.

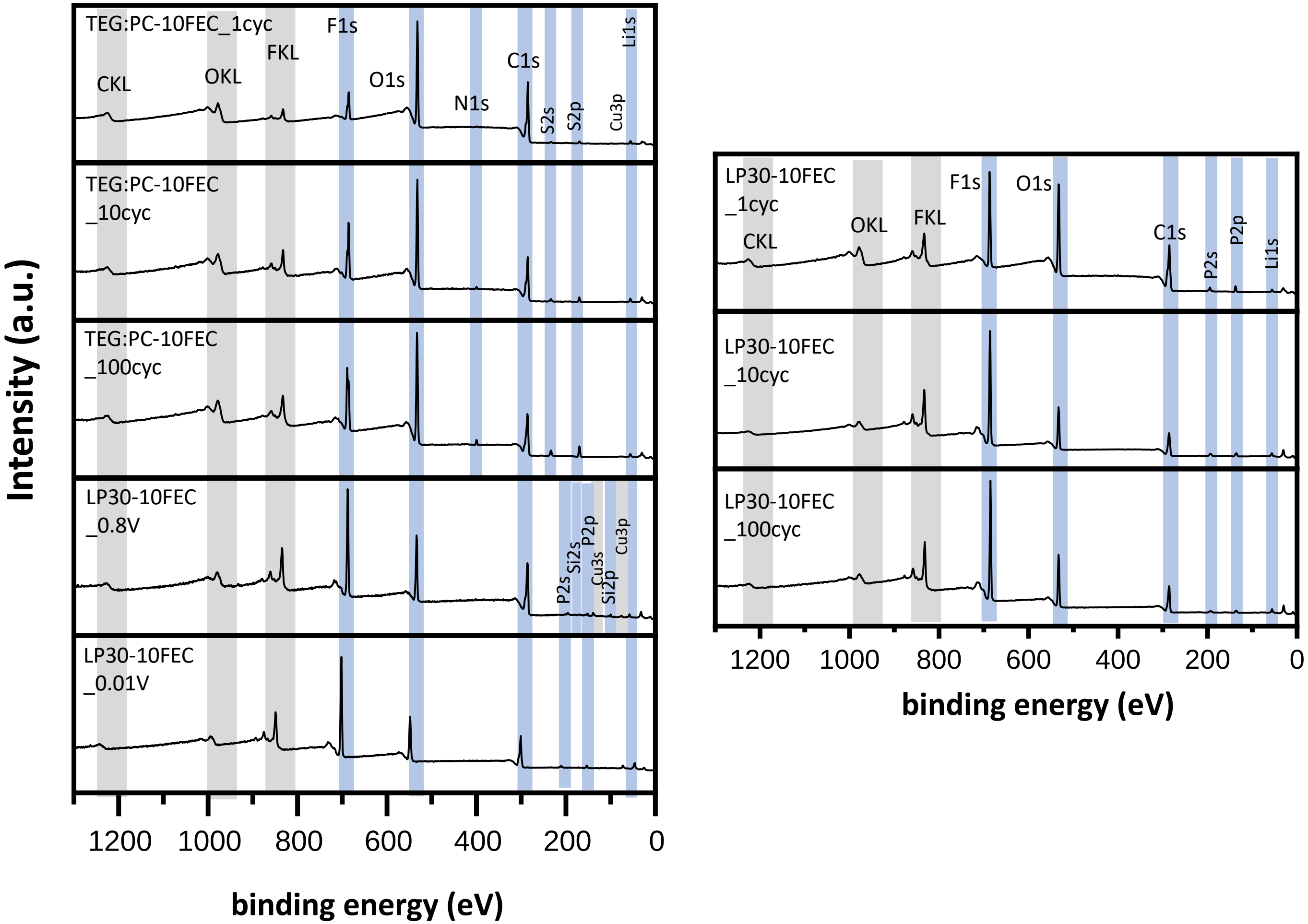

Figure A26: Survey spectra of Si/Gr electrodes cycled in 30TEG:70PC-10FEC to 1.5 V after the 1st, 10th, and 100th cycle. As well as survey spectra of Si/Gr electrodes cycled in LP30-10 to 0.8 V, 0.01 V during the 1st lithiation and to 1.5 V after the 1st, 10th, and 100th cycle.

Publications & Conference Contributions

Publications:

Gehrlein, L.; Njel, C.; Jeschull, F.; Maibach, J.; From Additive to Cosolvent: How FEC Concentrations Influence SEI Properties and Electrochemical Performance of Si/Gr Anodes, *ACS Applied Energy Materials* **2022**, 5, 9, 10710-10720. https://doi.org/10.1021/acsaem.2c01454

Gehrlein, L.; Leibing, C.; Pfeifer, K.; Jeschull, F.; Balducci, A.; Maibach, J.; Glyoxylic Acetals as Electrolytes for Si/Graphite Anodes in Lithium-Ion Batteries, *Electrochim. Acta* **2022**, 424, 140642. https://doi.org/10.1016/j.electacta.2022.140642

Bothe, A.; Gehrlein, L.; Fu, Q.; Li, C.; Maibach, J.; Dsoke, S.; Balducci, A.; Glyoxal-Based Electrolytes in Combination with Fe_2O_3@C-Based Electrodes for Lithium-Ion Batteries, *Batteries and Supercaps* **2022**, e202200152, 1-8. https://doi.org/10.1002/batt.202200152

Stockhausen, R.; Gehrlein, L.; Müller, M.; Bergfeldt, T.; Hofmann, A.: Mueller, F.J.; Maibach, J.; Ehrenberg, H.; Smith, A. Investigating the Dominant Decomposition Mechanisms in Lithium-Ion Battery Cells Responsible for Capacity Loss in Different Stages of Electrochemical Aging, *J. Power Sources* **2022**, 543, 231842. https://doi.org/10.1016/j.jpowsour.2022.231842

Zhao, Z.; Gehrlein, L.; Bothe, A.; Maibach, J.; Balducci, A.; Maibach, J.; Dsoke, S. Impact of 3-Cyanopropionic Acid Methyl Ester on the Electrochemical Performance of $ZnMn_2O_4$ as Negative Electrode for Li-Ion Batteries. *Energy Technol.* **2021**, 9 (8), 2100247. https://doi.org/10.1002/ente.202100247

Stockhausen, R.; Hofmann A.; Gehrlein, L.; Bergfeldt, T.; Müller, M.; Ehrenberg ,H.; Smith, A. Quantifying Absolute Amounts of Electrolyte Components in Lithium-Ion Cells Using HPLC. *J. Electrochem. Soc.* **2021**, 168 (8), 080504. https://doi.org/10.1149/1945-7111/ac1894

Dietrich, P. M.; Gehrlein, L.; Maibach, J.; Thissen, A. Probing Lithium-Ion Battery Electrolytes with Laboratory Near-Ambient Pressure XPS. *Crystals* **2020**, 10 (11), 1056. https://doi.org/10.3390/cryst10111056

Conference Contributions:

239th ECS Meeting (online presentation, 2021): Gehrlein, L.; Leibing C.; Pfeifer K.; Balducci A.; Maibach J. Glyoxales as New Electrolytes for Si/Graphite Anodes in Lithium-Ion Batteries: Analysis of the Solid-Electrolyte Interphase. *Meet. Abstr.* **2021**, MA2021-01 115.

Jena Summer School (live presentation 14.09.2020): Gehrlein, L.; Leibing C.; Pfeifer K.; Balducci A.; Maibach J. Solid Electrolyte Interphase of Glyoxal Electrolytes LiTFSI-TEG & LiTFSI-TMG on Si/Gr Anodes for Lithium-Ion Batteries.

EMRS Fall Meeting 2019 (poster): Gehrlein, L.; Zhao, Z.; Das, C.; Dsoke, S.; Maibach, J. Do Surface Reactions Contribute tot he Additional Capacity of $ZnMn_2O_4$ Anodes for Lithium-Ion Batteries?

Contributions of co-authors and other researchers

Chapter 5 is extracted from the scientific publication “From Additive to Cosolvent: How FEC Concentrations Influence SEI Properties and Electrochemical Performance of Si/Gr Anodes“, published in *ACS Energy Materials*. Planning, organization, and conception of the presented work and all included electrochemical and XPS experiments were done by Lydia Gehrlein and supervised by Julia Maibach. Furthermore, Lydia Gehrlein has written the manuscript. Christian Njel helped interpretating the XPS data and carried out all XPS sputtering measurements. Interpretation of electrochemical data was supported by Fabian Jeschull. Preliminary work on testing different electrolyte formulations was carried out by Tim Bastek and Celine Röder during their “*Vertiefer”* internship. Furthermore, Celine Röder did the electrochemical testing for the cell cycled in the 20FEC:40DMC:40EC and LiTFSI-20FEC:80DCM formulations, shown in Fig.27.

Chapter 6.1 is extracted from the scientific publication “Glyoxylic Acetals as Electrolytes for Si/Graphite Anodes in Lithium-Ion Batteries“, published in *Electrochimica Acta*. Planning, organization, and conception of the presented work and all included electrochemical and XPS experiments were done by Lydia Gehrlein and supervised by Julia Maibach. Furthermore, Lydia Gehrlein has written the manuscript. TEG and TMG electrolyte preparation was conducted by Christian Leibing. Kristina Pfeifer conducted all SEM measurements. Interpretation of electrochemical data was supported by Fabian Jeschull. Andrea Balducci and Julia Maibach helped with XPS and electrochemical data interpretation.

Danksagung

An dieser Stelle möchte ich allen danken, die mich während meiner Promotion unterstützt haben. Mein besonderer Dank gilt:

Prof. Dr. Helmut Ehrenberg, für die Ermöglichung dieser Arbeit am IAM-ESS und seine stetige Unterstützung.

Prof. Dr. Clemens Heske, für das Erstellen des Zweitgutachtens. Außerdem bedanke ich mich für die sehr klare und motivierende PES Vorlesung.

TT. Prof. Dr. Julia Maibach, meiner Betreuerin, die mir dieses interessante Thema zur Verfügung stellte. Ohne die ausführlichen Diskussionen meiner Ideen und meiner Messergebnisse sowie den hilfreichen Anmerkungen wäre meine Arbeit nicht das was sie heute ist. Danke, dass du immer sofort Zeit für meine Fragen und Anliegen hattest.

Prof. Dr. Andreas Balducci und Christian Leibing von der Universität Jena, für die erfolgreiche Kooperation, das Bereitstellen der Glyoxal-basierten Elektrolyte, die gewinnbringenden Diskussionen der Ergebnisse, sowie für die gemeinsame Publikation.

Allen, die mich fachlich bei meiner Arbeit unterstützt haben. Ohne euch hätte ich die jeweilige Messmethode lang nicht so ausschöpfen können. Dr. Fabian Jeschull für die Hilfe bei der Durchführung der Elektrodencoatings und der elektrochemischen Messungen sowie der Interpretation der elektrochemischen Daten. Dr. Njel Christian und Vanessa Trouillet für die fachlichen Diskussionen meiner XPS Messungen und Auswertungen. Dr. Kristina Pfeifer für die REM-Messungen. Ein besonderer Dank an Liuda Mereacre – ohne deine praktische Hilfe, wenn mal wieder was fehlt, kaputt ist oder einen Fehler zeigt, wäre die Laborarbeit nicht möglich! Weiterhin ein großer Dank an meine Studenten Jinjian Wang, Tim Bastek und Celine Röder für ihren außerordentlichen Fleiß und ihre Unterstützung.

Meinen Bürokollegen Ahmad, Anna und Hang für die gute Zeit, die lockere Atmosphäre, die fachlichen Diskussionen und die Menge Spaß. Charlotte, Xinyang und Jessi für die entspannten Abenden. Allgemein geht ein besonderer Dank an das gesamte IAM-ESS für die angenehme Arbeitsatmosphäre und die fachliche Hilfe.

Meinen Freunden außerhalb des IAM-ESS für die tolle Zeit – merci pour votre soutien et pour toutes ces soirées de jeu.

Meinen Eltern und Familie, ohne die das alles nicht möglich wäre. Danke Jan für deine Geduld, deine Hilfe und deinen Humor. Danke, dass ihr an mich glaubt und mich immer unterstützt.